Multi-Scale Modeling and Simulation of Polymeric Liquids in Fast Extensional Flows

by

Soroush Moghadam

A dissertation submitted in partial fulfillment
of the requirements for the degree of
Doctor of Philosophy
(Mechanical Engineering)
in the University of Michigan
2019

Doctoral Committee:

      Professor Ronald G. Larson, Chair
      Professor Katsuo Kurabayashi
      Professor Alan Wineman
      Professor Robert Ziff

Soroush Moghadam

soroushm@umich.edu

ORCID ID: 0000-0002-0382-6751

Dedication

To my beloved parents, Naser and Manijeh, for their endless love and support during my journey in life.

Acknowledgements

This dissertation is the result of great collaboration with my many colleagues and friends at the University of Michigan, University of South Florida, Dow chemical company and Procter and Gamble Company, through whom I have been educated, mentored, admonished and inspired. Specifically, I want to express my greatest thanks to the following individuals for their sustained help and support during my entire Ph. D studies.

First and foremost, I should thank my advisor Prof. Ronald G. Larson, who has been a wonderful teacher and inspiration for me. I learned a great deal from him and am utterly grateful for all his time, patience, kindness and ample scientific supervision in these years. He has been a great mentor to me, both professionally and personally and I consider myself deeply indebted to him.

I am thankful to my former group members Dr. Weizhong Zou and Dr. Wenjun Huang, with whom I collaborated during my graduate studies. I greatly appreciate the useful discussions and collaborations with Prof. Robert Hoy at University of South Florida and William "Trey" Porter III at Dow chemical company. In addition, I am indebted to Mechanical Engineering Department and Rackham Graduate School at University of Michigan, National Science Foundation (NSF), and Dow chemical company; without their funding and resource, my work and this dissertation would certainly not exist.

Table of Contents

List of Tables

List of Figures

and oriented with a folded shape are colored red, instead of green to show the appearance of kinks. (c) The numbers of "kinks" (defined later) per chain as functions of strain from MD simulations (dotted lines) under a constant extension rate of $\dot{\epsilon} = 2.5 \times 10^{-5}$ (in LJ units) and from HBD simulations (dashed lines) under constant extension rate of $\dot{\epsilon} = 10^{-5} \, s^{-1}$. As discussed in the text, these conditions give almost the same values of the product $\dot{\epsilon} t_w \sim 1$ in both MD and HBD simulations. 95

Abstract

This thesis contains simplified simulations of polymers in the entangled melt/solution state and in the glassy state in fast extensional flows where chains become locally stretched at modest strains. Comparisons to experiments show that the "Entangled Kink Dynamics" simulations for entangled chains and the "Hybrid Brownian Dynamics" simulations for glassy polymers improve on existing models. We also present atomistic Molecular Dynamics (MD) simulations of the interactions of for Poly(N-isopropylacrylamide)" (pNIPAAm) excipient with a hydrophobic drug, phenytoin, to improve drug release in the GI tract.

In the first part of the thesis, the conventional "tube-model" constitutive equation is found to predict overly rapid approach to a steady-state extensional viscosity of entangled polystyrene solutions in fast extensional flow. Based on an analysis of the conformation of polymer chains at high strains, a new and simple simulation technique, which we call the "Entangled Kink Dynamics" (EKD), is developed to study the late stage dynamics of polymer chains. In this approach, a highly strained polymer chain in extensional flow is modeled as a quasi-one-dimensional chain with kinks at which the polymer folds back on itself. Polymer strands between the kinks are considered fully stretched and Brownian force is neglected in comparison with drag and tension. The behavior of entangled chains in the kinked state is studied for the cases of dilute chains, affinely moving kinks, and kinks entangled with kinks on other chains. To compare the kink dynamics predictions with experimental results, input is needed from more detailed "single-chain slip-spring" simulations. With this input, EKD simulations show a much better prediction of experimental extensional viscosity of entangled long polystyrene solutions, compared to

conventional tube models. Validating our model, we explain the potential downfalls of the tube theory and provide insight into achieving a better constitutive equation for entangled polymeric melts and solutions.

Secondly, we present a modified Hybrid Brownian dynamics model to study the rheology of polymeric glasses. Using a Coarse-Grained Brownian Dynamics (CG-BD) model for polymer chains suspended in a glassy solvent that represents the segmental model of the glassy polymer, governed by a simple fluidity model, we study the stress and conformation evolution of glassy polymers under fast uniaxial extensional flows and compare our results with fine-grained molecular dynamics simulations of polymeric glass. Although our CG-BD simulations do not have the effect of entanglements explicitly, the conformation evolution of polymer chains in our hybrid technique is found to be similar to that found in MD results, where the entanglements are taken into account explicitly. This proves that in fast flows of glassy polymers, chain conformation is governed by sub-entanglement dynamics and formation of folds, or kinks. The importance of sub-entanglement scales in generating stress becomes hugely important at high strains where polymeric glass show strain hardening. By calculating the number of entangled folds on the chain in the strain hardening regime, we prove that the huge rise in the stress is not due to the effect of entanglements. Instead, we show that strain hardening behavior is caused because of the highly stretched strands between nascent fold points, below the length scales of entanglement spacing.

Finally, in the last chapter we scale down to atomistic levels and study the molecular level interactions between a thermo-responsive polymer called "Poly(N-isopropylacrylamide)" (pNIPAAm) and a hydrophobic drug "phenytoin". First, we validate the chosen forcefield (AMBERFF) and input parameters of our method by comparing the simulation results with the famous coil-to-globule transition of pNIPAAm and then investigate the design domain of chemical

composition to obtain a highly efficient excipient for drug dissolution purposes. By copolymerizing pNIPAAm and a hydrophilic polymer called Dimethylacrylamide (DMA), we show a much better performance of pNIPAAm based carriers for drug crystallization inhibition.

Chapter 1 : Introduction

Polymeric materials have become an inseparable part of our daily life due to their applications in different fields of science, technology and industry. During the past decades, the capability to predict the flow behavior of polymer liquids has been highly sought because of their importance in optimizing and controlling the performance of processing units, which eventually determines the cost and quality of final products. Polymers are processed in the solution, melt, and glassy states, most often by extensional flows, in blowing of films, drawing of fibers, stretching of polymer parts, and many more. Thus, understanding how the polymeric materials, in their liquid state, react to a strong extension is necessary for polymer processing, which is a massive industry worth well over $100 billion per year. For decades, researchers in the field of rheology have tried to develop reliable constitutive equations and models for polymer liquids. However, even with recent advances in computational techniques, quantitative approaches to predict the flow response of entangled polymer liquids are elusive, due to their complex molecular structure. Recent models are not capable of providing correct data for high molecular weight polymers under fast uniaxial extension which limits their applicability in complicated flow fields. Therefore, a systematic analysis is required to pinpoint the shortcomings of current models and connect the molecular behavior to measurable material's response such as stress or strain. To bridge molecular to macroscopic scale phenomena, multi-scale approach seems to be the most reliable method in which multiple models at different time/length scales are used simultaneously to describe the system.

Polymers, as a class of complex fluids, have interesting properties over a broad range of time/length scales including monomeric, coil radius of gyration/hydration and experimental measurement levels. Therefore, to systematically study a polymeric material, one should implement a multi-scale modeling approach to incorporate different physics at different time/length scales ranging from femtoseconds/angstroms to seconds/micrometers or even years in the case of polymer glasses. This broad range presents a unique challenge for computational studies of polymeric fluids. A comprehensive study should provide a clear picture of how the chemistry and structure of materials' composing blocks, or monomers, affect the large-scale dynamics of the polymer, such as its response to applied deformation, temperature/PH change, crystallization, etc. Under different processing conditions, polymers exhibit complex response to the applied force or deformation, spanning from the linear viscoelastic regime, where the stress varies linearly with deformation and the departure of the molecules from their equilibrium state is negligible, to the non-linear viscoelastic regime, where the deformation is large or rapid enough to stretch the molecules considerably. The goal is to develop rheological constitutive equations and simulation techniques capable of predicting the flow response of polymer fluids, such as stress or conformation evolution, under different conditions. However, even with recent developments in the field, our understanding of the underlying physics of polymer liquids is not yet complete and further investigation of their behavior is needed. In addition to conventional experimental techniques, which are used for model validation and material characterization, newly developed simulation approaches have become a nonseparable part of the polymer rheology in the past decade. Molecular dynamics simulations of polymers at different length scales, which can be viewed as "computational experiments", provide a unique opportunity to study polymer dynamics at molecular to meso-scale levels. Novel computational techniques have given new insights into

2

the field of polymer rheology and helped researchers to develop/modify new constitutive equations for polymers under different conditions. However, due to the broad range of time/length scales involved in polymer dynamics, different simulation approaches are required at each scale to appropriately addresses the important dynamics involved at a specific range. Therefore, the best modeling/simulation approach depends on the system one wishes to study and the questions that one wishes to answer. Generally, most models for molecular simulations of polymers fall into either (1) atomistic or (2) coarse-grained (CG) techniques.

For all types of polymer liquids, namely solutions, melts and glasses, if one wishes to study the local, monomer-level forces, fluctuations, or interactions of different species at functional group levels, then atomistic models are the appropriate choice. Many studies during the past decades have used atomistic simulations to analyze monomer-level fluctuations, monomer-monomer contacts/interactions, hydrogen bonding, phase separation at interfaces, solubility, absorption and diffusion of molecules in a fluid, and polymer glass transition [1–15]. However, due to the large system of equations needed to be solved and consequently, their computational expense, atomistic models are limited to time scales of 1 fs $-$ 100 ns and length scales of 1 $-$ 100 Å [7,13]. As a result, one cannot use these models to study phenomena happening at polymer chain-level, such as unraveling dynamics that occurs over larger length and time scales, as discussed in future sections of this thesis. Even with new advances in hardware, such as new CPU (core processing units) generations, and parallelization techniques to perform simulations on tens to hundreds of CPU cores, atomistic models can take days/weeks to run and give in a reliable result. For example, in chapter 4, all the equilibrium final results were gathered after 10 days of simulation runs on 64 processors.

On the other hand, if the goal is to predict conformation/morphology of long polymer chains at a broad range of conditions and applied forces, the best option is to use coarse-grained (CG) models, where some of the degrees of freedom in the system is removed by grouping selected atoms into a single CG bead [16–22]. This approach utilizes the wide separation of length and time scales inherent to polymer systems, where the dynamics at length scales around the polymer chain size, are largely unaffected by the local monomer structure and high frequency motions of individual chemical bonds. Thus, for the sake of computational efficiency, CG approaches remove some of these atomistic details. The removal or coarsening process which determines the resolution of the system, depends on the specific material and goal of the study. For example, in some studies, only hydrogen atoms are removed (i.e. united atoms models [23–26]) while in others, several monomers can be grouped into a single bead [27,28]. By reducing the degrees of freedom and removing the fast motions, one can take larger time steps with CG simulations as compared to atomistic simulations which enables the researcher to study phenomena such as polymer chain relaxation, deformation/stretch, crystallization, and branching. Note that the parameters used in CG models are inherently functions of atomistic details and structure of individual monomers at smaller scales. Computational efficiency and accuracy of coarse-grain models of polymers have made them a reliable choice for researchers to study material response under different conditions. Specifically, to study the rheological properties of polymers, almost all of the simulations use some level of coarse-graining.

While the basics of molecular modeling for polymer liquids in their different forms (melts, solutions and glasses) stay almost the same, due to the difference in the underlying dynamics, such as molecular interactions, the equations developed for each class of these polymer liquids are different. Thus, to analyze each case, one needs to focus on a specific material. In this thesis, we

focus on two classes of polymer liquids, entangled solutions/melts and polymer glasses. Underlying physics of polymer dynamics in each of these materials, our modeling techniques and current modeling/simulation challenges are discussed. Performance of conventional models are tested and possible solutions for their current shortcomings are provided.

We start with the polymer solutions and melts, since the ability to predict the flow behavior of entangled polymeric fluids in strong flows has a huge impact on the performance of processing units used in consumer products, pharmaceutical industries, electronics, etc. The molecular theory of Doi and Edwards [29,30] which is based on the "reptation" concept of De Gennes [31] has proved successful in describing the linear properties of entangled linear chains. The basic theory assumes that the polymer chain undergoes a one-dimensional diffusion inside a "tube", where the tube is the mean-field approximation of the influence of the surrounding mesh of entanglements. During the past few decades, versions of tube theory have been proposed to include several relaxation mechanisms relevant to equilibrium and weak flows [32]. In general, a polymer chain in an entangled network relaxes through (1) reptation, (2) contour length fluctuations and (3) constraint release, where the second and third mechanisms are related to the flexibility of the chain and relaxation of the surrounding network, respectively. A quantitative model combining these three relaxation physics was presented by Likhtman and McLeish [33] and its predictions were found to be in good agreement with the linear rheology of entangled monodisperse linear polystyrene (PS) and polybutadiene (PB) samples. In the nonlinear regime, when a strong flow is applied, other mechanisms need to be incorporated into the theory. The first of these is "segmental stretch," in which the chain inside the tube stretches out due to the frictional force imposed by the surrounding matrix. This concept, introduced by Marrucci and Grizzuti [34] and further examined by Pearson et al. [35] for startup of simple shear flow, results in the Doi-Edwards-Marrucci-

Grizzuti or "DEMG" model [36,37]. The second mechanism, introduced by Marrucci [38], is "convective constraint release (CCR)" whereby a fast flow sweeps away the spatial entanglement constraints around a sample chain, providing additional freedom for the chain to relax. Inclusion of CCR into the tube theory has resulted in different versions of the tube model for fast flows such as the Mead-Larson-Doi (MLD), Double-Convection-Reptation with Chain Stretch (DCS-CS), GLaMM, "Rolie-poly" and Marrucci-Ianniruberto (M&I) models [39–43]. These models result in reasonably good agreement with experimental data in shear; however poorer agreement is attained with experiments in transient fast extensional flows, where the polymer chain is highly stretched and aligned in the flow direction [44,45]. Although in some cases the disagreement is due to neglecting finite extensibility of the chain [41], it seems that there is a general disagreement for high molecular weight chains in fast flows, where the tube model predicts a much smaller Hencky strain ($\epsilon = \dot{\epsilon}t$) to reach the steady-state extensional stress (ϵ_{model}^{ss}) than is observed experimentally (ϵ_{exp}^{ss}) [46]. The recent addition of "friction reduction" to the tube model in extension [47–50] has resulted in better agreement between model predictions and experimental values of the steady-state extensional viscosity (η_e^{ss}), but this does not address the faster attainment of steady-state stress in the model compared to experiments. The inaccuracy of tube-model predictions of stress in extensional flows has attracted increasing attention in recent years and new simulation techniques [51–54] have been developed to shed light on the underlying dynamics of entangled polymers in fast extensional flows.

With recent advances in computational power, analysis of entangled polymers at the molecular level has become possible with the goal of improving the tube theory. In general, simulating the response of an entangled polymer chain can be done using (1) multiple-chain and (2) single-chain techniques. In the former, a simulation box is generated and filled with chains,

wherein the monomers on different chains interact with each other and chain connectivity is conserved. Exemplary of this approach is the work of Kremer and Grest [55] who, by visualizing the motion of a primitive chain, showed the existence of a tube-like region confining the motion of that chain in a melt at equilibrium. Applying this method to strong elongational flows at sufficiently large strains to reach steady state has in the past been challenging, due to excessive elongation and thinning of the simulation box in uniaxial flows [56–58]. While this limitation has now been overcome by a new method of re-mapping the box, still, performing these detailed simulations for long chains ($M_w > 1$Mkg/mol) under high, but not unrealistically high, extension rates ($\dot{\epsilon} > 1/\tau_R$, τ_R being the Rouse relaxation time of the polymer chain) remains computationally time consuming [52]. Therefore, coarse-grained versions of multiple-chain simulations (CG-MCS) have been developed, in which the basic length unit is chosen to be the subchain between consecutive entanglements. This is the approach taken in some slip-link simulation methods, in which entanglements between chains are replaced by slip-links through which the polymer slides longitudinally [59–64]. The recently developed "Primitive Chain Network (PCN)" method has shown good agreement with experimental data for high molecular weight polystyrenes in uniaxial extensional flow at moderate Rouse Weissenberg numbers ($Wi_R = \dot{\epsilon}\tau_R < 4$) [65]. However, the application of this method to higher Rouse Weissenberg numbers ($Wi_R > 4$) has not been tested [65]. Another limitation of the PCN technique is the coarse-graining of the chain at the entanglement level, which results in loss of conformational details at distances smaller than the entanglement spacing [60]. We will show in this thesis that at high strains, kink formation and the unraveling dynamics govern the stress evolution [46]. In this manuscript, we analyze the chain statistics at the kinked state in detail and will show that kinks can form between entangled regions along a chain. The number of these unentangled kinks below the entanglement length-scale

directly affects the stress evolution at high strains. Thus, chain configuration at sub-entanglement level, which is ignored by methods such as PCN, is important.

To limit the required computational power, single-chain techniques have been developed, where the effect of the entanglement network is replaced by slip-links, which confine the movement of the chain and require the chain to slide through them to relax. The concept of slip-links was first introduced by Doi and Edwards [30] and further improved by Schieber and co-workers [66–68] who added additional dynamics such as constraint release and nonlinear effects. Single-chain slip-spring models have also been developed in which the effect of neighboring chains is replaced by virtual springs (or slip-springs) along the backbone of a single chain that not only confine the motion of the chain, but also exert force on the chain [69,70]. Despite their simplicity compared to multi-chain simulations, single-chain results match very well with linear viscoelastic data and nonlinear data in shearing flow, and can provide an intermediate level of detail between multiple-chain simulations and the tube theory [61,70–75]. However, predictions of single-chain simulations have not been very successful for strong extensional flows at high strains [74,76]. Moreover, even for these single-chain models, the computational time becomes unaffordably large as the chains become longer ($N_k > 1000$, N_k being the total number of Kuhn segments in a polymer chain) [77]. Therefore, there is a need for new simulation methods that can correctly predict the late-stage evolution of long chains in strong extensional flows ($Wi_\mathrm{R} \gg 1$). In this thesis, I develop a simulation technique for fast uniaxial deformation of linear polymer chains and test its performance by comparing its results with that of experiments. My study shows the importance of folded or "kinked" regions in late stage dynamics of entangled polymer networks and sheds light on the shortcomings of conventional tube theories. In addition to the development of my "Entangled kink dynamics" technique, I modify the single chain slip-spring model of

Likhtman [70] for use in strong extensional flows, where most of the other models fail or are computationally inefficient.

As a different polymeric liquid under strong deformation, I worked on development of a rheological model for mechanical response of polymeric glass under fast uniaxial deformation. Glassy materials possess remarkable properties such as high stiffness and transparency, good corrosion resistance, low permeability, as well as ease of fabrication [78,79], making them ubiquitous in both traditional and emerging material applications [80–83]. The growing demand for low-cost, lightweight materials with sufficient mechanical strength has led to increasing use of polymeric glasses as substitutes for inorganic materials such as silicon and metals. Such advantages in mechanical properties make polymeric glasses widely-used in the manufacturing with applications being found in a variety of fields: printing and packaging, optics, surface protection and coatings, etc. To ensure their mechanical stability for a variety of loading environments, several methods for strengthening polymeric glasses are available, for example, mechanical preconditioning [84,85], subglass-transition-temperature annealing [86], etc. However, the complicated interplay of chemistry [87,88], entanglement /crosslink density [89], severity of confinement [90], as well as thermomechanical history in determining ultimate mechanical properties of polymeric glasses make it extremely difficult to ensure the above stability-enhancing procedures are reliable [80,82,91]. Moreover, the still-rapid pace of development of new glasses with remarkable performance, including vapor-deposited "ultra-stable" polymer glasses [83], plasticizer-mediated glasses [91], and rigid polymer-cast "superionic" films [92], show that we are still far from a complete understanding of how polymers' molecular structure affects the macroscopic mechanical properties of their bulk glassy state.

Unlike the polymer solutions, for which the relaxation times of the material (τ_R and τ_d) are considered constants, polymer glasses show an interesting phenomena known as physical aging and rejuvenation [93–95]. In simple words, a polymer glass at equilibrium constantly moves toward lower energy wells and re-configures itself and its monomer locations. This causes the relaxation time of the glass to increase as the sample stays intact. On the other hand, upon application of a deformation or stress, the relaxation time quickly decreases, "fluidizing" the glassy material. Adding the intricate relaxation behavior to the intramolecular cooperativity of polymeric glasses, including chain connectivity, stiffness, and finite extensibility, has made the rheological modelling of polymeric glasses a challenging topic for decades. Due to the aforementioned properties, a polymeric glass under constant deformation rate experiment, such as uniaxial extension, exhibits five strain amplitude regimes [94,96–98]. (1) linear elastic stress growth with strain, (2) "anelastic" regime where stress grows more slowly (3) a local stress maximum at yield point followed by a drop of stress (strain softening) (4) a "plastic flow" or "dynamic yielding" regime where the stress stays almost constant, showing a plateau region and (5) a "strain hardening" regime where at large strains, the stress increases rapidly. Therefore, in a more general scope, the mechanical response of a polymer glass under deformation can be divided into two regimes, the "pre-yield" and the "post-yield" regimes. In the pre-yield domain, the mechanical rejuvenation and the glassy or "segmental" relaxation are coupled while in the post-yield regime, the stress contribution from the polymeric part become hugely dominant and the glassy relaxation plays a small role in the dynamics of the system.

Some recently developed coarse-grained theoretical models [93,94,99–102] are beginning to yield important insights into the interplay of polymeric and glassy components at different regimes of deformation. By separating the polymeric and segmental contribution to the stress, and

10

assuming that polymer glass can be represented by a single polymer chain in a glassy solvent, Zou and Larson recently published a coarse-grained "hybrid" model [103], in which a one-mode Maxwellian equation for local segmental relaxation with time constant (τ^s) was used to predict the local frictional drag that a "glassy solvent" exerts on an isolated-chain representing the larger-scale "polymeric" relaxation (with time constant $\tau^p = \alpha\tau^s$, where α is the polymer-to-segmental relaxation time ratio). While the idea of separating glassy and polymeric modes had been previously examined by Fielding et al. [104,105], inclusion of a CG polymer chain, which inherently has multiple relaxation modes for the polymer chain, improved the model's predictions considerably. Using a simple fluidity model describing the nonlinear response of τ^s under applied deformation, the stress from the segmental mode was added to that produced by polymeric relaxation, whose dynamics were approximated by a bead-spring chain with bead drag coefficient proportional to τ^s. Although the interplay between segmental and polymeric stresses allows for this hybrid model to capture much of the experimental phenomenology of deformed polymeric glasses, the model ignores polymer entanglements. It also ignores energetic terms arising from pair, covalent-bond, or angular interactions that are known to be important in determining the overall mechanical properties of polymeric glasses [92,106–111]. One might therefore expect this model to break down in the post-yield regime, where effects of the above energetic terms become increasingly important [112]. Furthermore, the hybrid model approach uses a simple fluidity model for the segmental relaxation time of the polymeric glass while recent experimental measurements show a broad range of relaxation domain for glassy materials. The simple one-mode fluidity model of Zou and Larson also give rise to the question of their model's validity at pre-yield regime, where the interplay of aging and rejuvenation is important. On the other hand, there is considerable evidence that single-chain in-mean-field models can in fact capture much of the physics of large-

strain deformation, including strain hardening, at least up to the beginning of the "dramatic" supra-Gaussian regime of the stress-strain curve [113–115]. As suggested by Zou and Larson [103], strain-hardening results primarily from highly-stretched and folded chain conformations ("kinks") rather than from rheological entanglements. Significantly, the onset of strain hardening at Hencky strains of order unity is correctly predicted by this model, in agreement with experimental data, and with a hardening modulus greatly in excess of the polymer entanglement modulus, also consistent with experiments. These findings suggest strongly that entanglements are not the key feature of strain hardening, which is instead caused by the large stretch of sub-entangled strands of polymers at deformation rates much greater than the rate at which those strands can relax their configurations. Unfortunately, it is not yet possible to test this suggestion experimentally, despite the applications of many novel experimental methods to deformed polymeric glasses [80,86,116]. MD simulations, however, offer an alternative avenue for exploring and testing new theories [92,106,108,109,111,117–121], and can provide complete information on polymer conformations. Thus, MD simulations allow testing of the assumptions and findings of the coarse-grained hybrid-BD (HBD) model, in particular, its ability to predict strain hardening despite neglecting entanglements. In this thesis, we study the effect of multi-mode relaxation for glassy dynamics and by comparing the HBD model with MD simulations performed by our collaborator, Prof. Robert. S. Hoy at University of South Florida, we shed light on the role of entanglements in strain hardening of polymeric glass in strong uniaxial deformations.

As a different research direction, I also worked on another topic, in which I used atomistic molecular dynamics simulations to assess the efficacy of thermoresponsive poly(N-isopropylacrylamide) in drug delivery applications. Biocompatible and biodegradable polymeric excipients are used in solid dispersion techniques to improve the solubility of the newly developed

Active Pharmaceutical Ingredients (APIs), which are mostly hydrophobic and tend to aggregate and crystalize upon abrupt release in the gastrointestinal tract [122–124]. One of most interesting groups of polymers used in solid dispersion techniques are the stimuli-responsive polymers which change their properties due to the environmental variations in temperature, pressure, light, pH, etc. [125,126] Poly(N-isopropylacrylamide) or simply pNIPAAm, is a biocompatible, thermosensitive polymer that possesses a lower critical solution temperature (LCST). As the temperature increases above $\sim 32^o$C in a pNIPAAm aqueous solution, polymer chains tend to decrease their interaction with water, leading to a coil-to-globule transition resulting in a compact conformation in water, and release of the drug molecules inside the solution [126–129]. Many experimental studies have analyzed the collapse of pNIPAAm chains and hydrogels in aqueous solutions [130–134]. Yang et al. [135], Huang et al. [136] and Zhi et al. [137] used analytical solution theories to model these thermo-sensitive hydrogels, but to be accurate, such models need inclusion of parameters obtained by molecular simulations. With advances in molecular dynamics techniques, it has become feasible to simulate pNIPAAm chains directly to test the ability of different forcefields to predict chain collapse, and to determine the role of binding kinetics between different functional groups and solvent molecules [7,138–140]. As previous studies, both experimental and computational, have revealed, the collapse of pNIPAAm is driven by the weakening of hydrogen bonding with water at elevated temperatures, namely above 32^oC, leading to dominance of the hydrophobic interactions between isopropyl groups in adjacent monomers [141,142]. Interestingly, this happens at a temperature close to the body temperature (37^oC), which, along with other properties of pNIPAAm, such as the large design space of its copolymers, makes this polymer a potentially attractive possibility as an excipient for controlled drug release. Although aqueous solutions of pNIPAAm have been widely analyzed both experimentally and computationally, a detailed

13

simulation study of excipient-API interactions in water and their effect on crystallization is not yet available for pNIPAAm. In particular the promising alternative of analyzing the interactions between polymer and API molecules by molecular dynamics has not yet been carried out for pNIPAAm and its copolymers in aqueous solutions. In this thesis, I explore the backbone structural design of pNIPAAm chains for efficient absorption of hydrophobic drug molecules at body temperature by studying the effect of configurational tacticity and copolymerization on its interactions with Phenytoin, an anti-seizure drug molecule.

The thesis is organized as follows:

In chapter 2, we review tube theory based constitutive modeling of entangled polymer melts and solutions under fast extensional rheology and show the discrepancy between experimental data and theory's predictions. Hypothesizing that the disagreement between theory and experiment is due to a missing physics in the tube theory, we introduce the unraveling dynamics and develop a simulation technique called "Entangled kink dynamics (EKD)" to study the response of an entangled system when the unraveling is included. Using the EKD technique, we perform simulations corresponding to real entangled systems and compare experimental data and kink dynamics prediction.

The third chapter focuses on the development of a smaller scale simulation technique for nonlinear rheology of entangled polymer fluids. It discusses the development of a single-chain slip-spring simulation approach, inspired by the works of Likhtman and coworkers [70,143], and modified using the result of our developed EKD analysis. This coarse-grained single chain simulation approach provides a fast and reliable platform for analyzing the behavior of entangled linear polymer chains under non-linear deformation.

Switching to the polymeric glass, the hybrid model of Zou and Larson is reviewed, and its shortcomings are discussed in chapter 4. Then, implementation of multi-modes glassy dynamics and the effect of entanglements on the strain hardening behaviour of polymer glass at large deformations in extensional flow is analyzed. By studying the presence of folded or kinked regions on polymer chain using molecular dynamics data, we reveal the underlying physics behind the rapid stress rise in a polymeric glass at high strains. We show that although the model uses a simple segmental relaxation equation, it can quantitatively predict the overall stress-strain response of the polymeric glass under startup extension.

In the last chapter of my thesis, I focus on the atomistic simulation of thermo-responsive pNIPAAm chains. By testing different partial charge assignment techniques, behavior of single chain pNIPAAm oligomers in an aqueous solution and its response to temperature rise are studied. Using a validated forcefield and input parameters, I perform atomistic molecular dynamics simulations where both pNIPAAm and API molecules are present and show the effect of excipient presence in preventing the aggregation of hydrophobic drug molecules. We also add comonomers to the pNIPAAm chains and show that interactions of phenytoin (as a hydrophobic drug molecule) with copolymers of pNIPAAm are consistent with experimental results, proving that there is an optimal molar percent of co-monomer that maximizes the excipient efficiency at body temperature [144]. We can also provide a quantitative explanation of the physics behind the phenomenon.

Chapter 2 : Tube Model and Unraveling Dynamics

2.1   Abstract

The traditional Doi-Edwards tube model, applied to extensional flows at strain rates above the inverse Rouse time, predicts that the tube deforms affinely, which implies that the extensional stress reaches its plateau as soon as the chain has become locally fully stretched, even if the chain is still folded, and far from being completely unraveled. By starting from a state in which the chain is in a locally fully stretched, but folded, state, we develop an "entangled kink dynamics algorithm" that predicts the final unraveling of an ensemble of mutually entangled, folded chains, driven by a combination of drag forces and chain tension, with negligible Brownian motion. Equations for motions of both unentangled folds and entangled folds in which two chains hook together at a single fold point, are derived and solved, including the effects of constraint release that occurs when the end of one chain passes through the fold at which that chain is entangled. This model predicts that the stress approaches its final plateau stress only after complete chain unraveling, which for long chains is at much higher strains than in the tube model.

2.2   Introduction

The dynamics of entangled polymeric fluids and their rheological properties in linear and nonlinear deformations have a significant impact on polymer processing.   Entanglement

16

constraints in melts and concentrated solutions restrict the chain movement to "reptation," preferentially along the chain contour, as described by de Gennes [31] and Doi and Edwards [145]. The original Doi-Edwards (DE) theory for nonlinear deformations assumes instantaneous and complete chain retraction within a mesh of constraints affinely deformed by the flow. This assumption fails to predict accurately the steady-state shear viscosity and stress relaxation after flow cessation in shear. A more advanced version of the DE theory by Marrucci and Grizzuti (the DEMG theory) [34,36] adds chain stretch to the model, which addresses some of its shortcomings, but still fails to predict the monotonic dependence of first normal stress difference and shear stress on shear rate that is often observed [37].

More recently, convective constraint-release (CCR) was introduced into the model by Marrucci and Ianniruberto [146], assuming that when the flow is fast compared to inverse of relaxation time of the entangled system, spatial constraints around a sample chain are being swept away by the flow, providing freedom to the polymer chain to relax much faster compared to slow flow or pure reptation relaxation. Including this new physics leads to better agreement with experimental data, as shown by models such as the Mead-Larson-Doi (MLD), Double-Convection-Reptation with Chain Stretch (DCS-CS), GLaMM and "Rolie-poly" models [39–42,147], at least in shear flows. However, there are still significant inaccuracies in extensional flows, even with these improvements and with carefully determined material inputs, namely the Rouse relaxation time (τ_R), the reptation time (τ_d), the plateau modulus (G_N^0) and the maximum extensibility of a tube segment ($\lambda_{max} = \sqrt{N/Z}$), where N and Z are the number of Kuhn steps and tube segments in the chain, respectively. Bhattacharjee et al.[45] and Nguyen et al.[148], for example, give predictions of different tube models that clearly deviate significantly from the steady-state and transient stresses in uniaxial extension for the flow regimes $\tau_d^{-1} < \dot{\epsilon} < \tau_R^{-1}$ and $\dot{\epsilon} > \tau_R^{-1}$, where $\dot{\epsilon}$

is the rate of extensional strain. The disagreement worsens as the molecular weight (M_w) and the Weissenberg number ($Wi_R = \dot{\epsilon}\tau_R \gg 1$) increase [46,50], especially at high strains where the disentanglement and chain stretch dominate the entangled polymers. Although performing extensional rheometry for high molecular weight polymers at high extension rates is experimentally challenging, the disagreement between available data in the literature and model predictions is clear, for both transient and steady state response. A recent addition to the tube model, which generally improved tube theories' predictions for extensional rheometry, is the consideration of friction reduction in concentrated polymers or melts. It is suggested that the alignment of Kuhn segments results in reduction in local friction coefficient in fast flows, which decreases both τ_R and τ_d [47–49]. Although inclusion of friction reduction in tube model results in better agreement of steady-state extensional viscosity with that of experiment for polymer melts [50], its use for entangled solutions, especially for those of low polymer weight, is less justifiable.

A questionable assumption of tube theory is that the tube deforms affinely, which is a mean-field assumption in conflict with the argument of Rubinstein and Panyukov [149,150] that an entanglement network deforms non-affinely. Some recent coarse-grained models treat entanglements as local interactions between two chains with the velocity of the entanglement point set not by the affine motion assumption, but by a force balance involving the tension in the two chains at that point [60,65,149–151]. As we will discuss in the following, our fast, simplified, "entangled kink dynamics" simulation technique also solves a force balance at each entanglement point, and also results in non-affine motion. We, moreover, show that dropping this force balance in favor of affine motion of the entanglement point, as in the tube model, results in predictions for stress that disagree markedly both from our model and from experimental data.

Our analysis focuses on an entangled system at high strains where the effect of chain stretch becomes significant. In this work, we introduce new physics for the final stages of stress growth in extension without assuming affine motion and we consider tube models without friction reduction to reduce the number of input variables and avoid any data fitting to match our results with those of experiments. Therefore, we do not need any inputs other than those required by the basic tube model, $\tau_R, \tau_d, G_N^0, M_w, Z$.

First, we test the performance of two of the most popular models in predicting the extensional viscosity of high molecular weight polystyrene solutions. Figures 2.1-2.3 show the rather poor performance of the standard one-mode (or "toy") version of DEMG and MLD models [152,153] in predicting the transient extensional viscosity of three samples of linear polystyrene solutions at high Wi_R. To find the predictions of the theory, we use the one-mode, or "toy" version of the DEMG model developed by Pearson et al. [152,154]:

$$\overset{\triangledown}{\boldsymbol{S}}_{tube} + 2\boldsymbol{k}:\boldsymbol{S}_{tube}\boldsymbol{S}_{tube} + \frac{1}{\tau_d}\left(\boldsymbol{S}_{tube} - \frac{1}{3}\boldsymbol{\delta}\right) = \boldsymbol{0} \tag{2.1}$$

$$\dot{\lambda} = \lambda\,\boldsymbol{k}:\boldsymbol{S} - \frac{k_s(\lambda)}{\tau_R}(\lambda - 1) \tag{2.2}$$

$$\boldsymbol{\sigma} = 3G_N^0 k_s(\lambda)\lambda^2 \boldsymbol{S} \tag{2.3}$$

$$k_s = \frac{(3\lambda_{max}^2 - \lambda^2)/(\lambda_{max}^2 - \lambda^2)}{(3\lambda_{max}^2 - 1)/(\lambda_{max}^2 - 1)} \tag{2.4}$$

Where in equation (2.1), $\overset{\triangledown}{\boldsymbol{S}}_{tube}$ is the orientation tensor that describes the average orientation of the tube segments in three-dimensional space. The symbol $\triangledown$ above the orientation tensor $\boldsymbol{S}_{tube}$ is its "upper convective derivative" [152,155] and $\boldsymbol{k} = (\nabla v)^T$ is the transpose of the velocity gradient

tensor. Equation (2.2) represents the tube segments, or chain, stretch which consists of two terms, the first one being the affine deformation with the macroscopically applied flow and the second term stands for chain retraction. Equation (2.3) is the stress equation where the coefficient k_s accounts for the nonlinearity of the spring and is approximated using the Cohen-Pade approximation of the inverse Langevin function [156]. For MLD model, which includes CCR, Equations (2.5) - (2.9) are used:

$$\frac{1}{\tau} = \frac{1}{\lambda^2 \tau_d} + \frac{1}{\lambda}\left(k:S - \frac{\dot{\lambda}}{\lambda}\right) \tag{2.5}$$

$$\overset{\triangledown}{S}_{tube} + 2k:S_{tube}S_{tube} + \frac{1}{\tau}\left(S_{tube} - \frac{1}{3}\delta\right) = 0 \tag{2.6}$$

$$\dot{\lambda} = \lambda\, k:S - \frac{k_s(\lambda)}{\tau_R}(\lambda - 1) - \frac{1}{2}(\lambda - 1)\left(k:S - \frac{\dot{\lambda}}{\lambda}\right) \tag{2.7}$$

$$\sigma = 3G_N^0 k_s(\lambda)\lambda^2 S \tag{2.8}$$

$$k_s = \frac{(3\lambda_{max}^2 - \lambda^2)/(\lambda_{max}^2 - \lambda^2)}{(3\lambda_{max}^2 - 1)/(\lambda_{max}^2 - 1)} \tag{2.9}$$

Note that the main difference between DEMG and MLD models shown here is in Equation (2.5), which shows the evolution of representative relaxation time of the polymer chain due to entanglement convection effect [39].

Input data for the models are taken from experimental data reported by Huang et al. [157] and are summarized in Table 2.1. Note that the parameters listed in Table 2.1 are related to each other via well-established methods, for example knowing τ_e and Z, one can find τ_R using $\tau_R = \tau_e Z^2$ [50,157]. Although due to instrumental limitations experimental data may have not reached the final values, we can clearly observe that the tube model predicts a much smaller Hencky strain

to reach a steady-state extensional stress than is observed experimentally, $\epsilon_{ss}^{exp} > \epsilon_{ss}^{model}$. The magnitude of the difference depends on extension rate ($\dot{\epsilon}$) and molecular weight (M_w), as shown in the figures. In this chapter, we show that this difference in strain to achieve the plateau is due to an incorrect assumption of affine deformation of the tube throughout the unraveling process. This affine motion requires that, after polymer chains are locally fully stretched and oriented but still folded rather than fully unraveled, the fold points are able to support an arbitrarily high chain tension, and propagate this tension along the chain, culminating in a very high maximum tension at the center of the chain. We show that in entangled polymers at high strains, once tube segments become fully stretched, the monotonic increase in tension from the ends of the chain to its center, required by the tube model, would lead to a high tension at the center of the chain, which cannot in general be supported by the partner entangled chains. Instead, we show that the tension remains much more modest, even at the chain center, until the chain is fully unraveled into a globally extended state, which requires larger strain than predicted by the tube model for tension (and stress) to saturate. We begin, in this chapter, by introducing our kink dynamics model and the governing equations of unraveling dynamics in entangled polymeric systems. Kink dynamics results under different assumptions are found and compared. Specifically, we show how the stress data under affine motion assumption diverges from those under local force balance. Tracking the interchain forces at entanglement points, we find the maximum entanglement force in the system and evolution of tension along the polymer chain's contour length in an entangled system. However, to apply the kink dynamics to real systems, such as the polystyrene samples shown in Figures 2.1-2.3, input data about the chains' configuration and statistics are required. To find the input parameters for our kink dynamics technique, we need a smaller scale simulation method to find the conformation evolution of an entangled system from equilibrium to the kinked state.

Development of such a method is explained in chapter 3. We explain that for the high molecular weight chains, the presence of a significant number of kinks results in a gradual increase in the stress at long times, which is consistent with the experiments of Huang et al. [157]. For shorter chains, this unraveling effect becomes less important, since by the time the short chain achieves the locally fully stretched state, there exists only a few remaining kinks, which quickly unravel. This may explain the better performance of tube models in predicting the transient extensional viscosity of lower molecular weight chains. Our findings provide a new and entirely different picture of late-stage stress evolution of entangled polymeric systems, which can guide future improvements in the tube model.

Table 2.1. Parameters used in the tube models, reported by Huang et al. [157].

M_w(M gr/mol)	ϕ (wt%)	G_N^0 (Pa)	λ_{max}	Z	$\tau_e(s)$	$\tau_R(s)$	$\tau_d(s)$	$\dot{\epsilon}(s^{-1})$	Wi_R
0.9	33	27300	8.2	22.5	0.32	162	5844	0.04	6.48
								0.07	11.34
1.76	18	6850	11.1	22.8	0.66	344	12615	0.03	10.32
								0.06	20.64
3.28	13	2790	13	22.2	1.51	744	26373	0.01	7.44
								0.006	4.464
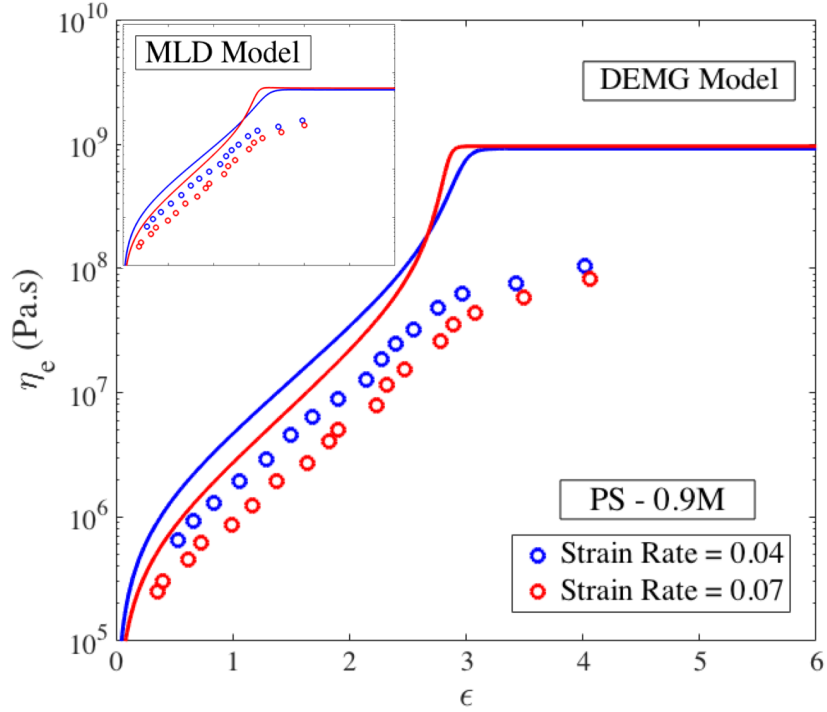
Figure 2.1. Comparison of experimental data [50,157] (o) for 33 wt.% 0.9M polystyrene (PS), with predictions (solid lines) of DEMG (main figure) and MLD (inset) models in uniaxial extension at strain rates $\acute{\epsilon} = 0.04 s^{-1}$ $[Wi_R = 6.48]$ (blue), and $0.07 s^{-1}$ $[Wi_R = 11.34]$ (red).
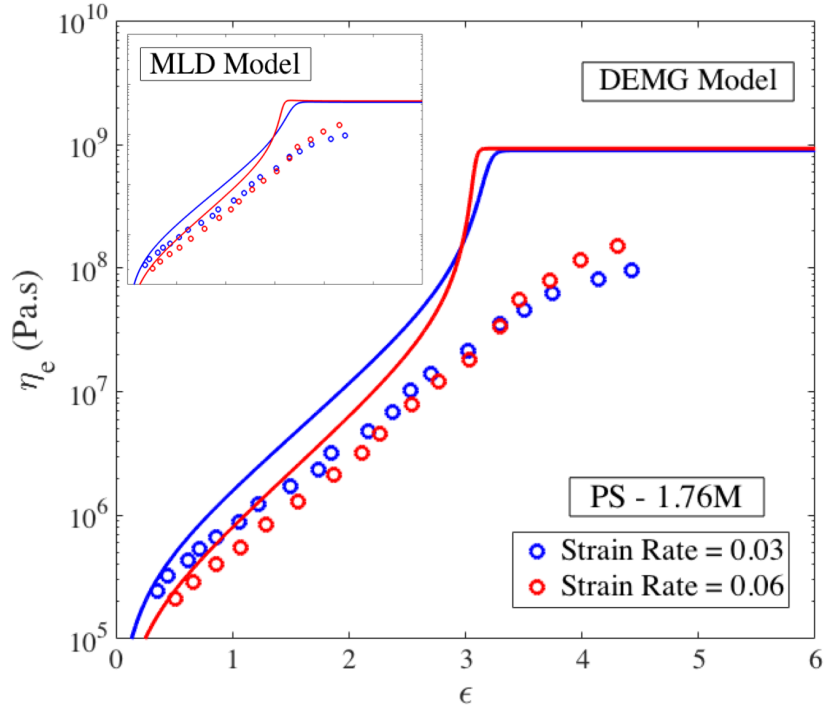
Figure 2.2. The same as Figure 2.1, for 18 wt.% 1.76M PS, at strain rates $\acute{\epsilon} = 0.03 s^{-1}$ $[Wi_R = 10.32]$ (blue), and $0.06 s^{-1}$ $[Wi_R = 20.64]$ (red).
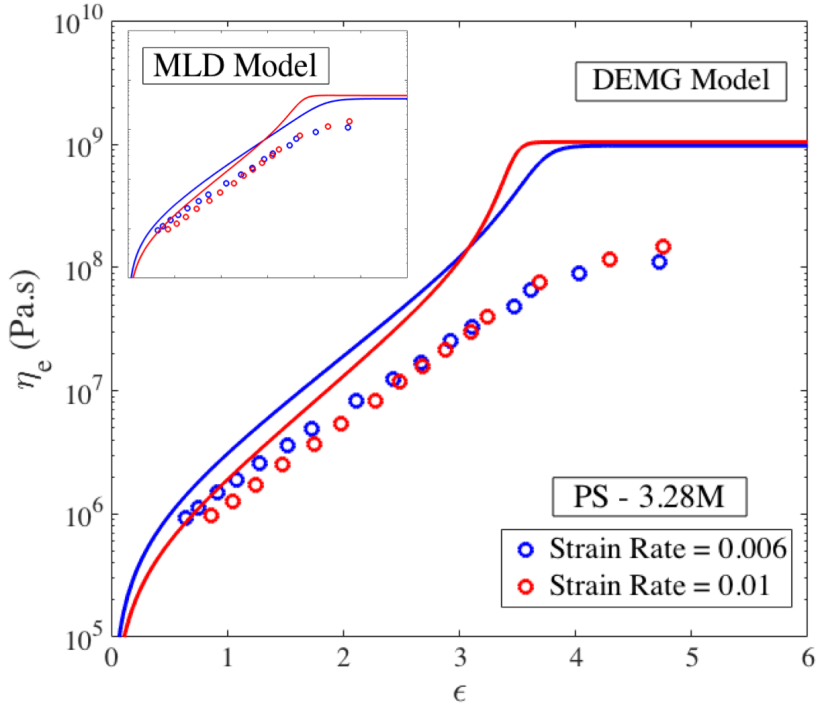
Figure 2.3. The same as Figure 2.1, for 13 wt.% 3.28M PS, at strain rates $\dot{\epsilon} = 0.006 s^{-1}$ $[Wi_R = 4.46]$ (blue), and $0.01 s^{-1}$ $[Wi_R = 7.44]$ (red).

2.3   Entangled Kink Dynamics (EKD) Model

The concept of kink dynamics in dilute solutions was first introduced in 1990 by Larson [158] and independently by Hinch [159]. Based on simulation studies of Rallison and Hinch [160], they suggested that an isolated, dilute, chain forms a folded state at large strain rates in which the chain consists of locally fully stretched and aligned chain segments connected by "kinks" or back-folds, and it takes several Hencky strains ($\epsilon = \dot{\epsilon} t$) for the chain to completely unravel in uniaxial extension. This prediction was confirmed by subsequent experimental studies of dilute DNA solutions [161,162]. Recent simulation studies of well entangled polymers have established that these folded, or "kinked," states also form in entangled polymers at high extensional strains [46,53,163–166]. In fast extensional flows, in the kinked state, the magnitudes of the drag force

and chain tension greatly exceed the Brownian force. Thus, one can neglect the effect of Brownian motion and assume that unraveling from a kinked to a fully unraveled state is driven by the balance of drag and tension.

Whether entangled or not, these kinks or fold points act like pulleys over which the chain travels, as the kinks are convected relative to each other. The chain thereby unravels by passing its chain ends through terminal kinks, and by the joining together and mutual annihilation of two kinks that meet each other. At high strains and strain rates the Brownian force becomes negligible compared to tension and drag, and the polymer chain collapses within a strain of around $\epsilon = \epsilon_T$ Hencky units into a nearly one-dimension conformation ($R_{g_x} \gg R_{g_y}, R_{g_z}$) and polymer strands between kinks become strongly aligned along the x, or extension, direction, Figure 2.4. Numbering the kinks sequentially along the chain from 1 to N_{Kinks} (with chain ends taken to be "kinks"), we let x_i be the x coordinate of kink i, ($1 < i < N_{\text{Kinks}}$), where the x direction is the stretching direction of the extensional flow. Balancing drag and tension forces on a small segment with a length $d\xi$ that lies between positions $x = \xi$ and $x = \xi + d\xi$, Larson derived the governing equation for the tension at position x of a chain in its folded state as [158]:

$$f^s(x) = -\frac{1}{2}\zeta'\dot{\epsilon}(x^2 - x_{i-1}^2) + \zeta'V_i(x - x_{i-1}) + f_{i-1} \qquad (2.10)$$

Here $\dot{\epsilon}$ is the extension rate, ζ' is the friction coefficient per unit length of the chain and V_i is the velocity of strand (i) which connects kinks (i) and ($i - 1$), and f_{i-1} is the force at kink ($i - 1$). To obtain the set of kink forces f_i at the kink positions x_i, we set $x = x_i$, and $f^s(x)$ equal to $f(x_i)$ in the above equation. Then, we combine this equation with a similar result relating $f(x_{i+1})$ to $f(x_i)$. Finally, the two equations are added to give ($\Delta x_i = x_i - x_{i-1}$) [46]:

$$\left(\frac{1}{\Delta x_{i+1}}\right) f_{i+1} + \left(\frac{1}{\Delta x_i} - \frac{1}{\Delta x_{i+1}}\right) f_i - \left(\frac{1}{\Delta x_i}\right) f_{i-1} = -\frac{1}{2}\zeta'\dot{\epsilon}(x_{i+1} + 2x_i + x_{i-1}) + 2\zeta'U_i \quad (2.11)$$
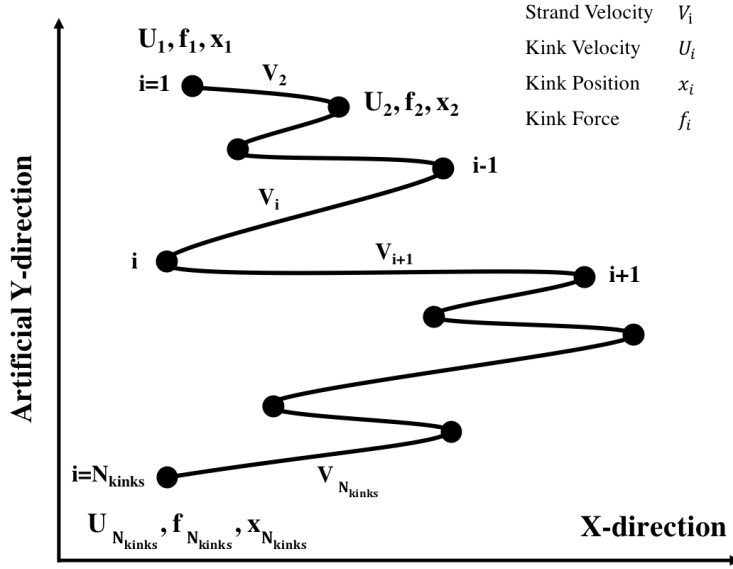
Figure 2.4. Schematic of the kinked state of a linear chain. Note that the y-dimension is exaggerated for clarity while the polymer chain is considered as a one-dimensional object. Kinks are shown by black circles and are connected by fully stretched strands.

Where U_i is the velocity of kink (i) and is equal to $U_i = (V_i + V_{i+1})/2$ due to conservation of the overall length of the chain. To solve the equation set (2), we need to know either the forces or velocities of the kinks. For a dilute solution, due to the absence of any neighboring chains entangling with our chain of interest, the forces at the kinks go to zero ($f_i = 0, 1 < i < N_{\text{Kinks}}$) and the evolution of the system can be found by integrating the kink velocities to obtain the positions of the kinks as a function of time. For dilute, unentangled, solutions, since there are no opposing forces at the kinks, the tension approaches zero at fold points $f_i = 0$, and Larson showed how in this case the unraveling process and stress evolution diverges from that of affine motion [158]. For the unentangled dilute chain, each strand between kinks has a quadratic tension distribution with zero tension at each fold point and maximum at the midpoint between two

adjacent kinks. In contrast, if the chain is fully entangled, and can be assumed to reside in a tube that deforms affinely, then the kinks or fold points in the tube move affinely, which implies $U_i = \dot{\epsilon} x_i$. Knowing the kinks' velocities, we can find the evolution of the kink position as a function of time and calculate the stress. For the stress, we use the one-dimensional form of general Kirkwood-Riseman formula [167]:

$$\sigma_{xx} = \nu \left\langle \sum_{i=1}^{N_{Kinks}} \left| \int_{x_{i-1}}^{x_i} f^s(x) dx \right| \right\rangle \tag{2.12}$$

Where ν is the number of molecules per unit volume and $\langle . \rangle$ stands for the ensemble average. A summary of the equations of motion under dilute and affine-deformation assumptions are given in Table 2.2.

Table 2.2. Evolution equations for vector x of kink positions under dilute and affine assumptions

	Position Evolution Matrix $\boldsymbol{A}$: $d\boldsymbol{x}/dt = \boldsymbol{A}.\boldsymbol{x}$	Stress: σ_{xx}
Dilute	$\dfrac{1}{4}\dot{\epsilon} \begin{bmatrix} 2 & 2 & 0 & 0 & 0 & . & . & . & . & . & . & . \\ 1 & 2 & 1 & 0 & 0 & . & . & . & . & . & . & . \\ 0 & 1 & 2 & 1 & 0 & . & . & . & . & . & . & . \\ . & . & . & . & . & . & . & . & . & . & . & . \\ . & . & . & . & . & . & 0 & 1 & 2 & 1 & 0 \\ . & . & . & . & . & . & 0 & 0 & 1 & 2 & 1 \\ . & . & . & . & . & . & 0 & 0 & 0 & 2 & 2 \end{bmatrix}$	$\dfrac{1}{12}\nu \zeta' \dot{\epsilon} \left\langle \sum_{i=1}^{N_{Kinks}} |x_i - x_{i-1}|^3 \right\rangle$
Affine	$\dot{\epsilon}\boldsymbol{I}$	$\nu \left\langle \sum_{i=1}^{N_{Kinks}} \left| -\dfrac{1}{6}\zeta'\dot{\epsilon}(x_i - x_{i-1})^2(x_i + 2x_{i-1}) \right. \right.$ $\left. \left. + \zeta'V_i \dfrac{(x_i - x_{i-1})^2}{2} + f_{i-1}(x_i - x_{i-1}) \right| \right\rangle$

For affine motion, the forces f_i at the kinks are found by solving the following system of linear equations, derived by explicitly writing Equation (2.11) for all the kinks on a chain (except for first and last kink, which, being chain ends, are free kinks):

$$A' \begin{bmatrix} f_2 \\ f_3 \\ \vdots \\ f_{N_{Kinks}-2} \\ f_{N_{Kinks}-1} \end{bmatrix} = \zeta' \dot{\epsilon} \begin{bmatrix} -\frac{1}{2}x_3 + x_2 - \frac{1}{2}x_1 \\ -\frac{1}{2}x_4 + x_3 - \frac{1}{2}x_2 \\ \vdots \\ -\frac{1}{2}x_{N_{Kinks}-1} + x_{N_{Kinks}-2} - \frac{1}{2}x_{N_{Kinks}-3} \\ -\frac{1}{2}x_{N_{Kinks}} + x_{N_{Kinks}-1} - \frac{1}{2}x_{N_{Kinks}-2} \end{bmatrix} \tag{2.13}$$

Where A' is given as:

$$\begin{bmatrix} \left(\frac{1}{\Delta x_2} - \frac{1}{\Delta x_3}\right) & \frac{1}{\Delta x_3} & 0 & 0 & 0 & . & . & . & . & . & . \\ \frac{-1}{\Delta x_3} & \left(\frac{1}{\Delta x_3} - \frac{1}{\Delta x_4}\right) & \frac{1}{\Delta x_4} & 0 & 0 & . & . & . & . & . & . \\ 0 & \frac{-1}{\Delta x_4} & \left(\frac{1}{\Delta x_4} - \frac{1}{\Delta x_5}\right) & \frac{1}{\Delta x_5} & 0 & . & . & . & . & . & . \\ . & . & . & . & . & . & . & . & . & . & . \\ . & . & . & . & 0 & \frac{-1}{\Delta x_{N_{Kinks}-3}} & \left(\frac{1}{\Delta x_{N_{Kinks}-3}} - \frac{1}{\Delta x_{N_{Kinks}-2}}\right) & \frac{1}{\Delta x_{N_{Kinks}-2}} & 0 \\ . & . & . & . & 0 & 0 & \frac{-1}{\Delta x_{N_{Kinks}-2}} & \left(\frac{1}{\Delta x_{N_{Kinks}-2}} - \frac{1}{\Delta x_{N_{Kinks}-1}}\right) & \frac{1}{\Delta x_{N_{Kinks}-1}} \\ . & . & . & . & 0 & 0 & 0 & \frac{-1}{\Delta x_{N_{Kinks}-1}} & \left(\frac{1}{\Delta x_{N_{Kinks}-1}} - \frac{1}{\Delta x_{N_{Kinks}}}\right) \end{bmatrix} \tag{2.14}$$

The affine motion of the kinks implies that the chain tension does not go to zero, but accumulates around the entangled, affinely moving, kinks. Hence, starting from the ends of the chain where the tension is zero ($f_1 = f_{N_{kinks}} = 0$), the tension accumulates monotonically around the folds to a maximum at the center *of the entire chain*, just as it would if the chain were already fully extended. The stress therefore reaches its plateau value as soon as the *locally* fully stretched state is reached and remains unchanged even as the chain unravels from *locally* fully stretched to the *globally* fully extended state. The accumulation of tension from the chain ends to the chain center implies that kinks near the chain center retain a very large tension which must be supported by the surrounding entangled matrix chains. In the tube theory, affine motion is a consequence of the mean-field nature of the tube as a representative of the confining effect of a large number of surrounding chains, large enough to represent the deformation of the continuum. Rubinstein and Panyukov, however, argued that the mesh of entanglements deforms nonaffinely [149,150]. If

entanglements are approximated as binary interactions between pairs of chains, then the tension on an entangled fold on one chain must be supported by a second chain with which it is locally entangled. If chains entangle randomly along their length, then the kink near the center of one chain is unlikely to have an entanglement partner whose entanglement with the first chain is also at its center, with a tension there that is high enough to balance the tension on the first chain. Thus, the entangled kink on the partner chain will likely give way, and be pulled nonaffinely by the first chain, which can exert a greater tension than can the partner chain. So, if the entanglements are pairwise interactions of chains, and the forces at the kinks of the two chains balance, we must abandon the affinely deforming tube, and instead solve the coupled force equations for a multiple-chain system where chains are pairwise randomly entangled. This concept is closely related to a local force balance criterion introduced into three dimensional primitive chain network (PCN) simulations of Masubuchi et al. [168] and have yielded good predictions in both linear and nonlinear (shear and extensional flows) regimes [62], over the limited range of chain lengths, strain rates, and strains to which it has been applied.

Here, we generate one dimensional random-walk chains with p steps by generating p random numbers from a truncated Gaussian distribution with small standard deviation and an average segment length L_{avg}^{s}. The steps are made nearly, but not exactly, the same length, so that chain configurations are smoothly distributed, which is important in our subsequent simulations. The direction (positive or negative) of a step from point P_i to P_{i+1}, with $i = 1, 2, \ldots p$, is decided randomly. A kink on a single chain is formed at point i when positions of neighboring points satisfy $(x_i - x_{i-1})(x_i - x_{i+1}) > 0$.
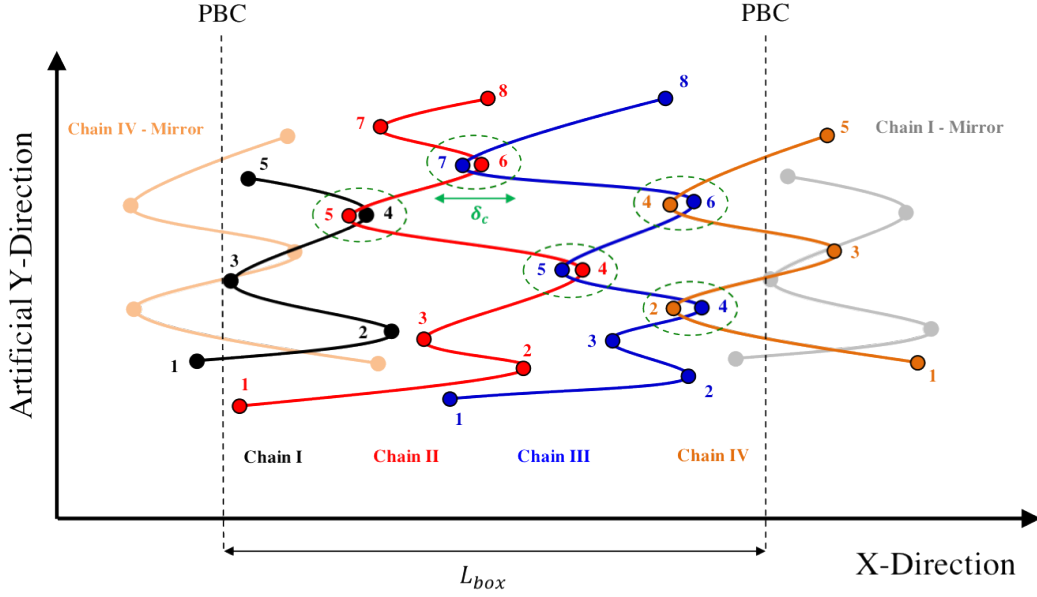
Figure 2.5. Schematic of EKD simulations. Dashed lines mark the periodic boundaries of the box; periodic images of chains I and IV are shown at box boundaries. Entangled kinks are determined by proximity of kinks of opposite polarity on a pair of different chains. Note that chains are one-dimensional objects and the Y-direction above is arbitrarily expanded for clarity.

Finally, we re-scale the strand lengths between kinks uniformly to achieve an overall chain length with exactly the desired value, pL_{avg}^s (p steps of unit size, $L_{\text{avg}}^s = 1$, would result in a chain of length $L = p$ with approximately $L/2$ kinks). Use of a narrow distribution of step sizes, as mentioned above, ensures that the scaling factor will not be very large or too small, usually fluctuating between 0.9 and 1.1. Note that the number of kinks, N_{kinks} is always less than the number of steps p. After determining a set of initial chain conformations for the desired number of chains, N_{chains} (typically $50 < N_{\text{chains}} < 100$), a one-dimensional simulation domain is created with length L_{box}, and N_{chains} points are uniformly distributed in the box, specifying the centers of mass of the chains generated in the previous step. After locating the chains within the one-dimensional domain, we determine entanglement points. Two kinks from two chains are considered entangled if (1) they have opposite polarity in the x-direction (the extensional axis) and (2) they are closer than a certain distance δ_c, Figure 2.5. The force equations of the two kinks that

are entangled are coupled. Coupling is done by requiring the force and velocity values of the shared kink between two chains should be the same. A sample of the coupling between two chains is shown in Figure 2.6.
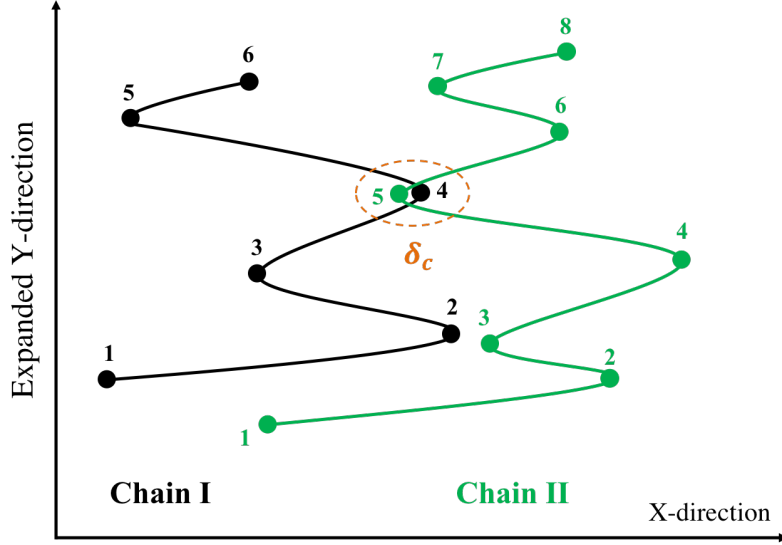
Figure 2.6. Schematic of an entangled kink between two chains in EKD model. The Y-direction above is arbitrarily expanded for clarity. Figure is adapted from [46].

Where for the shared kink, we have:

$$\left[\left(\frac{1}{\Delta x_5^I}\right)f_5^I + \left(\frac{1}{\Delta x_4^I} - \frac{1}{\Delta x_5^I}\right)f_4^I - \left(\frac{1}{\Delta x_4^I}\right)f_3^I\right] - 2\zeta'U_4^I = -\frac{1}{2}\zeta'\dot{\epsilon}(x_5^I + 2x_4^I + x_3^I) \quad (2.15)$$

$$\left[\left(\frac{1}{\Delta x_6^{II}}\right)f_6^{II} + \left(\frac{1}{\Delta x_5^{II}} - \frac{1}{\Delta x_6^{II}}\right)f_5^{II} - \left(\frac{1}{\Delta x_5^{II}}\right)f_4^{II}\right] - 2\zeta'U_5^{II} = -\frac{1}{2}\zeta'\dot{\epsilon}(x_6^{II} + 2x_5^{II} + x_4^{II}) \quad (2.16)$$

$$U_4^I = U_5^{II} \quad (2.17)$$

$$f_4^I = f_5^{II} \quad (2.18)$$

Here the subscript stands for the kink number and superscript for the chain index. The above four equations are used to solve for the four unknowns, U_4^I, U_5^{II}, f_4^I and f_5^{II}. These four equations are coupled to equations for other kinks through the forces f_3^I and f_6^{II} that also appear in Equations (2.15) – (2.18). Therefore, we have a system of $4 \times N_{EP}$ equations where N_{EP} is the

number of entanglement points in the simulation box; each entanglement point is shared between two entangled kinks on different chains coupled at the entanglement point ($N_{EK} = 2N_{EP}$, N_{EK} being the total number of entangled kinks in the box). The pre-factor of 4 in ($4 \times N_{EP}$) comes from the four equations we need to solve for each entanglement point, Equations (2.15) – (2.18).

To obtain a statistically uniform distribution of entanglement points in the system, we apply periodic boundary conditions across the periodic boundary $x_{box} = -L_{box}/2$ and $x_{box} = L_{box}/2$ so that chains passing these limits are allowed to entangle with chains on the other side of the box, Figure 2.5. Note that without the PBC, all the kinks at the boundaries would be free. If a chain crosses the periodic boundary, its image is created on the other side of the box and the kinks of the image chain will be entangled with other chains, based on the polarity and adjacency criteria explained earlier. Special care needs to be taken in imposing velocities on mirror-image chains. In our system of equations, the velocity of a kink on a chain (U_i^o) and that on its mirror image (U_i^m) are related by:

$$U_i^m = U_i^o + \dot{\epsilon} L_{box} \qquad (2.19)$$

Here superscript (m) stands for "mirror" and (o) for "original". The difference between center of masses of the original and mirror-image chains is equal to the simulation box length (L_{box}). Constraint-release by loss of an entangling chain is implemented self-consistently, as follows. Firstly, when one of the chain ends passes through an entangled kink, the end kink on that chain disappears and the corresponding entanglement condition on the partner chain is removed, so that the kink on the partner chain becomes a free, or unentangled, kink. Secondly, as a strand on a chain shrinks and the two kinks on the same chain on either end of that strand meet, whether the kinks are entangled or free, they disappear. If one of the disappearing kinks is entangled with a partner chain, the coupled force condition on the paired kink of the neighboring chain is dropped and it

becomes a free kink with zero tension. We do not consider re-entanglement of chains; however, we will show that re-entanglement is unlikely to have much effect on the results.

2.4   Results and Discussions

To explore the behavior of this model, we choose units such that $\zeta' = \dot{\epsilon} = \nu = 1$ and consider initial entanglement fractions $\rho_{EK}^0 = 80\%$, defined as the total number of entangled kinks divided by the total number of kinks. These values can be achieved by adjusting δ_c and L_{box} to obtain a certain entanglement density. Chain lengths of $L = 25, 50$ and 100 are considered. In our figures, ϵ is the total strain, starting from the equilibrium rest state, while $\tilde{\epsilon}$ is the strain starting from the kinked state. The strain at which kinked state is first achieved is given by ϵ_T, which we call the transition strain, and then $\tilde{\epsilon} = \epsilon - \epsilon_T$. In chapter 3, we find that for fast flows $\epsilon_T \approx 3$. Figure 2.7 shows the end-to-end distance and stress evolution of the chains under different entanglement conditions.
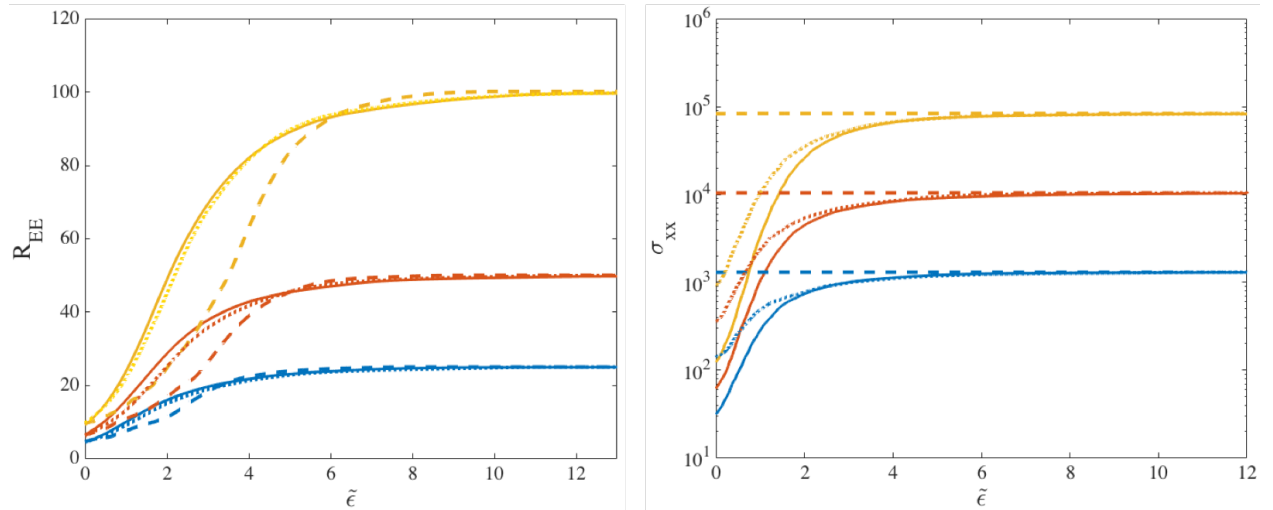
Figure 2.7. Evolution of end-to-end distance (left) and stress (right) for different chain lengths $L = 25$ (blue), $L = 50$(orange) and $L = 100$ (yellow) at asymptotically high strain rates, $Wi_R \gg 1$. For each length, ensemble averaged behavior under the following three conditions are shown: 1. no entangled kinks (solid lines), 2. Entangled Kink Dynamics with 80% initial entanglement density (dotted lines), and 3. affine motion of kinks (dashed lines). For all results here, $\zeta' = \dot{\epsilon} = \nu = 1$.

As expected, at asymptotically high strain rates, under the affine motion assumption, while the end-to-end distance evolves with time, the stress immediately (after formation of the locally fully extended kinked state at strain ϵ_T) reaches at its final plateau value of $\sigma_{xx}^p = \nu\zeta'\dot{\epsilon}L^3/12$, which either an unentangled or an entangled chain eventually attains. For both dilute chains, with 0% entangled kinks, and the entangled chains with 80% initially entangled kinks, the chain end-to-end distance R_{EE} evolves almost identically for each chain length. The stress rise also converges rather quickly to the same response in both cases although the starting points have almost a decade difference in stress, which is attributed to the forces generated at entanglement points in the entangled system. Figure 2.7 clearly shows the much more sluggish rise of R_{EE} when affine motion of the kinks is assumed, compared to that for the dilute and entangled chains, and this difference grows as the chain length increases. When affine kink motion is imposed, all kinks move away from each other ($U_i = \dot{\epsilon}x_i$) initially, and a kink can only be destroyed when a chain end passes through it. This slows the growth of R_{EE} relative to that for dilute and entangled kinks, which can annihilate each other, allowing faster unraveling of internal conformations and faster growth of R_{EE} for chains obeying kink dynamics rather than dynamics dictated by an affinely deforming tube.

To check how the forces in the mutually entangled kink method diverge from those in the affine motion assumption, we plot the maximum force generated at an entangled kink ($f_{\mathrm{kink}}^{\mathrm{max}}$) under affine and EKD assumptions. This calculation gives us the maximum entanglement force that is generated by the drag on the two entangling kinked chains in the kinked state. As we will discuss in the next chapter, this maximum force at an entanglement is required for the slip-spring simulations as well. To calculate the average maximum entanglement force, for each chain in our ensemble at a given strain, we first find the maximum force at any kink on that chain. Then, we

average this maximum force over all chains in the ensemble and call this the average maximum kink force $f_{\text{kink}}^{\text{max}}$. Figure 2.8 shows the evolution of $f_{\text{kink}}^{\text{max}}$ when the chains deform affinely (solid lines) and using the EKD technique (dashed lines) for three chain lengths, $L = 25, 50$ and 100. For affine-motion simulations, we solve the system of equations (2.13) at each strain ($\tilde{\epsilon}$) and find the maximum of the kink forces, f_i's, for each chain. In EKD simulations, the system of equations (2.15) – (2.18) is solved for all entangled kinks and the maximum value of the f_i's for each chain is found. For both affine-motion and EKD simulations, we averaged these maximum values over multiple chains ($N_{\text{chains}} = 100$).
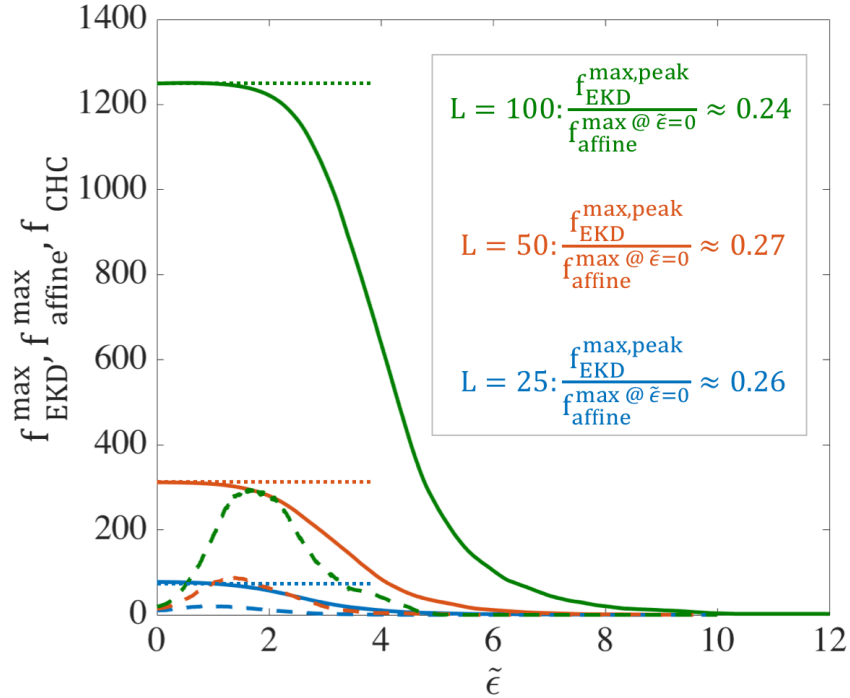
Figure 2.8. Evolution of the ensemble-averaged maximum kink force (f_{kink}^{max}) for different chain lengths $L = 25$ (blue), $L = 50$ (orange) and $L = 100$ (green) at asymptotically high strain rates. For each length, the ensemble averaged force is shown for both affine motion of kinks (solid lines) and EKD simulations with $\rho_{EK}^0 = 0.8$ (dashed lines). The horizontal dotted lines give the maximum possible force, f_{CHC} at an entangled kink for each chain length, obtained from Eq. (2.20) as discussed in the text. The units of the force are set by the parameter values $\zeta' = \dot{\epsilon} = 1$; i.e., the dimensional force is obtained by multiplying the plotted force by $\zeta'\dot{\epsilon}$ times the square of the unit of length.

Taking an entanglement as a pairwise interaction between two chains, the maximum possible force at an entangled kink between two chains is achieved when the two chains are

symmetrically entangled at the center of each chain; see Figure 2.9. We call this the "Center Hooked Conformation" (CHC). Solving the system of equations (2.15) – (2.18) for the center hooked conformation, the force at the entangled kink in the middle, which is the maximum possible force, is found to be:

$$f_{CHC} = \frac{1}{8}\zeta'\dot{\epsilon}L^2 \tag{2.20}$$

Values of f_{CHC} for three chain lengths are plotted as dotted horizontal lines in Figure 2.8. Figure 2.8 reveals that for affine deformation, f_{affine}^{max} initially takes this highest achievable value, f_{CHC}, which is at the center of the chain with force away from the center distributed along the quadratic curve shown by black line in Figure 2.10. Tube models predict that as tube segments stretch, the tension along the entire chain quickly saturates in a parabolic function with zero tension at the ends and maximum at the center [35], regardless of the number of folds remaining in the chain. As the chain unravels under affine motion, kinks near the chain center move away from each other and the strand length between them increases. With fewer kinks and fewer forces, the maximum of these is less likely to be near the peak of the black curve and more likely to be off to the side, and lower in value, producing the decrease in maximum force f_{affine}^{max} shown by the solid lines in Figure 2.8.

On the other hand, for the same chain length, with 80% initial entangled kinks in an EKD simulation, the evolution of the maximum kink force is drastically different as shown in Figure 2.8 by the dashed lines. First, the peak occurs at a finite strain ($\sim 1 - 2$ Hencky strains) rather than instantly after startup of the simulation and also the peak tension is much smaller than for affine motion. In EKD simulations, the tension distribution along the whole chain (not just at the kinks) is initially nearly uniform, except at the chain ends, and then eventually evolves into a quadratic

dependence, which takes almost 6 Hencky strain units to occur for the chain length considered. Our flat tension profile at strains high enough to form the folded state, but not high enough to unravel the chains (corresponding to $\tilde{\epsilon} = 0$), qualitatively matches the tension profile from recent molecular dynamics simulation results for entangled Kremer-Grest chains by Hsu and Kremer [53]. (The tension profile in the Hsu and Kremer work changes sign at every kink, because of the definition of tension used.) The tension distribution of a dilute chain, also plotted in Figure 2.10, is initially lower than that of the entangled chain, but merges with it at $\tilde{\epsilon} = 4$. This is because no re-entanglement is implemented, so that after annihilation of entangled kinks due to unraveling, the entangled chain becomes dilute and loses all its entanglements by $\tilde{\epsilon} \sim 4$.
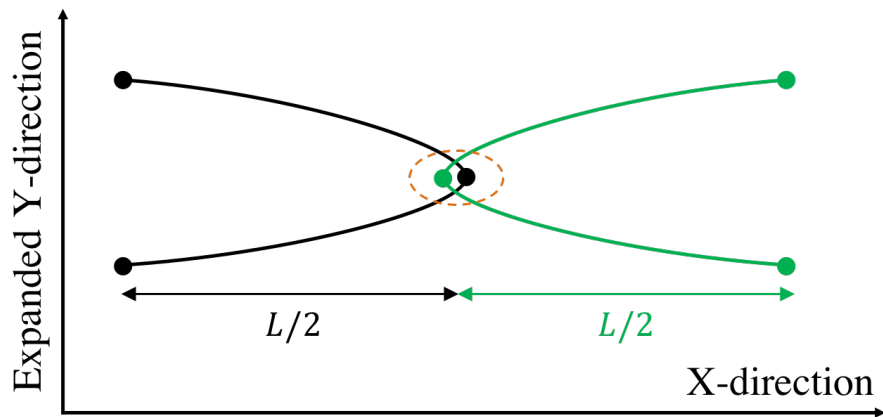
Figure 2.9. The "center-hooked" configuration between two chains entangled at the center of each chain. The Y-direction is arbitrarily expanded for clarity.
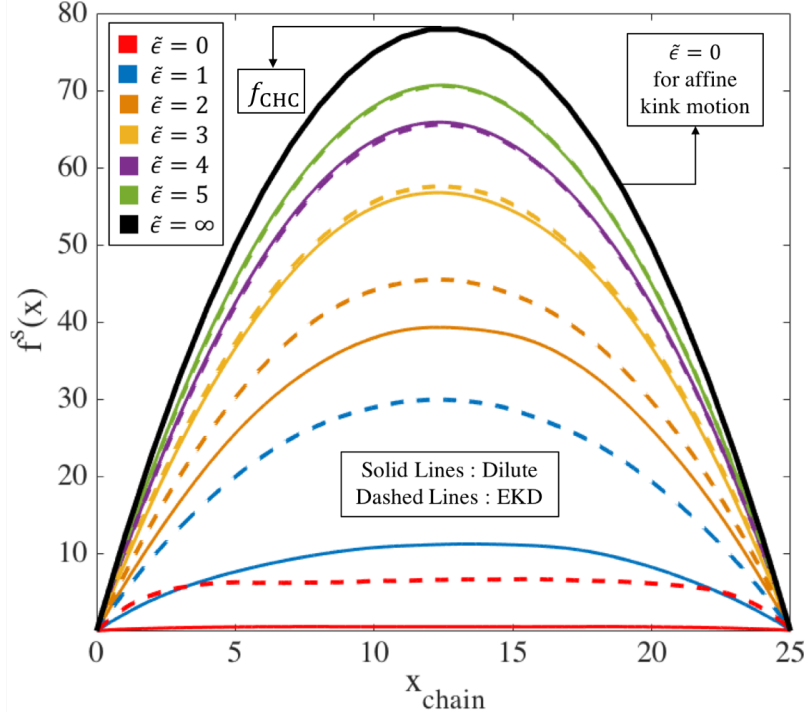
Figure 2.10. Evolution of tension distribution ($f^s(x)$) along an $L = 25$ chain under affine motion, and for dilute and entangled chains, the latter simulated by the EKD method and averaged over an ensemble of 150 chains. The arrow at the peak of black curve shows the maximum tension value a chain of length $L = 25$ will achieve when fully unraveled for a dilute and an EKD chain, which is attained immediately in the kinked state under affine motion of kinks. The peak value of this maximum tension is given by equation (2.20).

We observe in Figure 2.8 that the peak value of f_{EKD}^{max} in the EKD simulations for each chain length is much smaller than the initial value obtained in affine motion, by roughly a factor of four. Thus,

$$f_{EKD}^{max,peak} \cong 0.25 \, f_{affine}^{max,@ \, \tilde{\epsilon}=0} \cong 0.25 \, f_{CHC} = \frac{1}{32} \zeta' \dot{\epsilon} L^2 \qquad (2.21)$$

Finally, we check the influence of our initial ensemble of conformations. To do so, we simulate an ensemble of unentangled chains with $L = 50$, and, as the chains unravel, at a strain $\tilde{\epsilon}_{ce} = 0, 1,$ or 2, we entangle the chains with entanglement percent of $\rho_{EK}^0 = 50\%$ and resume the elongation from that strain ($\tilde{\epsilon}_{ce}$). The evolution of R_{EE} and σ_{xx} for dilute chains (yellow line) and the chains entangled as described above, are shown in Figure 2.11. Points at which the chains are

entangled are shown with circles corresponding to $\tilde{\epsilon}_{ce} = 0$ (red), 1 (blue) and 2 (green). We

observe that our results are not very sensitive to the method of generating the initial ensemble of

conformations, as long as the chain length is held constant. It can also be seen that stress and end-

to-end evolution curves are not very sensitive to this imposed entangling process; those entangled

at different strains ($\tilde{\epsilon}_{ce}$), quickly converge to those of dilute chains. As mentioned before no re-

entanglement is implemented in our method, but these results show that re-entanglement, should

it occur in real polymers, should have only a small effect on the evolution of stress and of end-to-

end length at high strains of strong flows.
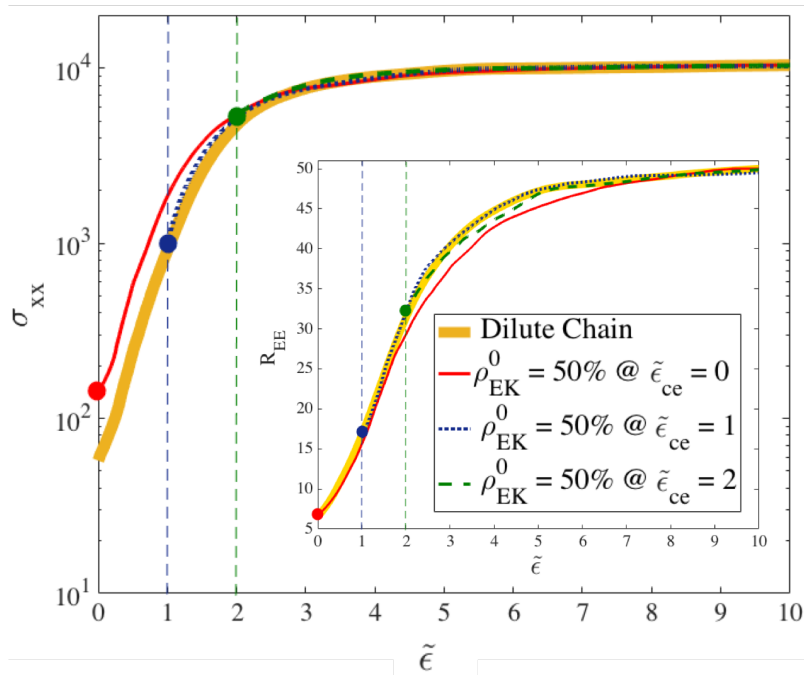
Figure 2.11. Evolution of stress (main figure) and end-to-end distance (inset) for dilute chains with $L = 50$ (Thick yellow line) compared with EKD simulations with 50% entanglements imposed at strains of 0 (thin red line), 1 (dotted blue line) and 2 (dashed green line).

The next step is to apply the kink dynamics analysis to experimental polymer solutions, e.g. the polystyrene samples of Hunag et al. [157] shown in Figures 2.1 - 2.3. To do so, the following questions need to be answered:

1. What is the transition strain (ϵ_T) beyond which the EKD results become valid?

2. What is the number of kinks for a chain of arbitrary chain length at the transition strain?

3. What is the ratio of the number of entangled to free kinks in an entangled sample?

4. What is the distribution of strand lengths between the kinks?

To answer above questions, we need a simulation technique that can track the evolution of the chain conformation from equilibrium at least to the kinked state. For this purpose, we perform Brownian dynamics simulations of entangled chains using the single-chain slip-link model of Likhtman [70]. In this model, entanglement forces on a chain are captured by slip springs that are anchored to the continuum. The anchor points are held fixed in position for simulations of linear viscoelasticity and move affinely in the case of imposed flow. This model has been shown to predict well the linear rheology and stresses in shear flow of entangled polymers [61,72,143], where the forces generated by entangled chains are small or modest. However, as emphasized above, in uniaxial extensional flow, the tension in the chain can become large enough to cause large deviations from affine motion of entanglement points. Thus, after introducing the slip-spring model, we will address this limitation of the original slip-spring model, by either pairing slip springs on one chain with those on another, to allow non-affine motion of the anchor point based on a simple force re-distribution condition, or by simply imposing a maximum-force constraint on the slip spring. We will show that both methods, though rather ad hoc, give similar results up to the transition to the kinked state, and fix the severe problems that the model otherwise encounters in extensional flow.

Chapter 3 : Slip-Spring Simulations of Entangled Linear Polymers Under Strong Extensional Flows

3.1   Abstract

We combine a slip-spring model with an "entangled kink dynamics" (EKD) model for strong uniaxial extensional flows (with Rouse Weissenberg number $Wi_\mathrm{R} \gg 1$) of long ($M_w > 1$ Mkg/mol for polystyrene) entangled polymers in solutions and melts. The slip-spring model captures the dynamics up to the formation of a "kinked" or folded state, while the kink dynamics simulation tracks the dynamics from that point forward to complete extension. We show that a single-chain slip-spring model using affine motion of the slip-spring anchor points produces unrealistically high tension near the center of the chain once the Hencky strain exceeds around unity or so, exceeding the maximum tension that a chain entangled with a second chain is able to support. This unrealistic tension is alleviated by pairing the slip links on one chain with those on a second chain, and allowing some of the large tension on one of the two to be transferred to the second chain, producing non-affine motion of each. This explicit pairing of entanglements mimics the entanglement pairing also used in the EKD model, and allows the slip spring simulations to be carried out to strains high enough for the EKD model to become valid. We show that results nearly equivalent to those from paired chains are obtained in a single-chain slip-spring simulation by simply specifying that the tension in a slip spring cannot exceed the theoretical maximum value of $\zeta' \dot{\epsilon} L^2 / 8$ where ζ', $\dot{\epsilon}$ and L are the friction per unit length, strain rate and contour length of the chain, respectively. The effects of Constraint-Release (CR) and regeneration of entanglements is

also studied, and found to have little effect on the chain statistics up to the formation of the kinked state. The resulting hybrid model provides a fast, simple, simulation method to study the response of high molecular weight ($M_w > 1\,\text{Mkg/mol}$) polymers in fast flows ($Wi_R \gg 1$), where conventional simulation techniques are less applicable due to computational cost.

3.2   Introduction

Kink dynamics simulations are only valid after the chain has reached a folded one-dimensional conformation with strands between folds almost fully extended. Larson used an approximation to determine the mean distance between two folds, $\Delta x = b_k (N_k^2 / 2\pi^2 \tau_R \dot{\epsilon})^{1/3}$ and average number of kinks $N_{\text{kinks}} = L/\Delta x = (2\pi^2 N_k \tau_R \dot{\epsilon})^{1/3}$ at the folded state for dilute solutions, where N_k and b_k are the total number of Kuhn steps and Kuhn step length in a polymer chain, respectively [158]. Here, going beyond a simple scaling analysis, we perform Brownian dynamics (BD) simulations of an entangled polymer using a single chain model developed by Likhtman [70]. As discussed in the introduction chapter, single chain techniques are developed to reduce the high computational demand of the multiple-chain methods. For single chain models of entangled polymer systems, effect of the entanglement network is replaced by slip-links [30] [66–68], which confine the motion of the chain. To add the force interactions between neighboring chains, slip-spring models have been developed where some virtual springs are placed along the polymer backbone and not only confine the motion of the chain, but also they exerts force on the chain [69,70]. Although the single chain simulations lack the detailed dynamics of multiple-chain techniques, their considerably good performance in predicting the linear viscoelastic and nonlinear shearing flow data of entangled melts and solutions [61,70–75], has made them well received models in the literature.

3.3   Slip-Spring Simulation Method

In the single chain slip-link model, a freely-jointed chain, with N_s springs between $N_s + 1$ beads, is generated in three dimensions. Each spring in the chain represents $N_{k,s}$ Kuhn segments with Kuhn length b_k resulting in a total of $N_k = N_{k,s}N_s$ Kuhn steps and a contour length of $L = N_{k,s}b_k$ for the chain. Each bead is a center of friction with a friction coefficient ζ_b. Slip-springs add potentials generated at random positions around the polymer chain. Each slip-spring is extended between $\vec{a}_j$ (its anchoring point) and $\vec{s}_j$ (location of slip-link) as shown in Figure 3.1 [70]. There are $N_{k,ss}$ Kuhn steps in each slip-spring with the same Kuhn length b_k as in the main chain, so that the maximum length of a slip-spring is $L_{ss}^{max} = N_{k,ss}b_k$. The initial number of slip-springs (Z_0) is determined by the number of beads between slip-springs (N_e), so that $Z_0 = N_s/N_e$. To find the location ($\vec{s}_j$) of a slip-link j (where j runs from 1 to the total number of slip links Z) on the chain, Likhtman used a continuous dummy variable (x_j), which can take any real value between 0 and N_s, so that $0 < x_j < N_s$. The dummy variable determines the relative position of the slip-link on a main chain spring with respect to the neighboring beads connected by that spring.
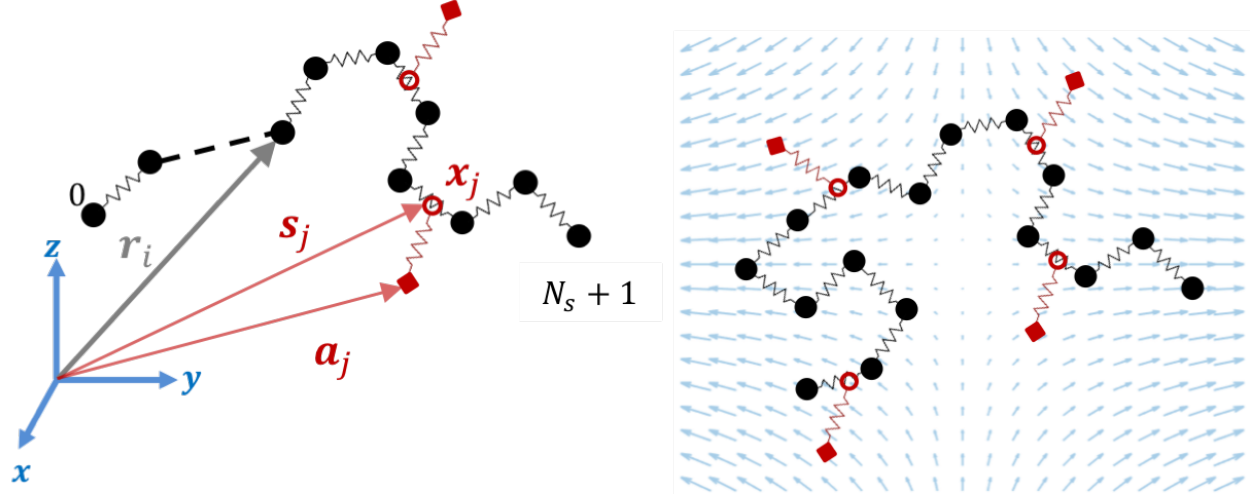
Figure 3.1. Schematic of Slip-Spring simulation in an extensional flow. Position vector of a bead (r_i), anchoring point of a slip-spring (a_j), position of a slip-link on the chain (s_j) and a dummy variable (x_j) of a slip-spring along a chain are shown on the left. On the right, a uniaxial extensional flow is applied to this single-chain model of an entangled polymer, where each slip-spring anchoring point (red squares) moves affinely with the flow until the force generated in the virtual spring (red) reaches a maximum value.

We use the Cohen-Pade spring law for both main springs and slip-springs. Each bead's position changes under the influence of the drag force ($\zeta(\frac{dr_i}{dt} - \kappa.r_i)$), the spring force ($F_i^S$), the Brownian motion ($F_i^R$) and the slip-spring force (F_j^{SS}). The position of the slip-link ($j = 1 \dots Z_{ss}$) on the chain (s_j) is defined by a one-dimensional continuous dummy variable x_j ($x_j = 0 \dots N_s$) which evolves under the action of the slip-spring (F_j^{SS}) and Brownian ($F_j^{R,SS}$) forces. The stochastic equations of motions for the chain and the slip-link positions along the chain are given below, taken from Likhtman. (In the following equations, $\lfloor x \rfloor$ returns the greatest integer less than or equal to the continuous variable x.)

$$\zeta \frac{dr_i}{dt} = \zeta \, \kappa.r_i + [F_{i+1}^S - F_i^S] + F_i^R + \sum_{j:\lfloor x_j \rfloor = i} \left(1 - (x_j - \lfloor x_j \rfloor)\right) F_j^{SS} + \sum_{j:\lfloor x_j \rfloor = i-1} (x_j - \lfloor x_j \rfloor) F_j^{SS} \qquad (3.1)$$

$$\zeta_s \frac{dx_i}{dt} = \zeta F_j^{SS} \left(r_{\lfloor x_j \rfloor + 1} - r_{\lfloor x_j \rfloor}\right) + F_j^{R,SS} \qquad (3.2)$$

$$s_j(x_j) = r_{\lfloor x_j \rfloor} + (x_j - \lfloor x_j \rfloor)\left(r_{\lfloor x_j \rfloor + 1} - r_{\lfloor x_j \rfloor}\right) \qquad (3.3)$$

$$\boldsymbol{\kappa} = \begin{pmatrix} \dot{\epsilon} & 0 & 0 \\ 0 & -\dot{\epsilon}/2 & 0 \\ 0 & 0 & -\dot{\epsilon}/2 \end{pmatrix} \rightarrow \text{ Transpose of velocity gradient tensor} \qquad (3.4)$$

$$\boldsymbol{F}_i^S = \frac{k_B T}{b_k^2 N_{k,s}} \left[\frac{3 - \left(\frac{|\boldsymbol{r}_i|}{N_{k,s} b_k}\right)^2}{1 - \left(\frac{|\boldsymbol{r}_i|}{N_{k,s} b_k}\right)^2} \right] \boldsymbol{r}_i \rightarrow \text{ Spring force for main chain} \qquad (3.5)$$

$$\boldsymbol{F}_i^R = \sqrt{\frac{6 k_B T \zeta}{dt}} \, \boldsymbol{n} \rightarrow \text{ Random force for beads on main chain} \qquad (3.6)$$

$$\boldsymbol{F}_j^{SS} = \frac{k_B T}{b_k^2 N_{k,ss}} \left[\frac{3 - \left(\frac{|\boldsymbol{a}_j - \boldsymbol{s}_j|}{N_{k,ss} b_k}\right)^2}{1 - \left(\frac{|\boldsymbol{a}_j - \boldsymbol{s}_j|}{N_{k,ss} b_k}\right)^2} \right] (\boldsymbol{a}_j - \boldsymbol{s}_j) \rightarrow \text{ Spring force for slip-spring} \qquad (3.7)$$

$$\boldsymbol{F}_j^{R,SS} = \sqrt{\frac{2 k_B T \zeta_s}{dt}} \, \boldsymbol{n} \rightarrow \text{ Random force for slip-link on the chain} \qquad (3.8)$$

Simulations are performed in a dimensionless form by reducing the dimensions of force, time and length by $k_B T / b_k$, $\zeta_b b_k^2 / k_B T$ and b_k respectively, which differs from the dimensionless variables used in the kink dynamics simulations. An explicit Eulerian forward time stepping is used to integrate the equations. The Rouse time of the coarse-grained chain is given by:

$$\tau_R = \frac{\zeta_b (N_s + 1)^2 N_{k,s} b_k^2}{6 \pi^2 k_B T} \Rightarrow \tau_R^* = \frac{(N_s + 1)^2 N_{k,s}}{6 \pi^2} \Rightarrow Wi_R = \dot{\epsilon}^* \tau_R^* \qquad (3.9)$$

Where the superscript $(*)$ denotes the dimensionless value and Wi_R is the Rouse-Weissenberg number of the chain. In the following, we report dimensionless values of the simulation parameters without the $(*)$ for simplicity. Simulation inputs are given in Table 3.1.

Table 3.1. Input parameters for slip-spring simulations

Input	N_s	$N_{k,s}$	N_e	$N_{k,ss}$	ζ_s	Wi_R
Value	$16, 32, 64, 128$	5	4	2.5	0.1	2,4,8,16,32

Here we use $N_e = 4$ and $N_{k,ss}/N_{k,s} = 0.5$ as suggested by Likhtman. However, our simulations differ from those of Likhtman in that we coarse grain a bit further and use $N_{k,s} = 5$ Kuhn steps for the springs on the main chain instead of $N_{k,s} = 1$ used by Likhtman and coworkers [70,169]. Using a larger number of Kuhn steps for the springs of the main chain, in comparison to what Likhtman used, make the chain more flexible and acts as a diluting effect, since the number of Kuhn segments between two consecutive entanglements increases to 20 in our simulations compared to Likhtman's 4 Kuhn segments. Therefore, the entangled chains in our slip-spring simulations are about 20% more dilute than a melt, which justifies the use of experimental data of entangled solutions, with concentration similar to this, to validate the model. Given $N_{k,s} = 5$, we use $N_{k,ss} = 2.5$ based on the given ratio $N_{k,ss} = 0.5N_{k,s}$ suggested by Likhtman [70] and Sukumaran and Likhtman [170]. With this coarse-graining relative to the original model, the number of Kuhn steps in each slip-spring is half that of the springs in the main chain for our coarse-grained chain with $N_e = 4$. The use of this somewhat more coarse-grained version of the model allows us to reach longer chain lengths and avoid overly small time-steps in fast extensional flow.

Before applying the extensional flow, all the chains in the ensemble are simulated in the absence of flow for a time $5\tau_R^*$ to relax the chain from its initially generated random conformation and ensure that the chain has reached equilibrium. During the equilibrium process only, we keep the number of slip-springs on the chain constant, by generating a new slip-spring at a random position along the chain whenever a slip-spring is released from the chain end. Therefore, during relaxation, the number of slip-springs is fixed at Z_0. To perform these equilibration simulations,

the drag term on the right-hand side of Equation (3.1) [46] is simply set to zero. When the flow is applied, the anchoring points of the slip-springs ($\vec{a}_j$) move affinely with the flow and the connecting vectors of the slip-springs increase in length gradually. While slip links on the chain are lost as they are convected off the chain, neither destruction of slip links by any constraint-release from the surrounding medium, nor regeneration of slip links are considered. Thus, the number of slip-springs on the chain (Z) starts from Z_0 and decreases to zero as the chain gradually achieves its fully unraveled state. As the chain orients in the flow direction and its springs stretch out, due to the imposed drag and slip-spring forces, the chain evolves into a folded state and kinks are formed. Figure 3.2 shows a sample chain of 32 springs evolving from the equilibrium state to a fully unraveled chain at $Wi_R = 16$. After the kinks appear in the chain at strains close to 2.5, some of the slip-links move towards the kinks and make an entangled kink. At this point the slip-link cannot escape the kinked region until the kink disappears by chain unraveling. We call this situation "slip-link trapping," since the slip-link is trapped between the three beads that form the fold, Figure 3.3, and cannot release itself unless the kink disappears or constraint release (which has not been implemented in this section) removes the trapped slip-link. As described below, trapping occurs because the flow affinely drives both the kink and the slip link in the same direction. Rewriting Equation (3.2) of in its numerically integrated form, the position x_j of slip-link (j), evolves as follows:

$$x_j^{t+\Delta t} = x_j^t + \frac{\Delta t}{\zeta_s} \left(\vec{F}_{j,SS} \cdot \left(\vec{r}_{\lfloor x_j \rfloor + 1} - \vec{r}_{\lfloor x_j \rfloor} \right) \right) + \Delta x_B \qquad (3.10)$$

Where $\vec{F}_{j,SS}$ shows the force in slip-spring (j). As the magnitude of the force in the slip-spring ($|\vec{F}_{j,SS}|$) increases, the second term on the right-hand-side of Equation (3.10) becomes dominant, and one can ignore the effect of Brownian motion Δx_B. As shown in Figure 3.3, when trapping

occurs, the direction of the force $\vec{F}_{j,SS}$ stays constant, but as the slip-link travels between beads $i -$ 1, i and $i + 1$, when it passes bead i, the sign of the position term $(\vec{r}_{\lfloor x_j \rfloor + 1} - \vec{r}_{\lfloor x_j \rfloor})$ in Equation (3.10) reverses. Thus, if x_j increases during one time-step, it will decrease in the next, so that the position of slip-link ($\vec{s}_j$) jumps from its location on the spring whose vector is $\vec{Q}_i = \vec{r}_i - \vec{r}_{i-1}$ (see Figure 3.3), to a location on $\vec{Q}_{i+1}$, and so on. Therefore, one end of the slip-spring, $\vec{s}_j$, fluctuates in the kinked region, while the other end, $\vec{a}_j$, moves affinely with the flow, independent of the chain conformation.
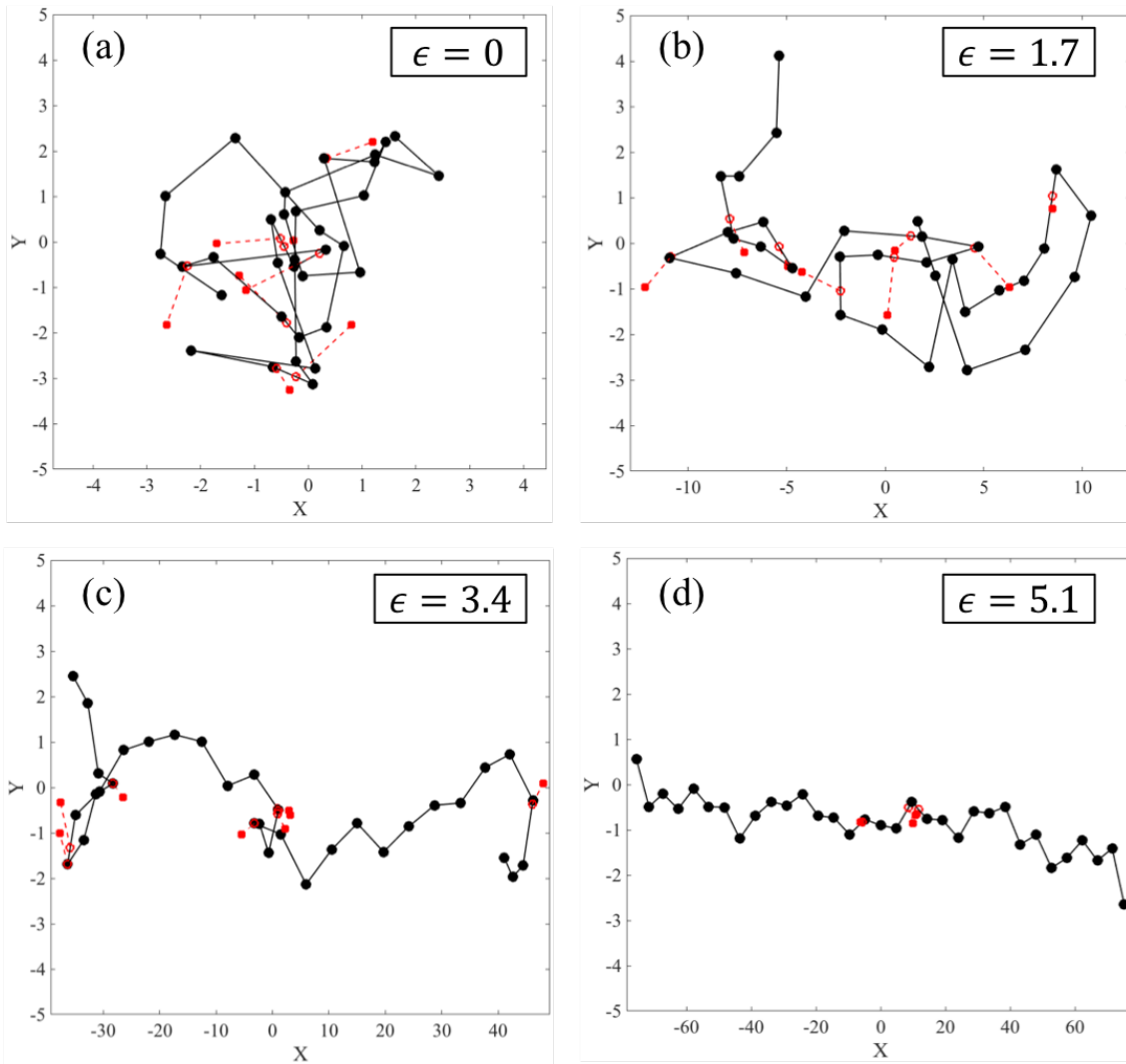
Figure 3.2. Evolution of a sample chain with $N_s = 32$ ($Z_0 = 8$) at $Wi_R = 16$, at Hencky strains of (a) $\epsilon = 0$, (b) $\epsilon = 1.7$, (c) $\epsilon = 3.4$ and (d) $\epsilon = 5.1$. Notice the x scale, but not the y scale, is increased in range at large strains. Main chain beads and springs are shown with black circles and lines, respectively, while slip-springs are shown in red, extending from their anchoring points marked with solid red circles to their positions on the chain, marked with open red circles. A maximum slip-spring force is used, and regeneration of slip-springs is turned off.

49
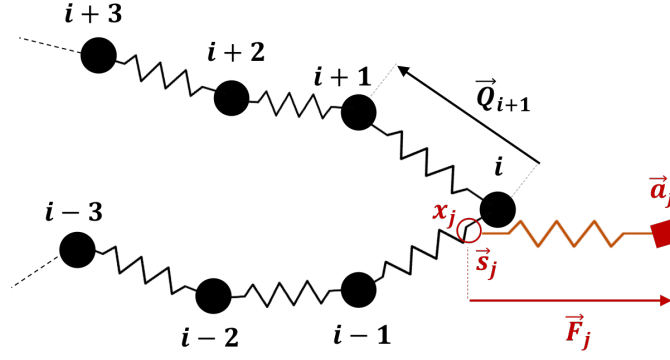
Figure 3.3. Trapping of slip-spring in the kinked region between three beads that define the folded area. The anchoring point ($\vec{a}_j$) moves affinely with the flow, while the position of the slip-link on the chain, determined by Equations (3.2) and (3.10), oscillates between spring $\vec{Q}_i$ and $\vec{Q}_{i+1}$.

This trapping dynamics in the kinked region results in a nearly complete extension of the slip-springs and consequently, high values of tension generated in the slip-springs, which exert non-physically high magnitudes of force on the main chain. The high slip-spring tension also causes slip-spring breakage when the spring stretches beyond its maximum extension within a single time state, even with very small Δt. Note that if the polymer chains were more highly resolved, say at the level of a Kuhn step, local Brownian motion would more readily allow beads on the chain to cross the slip link and trapping would then not occur. The chain would then slide through the slip link, which would keep the slip-spring force from exceeding the maximum chain tension for affine deformation, calculated in Equation (2.20). However, such a highly resolved chain would require much more computer time, and the advantage of the slip-spring algorithm over finer grained molecular dynamics simulations would largely be lost. Therefore, instead of a more highly resolved simulation, an upper limit of slip-spring force (F_{ss}^{max}) can be imposed to prevent the overextension of slip-springs and to keep the entanglement force within the physically meaningful range determined earlier by our kink dynamics analysis. For affine kink motion, the maximum entanglement force is given by $\zeta' \dot{\epsilon} L^2 / 8$ (Equation 2.20) and for EKD simulations, the actual average maximum force was found to be approximately four times lower, $\zeta' \dot{\epsilon} L^2 / 32$. Since

we initially impose affine deformation on the anchoring points of the slip-springs, we use the theoretical maximum force value $\zeta' \dot{\epsilon} L^2/8$ rather than the average maximum actually attained $\zeta' \dot{\epsilon} L^2/32$. Thus, from the kink dynamics analysis, we set a maximum entanglement force for the slip-springs that depends on the dimensionless contour length of the chain, $L = N_{k,s} N_s$, the strain rate $\dot{\epsilon}$ and the friction coefficient per unit length ζ'. The value of ζ', the friction coefficient per chain length that can be calculated from the Rouse theory, and the corresponding dimensionless value ζ'^*, are given as follows [158]:

$$
\begin{cases}
\zeta' = \dfrac{6\pi^2 kT \tau_R}{b_k^3 N_k^2} = \dfrac{6\pi^2 kT}{b_k^3 N_s^2 N_{k,s}^2} \tau_R \\
\tau_R = \dfrac{\zeta_b (N_s + 1)^2 N_{k,s} b_k^2}{6\pi^2 kT}
\end{cases}
\Rightarrow \zeta' = \frac{\zeta_b}{b_k} \frac{(N_s + 1)^2}{N_s^2} \frac{1}{N_{k,s}} \rightarrow \zeta'^* = \frac{(N_s + 1)^2}{N_s^2} \frac{1}{N_{k,s}} \quad (3.11)
$$

When the force in the slip-spring exceeds $F_{ss}^{max} = f_{affine}^{max} = \zeta' \dot{\epsilon} L^2/8 = 6\pi^2 Wi_R/8$, we therefore modify the position of the anchoring point by reducing the stretch of the connecting vector, without changing its direction, so that its force equals the maximum entanglement force. To do so, each time step the maximum force is exceeded, the anchoring point must be shifted backwards along the flow direction relative to the position the flow would otherwise take it, resulting in a non-affine motion of anchoring points at high strains where trapping tends to occur. If the force in the slip-spring is less than the maximum, the anchoring points move affinely. The expression $F_{ss}^{max} = 6\pi^2 Wi_R/8$ is obtained by combining Equations (2.20), (3.9) and (3.11) for the slip spring simulations. The imposition of a maximum force allows the slip springs to mostly avoid trapping, and hence the chain can slide through the slip link as it would do if the chain were more highly resolved. However, at the highest Weissenberg numbers, there are a few chains (~1-5) in an ensemble of 100 chains that show trapping even with the maximum entanglement force imposed. The imposition of the maximum slip-spring tension and non-affine motion of the slip-

spring is therefore an approximate method of preventing artificial trapping of the slip-link at the kink. We also examined the application of the lower maximum force $F_{ss}^{max} = \zeta' \dot{\epsilon} L^2 / 32$ on the chain conformation and same results were obtained which are not reported here.

Since the imposition of a maximum entanglement tension in slip springs is ad hoc, we also implement a more physical means of limiting the force on the slip springs, namely performing simulations with a pair of mutually coupled chains. In this method, we generate a pair of chains and equilibrate their conformation independently. After equilibration of the two chains and the application of extensional flow, the motion of a slip-spring anchoring point on one of the chains is coordinated with the motion of the anchor point on another chain, so that the pair moves on average affinely. To reduce the maximum tension on a slip spring, at each time-step, the anchoring point of the less stretched slip-spring (with a lower tension) located on one chain of the pair, is allowed to move farther than the anchoring point of the slip-spring on the other chain of the pair. For example, consider a pair of chains with $N_s = 32$ where each chain has 8 slip-springs randomly positioned along their contours. We randomly partner each slip-spring of the first chain with a slip link of the second chain. E.g., let's say we partner slip-spring 3 of chain 1 with slip-spring 7 of chain 2. Now, at each time-step, the force in each slip-spring is calculated from the Cohen-Pade equation [46]. Then, the motion of the anchoring points of slip-springs 3 of chain 1 and 7 of chain 2 follows:

$$\begin{cases} If\ F_{3,SS}^{1,t} > F_{7,SS}^{2,t} \rightarrow \begin{cases} \vec{a}_3^{1,t+\Delta t} = \vec{a}_3^{1,t} + \alpha \Delta t \boldsymbol{\kappa}.\vec{a}_3^{1,t} \\ \vec{a}_7^{2,t+\Delta t} = \vec{a}_7^{2,t} + (2-\alpha) \Delta t \boldsymbol{\kappa}.\vec{a}_7^{2,t} \end{cases} \\ If\ F_{3,SS}^{1,t} < F_{7,SS}^{2,t} \rightarrow \begin{cases} \vec{a}_3^{1,t+\Delta t} = \vec{a}_3^{1,t} + (2-\alpha) \Delta t \boldsymbol{\kappa}.\vec{a}_3^{1,t} \\ \vec{a}_7^{2,t+\Delta t} = \vec{a}_7^{2,t} + \alpha \Delta t \boldsymbol{\kappa}.\vec{a}_7^{2,t} \end{cases} \end{cases} \tag{3.12}$$

Where $F_{3,SS}^{1,t}$ and $\vec{a}_3^{1,t}$ are the tension and position vector of the anchor point of slip-spring 3 of chain 1 at time t. The value of the constant α determines the strength of the coupling between

entangled kinks, with $\alpha = 1$ giving ordinary affine motion of each anchor point. This algorithm, with $\alpha < 1$ lessens the build-up of tension in the highly stretched slip-spring, allowing the chain to slide more easily through the corresponding slip link, while keeping the average motion of the two coupled slip-springs affine. This method also allows us to implement constraint release in a self-consistent manner, where if a slip-spring on one chain is lost, the coupled slip-spring on the other chain is also removed. No-regeneration of slip links is implemented, consistent with our EKD method, where there exists no entanglement renewal. We repeat the two chains simulations for at least 100 different pairs and average the results.

Thus, we have three alternatives for managing the motion of the slip springs: 1.) Maximum Entanglement Force (MEF), 2.) Two-Chain (TC) simulations for four different values of $\alpha = 0, 0.25, 0.5, 0.75$, and 3.) Affine Motion (AM), which corresponds to method 2 above, with $\alpha = 1$ but without the inherent CR of method 2. Our EKD simulations suggest that the tension in slip-springs along the chain should be roughly uniform at the transition strain ($\epsilon = \epsilon_T$ or $\tilde{\epsilon} = 0$), as shown by the red dashed line in Figure 2.10. Note that, as explained earlier, the imposition of affine motion on the anchoring points of trapped slip-springs at the kinks results in huge tensions and eventual breakage of slip-springs, even with very small time-steps. Thus, to keep the slip-spring forces bounded for all three methods, whenever the length of a trapped slip-spring becomes greater than 0.99 of its dimensionless maximum length ($N_{k,ss}$), we calculate the tension of that slip-spring for a fixed value $L_{ss} = 0.99 N_{k,ss}$ and exert this force from the slip-springs on the main chain, independent of the length of the overextended slip spring which might take arbitrarily higher values than its maximum extension. Note that this is only required for alternatives 2 and 3 above where the maximum entanglement force, and relocation of slip-spring's anchoring point are not

applied. In comparison to MEF, where the maximum entanglement force is a function of strain rate, Equation (2.20), the slip-spring force calculated by considering $L_{ss}/N_{k,s} = \overline{L_{ss}} = 0.99$ is a constant $F_{ss}^{\overline{L_{ss}}=0.99} = 111.6$ (in dimensionless units) using the Cohen- Pade force equation in one-dimension [46]. At our high Weissenberg numbers, $Wi_R = 16, 32$, the MEF force for long chains will become high, $O(100)$, but as we will discuss in the next section, the modification of the anchoring point's position in the MEF method at each time step will give the chain time to move towards the slip-spring and relieve most of the generated stress in the slip-spring. The results of slip-spring simulations with these three methods of managing slip-spring motion and tensions are presented in the next section.
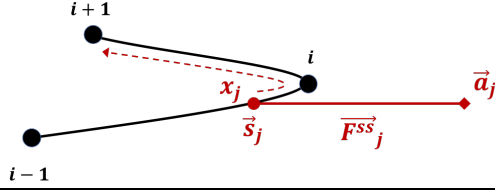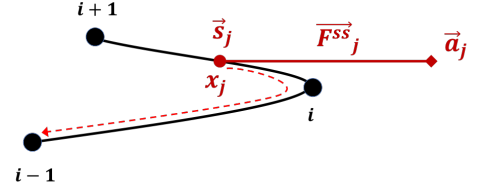
Before moving on to the results and discussion section, we present here our method of determining the time-step size (Δt) which, as we will discuss below, depends on our choice of ζ_s. In our slip-spring simulations using MEF technique, the choice of ζ_s, which is the friction coefficient of the slip links along the polymer chain's contour length, is very important, since it determines the escape time of an slip link from the chain, as mentioned by Likhtman [70]. Here, we develop a technique to determine the ratio of $\zeta_s/\Delta t$, where Δt is the size of the time step in our slip-spring simulations. Upon convection of a slip link to a kinked region, which is composed by three beads, Figure 3.3, the slip link position on the chain fluctuates along the length of the two springs composing the folded region, based on Equation 3.10. As the length, and consequently the generated force, of a slip-spring in the kinked region increases, the displacement of the slip link position at each time step increases, which may result in displacing the slip link position beyond one spring at a single time step, artificially making an entangled kink unentangled. In the absence of any form of constraint release, the only way that an entangled kink can disappear on a chain is that the chain destroys that kink, either by passing its ends through the kink or by shrinking the

length of a nearby strand length. Therefore, a slip-spring at a kink should not be able to escape the kinked region because of input simulation parameters such as ζ_s or size of the time-step, Δt. So, from t to $t + \Delta t$, the displacement Δx of the slip-link along the spring should not exceed a certain value (found below) that artificially moves the slip-link out of the kinked region without the chain needing to slide through the slip link. If Δx becomes too large the slip link will move past more than one bead, and the slip-spring gets out while the kink is not unraveled yet. This picture helps us determine the relationship between time-step size, Δt, and friction coefficient of slip-links on the chain, ζ_s. Based on the evolution equation for x_j, Equation (3.10), the maximum value of Δx during a single time-step Δt for a slip-link is achieved when the slip-spring force (F_j^{SS}) and neighboring beads' connecting vector ($\vec{r}_{|x_j|+1} - \vec{r}_{|x_j|}$) are at their maximum values, which we can estimate by a one-dimensional approximation:

$$
\begin{cases}
\text{1-D limit} \rightarrow \vec{r}_{|x_j|+1} - \vec{r}_{|x_j|} = X_{|x_j|+1} - X_{|x_j|} \xrightarrow{max} N_{k,s} \\
\text{1-D limit} \rightarrow F_{ss}^{max} = \frac{1}{8}\zeta'\dot{\epsilon}\left(N_s N_{k,s}\right)^2
\end{cases}
\Rightarrow \Delta x = \left(\frac{\zeta'\dot{\epsilon}N_s^2 N_{k,s}^3}{8}\right)\frac{\Delta t}{\zeta_s} + \sqrt{\frac{2\Delta t}{\zeta_r}}\,n
\qquad (3.13)
$$

Where X is the x-component of the position vector $\vec{r}$ of a bead and (n) is a random number between -1 and 1. Based on the position of the slip-link along a spring on the main chain in the kinked region, the Δx value in a single time-step should be prevented from moving across more than one bead. The criteria are summarized in Table 3.2.

Condition	Direction of slip-spring jump	Criterion for Δx
i		$\Delta x \leq \lfloor x_j \rfloor - x_j + 2$ $\left(\dfrac{\zeta' \dot{\epsilon} N_s^2 N_{k,s}^3}{8}\right)\dfrac{\Delta t}{\zeta_s} + \sqrt{\dfrac{2\Delta t}{\zeta_s}}\, n \leq \lfloor x_j \rfloor - x_j + 2$
ii		$\Delta x \geq \lfloor x_j \rfloor - x_j - 1$ $\left(\dfrac{\zeta' \dot{\epsilon} N_s^2 N_{k,s}^3}{8}\right)\dfrac{\Delta t}{\zeta_s} + \sqrt{\dfrac{2\Delta t}{\zeta_s}}\, n \geq \lfloor x_j \rfloor - x_j - 1$

Here we perform an analysis for condition (i) of Table 3.2, that can be extended to condition (ii) as well. For the first condition, we simplify Equation (3.13) by considering $\sqrt{\dfrac{\Delta t}{\zeta_s}}$ as the variable of the equation and replacing the coefficients of Equation (3.13) with A, B, C, as follows:

$$\begin{cases} A = \left(\dfrac{\zeta' \dot{\epsilon} N_s^2 N_{k,s}^3}{8}\right) \\ B = n\sqrt{2} \\ C = \lfloor x_i \rfloor - x_i + 2 \end{cases} \Rightarrow A\left(\sqrt{\dfrac{\Delta t}{\zeta_s}}\right)^2 + B\left(\sqrt{\dfrac{\Delta t}{\zeta_s}}\right) - C \leq 0 \tag{3.14}$$

By definition, we have following criteria for the parameters in the inequality (3.14):

$$\begin{cases} A > 0 \\ -\sqrt{2} < B < \sqrt{2} \\ C > 0 \\ \sqrt{\dfrac{\Delta t}{\zeta_s}} > 0 \end{cases} \tag{3.15}$$

To satisfy the inequality (3.14), two conditions should be met: (1) the discriminate of the equation $(A\left(\sqrt{\Delta t/\zeta_s}\right)^2 + B(\sqrt{\Delta t/\zeta_s}) - C = 0)$ should be positive, $\Delta = B^2 + 4AC > 0$ and (2)

56

the variable $\sqrt{\Delta t/\zeta_s}$ should take values within the two roots of the equation $\left(A\left(\sqrt{\Delta t/\zeta_s}\right)^2 + B\left(\sqrt{\Delta t/\zeta_s}\right) - C = 0\right)$, $P_1 \leq \sqrt{\Delta t/\zeta_s} \leq P_2$, where P_1 and P_2 are the two roots, given by:

$$\begin{cases} P_1 = \dfrac{-B - \sqrt{B^2 + 4AC}}{2A} < 0 \\ P_2 = \dfrac{-B + \sqrt{B^2 + 4AC}}{2A} > 0 \end{cases} \tag{3.16}$$

Since $4AC$ term in above expressions is always positive, for any value of B between $-\sqrt{2}$ and $\sqrt{2}$, numerator of P_1 will be negative, which results in an always negative P_1 as the smaller root of the quadratic equation. However, the value of $\sqrt{\Delta t/\zeta_s}$ is always non-negative. Thus, the final bounds for $\sqrt{\Delta t/\zeta_s}$ to satisfy the inequality (3.14) are:

$$0 \leq \sqrt{\frac{\Delta t}{\zeta_s}} \leq \frac{-B + \sqrt{B^2 + 4AC}}{2A} = P_2 \tag{3.17}$$

Based on A3, we have to make sure that our choice of time step size and ζ_s give us a $\sqrt{\Delta t/\zeta_s}$ less than P_2. However, the value P_2 can change based on B and C which themselves can vary based on the random number generator and location of slip-link, respectively. But, if for the smallest value of P_2, our choice of $\sqrt{\Delta t/\zeta_s}$ still meets (3.17) criterion, we can make sure that for any generated random number or slip-link location on the chain, (3.17), and consequently (3.14) are satisfied. The smallest value of P_2 is achieved in the limit of $B = \sqrt{2}$ and $C = 1$. A is calculated from the chain length (i.e., the number of Kuhn lengths per spring, $N_{k,s}$ and number of springs per chain, N_s), the applied strain rate, $\dot{\epsilon}$, and the friction coefficient per unit length, ζ', where the latter is given by Equation (3.11). Table 3.3 shows the values of P_2^2 for the choice of $B = \sqrt{2}$ and $C = 1$, for different chain lengths at difference Weissenberg numbers.

Table 3.3. Values of P_2^2 corresponding to the upper limit of $\Delta t/\zeta_s$ in the slip-spring simulations for various chain lengths and Rouse Weissenberg numbers.

	$N_s = 16$	$N_s = 32$	$N_s = 64$	$N_s = 128$
$Wi_R = 2$	0.0128	0.012	0.01181	0.01165
$Wi_R = 4$	0.00674	0.0063	0.0063	0.0061
$Wi_R = 8$	0.00347	0.0033	0.00326	0.00316
$Wi_R = 16$	0.00178	0.00173	0.00164	0.00162
$Wi_R = 32$	0.00091	0.00086	0.00084	0.00081

Based on P_2^2 values in Table 3.3, the choice of $\Delta t = 10^{-4}$ and $\zeta_s = 0.1$, which corresponds to $\Delta t/\zeta_s = 10^{-3}$, is justified for all chain lengths up to $Wi_R = 16$. For $Wi_R = 32$, we reduce the time step size and choose $\Delta t = 10^{-5}$ and $\zeta_s = 0.1$, corresponding to $\Delta t/\zeta_s = 10^{-4}$, to make $\Delta t/\zeta_s$ less than the values of the last row of Table 3.3. Since simulations are performed with explicit time-integration, possible spring breakage and slip-spring force in excess of the maximum value are also checked at each time step. Applying the same analysis to condition (ii) results in the same bounding values for Δt. Note that using an implicit technique may remove the need of such an analysis of maximum timestep to avoid the slip link moving past more than one bead, or the spring breaking, or the maximum force being exceeded. However, an implicit method for single-chain slip-spring simulations is not yet available, and having the artificial friction coefficient, ζ_s present in the slip-spring model makes above analysis for timestep size necessary. In deriving Δt, we imposed the maximum slip-spring force $F_{ss}^{max} = \zeta'\dot{\epsilon}(N_s N_{k,s})^2/8$; therefore for any slip-spring force below this, the conditions (i) and (ii) are satisfied if $\Delta t/\zeta_s$ is constrained as specified in Table 3.3.

3.4   Simulation Results and Discussions

3.4.1   Comparison of Maximum Entanglement Force (MEF), Two-Chain (TC), Affine Motion (AM) Methods

Figure 3.4 shows the evolution of slip-spring tension along a chain with $N_s = 32$ and $Z_0 = 8$ at $Wi_R = 32$ where the effect of trapping becomes important, for all three simulation methods.
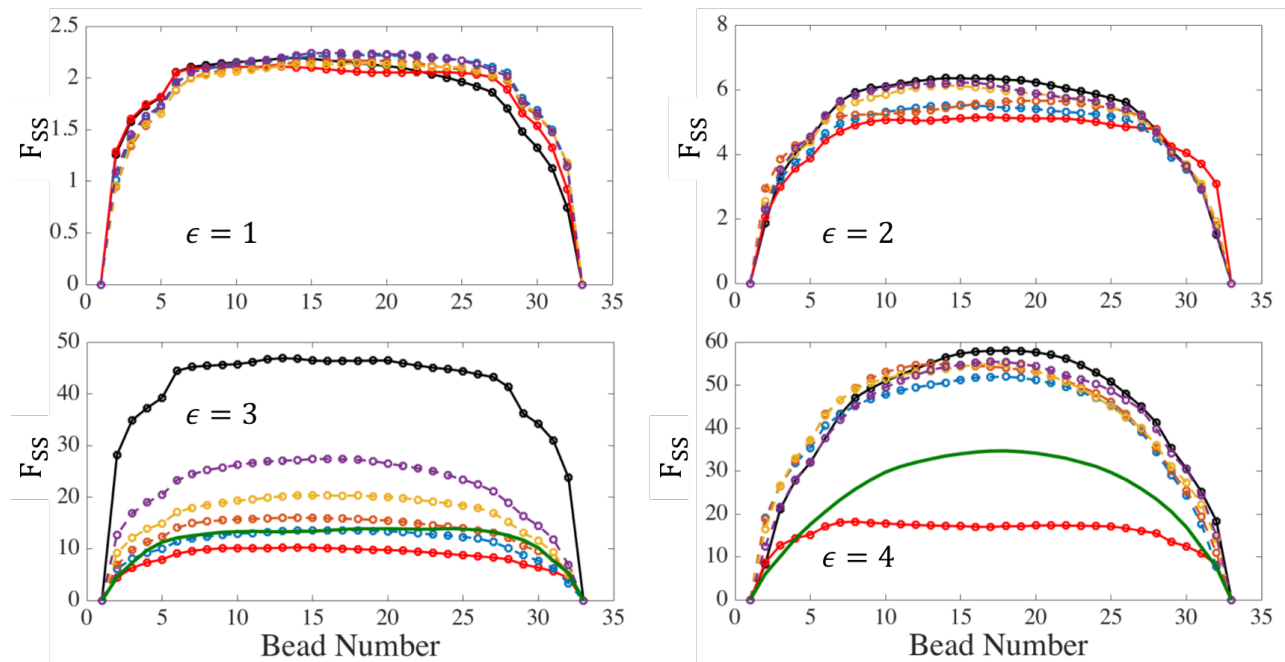
Figure 3.4. Distribution of tension in slip-springs on a chain with $N_s = 32$ at $Wi_R = 32$ at different Hencky strains. Affine Motion (AM) results are shown with black lines and maximum entanglement force (MEF) results with red lines. Results for the Two-Chain (TC) technique are shown with blue, orange, yellow and purple lines for the strengths of entangled kink coupling given by $\alpha = 0, 0.25, 0.5$ and 0.75 respectively. The solid green line without symbols shows the result of EKD simulations at Hencky strains of 3 and 4. All tensions are averages over an ensemble of 200 chains.

At small strains ($\epsilon = 0.01$ and 1) the tension distribution is nearly identical in all cases: a nearly uniform tension is found except near the chain ends. However, as the strain increases to around 2-3 Hencky units, the chain starts to align and elongate in the flow direction and the tension under affine motion of slip-spring anchor points diverges from the MEF and TC simulations. At a Hencky strain of $\epsilon = 3$, which we will later show is the transition strain at which the kinked state

emerges, the tension under affine motion is almost 5 times higher than for the other cases. Up to $\epsilon = 3$, both TC and MEF show nearly uniform, moderate, tension; however, as the elongation continues, the tension predicted by the Two-Chain (TC) method starts to rise faster and approach that for affine motion. We find that at high strain, the coupling technique does not prevent trapping, and the same behavior is obtained as in affine deformation. On the other hand, the tensions obtained for the maximum entanglement force technique remain at much lower values, even for $\epsilon = 4$. To compare the tension in slip-spring simulations to that of EKD simulation for the chains used in Figure 3.4, we perform EKD simulations by exporting the conformation of chains at $\epsilon = 3$ from slip-spring simulations and entangling 80% of the kinks (a percentage used in our previous publication for a highly entangled polymer). The results are shown by solid green lines in Figure 3.4. Note that we are not allowed to use kink dynamics for Hencky strains less than 3, below which the chain has not yet formed the folded state yet. This explains the absence of the green line at $\epsilon = 1$ and 2. Comparing EKD with MEF results, it can be seen that although the MEF method keeps the slip-spring tension at moderate values, it predicts lower tension in the chain center than does the EKD simulations of the same chain. However, as noted, both MEF and TC give similar tension distribution at the transition strain ($\epsilon_T \sim 3$) which also resembles that obtained from EKD simulations. Thus, the single-chain maximum entanglement force (MEF) method matches with that of the TC method up to the transitional strain, where both methods approach that of the EKD algorithm. For higher strains ($\epsilon > \epsilon_T$), the dynamics can be tracked by kink dynamics rather than coarse-grained slip-spring simulations. We shall show below, however, the MEF method within the slip spring simulations gives extensional viscosities similar to those of the EKD method from the transitional strain all the way to complete chain extension.

To check the performance of the MEF method beyond the transition strain and during the unraveling regime ($\epsilon > \epsilon_T$), a bead-spring chain in a kinked configuration with one kink is generated and a slip-spring with $F_{ss}^{max} = \zeta' \dot{\epsilon} L^2 / 8$ is located in the kinked region. The slip-spring force is at its maximum $F_{ss}^{max} = \zeta' \dot{\epsilon} L^2 / 8$ at the start of the slip spring simulations and we keep this force at this constant maximum value for the slip-springs in these calculations. A picture of the same chain in the kink dynamics approach is also generated and affine motion is applied to the kink, as illustrated Figure 3.5(b). We study the strain at which the chain achieves full unraveling (FU) with both MEF and affine kink dynamics approaches, which we label ϵ_{SS}^{FU} and ϵ_{Kink}^{FU}, respectively. Table B1 shows the values of ϵ_{SS}^{FU}, ϵ_{Kink}^{FU} and their ratios for the three conformations.

Table 3.4. Hencky strains at which the slip-spring and kink conformations of Figure 3.5 achieve a fully unraveled state.

Conformation	ϵ_{SS}^{FU}	ϵ_{Kink}^{FU}	$\epsilon_{SS}^{FU}/\epsilon_{Kink}^{FU}$
1	1.22	0.61	2.00
2	4.87	2.42	2.01
3	2.99	1.52	1.97

For all three cases, twice as much strain is required to fully unravel the chain from the kinked state in the slip-spring simulations than under the affine motion assumption. The factor of two can be attributed to the temporary trapping of the slip-spring between the two springs that compose the kinked region. Since the slip-spring spends half of its lifetime on the top strand and the other half on the bottom strand, the unraveling is delayed since the slip-spring exerts a drag alternately first on one strand and then on the other, which frustrates chain unraveling. Interestingly, we previously showed that, starting from the kinked state, the strain at which EKD achieves full unraveling is almost twice that of affine motion as shown in Figure 2.7, which matches with what find here with MEF. Thus, it seems that the slip-spring simulations under MEF assumption (a maximum force and re-location of slip spring's anchoring points) follow the same

chain evolution, as in the EKD. This means that for the full coil-to-stretch evolution of the chain, one can use the slip spring simulations with MEF assumption. However, as mentioned before, the computational time of the slip spring simulations increases as the chains get longer, which may limit its use for comparison with experimental data.

We also compare in Figure 3.6 the extensional stress predicted by the EKD model compared to that for the corresponding slip-spring model out to complete extension of polymer. The stress in the slip-spring simulations is calculated using the Kramers-Kirkwood equation for a Rouse chain [155]. The stresses using the EKD simulations are plotted from the transition strains of each chain length, shown by green circles in Figure 3.6. In the next section, we explain how these transition strains are found. Note that no vertical fitting of EKD results to the slip-spring results is done and the match between EKD and slip-spring stress at the transitional strain is remarkable. The results for the two models are in good agreement except at strains beyond the transitional value. Since very different methods are used in the two models, one involving paired ideally one dimensional chains with no Brownian force (the EKD method) and the other involving slip links with non-affine motion of entanglement points imposed by a maximum force criterion, the agreement of the two methods suggests the robustness of the results. The discrepancy between slip spring simulations and EKD at high strains, $\epsilon = 6$ to 8 can be attributed to the discreteness of chains in our bead spring model compared to the resolved kink dynamics approach. We will later show that the stress predicted by the EKD method also gives good agreement with experimental data.
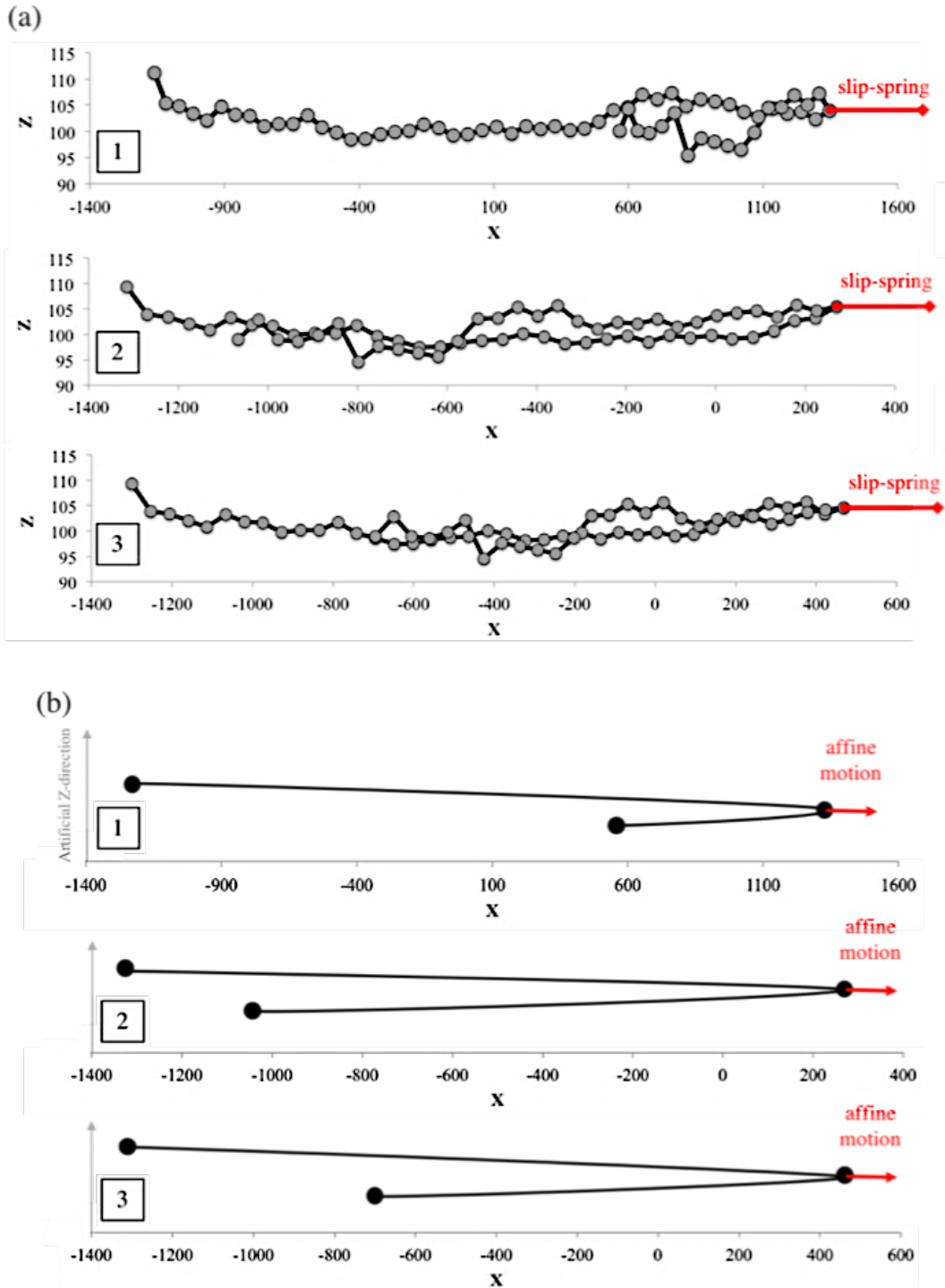
Figure 3.5. Three conformations used to compare the unraveling behavior of a chain from the kinked to fully unraveled state in (a) the slip-spring simulations and (b) kink dynamics simulations. In the slip-spring simulations, $N_s = 64$ and the maximum applied force, $F_{ss}^{max} = \zeta' \dot{\epsilon} L^2 / 8$, is applied. In the kink dynamics simulations, affine motion is imposed at the kink.
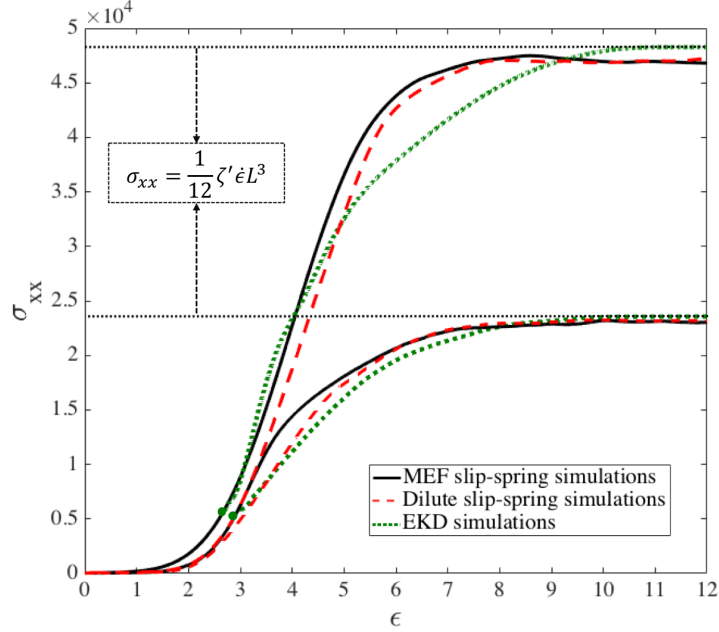
Figure 3.6. Extensional stress in x-direction (σ_{xx}) for chains of length $N_s = 32$ (lower set of curves) and $N_s = 64$ at $Wi_R = 32$ (upper set of curves). Black lines are obtained under the MEF assumption while the dashed red lines are for chains without slip-springs; i.e., dilute chains. EKD results, plotted starting from the transition strain $\epsilon = 3$, are shown with green dotted lines. The two horizontal dotted lines show the theoretical final stress value that an entangled or unentangled chain will achieve when fully unraveled. The results for both slip link methods and EKD are averaged over an ensemble of 150 chains.

3.4.2   MEF Results for Chain Conformation

Single-chain slip-spring simulations are performed for chains with $N_s = 16, 32, 64, 128$ springs which corresponds to $N_k = N_s N_{k,s} = 80, 160, 320, 640$ Kuhn steps in the chain ($N_{k,s} = 5$), respectively. The maximum entanglement force (MEF) method with the value of $F_{ss}^{max} = \zeta'\dot{\epsilon}L^2/8$ is used in all simulations. We seek to determine: (1) the transition strain to the kinked state (ϵ_T) as a function of chain length and Weissenberg number (2) the number of kinks (N_{Kinks}); (3) the ratio of entangled to unentangled kinks (ρ_{EK}^0); and (4) the strand length distribution between fold points, with the last three of these determined at the strain ϵ_T. To be consistent with our kink dynamics simulations, no regeneration of slip-springs is considered; therefore, when a slip-spring passes the chain end, it is lost, and no slip springs are re-introduced. As a consequence, the number of slip links, or entanglements, decreases from its initial value, Z_0, to 0, as the chain becomes

completely unraveled. Later in this section, we will study the effect of entanglement renewal and constraint release on chain statistics at the kinked state.

To find the number of kinks, we map the chain along the extension direction (x-axis in our simulations) and find the beads at which the chain folds back on itself, as depicted in Figure 3.7.
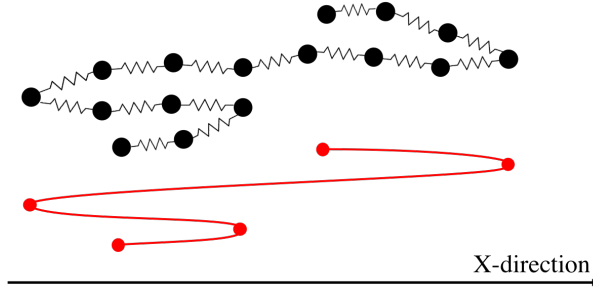
Figure 3.7. Schematic of mapping of a bead-spring chain into a kinked conformation. The chain has 5 kinks, including the first and the last beads.

To define the occurrence of the kinked state in the slip-spring simulations, the chain should meet two conditions. First, the chain should take on an "almost" one-dimensional conformation, and secondly, the springs on the main chain should be "highly stretched." The first criterion, one dimensionality, is quantified by measuring the ratio of radius of gyration in x-direction to those of the y- and z-directions:

$$R_{g_{x/y}} = \frac{R_{g_x}}{R_{g_y}} = \sqrt{\frac{\langle \sum_i (x_i - x_{c.m.})^2 \rangle}{\langle \sum_i (y_i - y_{c.m.})^2 \rangle}} \quad , \quad R_{g_{x/z}} = \frac{R_{g_x}}{R_{g_z}} = \sqrt{\frac{\langle \sum_i (x_i - x_{c.m.})^2 \rangle}{\langle \sum_i (z_i - z_{c.m.})^2 \rangle}} \quad (3.18)$$

Here $x_{c.m.}$, $y_{c.m.}$ and $z_{c.m.}$ are x, y and z components of center of mass of the chain at each time step, respectively. Satisfaction of the second criterion is determined by finding the average relative extension of springs (L_r^{spring}) on the main chain. To do so, we calculate the average length of all springs at each time step and then divide that by the maximum extensibility of a spring, which is $N_{k,s}$ in our dimensionless length units.

$$L_r^{spring} = \frac{\frac{1}{N_s}\langle \sum_{i=1}^{N_s}|Q_i|\rangle}{N_{k,s}} \tag{3.19}$$

where $\langle . \rangle$ denotes the ensemble average. We choose $L_r^{\text{spring}} > 0.7$ to be our criterion for "nearly fully stretched" of strands between folds. This value is chosen for two reasons. First, even in strong flows and for a fully unraveled chain, springs at the chain ends are not highly extended, which decreases the average relative extension. In addition, when the one-dimensional folded state is represented by a bead-spring chain, the springs near a kink shrink as they move around the kink, which further limits the average stretch. Thus, we cannot expect to have full extension for all the springs. We find as discussed below that around 70% average extension is an appropriate criterion to define the folded state
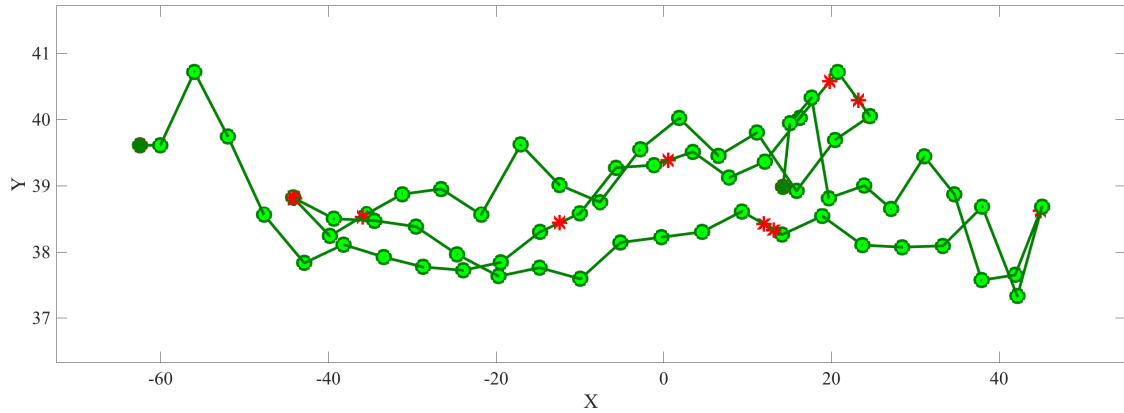
Figure 3.8. Conformation of sample chain in slip-link simulations at 70% relative average spring extension ($\epsilon \cong 3$). The chain has 64 springs (green lines) between 65 beads (green spheres) and the simulation starts with 16 slip-springs (red stars), with $N_e = 4$. Some slip-links are trapped at kinks and we define these as "entangled kinks." Other slip-springs move along the chain and are swept off the chain ends. Note the expanded Y axis compared to the X axis, to make the chain conformation clear. Without this expansion of the Y axis, the configuration would look more nearly one dimensional.

Figure 3.8 shows a sample chain in a folded state whose unraveling thereafter dominates the dynamics. We plot in Figure 3.9 the number of kinks and relative radius of gyration $R_{g_{x/y}}$ for a sample chain with $N_s = 32$ at different Weissenberg numbers. We also plot the average relative

extension of springs (L_r^{spring}) as the chain is elongated. All the results are ensemble-averaged over 100 chains.
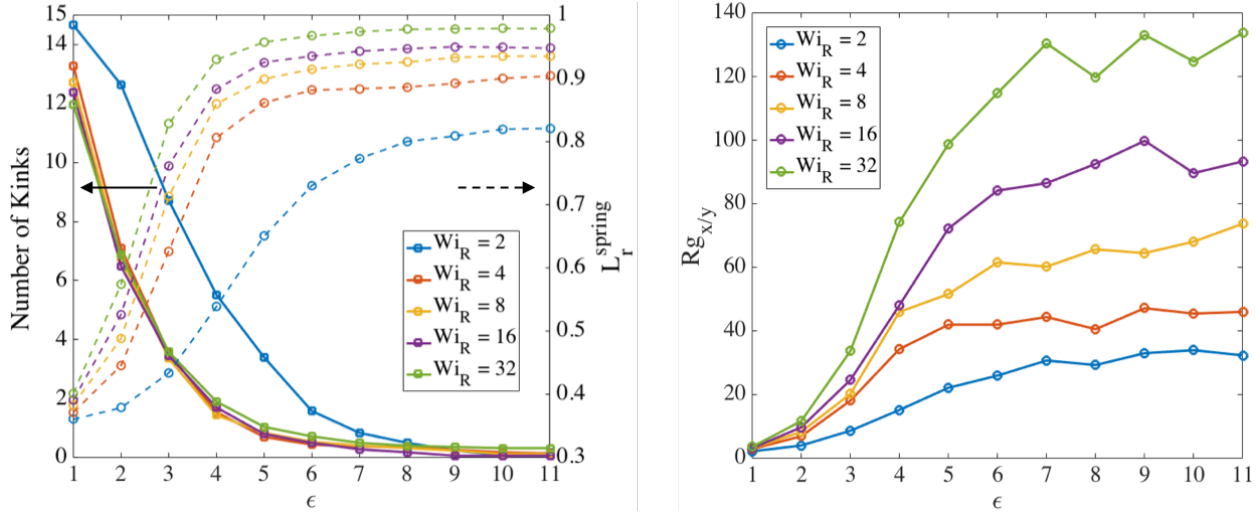
Figure 3.9. Evolution of (left) number of kinks (left axis) and averaged extension of springs (right axis) and (right) relative radius of gyration ($Rg_{x/y}$) for a chain with $N_s = 32$ at different Weissenberg from slip-spring simulations with Maximum Entanglement Force (MEF) condition. The averaged extension of springs is calculated using Equation 3.14.

Based on Figure 3.9, by a Hencky strain of around 3 the chain is almost a one-dimensional object with $Rg_x > 20Rg_y$ for high Weissenberg numbers. At around the same strain, the average extension of springs also reaches the 70% criterion chosen earlier. Based on our observation of chain's conformation evolution, e.g. Figure 3.9, we find the strain (ϵ_T) at which the two criteria (nearly 1D configuration and average spring stretch of 70%) are met and plot the results for different chain lengths in Figure 3.10.
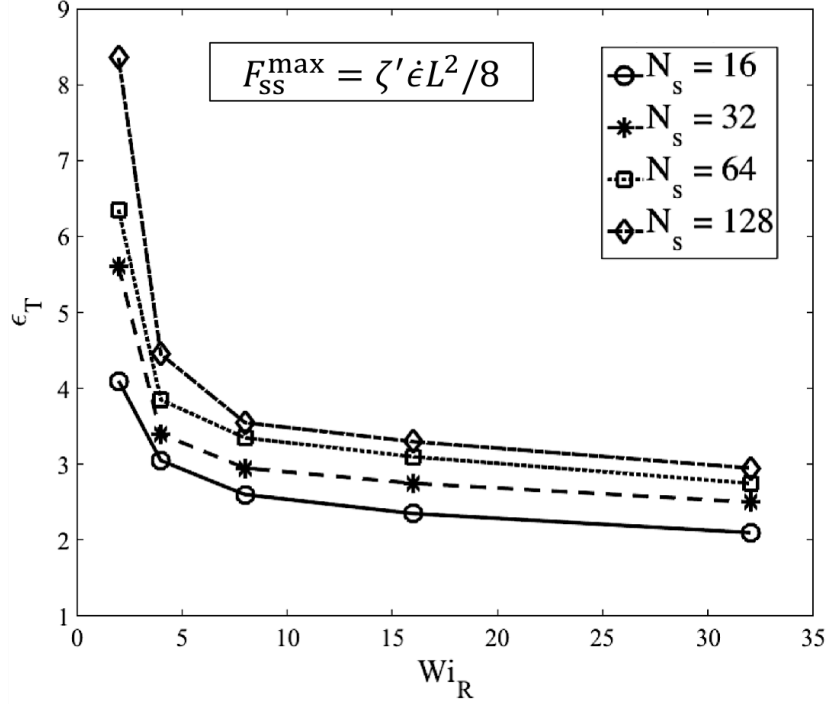
Figure 3.10. Transition strain for different chain lengths as a function of Rouse Weissenberg number for slip-spring simulations under MEF assumption.

Figure 3.10 shows that the transition strain (ϵ_T) for different chain lengths approach a value of around 3 at high Weissenberg numbers. To further investigate the transition strain, as another, independent, method to estimate the transitional strain, for each molecular weight of polystyrene sample shown in Figures 2.1 - 2.3, we solve the tube model at high strain rates, and find the strain at which stress starts to rise quickly to the asymptotic value. The strain at which this occurs is considered to be the strain at which kink dynamics start to dominate. Before this strain, the chain is still aligning into the flow direction and tube segment stretch is small. Figures 3.11 – 3.13 show the predictions of a tube model (DEMG) for entangled polystyrenes of molecular weights $M_w = 900K, 1760K$ and $3280K$ at different strain rates. All inputs for the tube-model predictions are taken from Huang et al. and are summarized in Table 2.1. We can see that the value of kinked state strain depends somewhat on chain length, it remains close to $\epsilon = 3$, as the slip-spring simulations also suggest. The largest deviation from $\epsilon_T = 3$ is observed for PS with $M_w = 900K$, which, as

might be expected, shows a smaller value of transition strain than for the higher molecular weights.

As the molecular weight increases, the formation of the kinked state should become progressively less sensitive to the presence of the chain ends, and we expect the transitional strain to converge to an asymptotic value. For the two higher molecular weights, the transitional strain indeed appears to be converging to a constant value of around $\epsilon_T = 3$, and for molecular weights above around 1,000K, the deviations from $\epsilon_T = 3$ are small. Very similar results were obtained using the MLD model, which are not shown here.
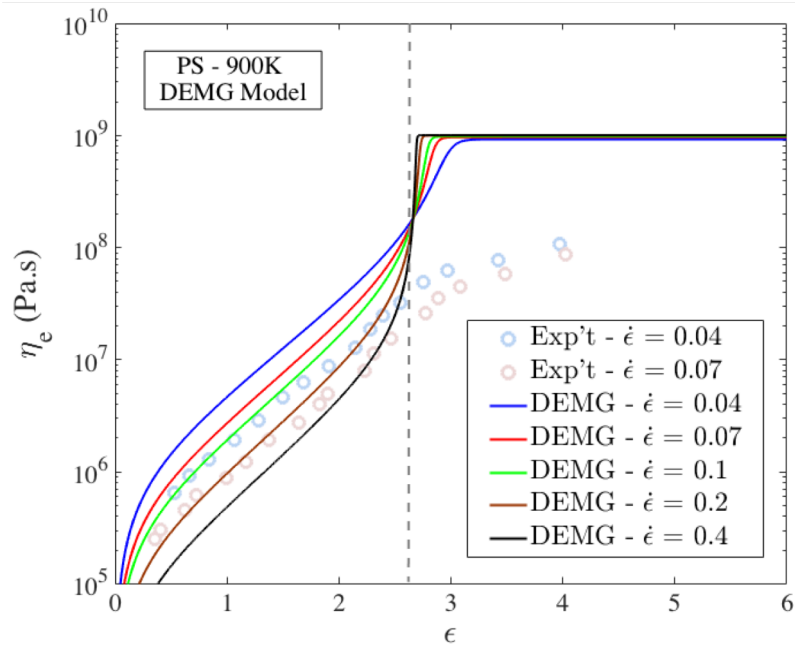
Figure 3.11. Predictions of DEMG model at high strain rates for a 33 wt% polystyrene (900K) solution. (Data from Huang et al. [157]).
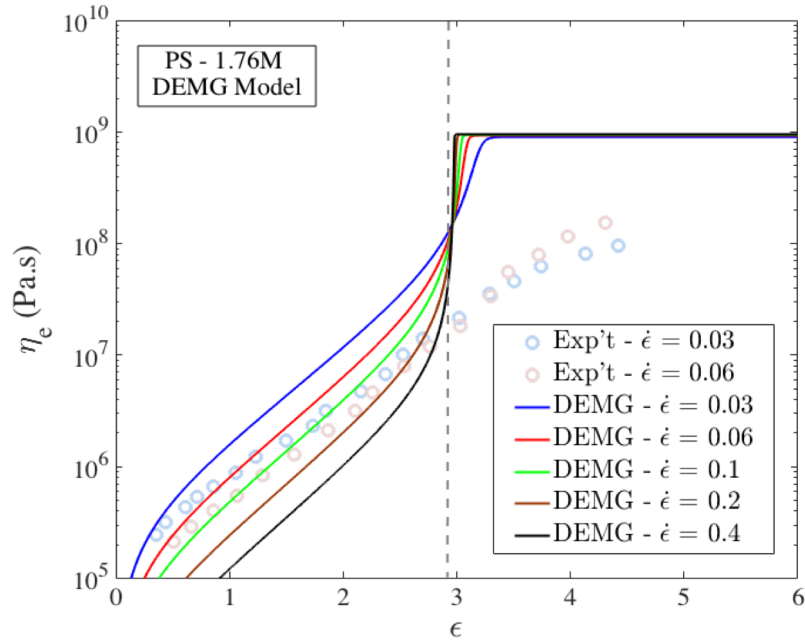
Figure 3.12. The same as Figure 3.11, except for a 18 wt% polystyrene (1760K) solution.
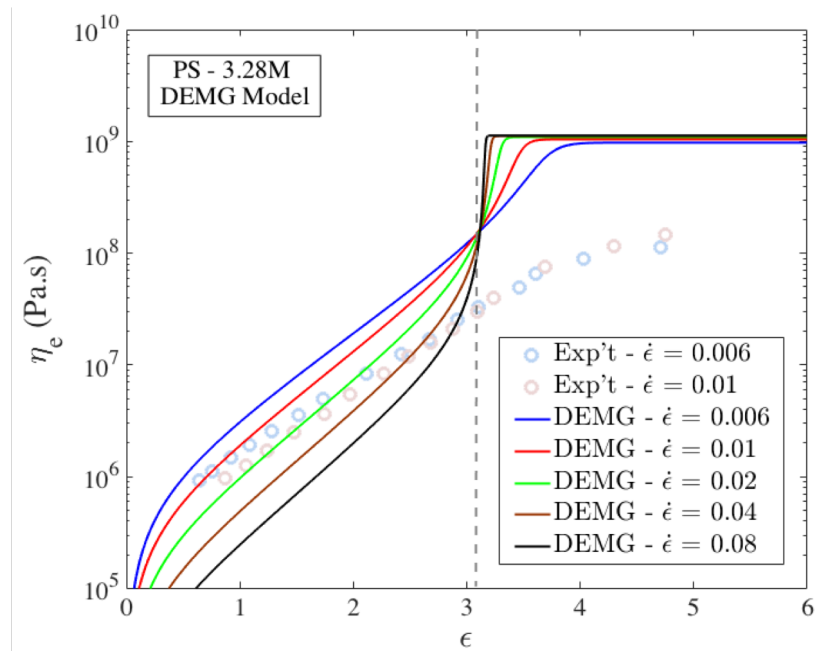
Figure 3.13. The same as Figure 3.11, except s for 13 wt% polystyrene (3280K) solution.

In an extensional flow, the distance in the extension direction between the ends of the chain tends to increase exponentially, in proportion to $\exp(\epsilon)$. Therefore, by the time $\epsilon = 3$, the chain ends have increased their separation by a factor of around 20, large enough for the configuration

to be approximated as a one-dimensional folded state. Therefore, we take $\epsilon = 3$ to be our transition strain (ϵ_T) for onset of the kinked state.

Figure 3.14 shows the number of kinks formed along the chain at the transition strains found in Figure 3.10.
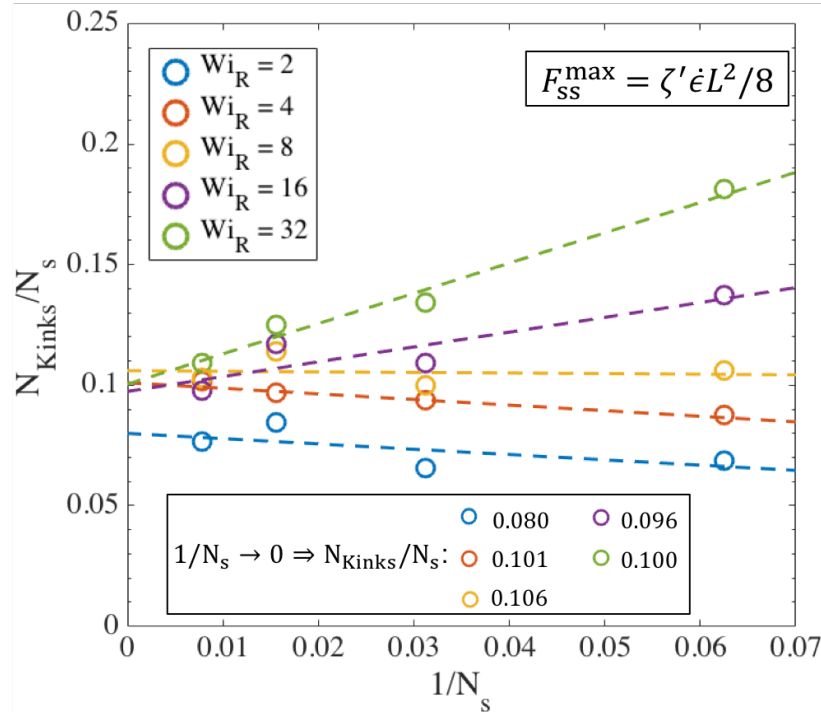
Figure 3.14. Number of kinks divided by the number of springs N_s plotted against $1/N_s$ for different values of Wi_R. The intercept with the y-axis is the asymptotic value of the ratio N_{Kinks}/N_s given in the legend for each Wi_R.

A linear correlation $N_{Kinks} = wN_s$, is observed between the number of kinks and number of springs, with the ratio w converging to 0.1 at high values of Wi_R. This relationship gives us the number of kinks at the transitional state for an arbitrary number of springs, and for an arbitrary chain molecular weight; e.g. $N_{kinks}^0 = 0.02(M_w/742)$ for polystyrene where the molecular weight to number of Kuhn steps relation is obtained from standard methods [17]. We use this equation to find the initial number of kinks for the polystyrene chains whose extensional viscosities were shown in Figures 2.1 – 2.3.

We also determine the ratio of entangled to unentangled kinks at the transition to the kinked state. We consider an "entangled kink" to be one for which there is a slip-link in a "folded region," which consists of the two springs on either side of a bead located at a "fold point," which is a bead for which the two neighboring beads are both either at small or larger values of x, the stretch direction. (If multiple slip-links are within the same kinked region, the kink only counts as a single "entangled kink."). We then compute the ratio of entangled to total kinks as:

$$\rho_{EK}^0 = \frac{N_{Kinks}^{Entangled}}{N_{Kinks}^{Total}} \qquad (3.20)$$

The superscript (0) is used because the entangled kink density is calculated at the transition strain determined from the slip-spring simulations; this value, given by Equation 3.15, is used as the initial entanglement fraction of kinks in the kink dynamics (EKD) simulations which start at $\tilde{\epsilon} = 0$. Figure 3.15 shows the ratio of the numbers of entangled to total kinks for different chain lengths obtained from slip-spring simulations, with no slip-spring regeneration or constraint release.
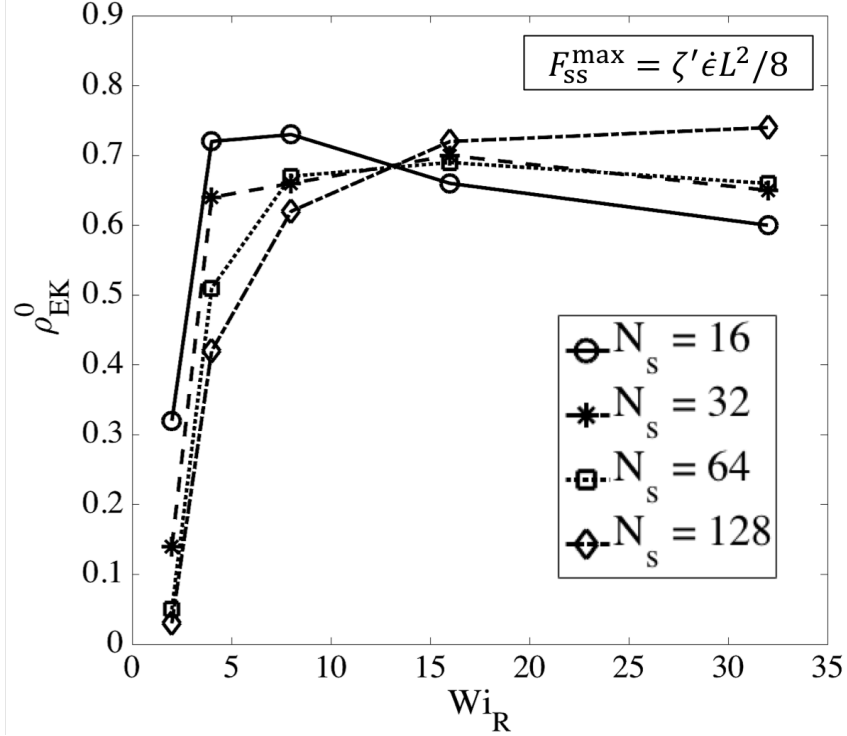
Figure 3.15. Fraction of entangled to total kinks (ρ_{EK}^0) for different chain lengths as a function of Weissenberg number at the transition to the kinked state.

Figure 3.15 shows that at high Weissenberg numbers, for all chain lengths, the fraction of entangled kinks converges to the range $[0.6 - 0.7]$. We had the value $\rho_{EK}^0 = 0.8$ in kink dynamics simulations for highly entangled polystyrene samples in the previous chapter [46]. Based on the results in Figure 3.15, however, we here choose $\rho_{EK}^0 = 0.65$ as a more appropriate value for EKD simulations. We note that this value is appropriate for entangled polymer solutions of volume fraction 0.2, but may well differ for other volume fractions. Different number of Kuhn steps between slip-links would be needed to explore further the dependencies of ρ_{EK}^0 on polymer concentration.

Finally, the strand length distribution at the transition to the kinked state is found by measuring the lengths of strands between fold points (beads located at the kinks). Strand lengths normalized by the contour length of the chains are plotted in Figure 16 for $Wi_R = 32$, which is our strongest flow. The distribution function is approximately exponential. Results for $Wi_R = 16$

and 8 were similar, except that there are significant deviations from an exponential form. Using

the MATLAB toolbox, we fit to an exponential density function for the two longest chains ($N_s =$

64 and 128), and find:

$$f(\hat{L}_{strand}) = (1/\mu)\,exp(-\hat{L}_{strand}/\mu)\ ,\mu = 0.193 \qquad (3.21)$$
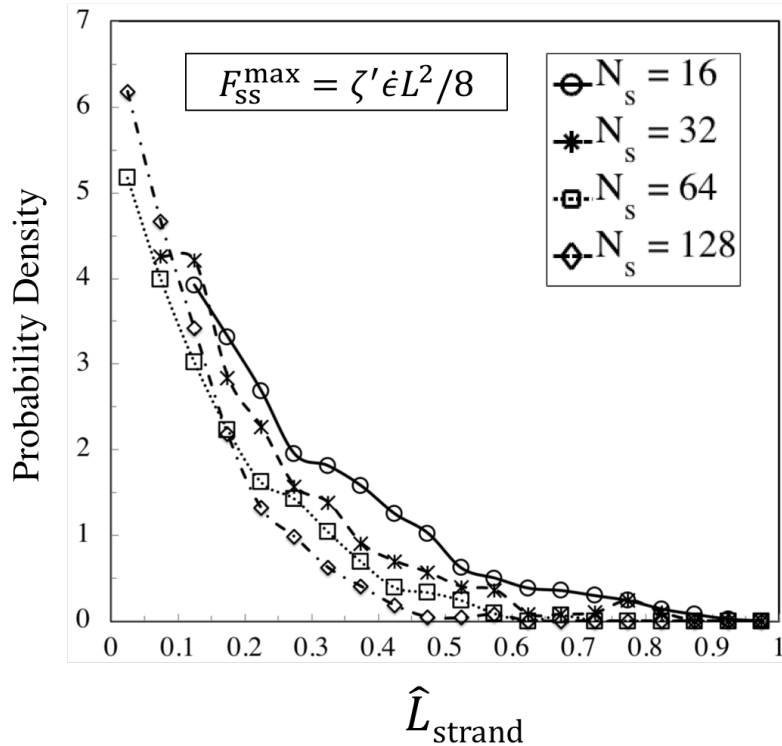
Figure 3.16. Strand length probability density for different chain lengths at $Wi_R = 32$. Strand lengths are obtained at the transition strain corresponding to formation of the kinked state of each chain at $Wi_R = 32$.

We summarize the above results with the following formulas for the statistics of a chain

with arbitrary length (or molecular weight) at its kinked state produced at asymptotically high

strain rates:

1. $\epsilon_T \cong 3$

2. $N_{\text{Kinks}} \cong 0.02 N_k$ (e.g. for polystyrene $N_k = M_w/742$) [46]

3. Fraction of entangled kinks: $\rho_{EK}^0 \cong 65\%$

4. Strand length probability distribution: $f(\hat{L}_{\text{strand}}) = \frac{1}{\mu}\exp\left(-\frac{\hat{L}_{\text{strand}}}{\mu}\right), \mu = 0.193$

Finally, we analyze the effect of slip-spring regeneration and constraint release (CR). Previously, Likhtman [70] and Del Biondo et al. [72] implemented constraint release by partnering slip-links between different chains within an ensemble of chains, in simulations of linear viscoelasticity and simple shear, respectively. In their method, when a slip-link passes off the end of its chain, it is destroyed, and, simultaneously, the partner slip link on the partner chain is destroyed. Then two new slip links are generated, one at the end of a randomly chosen chain and the other one on a random position along the contour length of another chain. This results in a constant number of slip-springs at all times, even during a deformation. In his single-chain simulations, Uneyama [29] defined destruction and creation probabilities following Glauber-type dynamics [171] and showed a reduction in the number of slip-links (Z) with time after start-up of shear flow [61]. A similar reduction under shear flow was also reported by Kushwala and Shaqfeh [172] and by Schieber and coworkers [74]. Here, we implement a simple single-chain technique to incorporate the addition/removal of slip-springs without needing an ensemble of chains or a partnering of slip-links on different chains. Although our method of regeneration and CR is not as detailed as in previous studies, the method targets some limiting cases. Four different conditions are considered:

1. *Regeneration Off; CR Off*: when a slip-link passes through its chain end, it is destroyed, and no further action is taken for other slip-links on the chain. This results in a continual reduction in the number of slip-links until all of them are gone. This condition has been used to obtain the results in section 3.2.

2. *Regeneration Off – CR On*: when a slip-link passes through its chain end, it is destroyed. Simultaneously, another slip-link on the same chain is randomly chosen and removed to represent constraint release produced by other chains, which are not simulated directly. Since there is no regeneration, slip-springs disappear faster than in Condition 1 above.

3. *Regeneration On; CR Off*: If a slip-link passes by the chain end, it is removed and instantaneously recreated at a random location on the chain. Thus, the total number of entanglements stays constant under this condition.

4. *Regeneration On – CR On*: If the chain end passes through a slip-link, the slip-link is destroyed and recreated at a random position on the same chain. Simultaneously, another randomly chosen slip-link is removed and recreated at a random position along the chain. Therefore, the number of slip-links stays constant.

Note that the actual constraint release dynamics should lie somewhere between these extreme conditions; however, we now show that our results are almost independent of these assumptions at high Wi_R. Figures 3.17 – 3.19 show the effect of our Regeneration/CR algorithms on the transition strain, the number of kinks, and the entanglement density for a chain with $N_s = 32$ ($Z_0 = 8$), respectively. Similar responses are obtained for other chain lengths, which we do not show here. The maximum entanglement force of $F_{ss}^{max} = f_{CHC} = \zeta' \dot{\epsilon} L^2 / 8$ is used for all cases.

According to Figures 3.17 - 3.19, at high Rouse Weissenberg numbers, the responses become nearly identical for the different cases, showing near independence of the results from the constraint release or regeneration processes at high Wi_R. Figure 3.17 shows that at lower Wi_R, there are differences; for example, with "Regeneration-On" (i.e., a constant number of slip-springs

at all strains), the kinked state is attained faster, but results converge as Wi_R increases. The same convergence at high Wi_R is obtained for the number of kinks, Figure 3.18, except for Regeneration Off – CR On where the number of kinks is, perhaps not surprisingly, somewhat less than for the other three conditions. The entanglement density at the onset of the kinked state also shows the same convergence at high Wi_R; see Figure 3.19. Interestingly, ρ_{EK}^0 under Regeneration Off – CR On is close to that obtained under the other conditions at high Weissenberg numbers; one might expect that with the rate of loss of slip springs doubled due to CR, and no slip springs regenerated, the density of entangled slip springs would be much reduced relative to the other cases. The behavior observed is explained by considering that first of all, at high Wi_R, there are fewer kinks under Regeneration Off – CR On as shown in Figure 3.18, and since ρ_{EK}^0 is the fraction of kinks that have a slip- link, the reduction in kinks tends to offset the decrease in number of slip links. Also, for this case, the fewer slip-springs that do remain tend to accumulate at the kinks, thus keeping the percentage of kinks with a slip link relatively high despite the fewer slip springs present. Thus, the entanglement percentage is close to that of the other algorithms. At high Wi_R, since the chain quickly aligns and stretches in the flow direction, by the time the initial slip-springs start to leave the chain by passing off the chain ends, the kinked state has been achieved, and renewal of slip-springs does not change the conformation. The newly added slip-links, under conditions 3 and 4 above, will be quickly convected to chain ends or existing folded regions. As mentioned before, the accumulation of newly generated entanglements (i.e., slip springs) at already entangled kinks does not change the entanglement percentage. Although the correct renewal algorithm lies between our arbitrary assumptions for CR and Regeneration of slip-springs, we see that at high Wi_R, the results under all renewal assumptions converge to the same values. Note that this independency of the results on the process of Convective Constraint Release (CCR) is only

valid for strong extensional flows where the chain conformation quickly falls into the folded region. The same is not true for shear flows, for example, where the regeneration of slip-springs, or entanglements in general, affect chain conformation and tumbling becomes important.
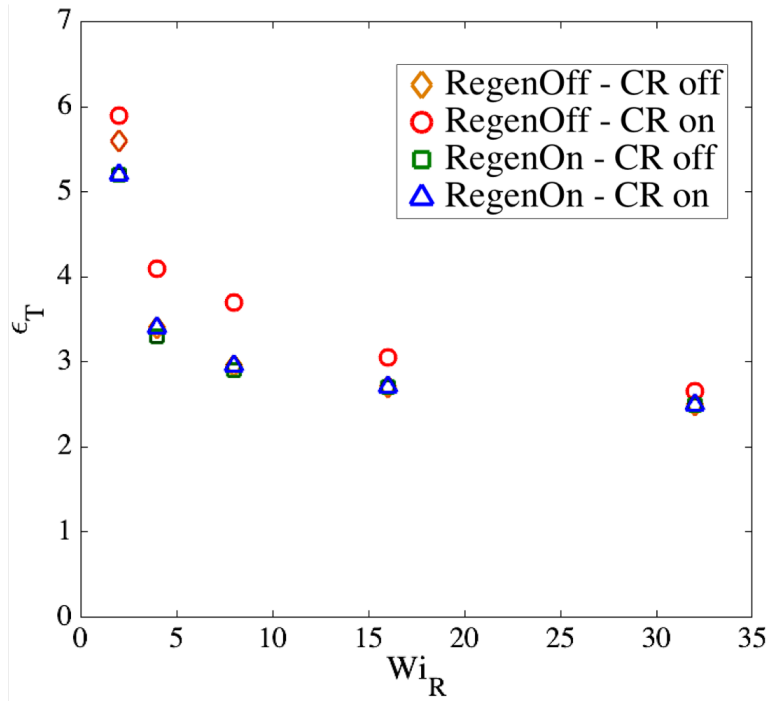
Figure 3.17. Transition strain (ϵ_T) as a function of Rouse Weissenberg number (Wi_R) for a chain with $N_s = 32$ springs under different renewal/CR algorithms. A constant value of F_{ss}^{max} is used for all four conditions.
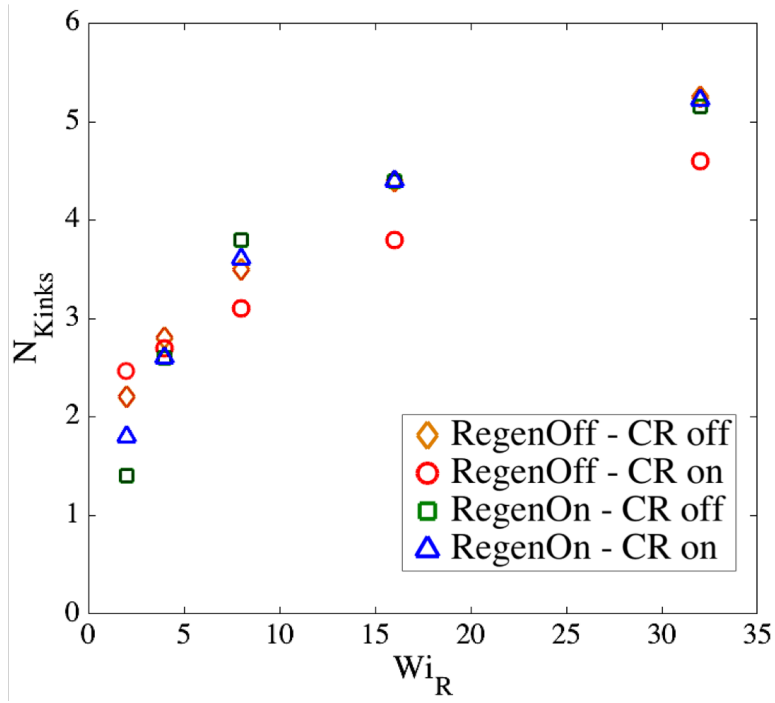
Figure 3.18. The same as Figure 3.17, except for the number of kinks (N_{Kinks}).
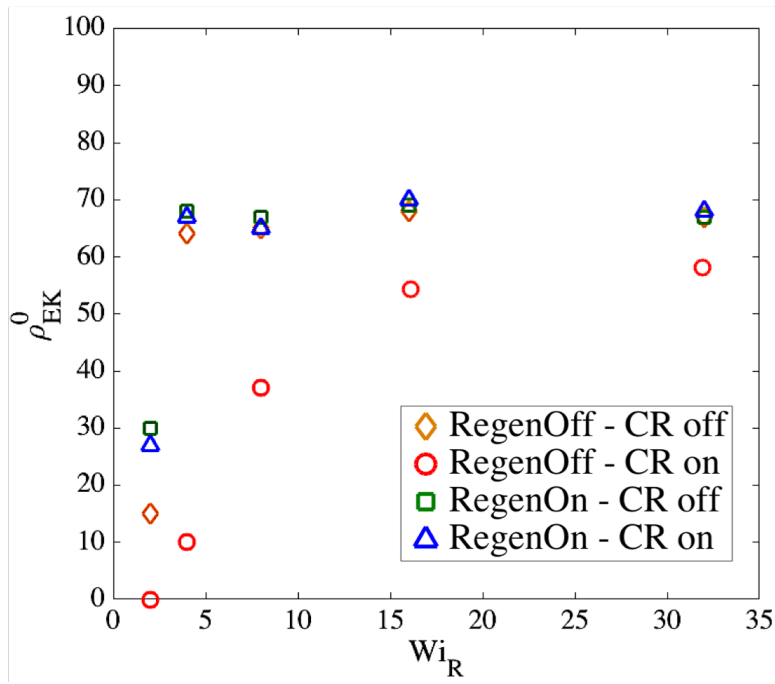
Figure 3.19. The same as Figure 3.17, except for the entanglement density (ρ_{EK}^0).

In the next section, we use the ϵ_T, N_{Kinks}, ρ_{EK}^0 and $\hat{L}_{\text{strand}}$ values obtained by the slip-spring simulations as initial conditions in our entangled kink dynamics algorithm (EKD) and compare the predictions of the kink dynamics model to experimental data.

3.4.3 Kink Dynamics Predictions for Entangled Polystyrene Solutions

Having used slip-spring simulations to obtain the details describing the conformational and entanglement state of polymer chains as they first enter the kinked state, we now perform EKD simulations using these realistic starting conditions. First, we determine the number of kinks for a specific molecular weight based on the linear correlation we found in previous section. Then, we use the exponential distribution to specify the strand lengths between the kinks. After generating the kinked conformation based on the average strand length and the number of kinks, we put the chains into a simulation box and mutually entangle 65% of the kinks. All results obtained with the EKD simulations are shifted to the Hencky strain of 3 which we showed is approximately the onset of the kinked state. To compare our predictions with experimental data, in Figures 2.1 – 2.3, ζ' is estimated using $\zeta' = 6\pi^2 kT\tau_R/N_k^2 b_k^3$ as approximated from Rouse theory [158] where b_k is the length of a Kuhn segment, k is the Boltzmann's constant and T is absolute temperature, and $\nu = cN_A\rho/M_w$ is the polymer number concentration, where c is the polymer mass fraction, N_A is Avogadro's number and ρ is polymer density. To find the number of kinks for the three samples, we use the slip-spring results and the linear scaling. Details of the input parameters for the kink dynamics simulations are given in Table 3.5.

Table 3.5. Input parameters of kink dynamics simulation for three polystyrene samples of Figures 2.1 – 2.3.

$M_w(M)$	$L(\text{nm})$	$v(\frac{1}{\text{nm}^3})$	$\zeta'(\text{Pa.s})$	N_{kinks}^0	ρ_{EK}^0
0.9	2183	2.3×10^{-4}	6220	25	0.8
1.76	4269	6.4×10^{-5}	3453	49	0.8
1.76	7957	2.1×10^{-5}	2150	92	0.8
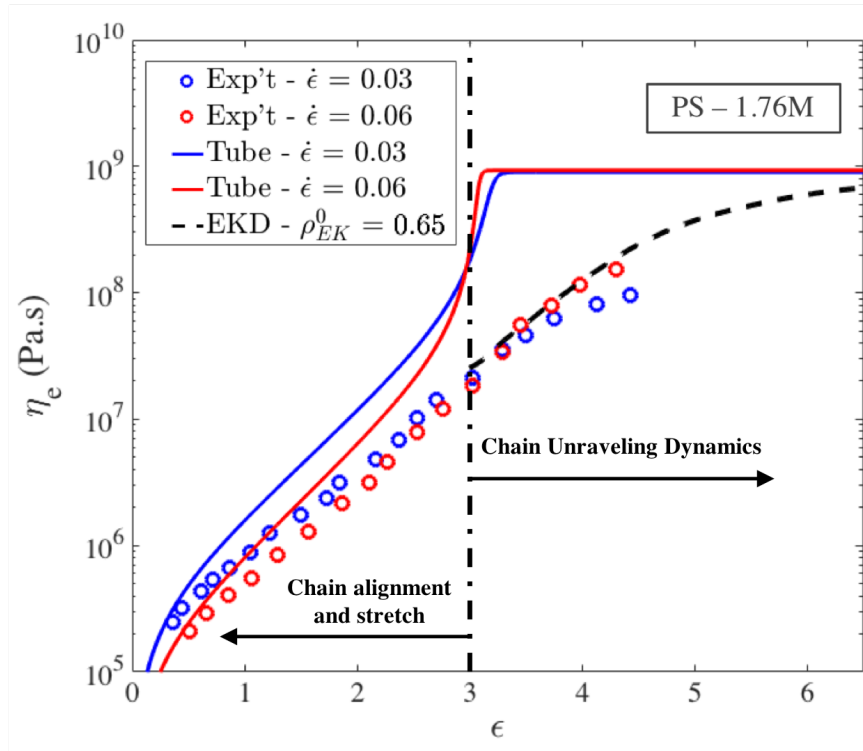
Figure 3.20. Comparison of experimental data [50,157] (o) of 18 wt.% polystyrene (PS) of molar mass 1.76M, with predictions of DEMG model in uniaxial extension and with predictions of entangled kink dynamics (EKD) model (dashed line) with 65% initial entanglement density, starting at a transition strain of $\epsilon_T = 3$.
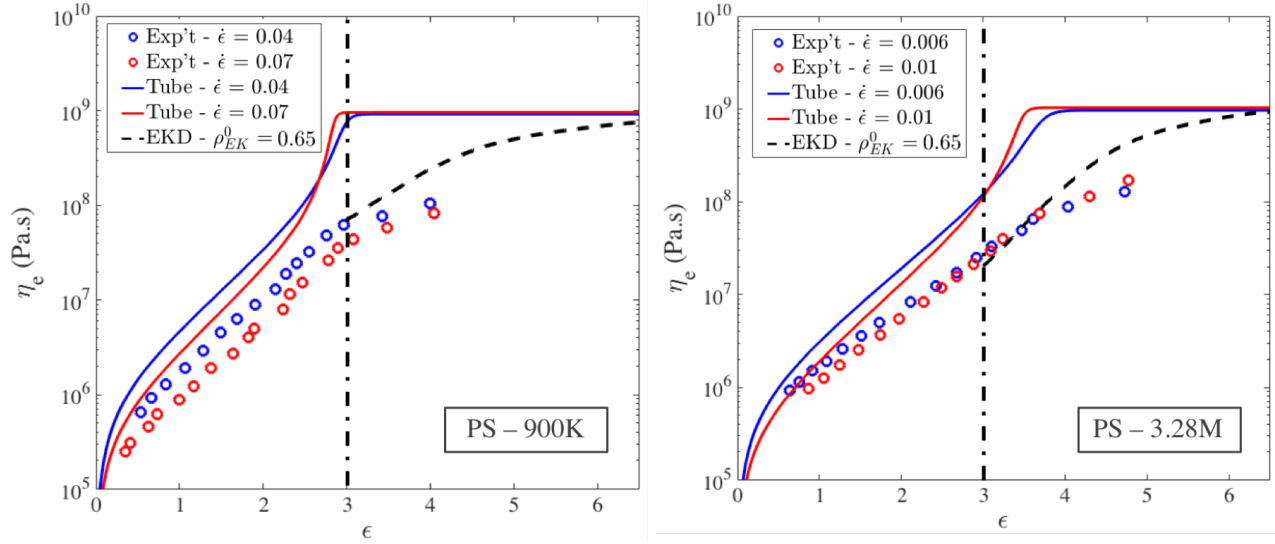
Figure 3.21. The same as Figure 17 for (left) 33 wt.% 0.9M PS and (right) 13 wt.% 3.28M PS. Again, Entangled Kink Dynamics simulations are shown by dashed lines.

Figure 3.20 and 3.21 show the predictions of the EKD model for the transient extensional viscosity of high molecular weight polystyrenes in strong extensional flows (black dashed lines). Kink dynamics results show that the final plateau stress is achieved at much higher strains when the chain dynamics is governed by unraveling rather than segmental stretch. This is much closer to experimental data, which shows, even at high strains, a gradual increase in η_e as a function of strain, in comparison with tube model (DEMG and MLD) predictions. Although experimental data points are not available at higher strains due to measurement limitations, predicted values of viscosity from the tube model are far from the experimental data both in value and trend.

Ianniruberto [50] showed that this discrepancy in the predictions of the tube model could be alleviated by reducing the friction coefficient as the chain orients. This brings down the final plateau stress value and for entangled solutions the amount of this decrease is determined by the value of a nematic interaction parameter (ε), that determines the coupling strength of nematic interactions between short molecules of the solvent and long polymer chains. Its value was found

82

by fitting the model to experimental data, leading to a value of $\varepsilon = 0.5$ for polystyrene solutions in 4K oligomeric styrene. While the idea of friction reduction is physically plausible and leads to improvements in the tube model's predictions, it mainly changes the final stress value the model achieves at high strains and it does not greatly change the strain ϵ_{ss}^{model} required to reach the plateau. The tube model used in the work of Ianniruberto [50] gives the same plateau stress as the DEMG and MLD models used here if the same polymer friction is used. But for strains below the plateau, the predictions of Ianniruberto's model agree somewhat more closely with experimental data than do the DEMG or MLD models, (although most of the seemingly improved agreement in Fig. 2b of reference 50 is due to the plotting of data on logarithmic time axis, rather than the linear axes of Figs. 3.20 and 3.21). We have here shown that the unraveling process influences the stress at high strains, causing the stress to approach steady state much more gradually than predicted by the tube model. Accounting for the chain unraveling results in smaller stresses at modest strains than in the tube model, without needing to incorporate a large nematic interaction term in entangled solutions. Note that without any data fitting or curve shifting the EKD algorithm provides better predictions at high strains than do conventional tube models. We nevertheless acknowledge that there is good evidence for friction reduction in highly aligned melts, and our findings here do not foreclose the possibility of such friction reduction in solutions as well, although we doubt the need for large reductions, especially when the polymer volume fraction is well below unity.

The reason the large failure of the tube model in extensional flows discussed here has not been much reported on the literature, is first, because polymers with N_K Kuhn steps are nearly fully extended at a strain of $\epsilon \approx \ln(\lambda_{max}) \approx ln\left(\sqrt{N_K}\right)$, where λ_{max} is the maximum extension ratio of the chain. For chains with less than $N_K \sim 400$ Kuhn steps, the chain is already fully extended at a strain high enough to create the folded state. Thus, polystyrene melts with molar

mass of < 400,000 Daltons will be fully stretched and the stress will reach a plateau value at modest strains, at which longer chains are still folded. Tube models can successfully predict the transient viscosity of such melts [153]. A second reason that large deviations from the tube model have not so often been reported is that extensional flows frequently do not extend beyond strains of $2 - 3$ Hencky units for high extension rates, sometimes due to filament breakage [41,173]. However, there are some data on well entangled polymer solutions for which $N_K \approx 4000$ and strains $\epsilon > 4$ are attained, such as those in Figures 3.20 and 3.21. The tube model predicts that the plateau stress for high strain rates is attained at a strain that is essentially independent of chain length, since the strain required to locally stretch the chain within the tube is given by $\ln(\lambda_{t,\max}) \approx \sqrt{N_{K,t}}$, where $\lambda_{t,\max}$ is the maximum stretch ratio of a tube segment. This value is set by the number of Kuhn segments $N_{K,t}$ in a tube segment and is independent of the molar mass of the whole polymer, although it does depend on concentration and entanglement density. Note in Figure 3.20 that our entangled kink dynamics simulation provides a much more realistic estimate of the strain required to attain steady-state stress for long chains, with $N_K > 1000$. Note also that, in contrast to the tube model, which predicts that the steady-state stress is attained at a strain that is independent of molecular length, but sensitive to entanglement density, our kink dynamics simulations predict the reverse: the strain required to reach steady state is dependent only on the molar mass of the chain and is independent of entanglement density. The strain required for unraveling a chain of given molecular weight in the melt is the same as in a dilute solution; in fact, the final unraveling process is essentially the same as for dilute solutions.

3.5   Conclusion of Chapters 2 and 3

A new multiple-chain simulation technique is developed that combines "kink dynamics," borrowed from dilute solution theory, with pair-wise entanglement between two chains. To use the entangled kink dynamics approach, input data are obtained from a modified slip-spring simulation technique. The slip-spring simulations gave the configurations and entanglement density of a linear polymer chain at the transition to the kinked state, before unraveling starts to dominate the behavior. To perform these slip-spring simulations under fast extensional flows, we imposed a maximum slip-spring force to prevent permanent trapping of slip links at nascent fold points along the chain, with force set by a simple analysis of the force at an entangled kink between two symmetrically hooked chains. We also carried out slip-spring simulations with the slip springs on one chain paired randomly with those on a second chain and allowed less-than-affine motion of the slip spring with high tension to be offset by super-affine motion of the partner slip spring so as to create affine motion on average. We found that this method of limiting the tension of the slip springs produced similar slip-spring tension distributions as the maximum force method, up to the formation of the kinked state. The results show that multiple methods of preventing overly high tensions on the slip springs produce similar results up to the formation of the kinked state. The effect of slip-spring renewal and constraint release on the number of kinks N_{kinks}, fraction of kinks that are entangled ρ_{EK}^0, and transition strain to the kinked state ϵ_T were found to converge at high Wi_{R} to similar values regardless of the constraint release and constraint renewal assumptions used in the slip-spring model. This provides a self-consistent picture of the late stage behavior of linear polymer chains in strong extensional flows. We find, using this theory, that the assumption of affine tube deformation in the Doi-Edwards theory breaks down for fast extensional flows of long chains once the tube segments are fully aligned and the chains are locally nearly fully stretched.

Beyond this point, continued affine deformation of a "test" chain would create tension at the center of this chain that is too high to be supported by the surrounding chains, which are entangled with the test chain at random points along the contours of the surrounding chains. Using a more realistic model in which the fold points, or "kinks" along the chain are supported only by tension supplied by a partner chain entangled at the kink, we find that the tension profile in the initially folded state is flat, rather than parabolic, and the stress can be more than an order of magnitude below that of the fully unraveled chain. Thus, tube model, which might be reasonably successful for strains up to that needed to form the folded state (i.e., Hencky strains of $2 - 3$), fails at high strains, unless the polymer molecules are short enough to be almost fully unraveled already by the time the 1D folded state is reached. A typical tube model predicts attainment of steady state at around $\epsilon \approx 3$ Hencky strain units, which is high enough to align the tube segments and nearly fully stretch the polymer locally, but nowhere near high enough to fully unravel the chain into a fully extended length. Our kink dynamics model, on the other hand, predicts that the final plateau value of the extensional viscosity is attained only at higher strains, at which the stretched segments of polymer chains have had time to fully unravel. The strain dependence of the stress growth resulting from this unfolding process agrees well with experimental data. Thus, we have provided an entirely different, and more realistic, picture of late-stage dynamics and stress of entangled polymers under fast extensional flow than is provided by the tube model. Future improvements in the tube model should address this limitation of the tube theory, guided by the work presented here.

Chapter 4 : Multiscale Modeling of Sub-Entanglement-Scale Chain Stretching and Strain Hardening in Deformed Polymeric Glasses

4.1   Abstract

Using both coarse-grained (CG) and fine-grained (FG) simulations we show that much of the strain hardening in polymeric glasses under uniaxial extension arises from highly-stretched sub-entangled strands that form as the polymer chains enter highly folded states. The coarse-grained simulations are performed using the hybrid Brownian Dynamics method (HBD) [*Zou, W. & Larson, R. G. Soft Matter 2016, 3, 3853-3865*], while the fine-grained simulations employ the Kremer-Grest bead-spring model. We find that the HBD model accurately predicts how the MD chain configurations evolve during deformation despite being a single-chain-in-mean-field model that does not account for entanglements. We show that a primary reason that the glassy strain hardening modulus G_R is so much larger than the melt plateau modulus G_N^0 is that chain segments shorter than the entanglement length become highly stretched at modest Hencky strain $\epsilon < {\sim}1$ owing to the high interchain friction in the glass. As deformation proceeds, chains begin to form kinks or folds (starting at a Hencky strain $\epsilon \sim 1.6$) analogous to those produced in extensional flows of dilute and entangled polymer solutions. Since stress is affected by glassy modes, and is not accurately predicted by the original version of HBD (in which the segmental relaxation time is determined by a one-mode fluidity model), we extend the HBD theory to multiple segmental relaxation modes, where segmental relaxation rates are obtained from small-molecule probe relaxation experiments by Ediger and coworkers [Bending, B. & Ediger, M. D. *J. Polym. Sci. B*

2016, *54*, 1957-1967]. This produces excellent agreement between the HBD model and experimental stress-strain curves through the yield point. **(Text and figures in this chapter are from the following manuscript, "Multiscale Modeling of Sub-Entanglement-Scale Chain Stretching and Strain Hardening in Deformed Polymeric Glasses" by Zou, W., Moghadam, S., Hoy, R.S., Larson, R.G.; Manuscript to be submitted soon to ACS macro letters journal**.)

4.2 Introduction

Glassy materials possess remarkable properties such as high stiffness and transparency, good corrosion resistance, low permeability, as well as ease of fabrication [78,79], making them ubiquitous in both traditional and emerging material applications [80–83]. The growing demand for low-cost, lightweight materials with sufficient mechanical strength has led to increasing use of polymeric glasses as substitutes for inorganic materials such as silicon and metals. However, polymeric glasses tend to fail in a catastrophic, brittle fashion through avalanche like plastic deformation, often manifested as crazing and necking. This often makes their ductility significantly lower than that of conventional metals, which can render them useless for many applications [106]. To ensure their mechanical stability for a variety of loading environments, several methods for strengthening polymeric glasses are available, for example, mechanical preconditioning [84,85], subglass-transition-temperature annealing [86], etc. However, the complicated interplay of chemistry [87,88], entanglement/crosslink density [89], severity of confinement [90], as well as thermomechanical history in determining ultimate mechanical properties of polymeric glasses make it extremely difficult to ensure the above stability-enhancing procedures are reliable [80,82,91]. Moreover, the still-rapid pace of development of new glasses

with remarkable performance, including vapor-deposited "ultra-stable" polymer glasses [83], plasticizer-mediated glasses [91], and rigid polymer-cast "superionic" films [92], show that we are still far from a complete understanding of how polymers' molecular structure affects the macroscopic mechanical properties of their bulk glassy state. For example, while it is well known that the restrictions imposed by the strength and directionality of covalent bonds along chain backbones (which distinguish polymeric from small-molecule glasses) play a critical role when a polymer glass is subjected to large strains [174–176], the details remain highly controversial [53,177]. Progress towards predicting the performance of polymeric glasses under large deformation therefore requires an explicit accounting both short-range segmental dynamics and long-range polymeric ones, as well as the interaction of the two.

Recently developed coarse-grained theoretical models [93,94,99–102] are beginning to yield important insights. Zou and Larson recently published one such "hybrid" model [103] in which a one-mode Maxwellian equation for local segmental relaxation with time constant (τ^s) was used to predict the local frictional drag that a "glassy solvent" exerts on an isolated-chain representing the larger-scale "polymeric" relaxation (with time constant $\tau^p = \alpha\tau^s$, where α is the polymer-to-segmental relaxation time ratio). With a simple fluidity model describing the nonlinear response of τ^s under applied deformation, the stress from the segmental mode was added to that produced by polymeric relaxation, whose dynamics were approximated by a bead-spring chain with bead drag coefficient proportional to τ^s. Although the interplay between segmental and polymeric stresses allows for this hybrid model to capture much of the experimental phenomenology of deformed polymeric glasses [103–105], the model ignores polymer entanglements. It also ignores energetic terms arising from pair, covalent-bond, or angular interactions that are known to be important in determining the overall mechanical properties of

89

polymeric glasses [92,106,108–111,117]. One might therefore expect this model to break down in the post-yield regime where effects of the above energetic terms become increasingly important [112]. On the other hand, there is considerable evidence that single-chains in-mean-field models can in fact capture much of the physics of large-strain deformation, including strain hardening, at least up to the beginning of the "dramatic" supra-Gaussian regime of the stress-strain curve [113–115]. Moreover, as suggested by Zou and Larson, strain-hardening below the dramatic regime results primarily from highly-stretched and folded chain conformations ("kinks") rather than from rheological entanglements. Significantly, the onset of strain hardening at Hencky strains of order unity is correctly predicted by this model, in agreement with experimental data, and with a hardening modulus greatly in excess of the polymer entanglement modulus, also consistent with experiments. These findings suggest strongly that entanglements are not the key feature of strain hardening, which is instead caused by the large stretch of sub-entangled strands of polymer at deformation rates much greater than the rate at which those strands can relax their configurations. Unfortunately, it is not yet possible to test this suggestion experimentally, despite the applications of many novel experimental methods to deformed polymeric glasses [80,86,116]. MD simulations, however, offer an alternative avenue for exploring and testing new theories [92,106,119–121,107–110,113–115,118], and can provide information on polymer conformations and entanglements. Thus, MD simulations allow testing of the assumptions and findings of the coarse-grained hybrid-BD (HBD) model, in particular, its ability to predict strain hardening despite neglecting entanglements. Thus, in what follows we will make quantitative comparisons between HBD and MD simulations. Moreover, a simple modification of segmental dynamics is implemented in the HBD model to improve the glassy dynamics before the yielding point.

4.3 Simulation Methods

4.3.1 Molecular Dynamics (MD) Simulations

Our standard MD simulations use a flexible Kremer-Grest bead-spring glass [55,178], consisting of $N_{ch} = 500$ chains of length $N = 600$ monomer beads. Since the Kuhn length of this model is $\sim 5/3$ beads, these chains would have $N_K = 360$ Kuhn segments in total with entanglement length $N_e \sim 51$ Kuhn segments [89], so that a chain has an average of $7 \sim 8$ entanglements. All monomers have mass m and interact via the truncated and shifted LJ potential:

$$U_{LJ}(r) = 4u_0\left[\left(\frac{a}{r}\right)^{12} - \left(\frac{a}{r}\right)^{6} - \left(\frac{a}{r_c}\right)^{12} + \left(\frac{a}{r_c}\right)^{6}\right] \tag{4.1}$$

where u_0 is the intermonomer binding energy, a is the monomer diameter and $r_c = 2^{7/6}a$ is the cutoff radius. Covalent bonds are modeled using the FENE potential defined as:

$$U_{FENE}(r) = -\left(\frac{kR_0^2}{2}\right) \times ln\left[1 - \left(\frac{r}{R_0}\right)^2\right] \tag{4.2}$$

with the standard [55] parameter choices $R_0 = 1.5a$ and $k = 30u_0/a^2$. The Lennard-Jones time unit is $\tau = (ma^2/u_0)^{1/2}$, and the MD time step we employ is $\Delta t = 0.005\tau$. As in Nguyen et al. [119], the system is first thoroughly equilibrated well above T_g (at $T = 0.47u_0/k_B \sim 1.3T_g$) [179], then slowly cooled to $T = 0.3u_0/k_B \sim 0.8T_g$. Since the cooling rate employed for $T <$ $T_g + 0.1u_0/k_B$ is $10^{-6}u_0/k_B\tau$, the aging time (t_w) of the glass, approximated as the time between attainment of the glass transition at $T_g = 0.37u_0/k_B$ and the final temperature $T = 0.3u_0/k_B$ is $0.07\tau/10^{-6} = 7 \times 10^4\tau$. After cooling the system, we uniaxially stretch the box containing the chains at a rate of $\dot\epsilon = 2.5 \times 10^{-5}/\tau$ while symmetrically reducing its transverse dimensions to maintain constant volume. Thus, the strain rate times the aging time is $\dot\epsilon t_w = 1.75,$

which is close to unity. Throughout all these simulations, periodic boundaries are applied along all three directions; the monomer number density of the glass is $\rho = 1.0578/a^3$. All MD simulations are performed using LAMMPS [180].

4.3.2 Hybrid Brownian Dynamics (HBD) Simulations

On the other hand, for HBD simulations, the polymeric glass is represented by phantom bead-spring chains with extensible FENE springs, suspended in an implicit "glassy" solvent, with each bead acting as a center of force. In the HBD model, the stochastic equation for bead motion and the polymer chain's contribution to stress is given by:

$$\zeta_b \dot{r}_i = \zeta_b (\nabla v)^T . r_i + F_i^{sp,t} + F_i^R \tag{4.3}$$

$$\Sigma^p = v \langle \sum_j^{N_{HBD}} R_j F_j^{sp} \rangle, R_j = r_j - r_{j-1} \tag{4.4}$$

$$F_j^{sp} = \frac{H_{FENE} . R_j}{1 - (|R_j|/R_0)^2}, \quad H_{FENE} = \frac{3k_B T}{N_{K,sp} b_K^2}, \quad R_0 = N_{K,sp} b_k, \quad N_{K,sp} = N_K/N_{HBD} \tag{4.5}$$

Where $F_i^{sp,t}$ is the total spring force (which is the sum of two spring forces for interior beads and only one for end beads) exerted on bead i, v is the number of polymer molecules per unit volume in the system, R_j is the connector vector of spring j between two neighboring beads j and $j-1$, N_{HBD} is the total number of springs in a bead-spring chain in the HBD model, and F_j^{sp} is the spring force on spring j calculated by the FENE model [162], F^R is the Brownian force defined in chapter 3 (Equation (3.6)). R_0, $N_{K,sp}$, N_K and b_k are the maximum extensibility of a spring in the bead-spring polymer chain, number of Kuhn steps per spring, total number of Kuhn steps and Kuhn step length, respectively. The segmental, or glassy solvent, is represented by a phenomenological

fluidity equation. Evolution of segmental configuration tensor, relaxation time and glassy solvent's contribution to stress is given by:

$$\dot{\sigma}^s + v.\nabla\sigma^s = \sigma^s.\nabla v + (\nabla v)^T.\sigma^s - (\sigma^s - I)/\tau^s \qquad (4.6)$$

$$\dot{\tau}^s = 1 - \lambda(\tau^s - \tau_0^s) \qquad (4.7)$$

$$= \mu\sqrt{2tr(D:D)}, \quad D = [\nabla v + (\nabla v)^T]/2 \qquad (4.8)$$

$$\Sigma^s = G^s(\sigma^s - I), \tau^s|_{t=0} = t_w \qquad (4.9)$$

Here, τ_0^s is the fully rejuvenated relaxation time, which is fixed at the value of $6s$, which is far smaller than τ^s and so its exact value is not very important [104]. D is the deformation rate tensor, and ∇v is the deformation gradient. The rejuvenation parameter μ determines how much strain (i.e., roughly a strain of $1/\mu$) is required for the glassy mode to "rejuvenate" and become liquid-like under a flow field. (We will show below that this parameter has a significant effect on the formation of "kinks" or folds in the chain at high strain rate.) σ^s and G^s represent glassy configuration tensor and plateau modulus. The total stress is given by the sum of polymeric and "segmental" contributions, Σ^p and Σ^s, where superscripts "p" and "s" represent "polymeric" or "segmental" mode, respectively ($\Sigma^{tot} = \Sigma^p + \Sigma^s$). The segmental component satisfies an upper convected Maxwell model, with relaxation time τ^s and modulus G^s. The polymeric stress Σ^p is obtained from the BD simulations of a bead-spring chain and assigned a modulus G^p. The bead drag coefficient used in the BD simulations of the polymer is made proportional to the instantaneous value of the segmental relaxation time τ^s whose evolution is described by Equation 4.7. Since the polymer chain is a Rouse chain, its longest relaxation time τ^p will be roughly equal to the square of the number of Kuhn steps in the chain N_K^2, times the local relaxation time of a single Kuhn segment, which can be taken to be approximately τ^s. The ratio $\alpha \equiv \tau^p/\tau^s \approx N_K^2$ is

therefore proportional to the square of the chain length. For chains of 360 Kuhn lengths used in the MD simulations, $\alpha \approx 10^5$, close to the value we use here, given in Table 4.1. A detailed description of the model can be found in the previous work by Zou and Larson [103].

4.4   Results and discussion

4.4.1   Comparing MD and HBD Results on Chain Conformation

To directly compare MD results with our HBD results where a modest number of springs ($N_{HBD} = 10, 20,$ or 30) is used, the MD chain conformations need to be coarse-grained. We do this by mapping each MD chain subsection of length N_{MD}/N_{HBD} beads onto a single coarse-grained "MDCG" vector connecting its endpoints. For the "base" case $N_{HBD} = 20$ coarse-grained strands, we map 30 MD beads into a single "MDCG" vector, and both MDCG strands and HBD springs contain the same number ($N_{MD}/N_{HBD} = 18$) of Kuhn segments. We use N_{MDCG} and N_{HBD} as the number of springs in MDCG and HBD models, respectively. With an initial ensemble of chain configurations taken from the set of MDCG chains from the starting state of an MD simulation, we run an HBD simulation under fast extension so that large-scale chain relaxation is negligible, and the responses of our coarse-grained (HBD) and fine-grained (MD) models are only weakly dependent on the deformation rate. The "age" of the glassy mode of the HBD model is the "waiting time" t_w, which is set to $26.4\,h = 9.5 \times 104\,s$ (see Table 4.1). A high extension rate of $\dot{\epsilon} = 10^{-5}\,s^{-1}$ is applied for HBD simulations giving $\dot{\epsilon} t_w = 0.95$, which is around unity, close to the corresponding value for the MD simulations discussed above. Since the relaxation time of the polymer chain τ^p is many orders of magnitude longer than the relaxation time of the glassy mode, which is close to t_w, the value $\dot{\epsilon} t_w$ of around unity implies that the Weissenberg number $\dot{\epsilon} \tau^p$ is

very much higher than unity and nearly the same in both MD and HBD simulations. The chain conformations at two Hencky strains $\epsilon = 1.6$ and 2.5 from both MD and HBD simulations under uniaxial extension are shown in Figure 4.1, with the values of the HBD parameters given in Table 4.1.

Table 4.1. Standard values of model parameters for HBD simulations in Figs. 4.1-4.4.

$\dot{\epsilon}\ (s^{-1})$	α	N_{HBD}	μ	N_K	$t_w\ (h)$	G^p (MPa)	G^s (MPa)
10^{-5}	8.0×10^4	20	143	360	26.4	0.117	500
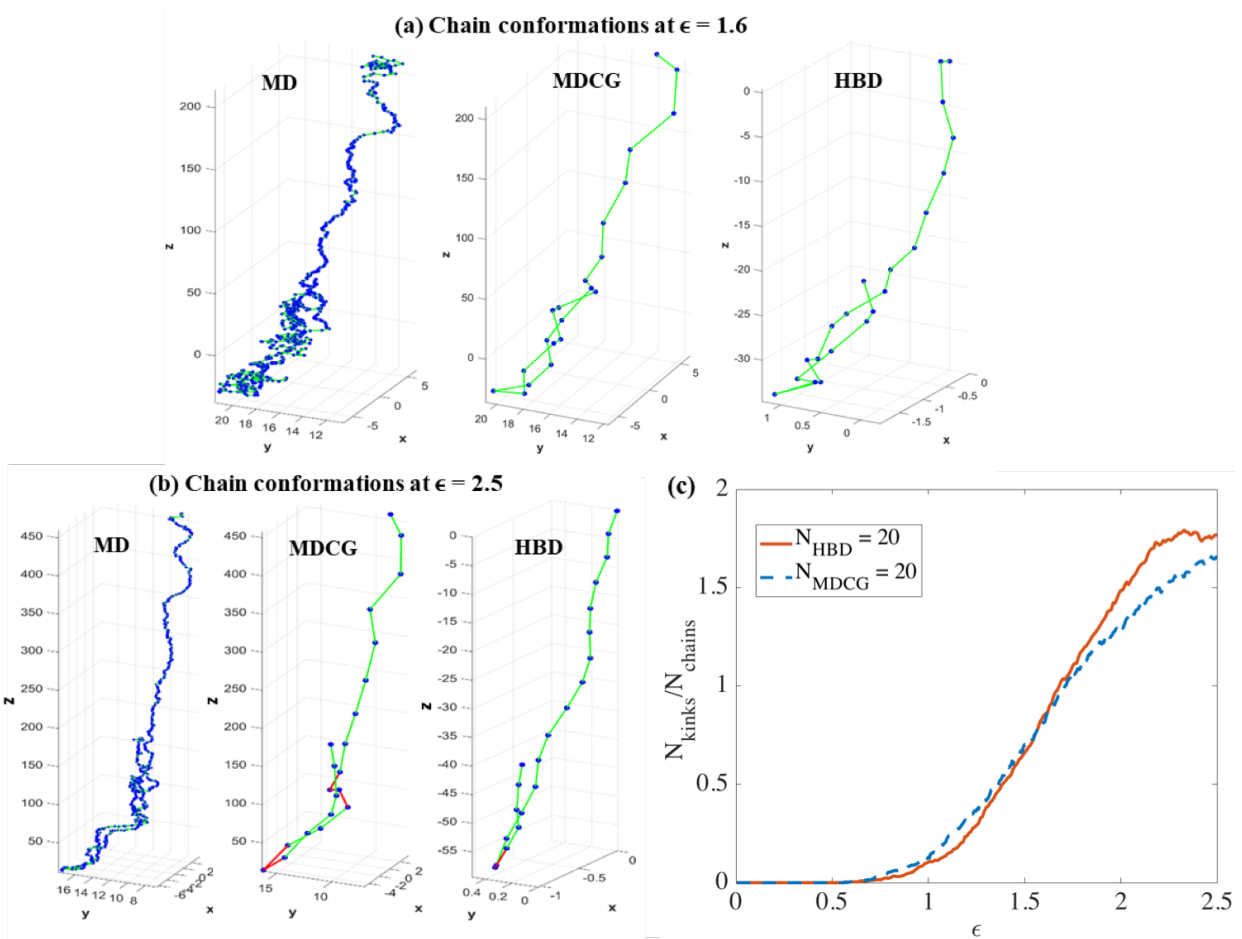
Figure 4.1. Chain conformations predicted from MD simulations with/without coarse-graining (i.e., MD and MDCG) and from HBD simulations with $N_{HBD} = 20$ for an example chain at (a) $\epsilon = 1.6$; (b) $\epsilon = 2.5$. Beads, colored as blue, are connected via green springs in MD, MDCG and HBD figures. In the MDCG and HBD panels, pairs of adjacent springs that highly stretched and oriented with a folded shape are colored red, instead of green to show the appearance of kinks. (c) The numbers of "kinks" (defined later) per chain as functions of strain from MD simulations (dotted lines) under a constant extension rate of $\dot{\epsilon} = 2.5 \times 10^{-5}$ (in LJ units) and from HBD simulations (dashed lines) under constant extension rate of $\dot{\epsilon} = 10^{-5}\ s^{-1}$. As discussed in the text, these conditions give almost the same values of the product $\dot{\epsilon} t_w \sim 1$ in both MD and HBD simulations.

4.4.2 Effect of Coarse-Graining (CG) on Parameters in HBD Model

Here we discuss how the HBD parameters shown in Table 4.1 are affected by the level of coarse graining, i.e., the value of $N_{K,sp}$, which is the number of Kuhn steps represented by a single spring in the HBD simulations. We use the Rouse model [162,181] for the longest relaxation time of the polymer, that is:

$$\tau^p = \zeta_b \frac{(N_{sp} + 1)N_K b_K^2}{6\pi^2 k_B T} = \zeta_b \frac{(N_{sp} + 1)N_{sp}N_{K,sp}b_K^2}{6\pi^2 k_B T} \equiv \alpha \tau^s \qquad (4.10)$$

where ζ_b is the drag coefficient per bead, $N_{sp} + 1$ is the number of beads per chain in the HBD simulations (N_{sp} is the number of springs), and b_K is the Kuhn length. The total number of Kuhn steps in the chain is $N_K = N_{sp}N_{K,sp}$ where $N_{K,sp}$ is the number of Kuhn steps per spring. τ^p and τ^s are the polymeric and the segmental relaxation times, respectively, and α is defined as the ratio τ^p/τ^s. Equation (4.10) can be re-arranged to:

$$\alpha = \frac{\zeta_b}{\tau^s} \frac{(N_{sp} + 1)N_{sp}N_{K,sp}b_K^2}{6\pi^2 k_B T} \qquad (4.11)$$

Since the segmental relaxation time τ^s should be roughly independent of polymer chain length at a given temperature, and represents local relaxation at a length scale of order b_K, and since ζ_b is proportional to $N_{K,sp}$, so that $\tau^s \sim \zeta_b b_K^2/N_{K,sp}k_B T$, we can estimate the value of α to be:

$$\alpha \propto (N_{sp} + 1)N_{sp}N_{K,sp}^2 \cong N_K^2 \qquad (4.12)$$

Thus, for a fixed polymer length, the value of α (taken in our simulations to be 8.0×10^4), remains constant regardless of the CG level. Note that for the chain simulated in here, $N_K = 360$, so that $N_K^2 = 1.3 \times 10^5$, close to the value of α used here. The values of other HBD parameters, namely, the total number of Kuhn steps N_K, the initial age of the glass or the so-called "waiting time" t_w,

the glassy modulus G^s, and the deformation rate $\dot{\epsilon}$, reflect the chain length, the thermomechanical history of the glass, or other experimental conditions. Since both HBD and MD simulations start from the same initial chain conformations, the values of these parameters are unaffected by the coarse-graining level. This leaves two parameters, the polymeric modulus G^p and the fluidity parameter μ to be set. In the formula for the polymeric stress used in Eq. (4a) of Zou and Larson [103], G^p is a "spring modulus":

$$G^p \equiv \frac{3\rho RT}{M_S} \sim N_{K,sp}^{-1} \tag{4.13}$$

where ρ is the density of the glass, and M_s is the molecular weight of a single spring whose value is inversely proportional to the number of Kuhn steps per spring and hence to the CG level. (Note that in [103], Eq. (4b) gives the formula $G^p = \nu k_B T$, ν where had been defined as the number of molecules per unit volume. However, ν must instead be taken to be the number of springs per unit volume, because the expression for stress in Eq. (4a) in [103] contains a sum over all springs in the denominator. Note also that the denominator in this expression in Eq. (4a) must contain a dot product of end-to-end vectors rather than an outer product so that the denominator is a scalar.) Thus, the value of G^p used here depends on the level of coarse graining since it is proportional to the stress contributed by a single spring.

Thus, for chain conformations under asymptotically high deformation rate, with the identical initial glass state, i.e., the values of t_w, G^s, N_K, and α remain constant as mentioned above, the only parameter that can be readjusted to match with the results of MD simulation at different CG levels is μ. The resulting excellent agreement in the chain conformations as well as the predicted number of kinks between HBD and MD simulations by adjusting μ for different levels of CG is shown in Fig. 4.2.
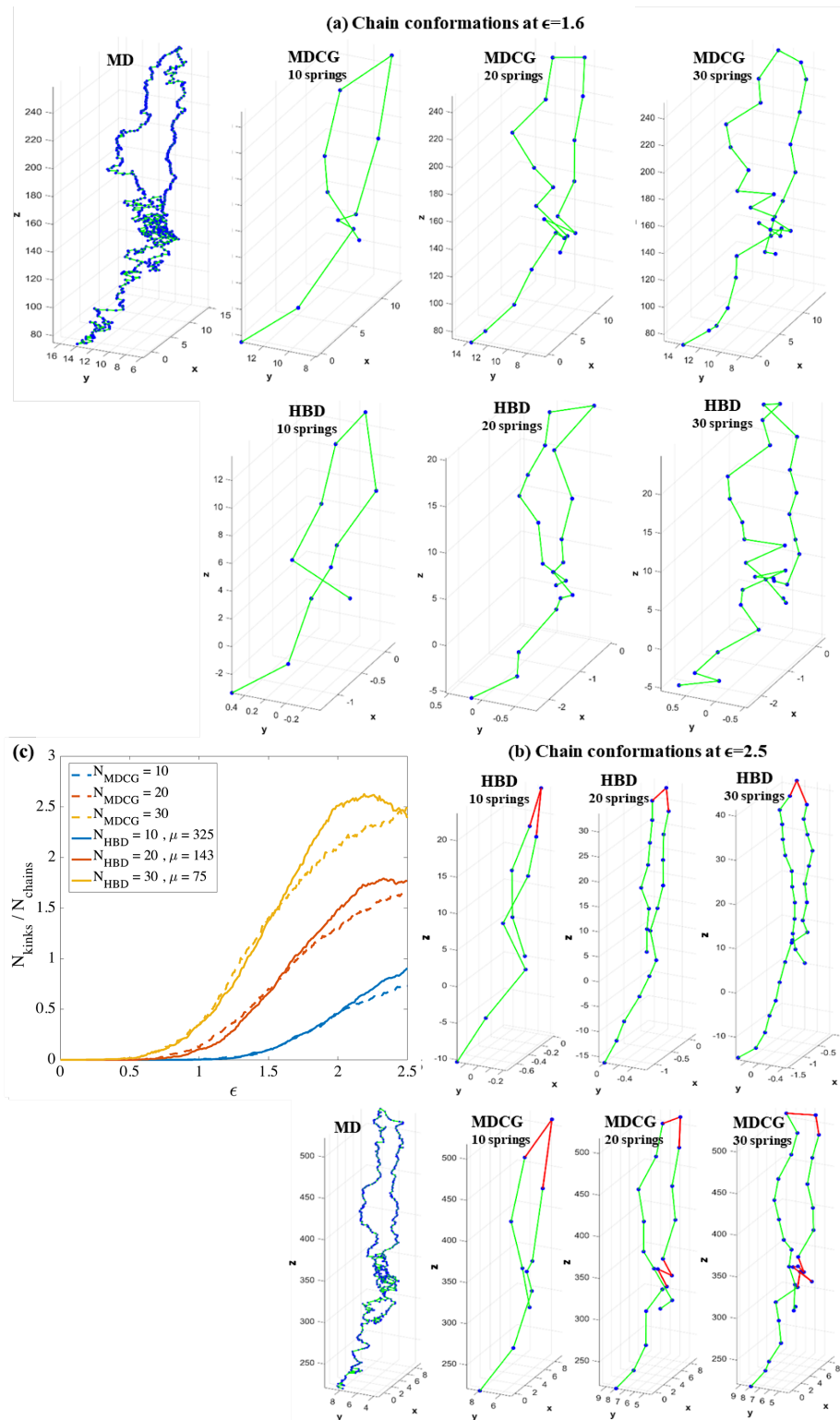
Figure 4.2. The same as Fig. 4.1 except different levels of coarse-graining are used for HBD simulations with $N_{HBD} = 10, 20$, and 30 springs at the corresponding values of $\mu = 325, 143$, and 75, respectively. Note that the example chain taken here from the ensemble of MD chains is different chain than the example taken in the main text, to further prove the excellent agreement between the strain-dependent conformations of HBD and MD chains.

4.4.3 Non-affine Stretching, Highly Stretched Segments and Kinks

Figure 4.1 makes evident that both MD and HBD simulations predict similar strain-dependent chain conformations, given that the initial chain conformation of the MD simulation was mapped onto the initial HBD coarse-grained configuration. We quantify the ensemble-averaged configurations and their similarity between MD and HBD simulations in Figure 4.3. Figure 4.3(a) shows the mean-squared end-to-end distance of a strand containing n Kuhn segments under an affine deformation follows $\langle R_n^2 \rangle_{\text{aff}}/\langle R_n^2 \rangle_{\text{eq}} = (e^{2\epsilon} + 2e^{-\epsilon})/3$ at a strain ϵ of uniaxial extension, where $\langle R_n^2 \rangle_{\text{eq}}$ is the mean-squared end-to-end distance at equilibrium. However, the near-inextensibility of covalent bonds forces chains to deform sub-affinely on short scales, and the length scale above which chains' deformation is essentially affine increases as deformation proceeds [182]. A continuous crossover from sub-affine to affine deformation is shown by both HBD and MD results in Fig. 4.3(a) with the crossover strand length n^* increasing with strain [118]. For the mean segmental stretch $S(n) = (\langle R_n^2 \rangle^{0.5}/nb_k)$, Figure 4.3(b) shows that even at small strain ($\epsilon \sim 0.5$) when segments of length $n > N_e$ ($= 51$ Kuhn steps) remain close to their initial unstretched length, shorter chain segments (i.e., $n = N_e/3$) can still be highly stretched. As the strain reaches unity and beyond, $S(n)$ at the sub-entanglement scale increases dramatically. Figure 4.3(c) quantifies the fraction of "highly stretched chain segments" $F_{hs}(n)$ that have $S(n) > S_{\min}$ ($= 0.7$). It is clear that F_{hs} becomes large around the onset of strain hardening (at $\epsilon \sim 1.0$,), and well before fully-formed kinks/well-folded chains appear (at $\epsilon \sim 1.6$, see Fig. 4.1(c)). We will now argue that it is these highly stretched chain segments (which appear as precursors to kinks) that lead to the onset of strong strain hardening. While the HBD model in Figure 4.3 uses $N_{HBD} = 20$ coarse-grained springs corresponding to 30 MD beads/strands, we will show that the similarity

between the MD and HBD chain configurations is insensitive to values of N_{HBD} between 10 and 30.
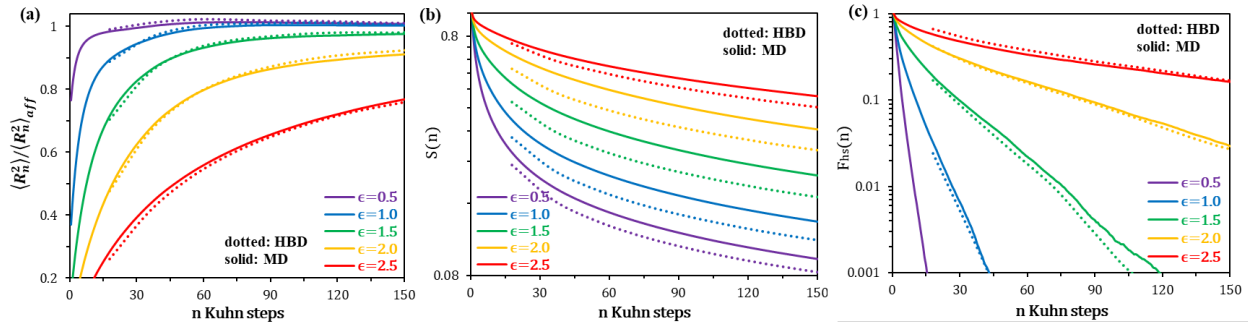
Figure 4.3. Structural response of fine-grained Kremer-Grest polymer model (solid lines) vs. the coarse-grained HBD model (dotted lines). (a) The ratio of the mean-squared distance $\langle R_n^2 \rangle$ between monomers separated by n Kuhn steps to its affine value $\langle R_n^2 \rangle_{aff}$ for various n and ϵ; values below unity indicate sub-affine deformation; (b) the mean segmental stretch $S(n)$ relative to full extension; (c) the fraction of "highly stretched segments" $F_{hs}(n)$ as defined in the text with $S_{min} = 0.7$. Note that in MD simulations, the entanglement spacing N_e is 51 Kuhn steps [89]. In panel (c) at $\epsilon = 0.5$, due to the relatively high level of coarse-graining, HBD only predicts a single non-zero point of $F_{hs} = 4.0 \times 10^{-4}$ for $n = 18$ Kuhn, which is located outside the range of the plot. However, this value is still consistent with that from MD, i.e., $F_{hs} = 3.4 \times 10^{-4}$ at $n = 18$ Kuhn steps.

We note in Figure 4.1 the appearance of "kinks" or folds, i.e., highly stretched and oriented pairs of adjacent springs with a folded shape as denoted by red springs in Fig. 4.1(b) at large deformations, whose formation can, however, be traced locally back to a lower strain level at around 1.6 Hencky strain units as indicated by Fig. 4.1(a). To quantify the chain conformation and local formation of kinks, the following procedure is taken to find "kinks" in MD simulations:

1. First, we examine all beads (600 beads) in a given chain and check whether they can be considered as "potential" kink points. To qualify as a "potential" kink point, the z-coordinate of the bead must satisfy $(z_i - z_{i-1})(z_i - z_{i+1}) > 0$, where i is the bead index which varies from 1 to 600.

2. After finding a potential kink-point bead, say bead i, we find the positions of bead $i + N_{conn}$ and bead $i - N_{conn}$, respectively, where N_{conn} is the number of beads we choose to be included in a strand bounding each side of the potential kink point. Using the locations

of beads $i + N_{conn}$ and $i - N_{conn}$ and that of the potential kink bead i, we create the connecting vectors of the kink, as illustrated in 4.4(a).

3. We compute the relative stretch of each of these bounding strands and the angle each makes with the z-direction.

4. To consider bead i as a kink, we require that the fractional stretch of both connecting vectors exceed a value λ_c and that both connecting vectors make an angle smaller than θ_c with the z-direction.

We show the sensitivity of the number of kinks in the MD results on the values of N_{conn}, θ_c and λ_c in following sections. Using $N_{conn} = 20$, $\lambda_c = 0.5$ and $\theta_c = 20^o$ gives the results in Figure 4.4(b). Note that this criterion for a kink differs from that used in Moghadam et al. [46,165] which applied at a strain high enough that the chain was in a "kinked state," where most strands were aligned near the flow direction and highly stretched. In this work, although the kinks form locally along the chain, the chain has not reached the folded or kinked state, as defined by Moghadam et al. [46,165]

To compare consistently results from the MD simulations with those of the HBD model, since the HBD model is coarse-grained, we first coarse-grain the MD chains into MDCG chains with the same number of MDCG vectors as there are springs in the HBD chains. After doing so, we use the same local criteria to identify kinks in MDCG and HBD models. The main difference is that in the MDCG and HBD models, we do not use the local process involving every bead of the fine-grained MD chain, but instead use the MDCG coarse-grained vectors that are at the same level of resolution as the HBD chains. So after finding beads at which $(z_j - z_{j-1})(z_j - z_{j+1}) > 0$

is satisfied, j being the index of beads in MDCG or HBD, we check if the connecting vectors satisfy the λ_c and θ_c conditions.
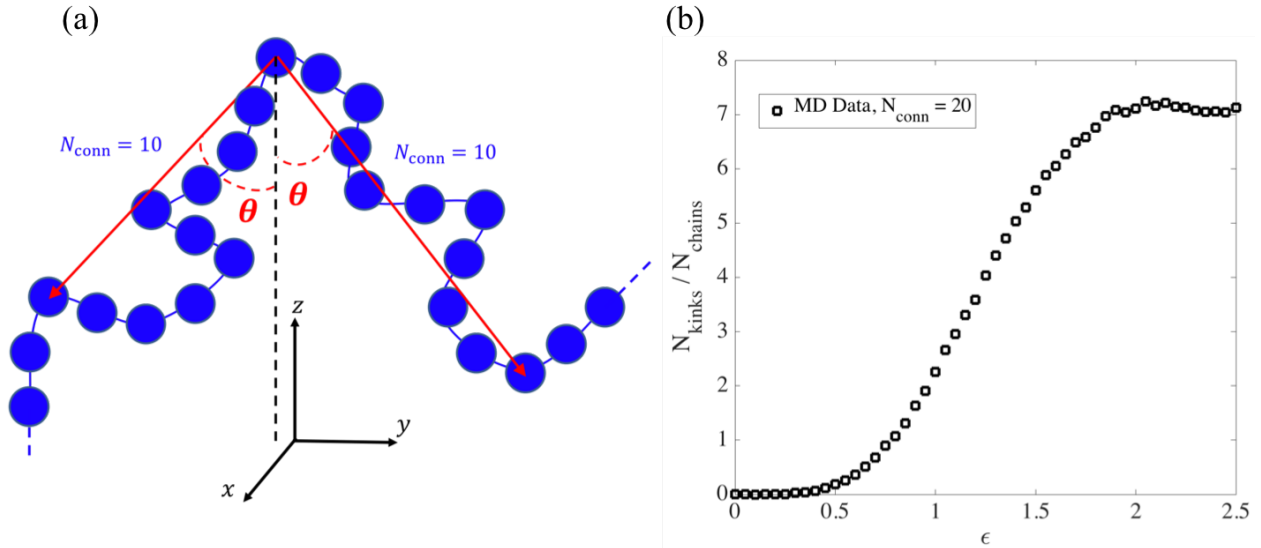
Figure 4.4. (a) Definition of connecting vectors used to identify local kinks in MD chain conformations, as described in the text. For illustration, we here use $N_{conn} = 10$ as an example. (b) Number of kinks per chain in MD chains, with $N_{conn} = 20$, $\theta_c = 20^o$ and $\lambda_c = 0.5$.

The MD results in Figure 4.4(b) show that the kinks emerge at the onset of strain hardening at Hencky strain of around 1, consistent with the the HBD model. Between Hencky strains of 2 and 2.5, the number of kinks per chain stays almost constant, suggesting an approach towards the kinked state, where now the strands between the folded points become highly stretched until finally the unraveling dynamics become dominant [46,165]. We plot in Figure 4.5(a)-(c) the average number of kinks as a function of the imposed strain for MDCG and HBD conformations for three different values of N_{HBD} and three different values of the rejuvenation parameter μ. We note that, unlike the properties plotted in Figure 4.3, the number of kinks is sensitive to both N_{HBD} and μ. However, for each N_{HBD} there is a value of μ that gives a match between the number of kinks predicted by the HBD model and the MD simulations, where the MD configurations are mapped into the same number of "MDCG" vectors as the number of springs in the HBD model. The best

match with the MD results is obtained when the product $\mu N_{HBD} = 2860$. Since μ controls the

rate of rejuvenation, the results suggest an interesting coupling between the rate of rejuvenation

used in the model for the segmental glassy mode and the degree of coarse-graining used for the

polymeric mode. A high value of μ means faster mechanical rejuvenation, leading to a faster

relaxation of local segmental modes. A sensitivity of kink formation to this value is explained by

its effect on local motion and the locking of two neighboring segments into a kink that is not easily

unfolded. The value of μ also strongly controls the time dependence of the segmental relaxation

during start-up or creep deformations, as explored in the previous work [103].
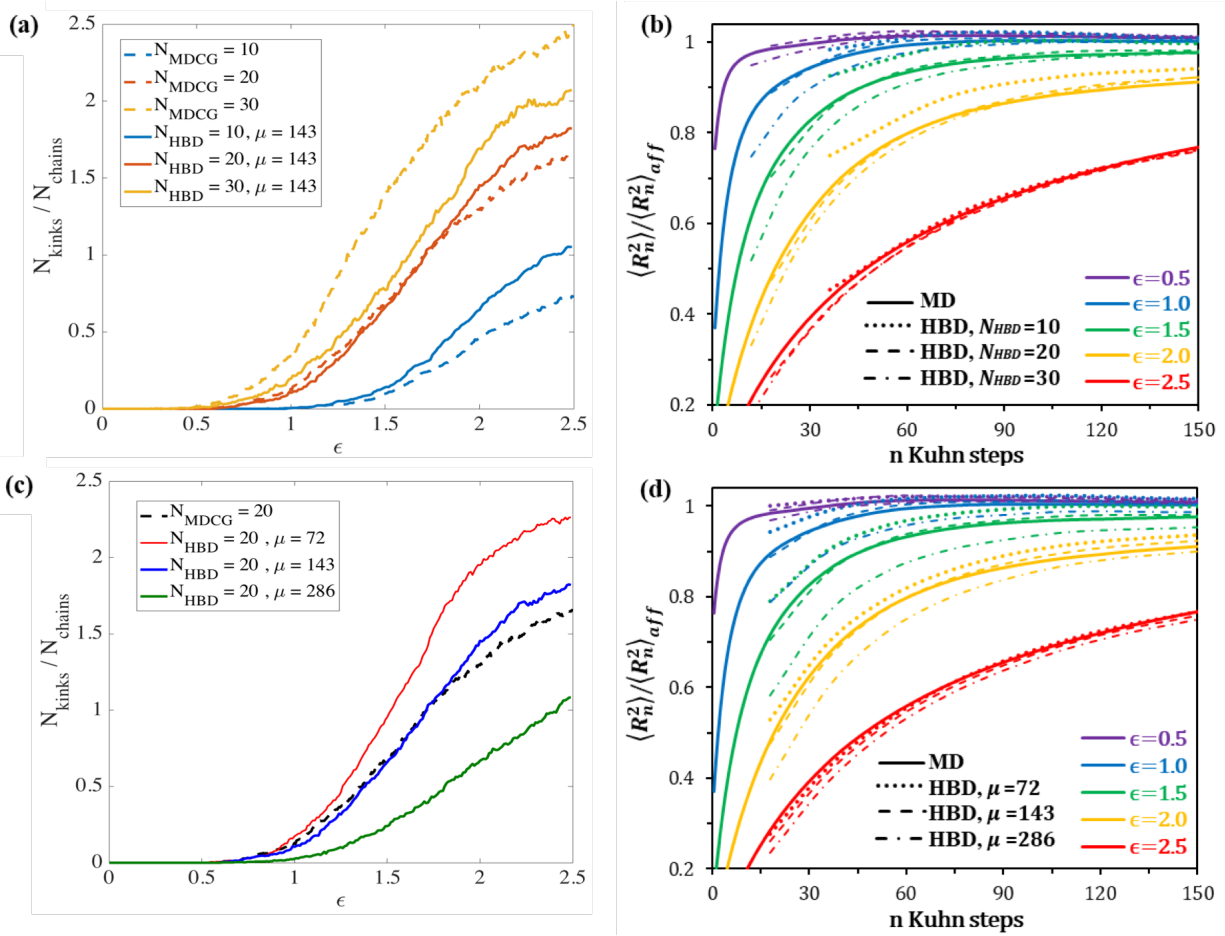
Figure 4.5. Sensitivity of the average number of kinks and the degree of deformation non-affinity for HBD model to the level of coarse-graining N_{HBD} (a)-(b) and detailed rejuvenation parameter μ (c)-(d) as a function of the imposed strain. Value of α is equal to 8×10^4 for all HBD results in this figure.

Using the ratio $\mu N_{HBD} = 2860$ for different levels of coarse-graining, we plot in Figure 4.6, the evolution of the number of kinks per chain in MD, MDCG and HBD models.
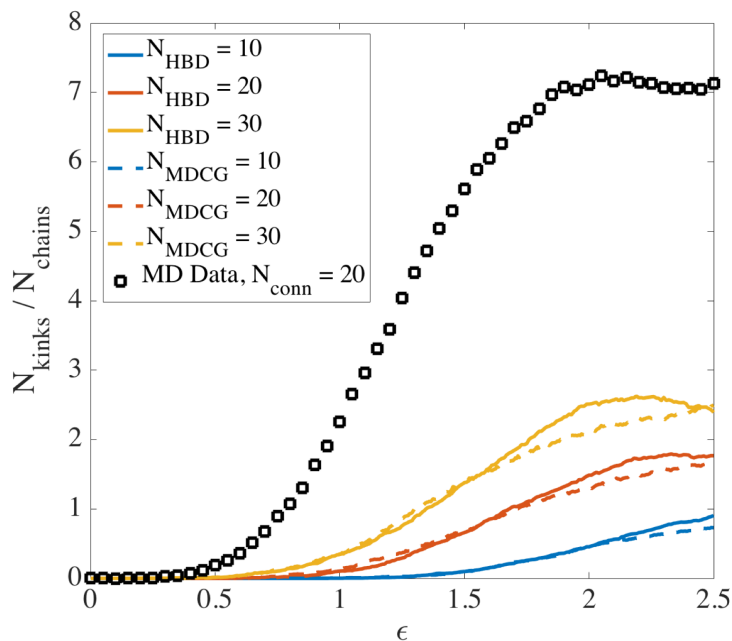
Figure 4.6. Comparison of the number of kinks between MD, MDCG and HBD models. For the HBD model the value of μ is chosen so that $\mu N_{HBD} \cong 2860$ to give closest results with MDCG model. The value of α for all the HBD results is 8.0×10^4.

Figure 4.6 shows that by coarse-graining the chain, we lose some of the conformational details of the polymer chains, in particular an accurate count of the number of kinks per chain, since the "kinks" occur at highly localized points along the chain. However, the degree of non-affinity, degree of strand stretching, and fraction of highly stretched strands are rather insensitive to coarse graining, as shown in Figure 4.3. In Figures 4.1 and 4.2 we showed that MDCG, although losing some of the details of the MD chain, retains the overall conformations of the polymer chains, making the coarse-graining reasonable for at least some purposes.

Further progress will require a better segmental model to describe yielding and rejuvenation, and steps in this direction will be discussed shortly. As mentioned above, the results

in Figures 4.1 – 4.4 are obtained at asymptotically high strain rates where the dependency of chain conformation on strain rate is weak. Since the MD chains are entangled and the HBD chains are not, the excellent agreement between conformations shown in Figures 4.1 – 4.3 strongly suggests that the straightening of chain segments and kink formation are not much affected by entanglements.

While Ediger and co-workers [183–186] have shown that the segmental relaxation time probed by fluorescence spectroscopy τ_{prb}^s is a function of $\dot{\epsilon}$, it usually approaches a plateau value τ_{ss}^s beyond the yield strain for uniaxial extension at constant $\dot{\epsilon}$. Such behavior has been modeled empirically by a fluidity equation in the HBD model, where Equation (4.7) gives $\tau_{ss}^s \cong 1/(\sqrt{3}\mu\dot{\epsilon})$, and μ controls the rate of glass rejuvenation, and τ_0^s is too small to be important. Hence the post-yield Weissenberg number for the polymeric mode is $Wi^p \equiv \tau^p\dot{\epsilon} = \alpha\tau_{ss}^s\dot{\epsilon} = \alpha/(\sqrt{3}\mu) = 323$ for the values of α and μ in Table 4.1. Our HBD simulations in Figure 4.7 show that the number of kinks versus the strain collapses onto a common curve if α/μ is held fixed so that Wi^p remains the same. This may be understood in terms of the effect of strain and strain rate on the orientation of chain segments in the polymeric glass. One corollary of the above commonality in number of kinks at constant Wi^p (and strain) is that the chain statistics and orientation, or birefringence, on sub-entanglement scales are governed by the strain and Wi^p at fixed temperature. While our HBD model does not yet encompass thermo-mechanical history, it is interesting that recent simulations and experiments indicate that many aspects of polymer glasses' mechanical response depend primarily on orientation or birefringence and are otherwise insensitive to the detailed thermo-mechanical treatment [108,174]. The above results also suggest that improved understanding through modeling may provide rational guidance for the design of polymeric glass through thermo-

mechanical treatment. According to Figure 4.7, for fixed value of μ, a higher molecular weight, and therefore a larger relaxation time ratio α of polymeric to segmental dynamics, should lead to more kinks per unit chain length, which should have implications for controlling the thermo-mechanical properties of glassy polymers.
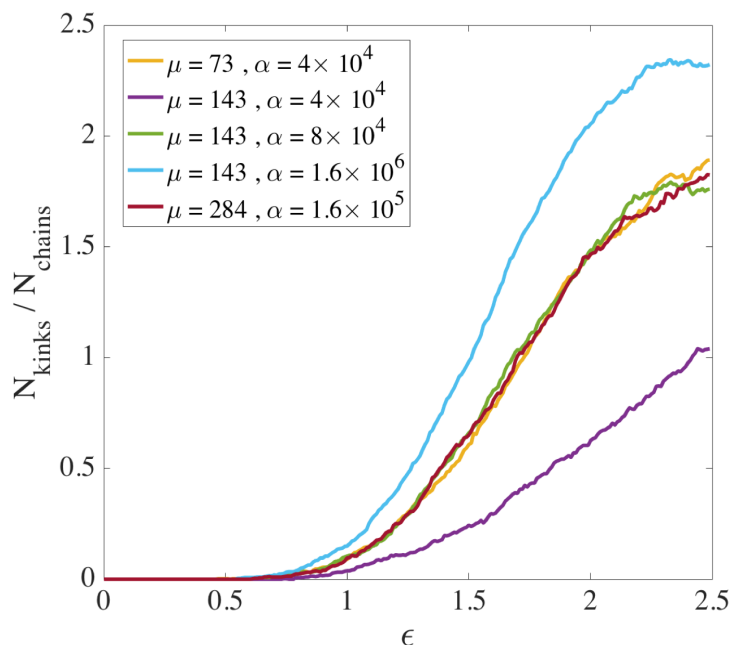
Figure 4.7. The number of kinks vs. strain from HBD simulations for different values of α and μ. The three data sets for which α/μ is the same (orange, blue, and red) collapse onto a common curve with the same post-yield polymeric-mode Weissenberg number ($Wi^p = \tau^p \dot{\epsilon} = \alpha \tau_{ss}^s \dot{\epsilon}$, where τ_{ss}^s is the steady-state value of τ^s defined in the text). The values of the other parameters are the same as shown in Table I.

4.4.4 Insensitivity of Segmental Stretch and Fraction of Highly Stretched Segments to Model Details

We plot in Figure 4.8 the average segmental stretch and fraction of highly stretched segments as functions of the imposed strain for MDCG and HBD conformations for three different values of N_{HBD} and three different values of the rejuvenation parameter μ. These plots show that both quantities are rather insensitive to N_{HBD} and μ, as was shown for the non-affinity of deformation in Figure 4.3.
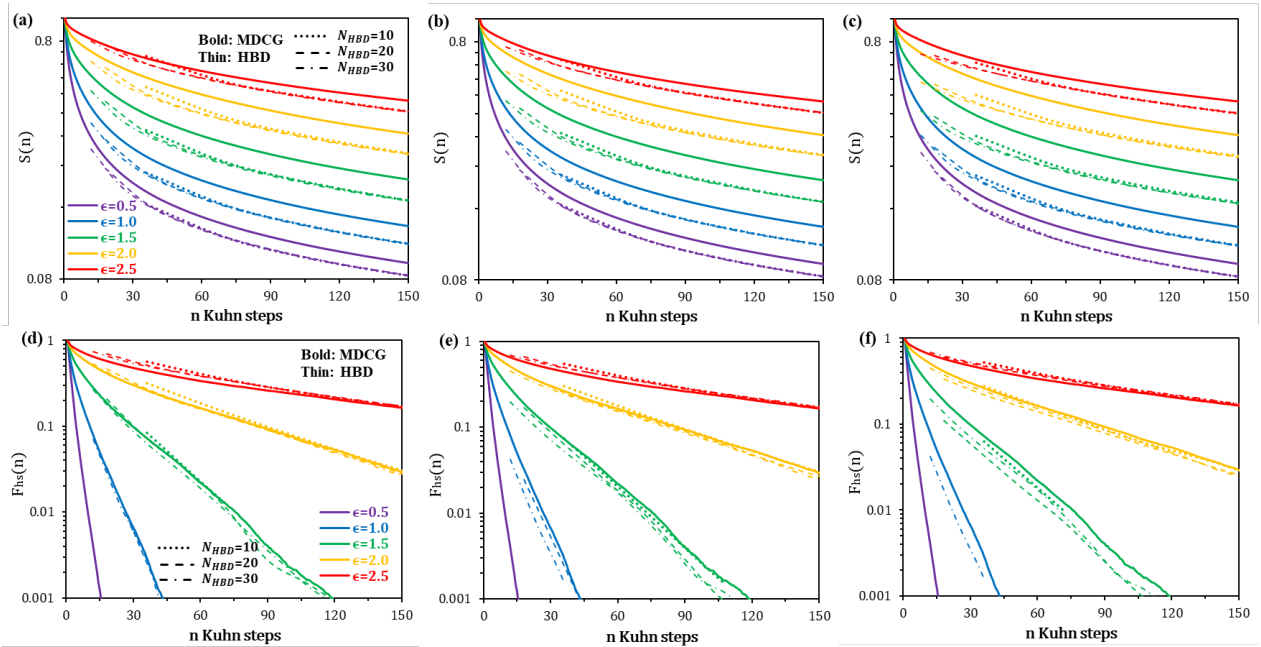
Figure 4.8. The mean segmental stretch $S(n)$ (a)-(c) as well as the fraction of "highly stretched segments" $F_{hs}(n)$ (d)-(f) as functions of the imposed strain at various level of coarse-graining N_{HBD} and rejuvenation parameter: for (a) and (d) $\mu = 72$; for (b) and (e) $\mu = 143$; and for (a) and (d) $\mu = 286$.

4.4.5 Entangled Kinks Identification

So far, our analysis has ignored the existence of entanglements. To investigate their effects

on kink formation and strain-hardening, we wish to find which of these kinks that form in the MD

simulations can be considered "entangled." A seemingly obvious way to identify such "entangled

kink pairs" is to perform primitive path analyses [187,188] and find pairs of contacting primitive

paths that satisfy some predefined kink criterion. However, recent work has shown that it is more

accurate to regard chains in deformed polymer glasses as being constrained by their rheological

tubes rather than by individual, crosslink-like entanglements [79]. In any event, our objective is

not to locate all entanglements, but rather to identify the entanglements that are localized at kinks.

Hence, we count a pair of kinked chain segments as entangled when they lie within a specific

distance of each other, belong to different chains, and mutually interwind. Kinks, defined earlier for the MDCG vectors, are here identified as entangled kinks if:

1. The two kinks have opposite polarity, as illustrated in Figure 4.9(a).

2. The two kinks are "intertwined" with each other. This is determined by defining a "kink triangular surface" as the surface bounded by the two kink-forming connecting vectors (red arrows in Figure 4.4-(a)) of each kink (see the in Figure 4.9(a)) and by a third vector formed by linking the free ends of the two connecting vectors. If the two kink triangular surfaces formed by two kinks intersect each other, and only one of the end-to-end vectors of a kink intersects the triangular surface of the other, then the two kinks are considered entangled.

These criteria allow us to quantify the numbers of "entangled kinks pairs" in Figure 4.9(b). The effect on the number of total and entangled kinks of the angle θ_c used to define whether a kink is formed at a given bead is studied in the next section, which shows that for a wide range of angles, around 1/3 of the kinks are entangled.
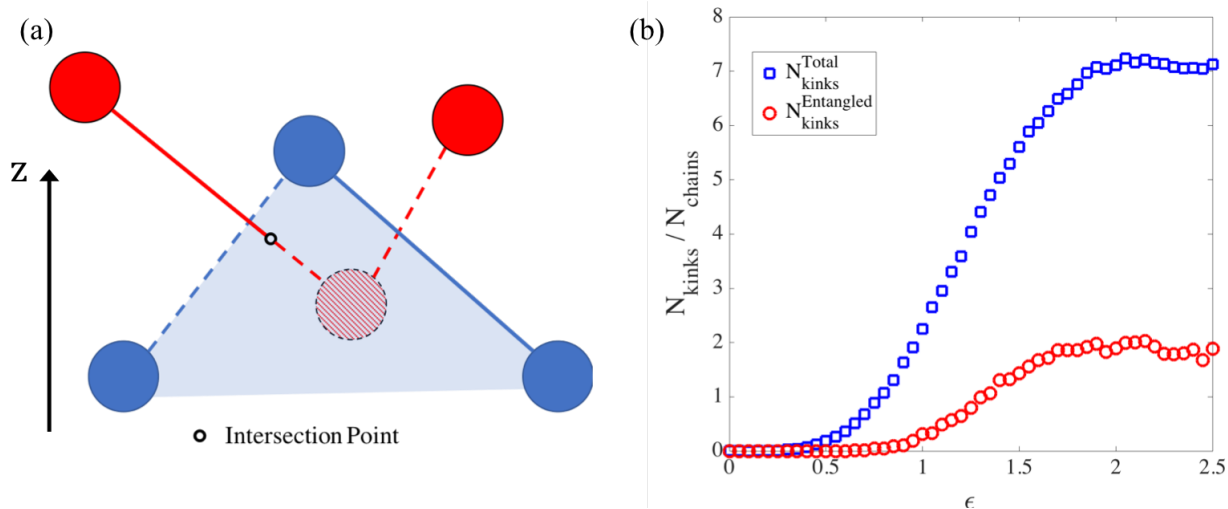
Figure 4.9. (a) Schematic of how an entangled kink is determined in MD simulations using the kink's connecting vectors obtained as defined in Figure 4.4-(a). (b) Average numbers of kinks (blue squares) and entangled kinks (red squares) per chain as a function of imposed strain in MD simulations. For all data, $N_{conn} = 20, \theta_c = 20^o$ and $\lambda_c = 0.5$.

The strain hardening observed in rapidly deformed melts and crosslinked rubbers can be entanglement- or crosslink-driven because sub-entangled chain segments relax rapidly compared to the inverse strain rate. In glasses, this is no longer the case; here, for example, the post-yield Weissenberg number in both our MD and HBD simulations is $\sim 10^3$. The highly stretched strands discussed above, which first begin to appear at a strain of $\epsilon \sim 0.5$, become prominent by $\epsilon \sim 1.0$.

As deformation continues, they become highly oriented along the direction of extension, leading to the build-up of the "kinked state" starting at $\epsilon \approx 1.6$. Chains only become fully folded at strains well above $\epsilon \approx 2.0$; it is likely that fracture would occur first in a real polymer glass. Strong strain hardening does not require fully formed folds, but only their precursors, the highly stretched strands. The results in Figures 4.3 and 4.5 are consistent with the view [113–115,118] that the increasingly sub-affine deformation as strain increases requires an increasing level of microscale plastic deformation which, in turn, drives the dominant dissipative component of strain hardening. However, our results significantly extend this picture, both by making the role played by the strand stretching much more explicit and by showing, for the first time, that the same underlying phenomenon is predicted by a single-chain-in-mean-field model. Our results also clarify that entanglements are not primary in this picture because the length scale controlling strain hardening is not the rheological entanglement length N_e obtained from measurements of the melt plateau modulus. Instead it is the smaller length scale n^* associated with the abovementioned strand-stretching. It can be seen in Figure 4.9(b) that at Hencky strain of unity where strain hardening begins, there are almost no entangled kinks per chain. Our picture is also consistent with the observation that the length scale over which chains are pulled taut in stable crazes is $\sim N_e/3$ rather than $\sim N_e$ [121]. Note that we do *not* claim that strain hardening can occur in experiments

on unentangled systems — it is now well established that the entanglement network is required to prevent brittle fracture before the onset of strain hardening [91,111,174,189].

The very good agreement between configurations from the HBD simulations and from the much finer-grained MD simulations is particularly noteworthy. Since the HBD model uses a very simplistic one-mode model for the glassy segmental mode (that is coupled only through a friction coefficient to the polymeric mode), while the MD simulations are resolved at the level of the segmental mode, the good agreement between the two models in Figure 4.3 is strong evidence that the polymer configurations are not sensitive to the details of the glassy dynamics. In addition, the insensitivity of the results to the inclusion of entanglements suggests that the polymeric modes can be modeled (as we have done here) using rather simple bead-spring chains. This opens the door to modeling glassy polymers accurately by combining an accurate model of the glass (without polymeric modes) with a rather simple model of the polymer. It is found in earlier work [103] that the strain hardening of glassy polymers in creep is qualitatively predicted correctly by our HBD model, including the onset of hardening at a strain of around unity, near the strain at which "highly stretched strands" begin to become prominent in Figure 4.3. Since this strain is well below the strain required to fully stretch the entire molecule or even to stretch fully the entanglement strands, we infer that strain hardening is initiated by a few highly stretched sub-entanglement strands. However, the earlier work also showed that stresses at high strains are only qualitatively predicted by the model presented so far [103] despite the excellent prediction of polymer conformations. Thus, a better glassy model than the simple fluidity model used up to this point is clearly needed. Although the stress is dominated by highly stretched strands, it is also governed by the friction that is exerted on those strands by surrounding segments, and this friction depends strongly on the glassy modes. Hence, having developed an acceptable model for the polymeric modes, a more

accurate glassy polymer model requires an improved segmental model, and in section 4.4.8, we turn our attention to the segmental model.

4.4.7   Sensitivity of the Number of Kinks in MD Simulations to Identification Parameters

Before moving to segmental mode analysis of HBD model, here we report the sensitivity of the number of kinks per chain in MD simulations to the kink identification parameters, namely θ_c, N_{bead} and λ_c. Figure 4.10(a) shows that by increasing the value of N_{conn} to find the connecting vectors of the kinks in MD simulations, the number of kinks per chain initially rises and then drops again, with identical plateau values for $N_{\text{conn}} = 10$ and 20. This is expected since by increasing N_{conn} beyond a threshold, the connecting vectors of the potential kink point eventually extend beyond the region of a single kink and therefore no longer satisfy the angle criterion. We therefore chose $N_{\text{conn}} = 20$ for our MD analysis in previous plots. Figure 4.10(b) shows that increasing θ_c initially results in an increase in the number of local kinks in the MD simulations; however, increasing it more that $\sim 20^o$ no longer affects the number of kinks, unless the angle is made so high that it is no longer reasonable to consider the conformation to be that of a "kink," which is intended to be a relatively sharp fold of the chain back on itself along the flow direction. Based on these results, $\theta_c = 20^o$ was chosen as the critical limiting angle limit for defining a kink in the figures main text. Finally, we study the effect of stretch ratio of the kink's connecting vectors on N_{conn}. As expected, as the minimum stretch ratio, λ_c, gets larger, the number of kinks decreases. Since in this manuscript, we are considering locally formed kinks at strains below that needed for the chain to reach the "kinked" or folded state [46,165], we choose a minimum stretch ratio of 50% to define a locally stretched state for the two strands bounding the kink. Figure 4.10(d) shows that although the absolute value of N_{kinks}, and both the "Total" and "Entangled" numbers of kinks depends on θ_c, the ratio of the two remains around 30%.
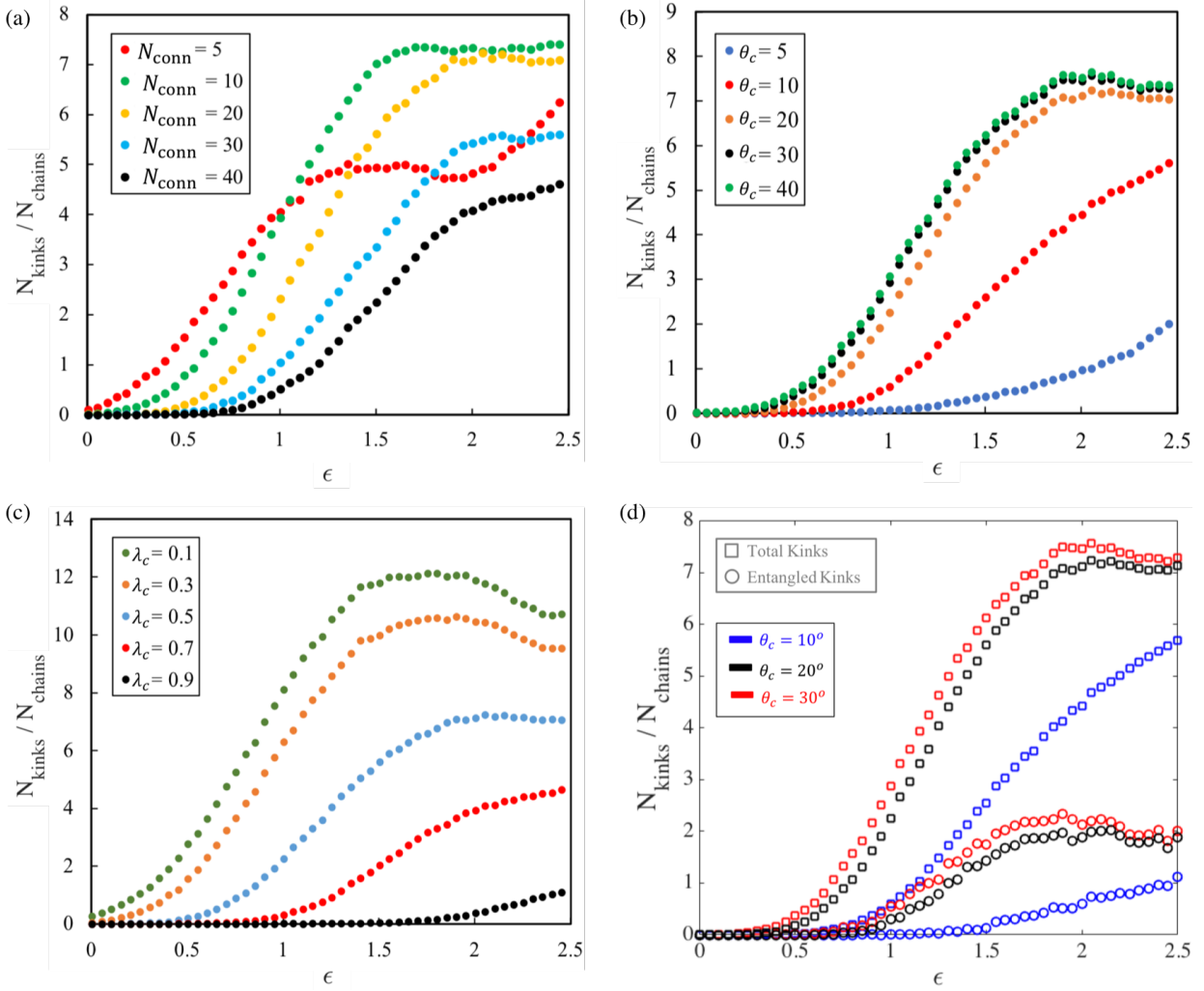
Figure 4.10. Sensitivity of the number of kinks per chain in the fine-grained MD simulations on (a) N_{conn}, (b) θ_c and (c) λ_c. (d) Sensitivity of the number of entangled kinks on θ_c. The default values of parameters are $N_{bead} = 20$, $\theta_c = 20$ and $\lambda_c = 0.5$, unless stated otherwise.

4.4.6 Predictions of Stress: Empirical Three-Model Segmental Model

The above successes of our simplified modeling, in particular in the agreement of MD and HBD simulations of chain configurations shown in Figure 4.3 and 4.5, is not sufficient to allow accurate predictions of stresses. This is primarily because the single-mode segmental model is over-simplified, and, in particular, ignores the heterogeneity of the segmental dynamics, where

rates of molecular rearrangements vary significantly because of heterogeneity across spatial and temporal scales [85,87].

Although it allows semi-quantitative fits to the experimental data of Lee *et al.* [183,184], the single Maxwell mode model for segmental dynamics with characteristic time controlled by a simple fluidity equation has major disadvantages as illustrated in Figure 4.11: The phenomenological fluidity equation (see Eq. (4.7)) is too crude to predict accurately the change in segmental mobility under constant deformation rate. In fact, as shown by the inserted plot in Figure 4.11(a), the fluidity model greatly underestimates the rate of drop in τ_{prb}^s at strains of less than 0.02 during the period of rising stress in the start-up deformation, while underestimating the rate of decrease at a strain of around 0.02, near the maximum in stress. As a result, the decay in stress after the maximum is reached is much larger than in the experiments [185,186]. (Note that for the purpose of comparison, the linear elastic deformation, i.e., strain below 1%, as well as the height of stress overshoot predicted by different version of segmental models were fitted to the experiments through the choice of the glassy modulus G^s and waiting time t_w.) This deficiency in modelling the evolution of segmental relaxation time can, however, be fixed easily by the use of experimentally measured τ_{prb}^s from fluorescence spectroscopy. After reoptimizing the value of some parameters, the corresponding new simulation prediction, as shown in Figure 4.11(b), gives a stress-strain curve that is in much better agreement with experiment, but still shows a larger strain-softening, due to the single time-constant segmental relaxation assumed here even though the stretched exponential relaxation of segmental mobility is observed experimentally [183,184].
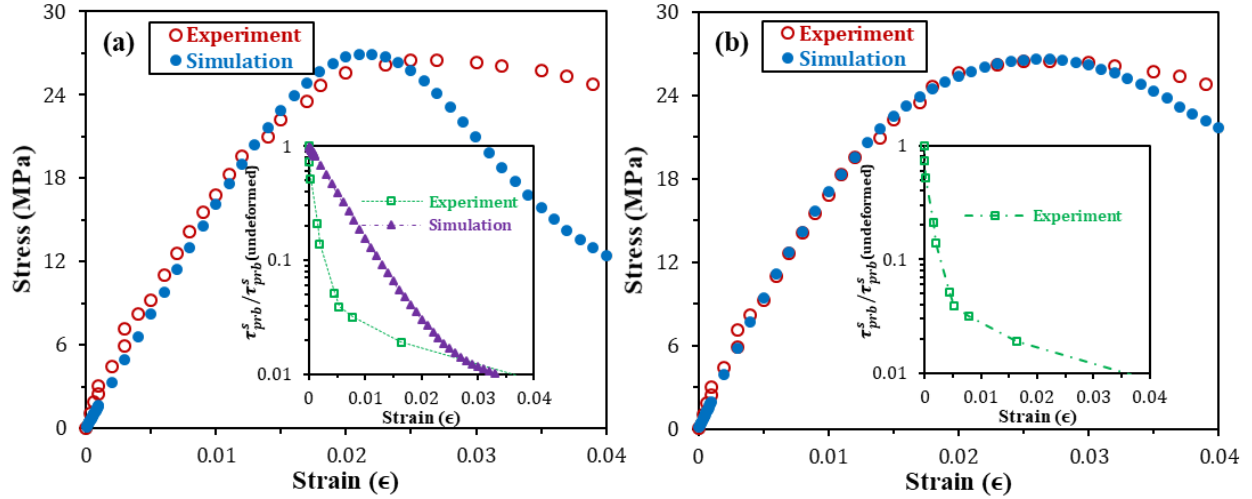
Figure 4.11 Comparison of the experimental stress-strain curves of Ediger and coworkers with fitted by the HBD model with single-mode segmental dynamics with relaxation time given by (a) simple fluidity equation (filled purple triangles in the inserted plot); (b) direct measurement from fluorescence spectroscopy (hollow green squares in the inserted plot). Note that in contrast to values used in the multi-mode HBD model (Fig. 4.16(b)) the values of t_w and G^s used here are given in Table 4.2.

In addition to the above issues on segmental dynamics, like most constitutive models, the values of model parameters are not set a priori, but are fitted to the measured data. Thus, an inadequate physical model for segmental dynamics can also result in uncertainties and errors in the values of parameters obtained by fitting with experimental data, especially when the data is rich in features. Since the applied deformation in Figure 4.11(b) extends only into the strain-softening regime, the stress contributed from polymeric mode remains mostly inactivated, and only the initial age of the sample t_w ($=21000\ s$ or $5.8\ h$, see Table 4.2) and the glassy shear modulus G^s ($=0.8\ GPa$, see Table 4.2) are relevant and can be estimated directly by matching the simulation predictions with the experimental data. Relative to the multi-mode segmental model discussed later G^s is roughly halved in the single mode model, while t_w is increased by a factor of two. Thus, in the single-mode glassy model, the best-fit values of parameters deviate from ranges that reasonably reflect the physical properties of a young glass with G^s around $1\ GPa$ and t_w

114

roughly several hours long. This further supports the importance of stretched exponential relaxation for development of a more rigorous physics-based segmental model.

Table 4.2. Value of segmental parameters for single- and multi-mode HBD simulations in Fig. 4.11 and Fig. 4.14(b) with segmental relaxation time from experiment or simple fluidity model.

Figures	No. of modes	Segmental time	G^s (MPa)	t_w (h)	μ
Fig. 4.11(a)	1	Fluidity equation	550	5.8	143
Fig. 4.11(b)	1	Experiment	500	11.1	N/A
Fig. 4.14(b)	3	Experiment	800	5.8	N/A

Note that the 3-mode segmental dynamics were achieved by decomposing the KWW function through the modified genetic algorithm with the nonexponentiality β determined from the experiment (see the section below).

Thus, we need improvements in our description of the dynamics at the segmental level to include the effects of stretched exponential relaxation (known as the Kohlrausch-Williams-Watts, or KWW function) on the nonlinear deformation behaviors, especially for loading and unloading. This is achieved below by employing *multiple* segmental relaxation times (as opposed to the single one assumed previously) within the abovementioned "glassy solvent" description of segmental dynamics. Since the characteristic probe relaxation time τ_{prb}^s and the stretching exponent β of a KWW function has been accurately measured by fluorescence spectroscopy at each instantof deformation time [183–186], we construct a small set of distinct Maxwell modes from the decomposition of these KWW functions into a discrete spectrum of Maxwell time constants with the corresponding amplitude of each mode tuned iteratively at given τ_{prb}^s and β. The set of equations for the multi-mode glassy model is given by:

$$\dot{\sigma}_j^s + v \cdot \nabla \sigma_j^s = \sigma_j^s \cdot \nabla v + (\nabla v)^T \cdot \sigma_j^s - (\sigma_j^s - I)/\tau_j^s \qquad (4.14)$$

$$\Sigma^s = G^s \sum_j^M C_j(\sigma_j^s - I) \qquad (4.15)$$

$$exp\left[-\left(\frac{x}{\tau_{prb}^s}\right)^\beta\right] = \sum_j^M C_j exp\left(-\frac{x}{\tau_j^s}\right) \qquad (4.16)$$

$$\frac{\tau^p}{\sum_j^M C_j \tau_j^s} = \alpha, \quad \tau_{prb}^s \big|_{t=0} = t_w \tag{4.17}$$

In the above, $\boldsymbol{\sigma}_j^s$ stands for the segmental configuration tensor for mode j with the corresponding amplitude C_j and characteristic time τ_j^s determined by a genetic algorithm, whose details are given below. $M = 3$ is the total number of segmental modes used here to represent the KWW function with experimental determined *time-dependent* τ_{prb}^s and β. This means that C_j and τ_j^s are also time dependent.

Here we present the procedure for decomposing the KWW function with known characteristic time τ_{prb}^s and stretching exponent β from fluorescence spectroscopy into a set of single exponential relaxation terms using optimization with a genetic algorithm (GA). This is necessary to obtain the constants used in the multi-mode segmental relaxation model. Since a generalized protocol for fitting an arbitrary time-dependent function with a discrete spectrum of mono-exponentials has been elaborated in [190], in what follows we focus on utilizing this protocol for our case without a detailed discussion of the GA method itself.

The GA is used to generate the times constants τ_j^s and prefactors C_j in Equations 4.10 – 4.13, for a set of exponential functions whose sum represents adequately the stretched-exponential function $exp[-(x/\tau_{prb}^s)^\beta]$ with given values of τ_{prb}^s and β. We first generate a set of values of the stretched exponential function at times spaced logarithmically over a finite time interval whose upper boundary (t_{max}) is determined by the following criterion,

$$exp\left[-\left(\frac{t_{max}}{\tau_{prb}^s}\right)^\beta\right] = 1\%, \quad t_{min}/t_w = \frac{t_w}{t_{max}} \tag{4.18}$$

Note that the lower boundary (t_{min}) is chosen so that these boundaries are symmetric on the logarithmic scale. Thus, the ratio t_{max}/t_{min} represents the width of the spectrum of the decomposed single exponential terms, which depends on the value of β since the spectrum narrows as β increases. By normalizing the characteristic times for each exponential mode by τ_{prb}^s, which is equivalent to setting $\tau_{prb}^s = 1$, we were able to use the GA to create a library of output values of τ_j^s/τ_{prb}^s and C_j for values of β varying from 0.2 to 0.75. With this library, the amplitude C_j and the normalized time constant τ_j^s/τ_{prb}^s for each mode j can be retrieved at any time required by fitting to the stretched exponential function in Equations (4.12) and (4.13), upon inputting β. Thus, the parameters C_j and τ_j^s/τ_{prb}^s change with time as required by the time-dependent values of β and τ_{prb}^s from the experimental data. We carried out the fitting for three different numbers of exponential modes, i.e., $M = 3, 4$, and 5 and results are shown in Figure 4.12 with their corresponding fitting errors (defined in Equation (4.15)) given in Figure 4.13.

$$\varepsilon_k = \frac{1}{N}\sum_{i=1}^{N}\left\{\frac{\left|exp\left[-\left(\frac{x_i}{\tau_{prb}^s}\right)^{\beta_k}\right] - \sum_{j=1}^{M}C_j exp\left(-\frac{x_i}{\tau_j^s}\right)\right|}{exp\left[-\left(\frac{x_i}{\tau_{prb}^s}\right)^{\beta_k}\right]}\right\} \tag{4.19}$$
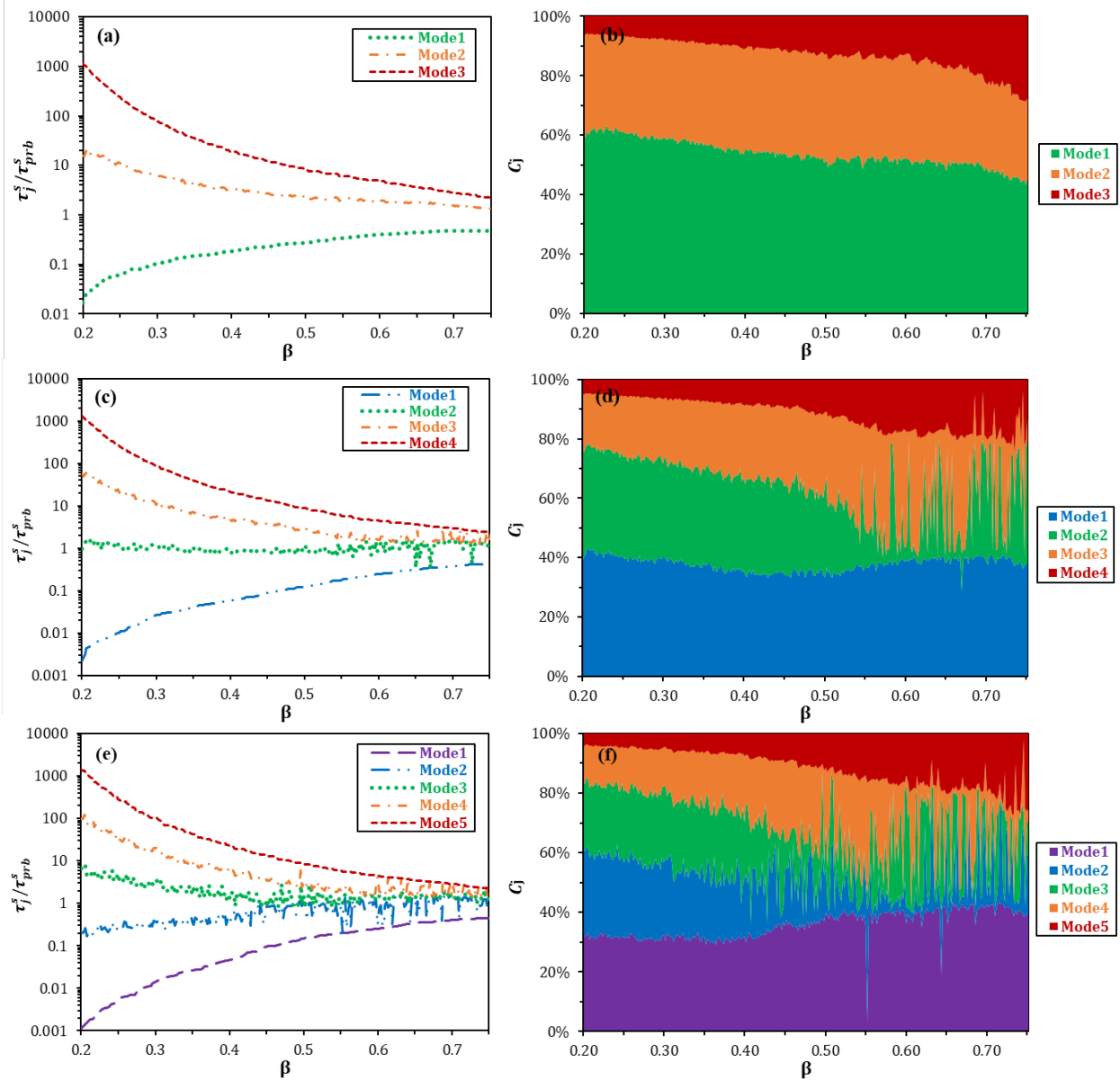
Figure 4.12. The normalized characteristic times τ_j^s/τ_{prb}^s in (a), (c), and (e) with corresponding amplitudes C_j in (b), (d), and (f) obtained from the GA as functions of β at three different total numbers of exponential modes: (a) and (b) for $M = 3$; (c) and (d) for $M = 4$; (e) and (f) for $M = 5$.

Here, ε_k is the averaged relative error when using M different mono-exponentials to represent the KWW function of β_k. The subscripts "i" and "j" stand, respectively, for the ith data point at time x_i and the jth mode with amplitude C_j and normalized time constant τ_j^s/τ_{prb}^s. The subscript "k" is the index for the set of values of β_k, from smallest to largest, in the library. An empirical constraint (see Equation (4.16)) is also introduced so that the smallest and the largest

118

values of τ_j^s/τ_{prb}^s, respectively, increase and decrease with increasing β values. This is done to smooth out the fluctuations of τ_j^s/τ_{prb}^s as β increases.

$$\begin{cases} max[\tau_j^s(\beta_k)] \geq max[\tau_j^s(\beta_{k+1})]; \\ min[\tau_j^s(\beta_k)] \leq min[\tau_j^s(\beta_{k+1})]; \end{cases} \quad j = 1, \cdots, M \quad (4.20)$$
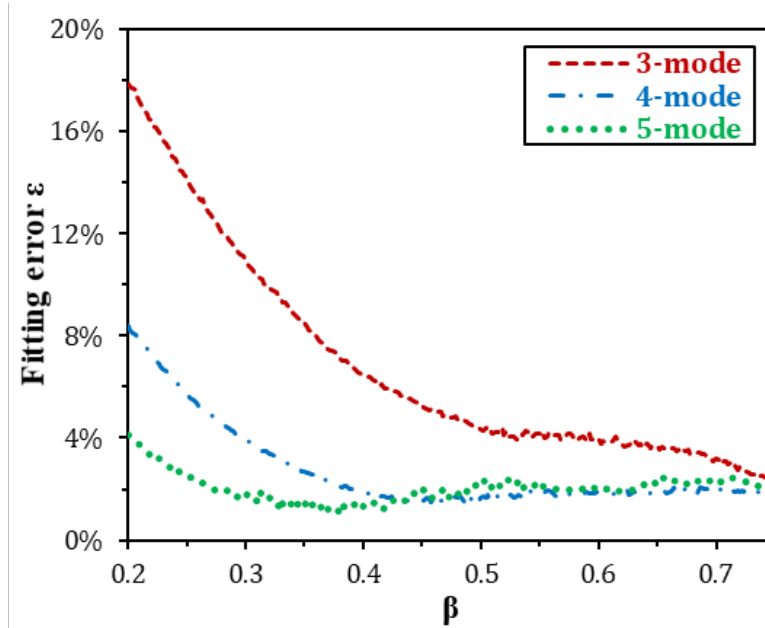
Figure 4.13. The relative error in representing the KWW function with different numbers of mono-exponential terms with amplitude and characteristic time optimized by a GA.

According to Figures 4.12 and 4.13, using more exponential terms reduces the fitting error for small β values with broad relaxation spectra on one hand, but loses the distinction in τ_j^s/τ_{prb}^s between different modes for large β values with narrow spectra on the other hand. Since the relaxation time spectrum narrows down effectively to a nearly single-Maxwell model at large deformation as β increases to unity, the latter situation is more troublesome under the creep measurements, for which the fluctuations in C_j would induce a significant level of noise in deformation rate, therefore making quantitative prediction rather challenging. Thus, we choose a constant value $M = 3$ as a trade-off between accuracy and robustness of the results. Note that

since β is time-dependent, a constant value of M is needed to avoid adding and removing modes during a simulation.

Based on above procedure, we extend the single-mode segmental dynamics in the original HBD model [103], whose relaxation time is governed by the fluidity equation, to a discrete spectrum of modes with relaxation times derived from the decomposition of the stretched exponential function at given τ_{prb}^s and β, i.e.,

The two modes, polymeric and segmental, contribute to the stress ($\Sigma^{p,s}$) through their moduli $G^{p,s}$. t_w is therefore controlled by how long the sample has been aged since the last deformation. Thus, assuming that rejuvenation is governed by the deformation-rate-dependent fluidity equation (Equation (4.7)), the values of G^s and t_w are further adjusted by fitting to the experimental stress-strain curve using τ_{prb}^s and β directly measured from fluorescence spectroscopy.
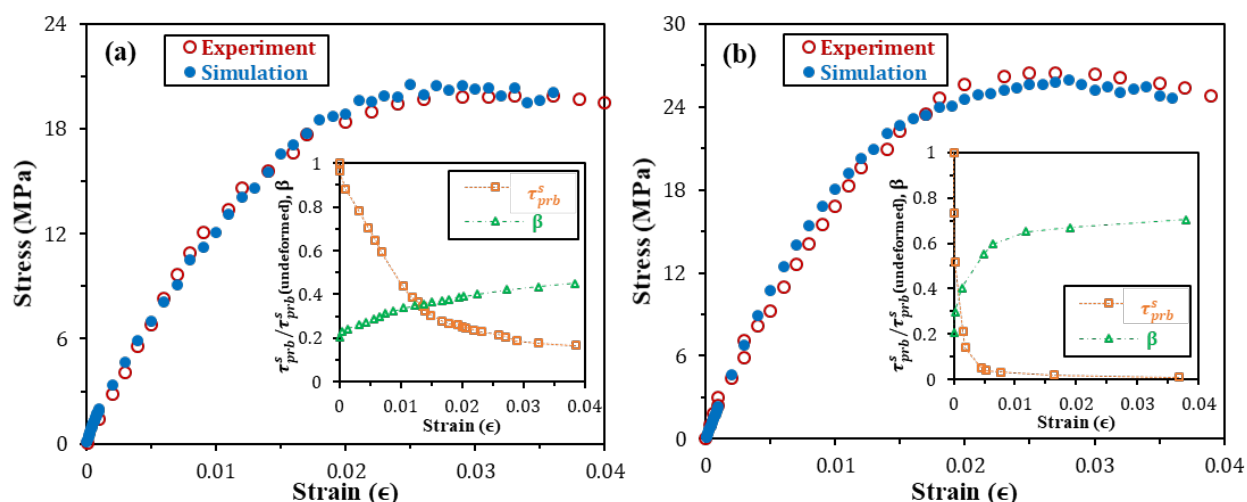
Figure 4.14. Comparison of HBD simulation results predicted by the 3-mode segmental model with parameters given in Table I (except using a shorter initial age of the glass t_w and a larger glassy modulus G^s) with stress-strain curves of Ediger and coworkers [183–185] under steady uniaxial extensional straining at $373\ K$ with (a) $\dot{\epsilon} = 1.5 \times 10^{-6}\ s^{-1}$ and (b) $\dot{\epsilon} = 3.1 \times 10^{-5}\ s^{-1}$. The time-dependent probe segmental relaxation time τ_{prb}^s and stretched exponential exponent β taken from their smoothed fluorescence spectroscopy data are shown in the inserted plots. To be consistent with the experimental results in references [183–185], the strain along the horizonal axis is taken as the global strain, but the simulations used the actual strain measured near the mid-point of the sample where segmental relaxation was monitored. Note that since the final strains considered here are in the pre-strain-hardening

regime, the predicted mechanical responses are dominated by the segmental dynamics, with insignificant contributions from the polymeric mode. Therefore, the relevant parameters t_w and G^s can be estimated directly by matching the simulation predictions with the data of experiments, the resulting fitted values, i.e., (a) $G^s = 900\ MPa$, $t_w = 3.3\ h$ for $\dot{\epsilon} = 1.5 \times 10^{-6}\ s^{-1}$; (b) $G^s = 800\ MPa$, $t_w = 5.8\ h$ for $\dot{\epsilon} = 3.1 \times 10^{-5}\ s^{-1}$, semi-quantitatively reflecting the effects of temperature and preparation history of the testing samples.

As illustrated in Figure 4.14, we performed HBD simulations using this new modified segmental model based on experimental data points for τ_{prb}^s and β, and obtained good agreement with the experimental stress at the beginning of startup flow. This agreement is much better than we can obtain with a one-mode glassy model. The importance of a good segmental model in capturing both pre-yielding and post-yielding behaviors of polymeric glasses is further indicated by the uniaxial stresses predicted from MD and HBD simulations for strains ϵ up to 2.0 in Figure 4.16. To apply the multi-mode model to the MD data, we used the empirical correlation between the segmental relaxation time and the stretching exponent β, obtained from fluorescence probe experiments. In general, the lack of quantitative data limits the development of a heterogeneity model, since it requires experimental data for the segmental relaxation time τ_{prb}^s and its stretching exponent β, and these are frequently not experimentally inaccessible. Recent findings for polymeric glasses indicate that the heights of barriers between local energy minima in the potential energy landscape (PEL) become larger as the system moves towards the lower-energy regions of the PEL, suggesting that the heterogeneity can be linked to the segmental mobility [176,191]. For example, the thermally excited sampling of the PEL should be especially retarded in lower-energy regions of the PEL due to their higher barriers, thus leading to a more pronounced heterogeneity and hence smaller β. Inspired by the plot of stretching exponent β vs. the dimensionless segmental relaxation time τ_{prb}^s/t_w in Lee *et al.* [183,184] we show in Figure 4.15 that a crude "master curve" can be obtained empirically, whose mathematical expression is given by Equation (4.21), by extracting β and τ_{prb}^s/t_w from multiple measurements of fluorescence spectroscopy by Ediger and

coworker [183–186], at various temperatures, type of probes, preparation history, as well as deformation processes.

$$\beta = 0.25 - 0.61 ln\left(\frac{\tau_{prb}^s}{t_w}\right) \tag{4.21}$$
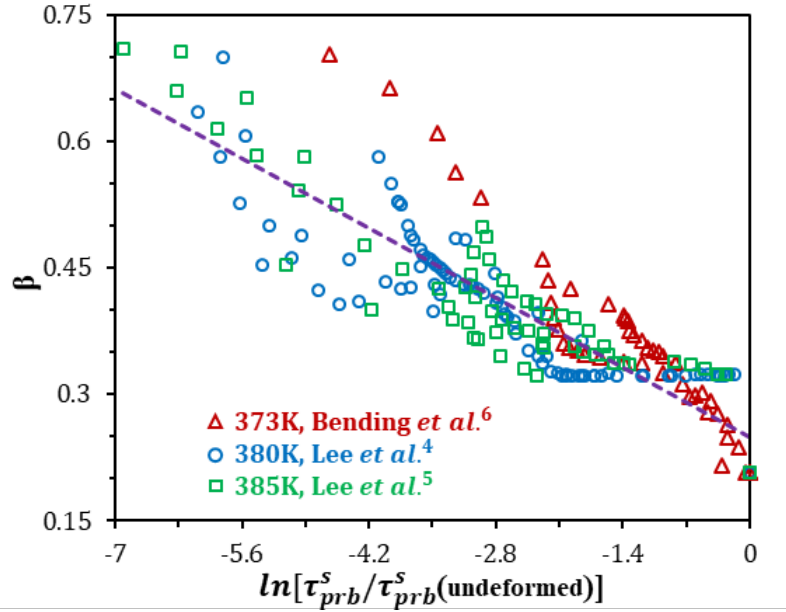
Figure 4.15. Correlation between the enhanced segmental mobility τ_{prb}^s/t_w and stretching exponent β from results of fluorescence spectroscopy in Refs. [183–185] R^2 value for the dashed line fit, given by Eq. (4.21) is 0.755.

This correlation between segmental mobility and heterogeneity, in Figure 4.15, offers us an empirical route to incorporate multi-mode segmental dynamics into the HBD model. Thus, Equation (4.21) is added to Equations (4.10) to (4.13) to complete the empirical model.

While the HBD model with only one segmental relaxation mode shows a much larger stress overshoot than does the MD simulation, this deviation is reduced significantly in the 3-mode model. Note that this overshoot arises primarily from the segmental contribution to stress. The results in Figure 4.16 for the one-mode and three-mode segmental models show that the near-universal behavior of the chain orientation, stretch, and kink formation illustrated in Figure 4.3

does not extend to the stress-strain behavior, which is much more sensitive to the dynamics of the segmental mode.
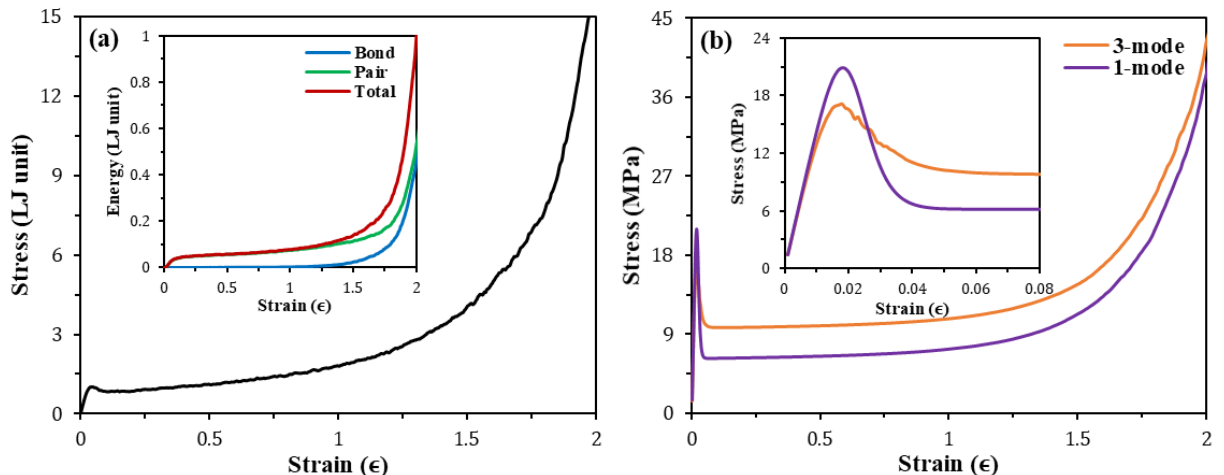
Figure 4.16. Mechanical response of (a) the fine-grained Kremer-Grest polymer model and (b) the coarse-grained HBD model with 1-mode (dotted line) and 3-mode (orange line) segmental relaxation. The insert in (a) gives the contributions to energy from bond and pair interactions as well as the sum of the two, while the insert in (b) is a blow-up of the stress at small-strain region. The LJ units of stress are u_0/a^3.

Much progress has been made recently in understanding segmental-level dynamics of both small-molecule and polymeric glasses [192–195]. However, segmental-scale theories such as the PNLE theory of Schweizer *et al.* [93,94,99,196] typically do not treat polymeric relaxation modes; indeed they typically assume chains deform affinely above segmental scales. Efforts to obtained improved predictions of glassy-polymeric mechanical response should combine accurate treatments of both segment-scale and chain-scale physics, including the physical phenomena described here (in particular, the formation of highly stretched segments, and kinks). We hope that the findings presented here will help the community achieve a useful synthesis of these ideas and hence a more complete understanding of polymeric glasses and their rheology.

4.5   Conclusions

Analyses at two different levels of resolution have provided insight into the effect of multiple segmental relaxation times and sub-entanglement chain stretching on strain hardening and stress-strain relationships in tensile deformations of polymeric glasses. Both our HBD model and the finer-grained MD simulations suggest that sub-entanglement chain stretching and orientation trigger strain-hardening in polymeric glasses at a strain level ($\epsilon < 1$) that is far smaller than would be required if strain-hardening originated from the affine deformation of an entangled network. MD simulations clearly exhibit the emergence of highly-stretched segments with chain conformations very similar to those found in HBD simulations, and indicating that strain hardening is controlled primarily by chain stretching at high Weissenberg number, and not by entanglements or details of the glassy dynamics. This similarity of results from both fine-grained and coarse-grained models offers a clear explanation of the large magnitude of glassy-polymer strain-hardening: hardening in the glassy state arises primarily from chain stretching and orientation at scales below that of the entanglement mesh. This picture supports the notion[39] that while entanglements are essential for stabilizing glassy polymers against brittle fracture, they are of less importance in strain hardening itself. This improved understanding, if confirmed by additional work (in particular, studies of systems possessing a wide range of chain stiffnesses and entanglement densities), should help in the design of deformation and temperature protocols that maximize properties of polymeric glasses for improved product performance.

The successful prediction of chain stretching and strain hardening from our original coarse-grained model does not extend to the yielding behavior, which requires a more accurate description of the glassy mode, than is provided in our original very simple one-mode fluidity model. We

therefore further modified our model by extending the segmental relaxation from one mode to three modes whose dynamics were drawn from experimental measurements, and observed much better performance, especially in pre-yield and yielding regimes where segmental mode attributes most of the stress and where overshoot occurs. The new three-mode HBD model explicitly accounts for local heterogeneity represented by time-dependent values of segmental relaxation time τ_{prb}^s and exponential stretching exponent β probed by fluorescence spectroscopy on deforming polymeric glasses. Future work should endeavor to develop a segmental constitutive model that accurately predicts the experimental segmental relaxation in arbitrary strain histories and incorporates this into HBD simulations to get a complete depiction for polymer glasses under deformation.

Chapter 5 : Assessing the Efficacy of Poly (N-isopropyl acrylamide) for Drug Delivery Applications using Molecular Dynamics Simulations

5.1   Abstract

All-atom molecular dynamic simulations (AA-MD) are performed for aqueous solutions of hydrophobic drug molecules (phenytoin) with model polymer excipients, namely (1) N-isopropyl acrylamide, (pNIPAAm), (2) pNIPAAm-co-Acrylamide (Am), and (3) pNIPAAm-co-Dimethylacrylamide (DMA). After validating the forcefield parameters using the well-known lower critical solution behavior of pNIPAAm, we simulate the polymer-drug complex in water and its behavior at temperatures below (295K) and above the LCST (310K). Using radial distribution functions, we find that there is an optimum comonomer molar fraction of around 20-30% DMA at which interaction with phenytoin drug molecules is strongest, consistent with recent experimental findings. The results provide evidence that molecular simulations are able to provide guidance in the optimization of novel polymer excipients for drug release.

5.2   Introduction

For an active pharmaceutical ingredient (API) to be absorbed from the gastro-intestinal tract into the bloodstream, it must be sufficiently soluble in the GI fluid [122]. However, more than 40% of new chemical entities in the pharmaceutical industry are poorly soluble, leading to drug aggregation and crystallization [123]. To improve solubility, drug particle size reduction, solid

dispersion, modification of crystal habit, cryogenic preparation, as well as use of buffers, micellar solubilization and complexation have been employed [123,197]. All of these techniques are intended to inhibit precipitation and crystallization of APIs and enhance solubility. Solid dispersions [124,125], which are solid-state molecular mixtures of a hydrophilic matrix or network and a hydrophobic drug, can maintain the API in an amorphous form and result in a supersaturated API solution upon its dissolution in the GI tract. Many studies suggest using biocompatible stimuli-responsive polymers as the hydrophilic network in solid dispersions. In particular, stimuli-responsive polymers [126,127] undergo a dramatic change in properties with a change in environmental conditions such as temperature, pH, light, ionic concentration, and electric and magnetic fields. Water-soluble bio-compatible polymers such as HPC (hydroxypropyl cellulose) HPMC (hydroxypropyl methylcellulose), PEG (poly(ethylene glycol)), and PLGA (poly(lactic-co-glycolic acid)) have been widely studied for API release properties during the past decade [125,198,199]. A group of these stimuli-responsive polymers, which react to a change in temperature, are called thermo-sensitive polymers. For the past years, one of the most widely investigated thermo-sensitive polymers for potential drug delivery applications has been poly(N-isopropylacrylamide), namely pNIPAAm (Figure 5.1) and its various copolymers such as poly(N-isopropylacrylamide-co-acrylic acid) and poly (N-isopropylacrylamide-co-dimethylacrylamide) [126–128,200]. The most interesting property of pNIPAAm, along with its biocompatibility, is its lower critical solution temperature (LCST). As the temperature increases above $\sim 32^{\circ}C$ in a pNIPAAm aqueous solution, polymer chains tend to decrease their interaction with water, leading to a coil-to-globule transition resulting in a compact conformation in water [129].
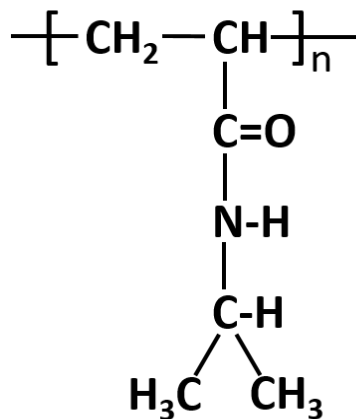
Figure 5.1. Chemical formula of pNIPAAm sub-unit. The chains are synthesized by free radical polymerization that generally results in atactic chains with head-to-tail assembly.

Many experimental studies have analyzed the collapse of pNIPAAm chains and hydrogels in aqueous solutions. In particular, Wang et al. [130] observed hysteresis in the heating-cooling cycle of dilute pNIPAAm chains in water. Zhou et al. [131] studied the effect of intrachain hydrogen bonding in dilute aqueous solutions of pNIPAAm and found that these bonds are responsible for the hysteresis behavior of the chain's dimension upon heating and cooling. Tanaka et al. analyzed how the diffusion coefficient of water molecules decreases at temperatures above the LCST in pNIPAAm crosslinked hydrogels [132]. Ray et al. and Biswas et al. showed how increasing isotactic content in chains will result in a decrease in phase separation and glass transition temperatures of pNIPAAm accordingly [133,134]. Besides the studies on pure pNIPAAm, Nan et al., Prasannan et al., Chung et al., and Cao et al. [200–203] investigated its copolymers for possible drug delivery applications. Yang et al. [135], Huang et al. [136] and Zhi et al. [137] used analytical solution theories to model these thermo-sensitive hydrogels, but to be accurate, as discussed below, such models need inclusion of parameters obtained by molecular simulations. Solution theories have also been applied to understand and explain excipient-API interactions and their effect on API crystallization. Theoretical work in this area has mostly been limited to the use of Flory-Huggins models to predict excipient-API miscibility in the solid state

128

[204,205]. In these studies, solubility parameters of the drug and excipient, which is mainly found by experiments or group-contribution methods are used to find the Flory parameter (χ) which along with entropic terms are used to define the free energy of the API-excipient complex. Relative miscibility of different excipients and API is then predicted by Thermodynamic analysis. The major challenge of thermodynamic methods, in which excipient-API interaction is assessed using the Flory parameter (χ), is the unreliability of solubility parameter estimates. Molecular dynamics (MD) simulations can be a promising approach to determine these parameters and analyze the mixture, but unfortunately no such study is at hand for pNIPAAm solutions.

Recently, with advances in molecular dynamics techniques, it has become feasible to simulate pNIPAAm chains directly to test the ability of different forcefields to predict chain collapse and to determine the dynamics of binding kinetics between different functional groups and solvent. Walter et al. [138,206] performed simulations with three forcefields (GROMOS-87, GROMOS-96, OPLS-AA) combined with two water models (SPC/E, TIP4P) to find the right combination to account for the collapse transition of a single pNIPAAm chain, which they suggested is OPLS-AA+SPC/E. Tucker and Stevens [139] studied the polymer length dependence (over the range of 3-30mer) of the transition temperature for a single syndiotactic pNIPAAm oligomer, found higher LCST for shorter chains. Gangemi et al. [140] simulated a single chain of pNIPAAm doped with amino acid-based comonomers and compared the chain collapse parameters (e.g. radius of gyration) with those for pure NIPAAm. They showed that the presence of comonomers in the chain prevents the chain collapse upon heating above 315K. Based on the partition coefficient of a dimer model compound of pNIPAAm in a water/chloroform mixture, Katsumoto et al. [207], via molecular dynamics simulations, showed how isotacticity of a dimer reduces the hydrophilicity of pNIPAAm, in agreement with experimental results of Ray et al.

[133]. Du et al. [208] simulated the effect of added salts (NaCl, NaBr, NaI and KCl) on the LCST shift towards lower temperatures for a single chain, and Kamath et al. [209] compared the effect of popular forcefields (AMBER, OPLS-AA, GROMOS, CHARMM) on the enthalpy of hydration and of solvation of a pNIPAAm monomer in water. As they discussed, thermodynamic analysis of a single monomer may not be sufficient for forcefield comparison, since the coil-to-globule transition is the result of collective effect of adjacent pNIPAAm monomers.

As these experimental and computational studies suggest, the collapse of pNIPAAm is driven by the weakening of hydrogen bonding with water at elevated temperatures, namely above 32^OC, leading to dominance of the hydrophobic interactions between isopropyl groups in adjacent monomers [141,142]. Interestingly, this happens at a temperature close to the body temperature (37^oC), which, along with other properties of pNIPAAm, such as the large design space of its copolymers, makes this polymer a potentially attractive possibility as an excipient for controlled drug release. In addition, the hydrophobic isopropyl groups of pNIPAAm can interact with hydrophobic API molecules while its hydrophilic groups maintain interaction with water, thus inhibiting aggregation and crystallization of API molecules in the GI tract. Although aqueous solutions of pNIPAAm have been widely analyzed both experimentally and computationally, a detailed simulation study of excipient-API interactions in water and their effect on crystallization is not yet available for pNIPAAm. In particular the promising alternative of analyzing the interactions between polymer and API molecules by molecular dynamics has not yet been carried out for pNIPAAm and its copolymers in aqueous solutions.

In this study, we perform atomistic MD simulations of pNIPAAm oligomers and two of its copolymers, namely pNIPAAm-co-acrylamide (p(NIPAAm-co-Am)) and pNIPAAm-co-dimethylacrylamide (p(NIPAAm-co-DMA)) and study the formation of excipient-API complexes

130

which inhibit API aggregation and nucleation. Phenytoin, an anti-seizure drug with an aqueous solubility of 26 µg/mL, is chosen for our simulations [210]. Our simulations show that interactions of phenytoin with copolymers are consistent with experimental results showing that there is an optimal molar percent of co-monomer that maximizes the excipient efficiency at body temperature [144]. We can also provide a quantitative explanation of the physics behind the phenomenon. Although the length and time scales of our simulations are not high enough to be conclusive, they may provide a benchmarking scheme to rank excipients' relative efficiency for precipitation inhibition.

5.3 Computational Methods and Simulation Details

MD simulations are performed with the GROMACS simulation package [211,212] with AMBER99SB [213], a modified version of the general AMBER FF [214,215] capable of analyzing different chemical species including polymers and drugs. The TIP3P model is used for water. Model oligomers are constructed in the Materials Studio® software package by Accelrys® and the molecular model for phenytoin is obtained from the ZINC40 database. Figure 5.2 shows the 3-D representations of the polymer chains and phenytoin. Initial chain conformations used in simulations are available in supporting information.
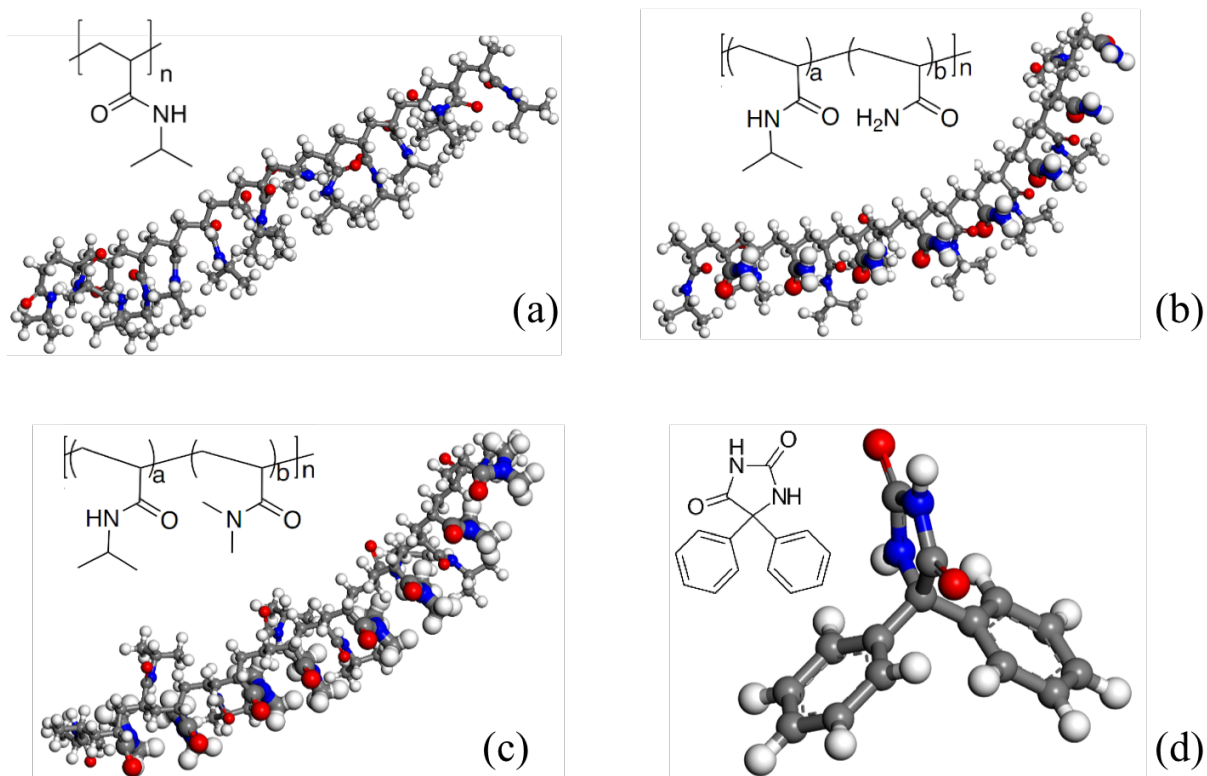
Figure 5.2. The chemical structures and 3-D representation of the polymer chains (a) PolyNIPAAm, (b) PolyNIPAAm-co-Acrylamide alternating copolymer, (c) PolyNIPAAm-co-Dimethylacrylamide alternating copolymer, and (d) phenytoin molecule. The polymer chains shown are 15 monomers long and the atoms of side chains of the comonomers of Am and DMA are magnified.

Synthesis of pNIPAAm via free radical polymerization leads to atactic chains. The isotactic and syndiotactic content can be tuned experimentally [216], and it is of interest to consider the effect of tacticity on the oligomer binding with drug molecules. We use atactic chains with roughly 58% syndiotactic and 42% isotactic bonds unless stated otherwise. A cubic simulation box and periodic boundary conditions are used in all simulations. Simulation box lengths are chosen to be comparable to the contour length of the oligomers to avoid periodicity artifacts. The box lengths vary from 5-10 nm for 5-26mer chains. The required numbers of polymer chains and API molecules to achieve certain weight percents are determined using the Amorphous Cell construction tool in Materials Studio. Except for single-chain simulations of pure pNIPAAm, we use 10 wt% excipient, 3.3wt% API and 86.7 wt% water. Species are placed randomly in the simulation box using GROMACS command tools. The initial density is close to the bulk density

of water, 1 g/cm^3. Figure 5.4 shows a sample of the initial simulation box (before a simulation run). All systems are first subjected to up to 20,000 steps of energy minimization using the steepest descent method. A 0.5 ns NVT equilibration followed by a 10ns NPT equilibration is conducted for each system using a time step of 1 fs. The production run is in an NPT ensemble, with a 1 fs time step and total run time of 70 $-$ 80 ns. Therefore, including the equilibration period, each run extends to 90 ns. A weak temperature coupling using a velocity-rescale thermostat with a coupling constant of 0.2 ps, and a weak pressure coupling using a Berendsen barostat with a coupling constant of 0.5 ps are used for these two equilibration runs. For the production runs, a Nosé-Hoover thermostat with a coupling constant of 0.5 ps and Parrinello-Rahman barostat with a coupling constant of 0.5 ps are employed for temperature and pressure coupling, respectively. Unless otherwise stated, the reference temperature and pressure are 298 K and 1 bar, respectively. A cut-off radius of 12 Å is adopted for nonbonded interactions and long-range electrostatics is handled by the Particle-Mesh Ewald (PME) method with dielectric constant set to be 61 for the water model. The LINCS algorithm constrains the bonds containing hydrogen atoms and the velocity-Verlet integration method is used. The neighbor lists are updated every 5 time steps in the equilibration runs and every 10 timesteps in the production runs.

Due to the importance of electrostatic potentials in pNIPAAm studies (hydrogen bonding and hydrophobic interactions), determination of partial charges is of great importance. To test the performance of different charge methods and make sure that the ab initio calculations can account for the physics of the transition, we test two commonly used quantum mechanical schemes, the Bond Charge Correction (BCC) [217] and the Restrained Electro-Static Potential (RESP) [218]. They use different quantum calculations to assign the charges and the resultant values are therefore different. BCC charges are calculated using the ACPYPE toolkit [215,219] and RESP charges are

obtained using Gaussian09 [220] at the RHF/6-31G* level. Moreover, to deal with the limitations of common methods for assigning partial charges for flexible pNIPAAm long chains (no. monomers ≥ 10; persistence length, $l_p > 3.3nm$) [221] and especially to deal with the computation cost, an averaging process is utilized. For both BCC and RESP methods, we use ensemble averaging of charge values. The process consists of the following steps. First, we assign partial charges to the model oligomers (outputs of Material Studio). Using these values, a simulation in water is initiated, run for $40ns$, and 10 different conformations are sampled randomly from the trajectory. Then, partial charges for these conformations are computed. This is applied for different chain lengths of $5 - 15$ monomers, and different chain tacticities (isotactic, syndiotactic and atactic chains).

Table 5.1. Averaged partial charges for atoms of pNIPAAm monomers along the chain using BCC and RESP charge methods and their standard deviations.

Atom	BCC	σ	RESP	σ
C	−0.137	0.0025	−0.404	0.0083
C1	0.660	0.0016	0.887	0.0042
N	−0.564	0.0028	−0.796	0.0071
C2	0.095	0.0013	0.621	0.0044
C3	−0.111	0.0003	−0.453	0.0023
C4	−0.111	0.0003	−0.453	0.0023
O	−0.634	0.0029	−0.637	0.0044
C5	−0.072	0.0014	−0.214	0.0034
H	0.041	0.0004	0.106	0.0006
H1	0.041	0.0004	0.106	0.0006
H2	0.041	0.0004	0.106	0.0006
H3	0.084	0.0009	−0.006	0.0010
H4	0.041	0.0004	0.106	0.0006

H5	0.041	0.0004	0.106	0.0006
H6	0.041	0.0004	0.106	0.0006
H7	0.321	0.0026	0.374	0.0033
H8	0.077	0.0041	0.162	0.0037
H9	0.064	0.0021	0.159	0.0037
H10	0.064	0.0021	0.159	0.0037
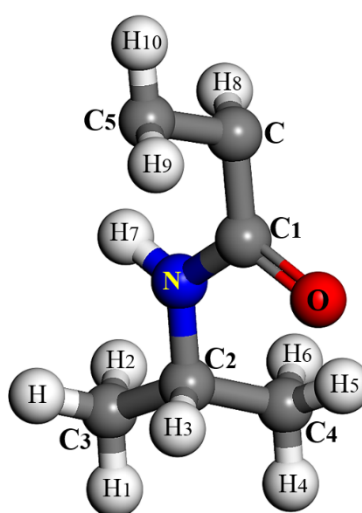
Figure 5.3. Labeling of pNIPAAm monomer atoms used in Table 1.

Then, we perform simple ensemble averaging over all the obtained set of charges for a specific atom to find the averaged value for the atom in the monomer. Note the averaging takes place over chains of all different lengths and tacticities to produce a single charge for a given atom. Using this approach we can account for the conformational dependence of charge values, especially for the RESP charges that have been shown to be more conformation dependent than the BCC ones [217]. The obtained averaged values and their standard deviations for both methods are shown in Table 5.1. The corresponding atoms are labeled in Figure 5.3. As will be discussed in results section, when using the BCC charge values, we cannot predict the collapse behavior of pNIPAAm.

Analysis tools of the GROMACS package are used to interpret the systems dynamics and all simulation snapshots are obtained by VMD [222] software. In the first part of the results section, which is related to the validation of the forcefield and partial charge method, the affinity of polymer chains for the environment (aqueous solution) is quantified by the radius of gyration of a single chain, which is calculated as follows:

$$R_g^2 = \frac{1}{2N^2} \sum_{i,j} (r_i - r_j)^2 \tag{5.1}$$

Here N represents the number of monomers and r_i, r_j are the positional vectors of each monomer. (R_g has been used in previous experimental and simulation studies to track the collapse of pNIPAAm chains upon heating.) To compare the distribution of API molecules around the polymer chains and measure API aggregation, Excipient-API and API-API radial distribution functions (RDFs) have been calculated. The excipient-API RDF is defined as the normalized probability of finding an atom of API molecule at a radial distance r from an atom of an excipient molecule. The API-API RDF on the other hand is defined as the normalized probability of finding an atom of an API molecule at a radial distance r from an atom of any other API molecule. The normalization of the RDF is performed with respect to the probability of finding a pair of atoms at a radial distance r in a hypothetical ideal gas at the same average density as in the simulated solution. The general formula to find the RDF is as follows:

$$g_{AB}(r) = \frac{\langle \rho_B(r) \rangle}{\langle \rho_B \rangle_{local}} = \frac{1}{\langle \rho_B \rangle_{local}} \frac{1}{N_A} \sum_{i \in A}^{N_A} \sum_{i \in B}^{N_B} \frac{\delta(r_{ij} - r)}{4\pi r^2} \tag{5.2}$$

Here $\langle \rho_B(r) \rangle$ is the particle density of type B at a distance r around a particle A, and $\langle \rho_B \rangle_{local}$ is the particle density of type B averaged over all atoms at a radial distance r_{max} (half of the box length) around particle A. r is the position vector. It should be noted that the RDF plots depicts the time-averaged values of distribution functions after apparent equilibration of the system.

A hydrogen bond between two atoms is defined as a donor-acceptor pair with center-of-mass distance within a threshold distance (0.35 nm) and a hydrogen-donor acceptor angle of less than 30 degrees. Here, we define the normalized number of hydrogen bonds N_H, to be the number of hydrogen bonds between excipient and some other species, divided by the total number of hydrogen donor/acceptor atoms of excipient molecules in the simulation box. The normalized "number of contacts" between excipient and API, $N_{ex,API}$, is calculated as follows. We take an atom of excipient and consider a sphere of radius 0.6 nm around it; then we count the number of atoms of API molecules within that sphere and count each of them as a "contact" between excipient and API. Then, we repeat this for the next atom of excipient and include as new "contacts" any atoms of API within the radius of 0.6 nm of this next excipient atom, even if some of those API atoms already are counted as contacts of previously counted excipient atoms. After going through all atoms of excipient, we add up all the counted contacts and normalize by the number of atoms of excipient molecules in the simulation box to give the normalized excipient-API contact number $N_{ex,API}$. Note that the number of atoms in an API molecule is 31 and the diameter of an API molecule is roughly 0.8nm.

In figures with standard errors, the error bars are calculated from a simulation run in the following way. First, we discard the early portion of the run, prior to equilibration. Then we number from 1 to N the remaining time steps in the run, and determine the mean, $\bar{x}$ and the standard

deviation of the quantity of interest over this series. To determine the number of statistically uncorrelated sampling points, we first define the autocorrelation function $r(k)$ as follows:

$$r(k) = \frac{\sum_{i=1}^{N-k}(x_i - \bar{x})(x_{i+k} - \bar{x})}{\sum_{i=1}^{N}(x_i - \bar{x})^2} \tag{5.3}$$

where x_i is the datum at time step i, k is the lag number, and therefore $k\Delta t$ is the autocorrelation time interval. Approximating $r(k)$ by an exponential function of k, we take the autocorrelation time step interval k_{corr} to be the value of k at which $r(k) = 1/e$. Dividing N by k_{corr} gives the effective number of sampling points, N_e. Finally, we divide standard deviation by the square root of N_e to give the standard error.
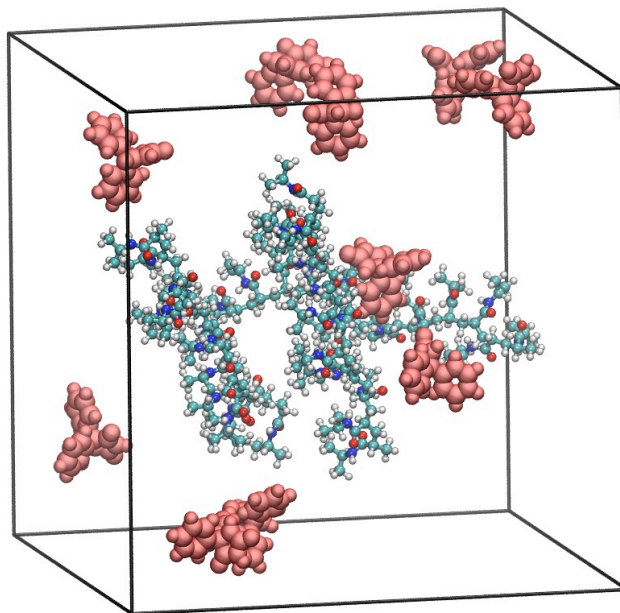
Figure 5.4. A sample simulation box including atactic polyNIPAAm chains (~10wt%) and Phenytoin molecules (~3.3wt%). API molecules are colored in red and shown in VDW format. Water molecules are left invisible.

Two different sets of copolymers are employed in this study, alternating (for both Am and DMA) and block copolymers (DMA only). First, the alternating copolymers are studied to see the effect of Am and DMA monomers in the chain. Then, tetra-block copolymers of NIPAAm and

DMA with different block lengths (shown in Table 5.2) are considered. Both of Am and DMA are hydrophilic and DMA has an LCST of around 50°C [223]. As stated before, except for the single chain simulations of pNIPAAm where we analyze the effect of tacticity, all other chains are atactic.

5.4   Results and Discussion

A step-by-step approach is used to study pNIPAAm and its interactions with drugs. First, a single chain of pNIPAAm is simulated in water at different temperatures to see whether the applied partial charge method and Forcefield can represent correctly pNIPAAm collapse or not. Next, the drug molecules are introduced to study the effect of the polymer on inhibition of drug aggregation and how the tacticity affects the polymer-API interactions at room temperature. In the next step, we examine the temperature dependence of pNIPAAm, pNIPAAm-co-Am, pNIPAAm-co-DMA conformations and interactions with drug molecules. In addition, we consider the influence of the molar percent of DMA in the block copolymer NIPAAm-co-DMA and compare our results with recent experimental result of Ting et al. [144].

5.4.1   Single Chain in Aqueous Solutions

First, to validate the forcefield and the implemented partial charge method, simulations are performed for a single chain in water. Figure 5.5 shows the evolution of the radius of gyration of a 20-mer atactic (42% isotactic, 58% Syndiotactic) pNIPAAm chain at two temperatures, T = 280K and T = 320K for the two charge schemes, BCC and RESP. (We note here that the persistence length l_p of pNIPAAm corresponds to 10 monomers. [221]) The first 20ns of the simulation contains large fluctuations and is therefore omitted. It can be seen that after the initial

fluctuations of the chain's dimensions, at higher temperature (T = 320K), the chain tends toward a collapsed conformation (as shown later in Figure 5.7) and the R_g values are much lower than at T = 280K for RESP partial charges (Figure 5.5(a)). However, with BCC partial charges (Figure 5.5(b)), we do not see the collapse. We have tried a higher temperature (T = 340K) for BCC but still no transition is observed. Using RESP charges, as the temperature is raised above the predicted experimental value of LCST, the chain decreases its exposed surface to the water from $\sim 27\text{nm}^2$ ($R_g = 1.2$ nm) to 23 nm^2 ($R_g = 0.8$nm) as shown by the plot of solvent accessible surface area (SASA) versus time in Figure 5.6. SASA has been computed using GROMACS command tool, which uses the double cubic lattice model [224].
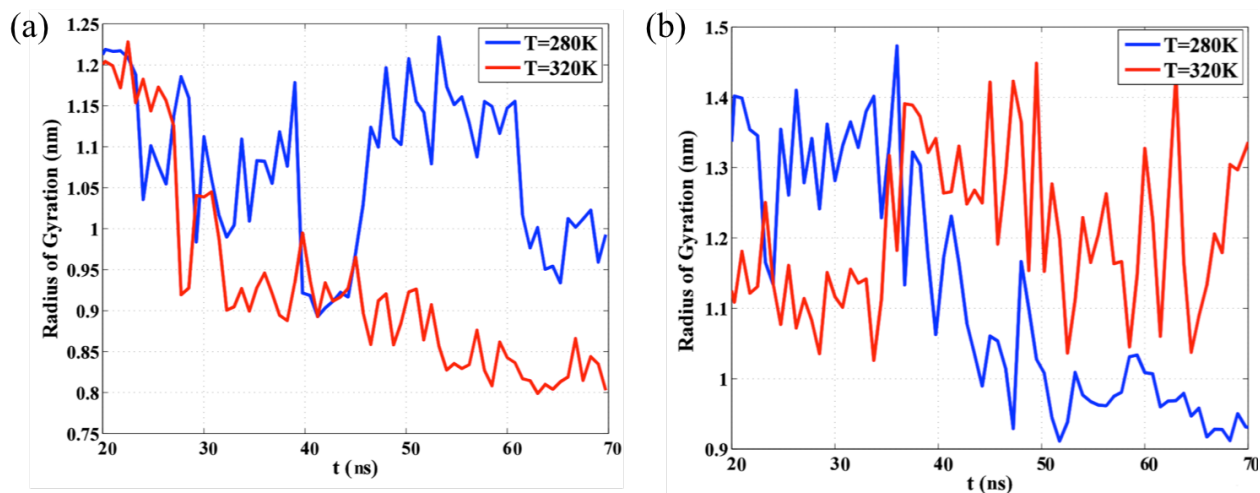
Figure 5.5. Evolution of radius of gyration for two partial charge schemes used in the simulation of an atactic 20-mer atactic pNIPAAm chain. (a) RESP (b) BCC.
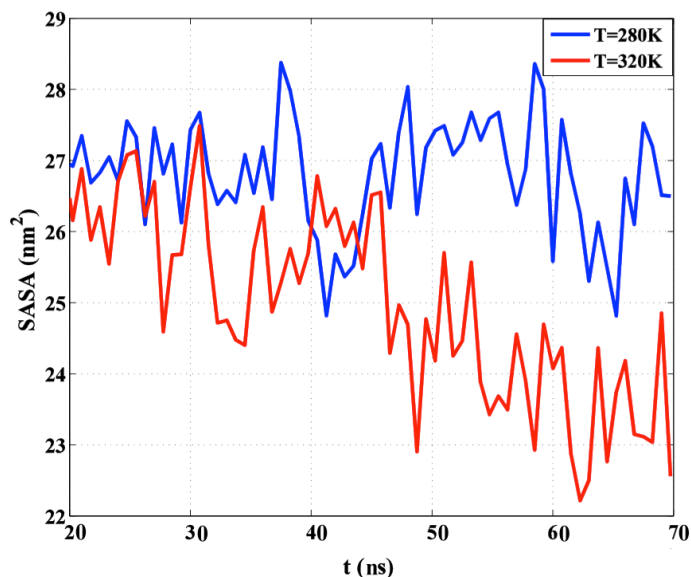
Figure 5.6. Solvent accessible surface area (SASA) of an atactic 20mer at 280K (below LCST) and 320K (above LCST). The radius of solvent probe is 0.14 nm. RESP charges has been used for this simulation.

We also perform simulations for temperatures over the range of $280 - 320K$ for a 26mer chain, matching the chain length simulated by Gangemi et al. [140]. Figure 5.7 shows the resulting temperature dependence of the average values of R_g. This graph is in very good agreement with both experimental data and previous simulation studies since it clearly shows the collapse of the single chain by increasing the temperature and it also predicts the LCST of pNIPAAm to be around $300 - 305$K. Short chains (10mers) are also simulated, and since these chains are one persistence length long, as expected, the collapse cannot be clearly seen due to the insufficient dihedral movements [139]. The number of hydrogen bonds between the polymer and solvent, given in Figure 5.8, shows a 35% drop with increase in temperature from 280 K to 320 K, and therefore a rise in hydrophobicity of the polymer; in agreement with previous studies [225]. These results clearly show that our parameters and methods can predict the coil-to-globule transformation of pNIPAAm. In the following, the same successful partial charge method (Solvated ensemble averaged RESP) and forcefield are applied.
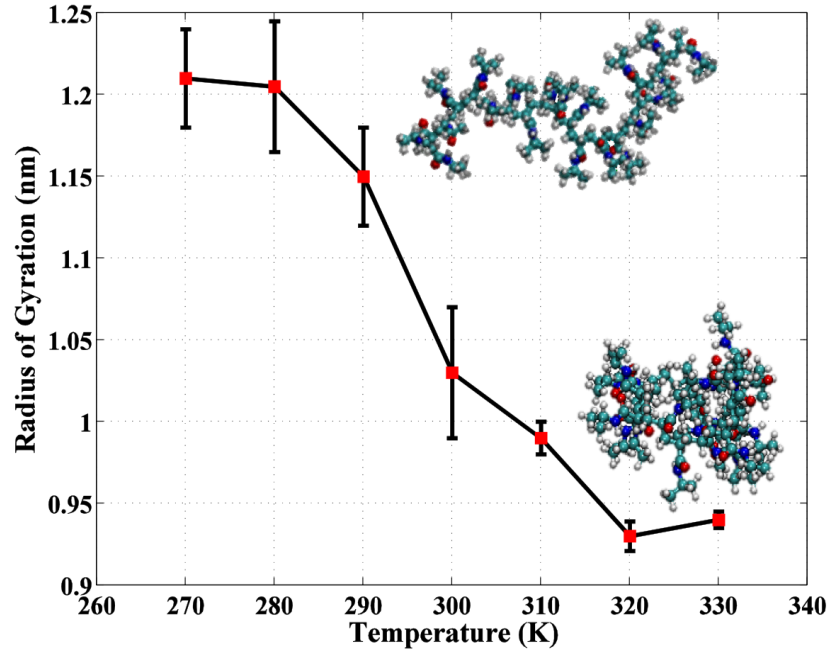
Figure 5.7. Radius of gyration of an atactic 26mer NIPAAm vs. temperature. Each run was performed for $85\,ns$ and the averaged values shown here are calculated after equilibration, namely $23 - 30\,ns$. Two chain conformations are shown representing the typical chain geometry below and above the LCST.

	T=280K	T=320K
N_H	1.25	0.81
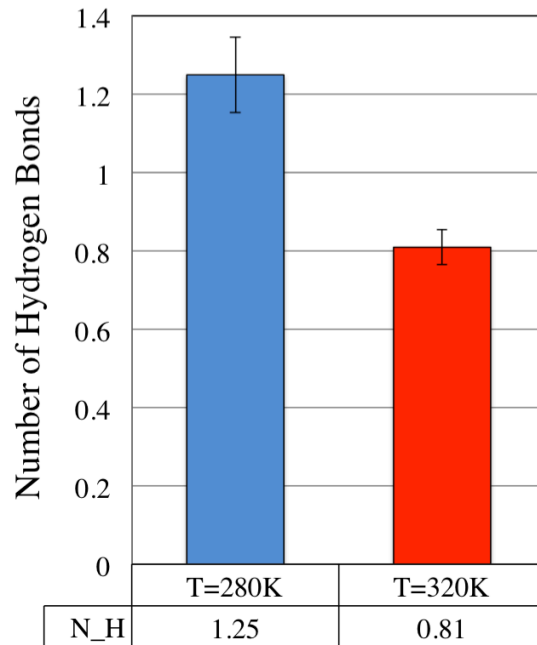
Figure 5.8. Normalized number of hydrogen bonds between polymer chain (26mer atactic) and water at $280K$ and $320K$.

5.4.2 Single Chain in Presence of Drug

Experimental studies have shown the importance of isotactic content on transition dynamics of pNIPAAm chains [133]. To analyze the effect of tacticity on pNIPAAm-API molecular interactions, single 15mer chains of pNIPAAm with molecular weight of $1.52 \frac{\text{kg}}{\text{mol}}$ and different tacticities are simulated in the presence of 10 API molecules of phenytoin (corresponding to 2.3wt% polymer and 6wt% API) at $T = 295$K. Figure 5.9 shows the behavior of the API molecules with and without the existence of an excipient chain in the simulation box. The excipient-API and API-API RDFs ($g(r)$) are shown in Figure 5.10(a)-(b). Without the excipient in the simulation box, API molecules tend to aggregate, as is shown in Figure 5.9(a)-(b) and give the highest API-API radial distribution function (RDF), $g(r)$. However, the presence of pNIPAAm inhibits their aggregation by making contact with hydrophilic and hydrophobic parts of phenytoin causing a ~35% drop in API-API $g(r)$ peak height from 10 to around 6.5. However, the magnitude of this inhibition of aggregation depends on the interaction sites that the excipient provides for the APIs. Syndiotactic chains, due to their ordered arrangement of functional groups on both sides of the backbone, provide more sterically accessible interaction sites. On the other hand, the isotactic chain has the fewest accessible sites because of its compact arrangement and one-sided display of side groups. In Figure 5.10, the syndiotactic chain gives the lowest API-API RDF and highest excipient-API RDF. For an aqueous solution of pNIPAAm, Ray et al. [133] showed that the higher the syndiotactic content, the higher the collapse transition temperature, indicating that increased isotacticity decreases the solubility because of the close packing of the functional groups. A similar trend is seen in the average number of contacts between polymer and drug, given in Figure 5.11. The error bars, which represent standard deviations, are relatively large

because of significant fluctuations due to the low molecular weight of the single polymer chain in the simulation box (~2.3 %wt).
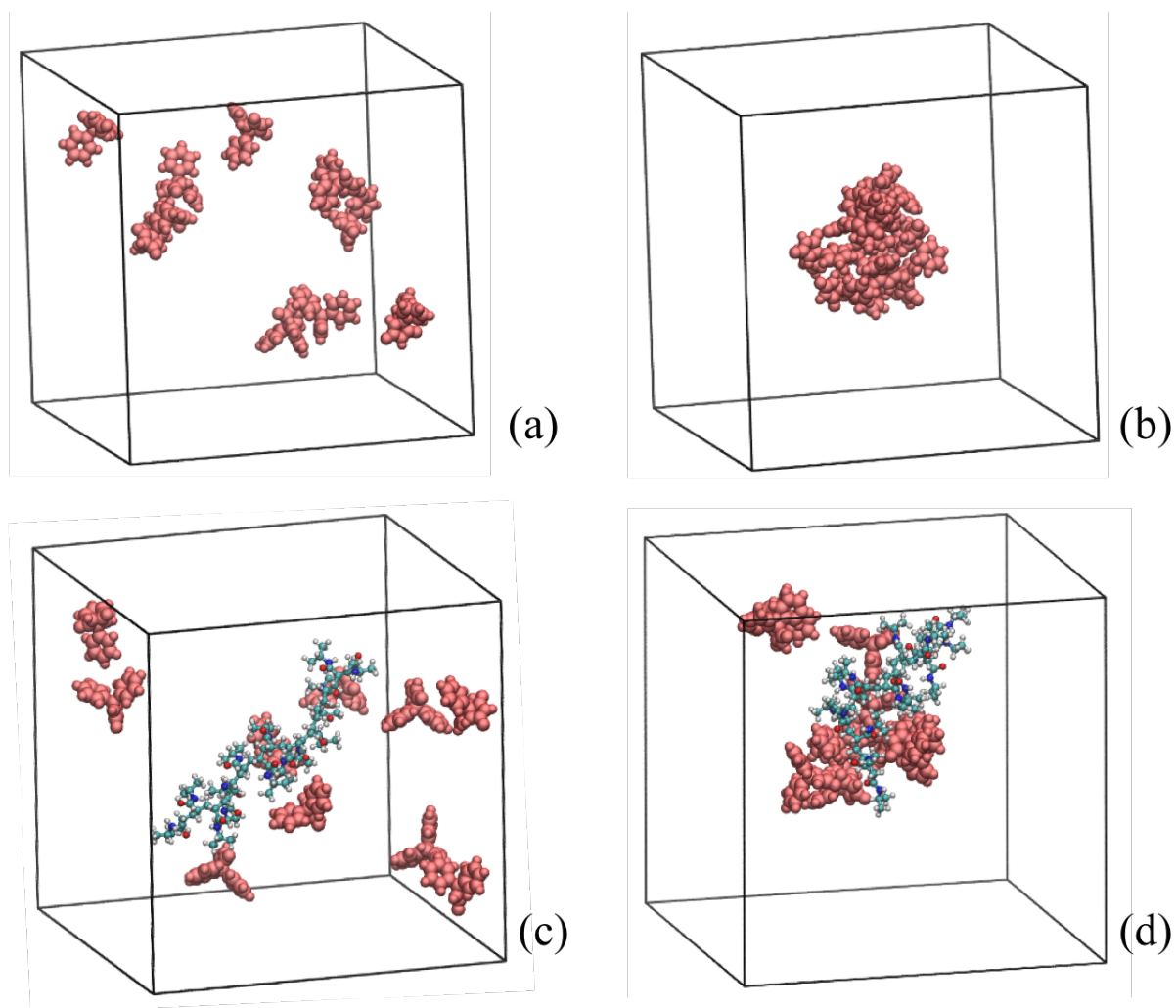
Figure 5.9. The evolution of (a-b) water-drug and (c-d) water-drug-excipient systems. Figures 5.9(a) and 5.9(c) show the initial random distributions of API molecules and 15-mer pNIPAAm in 5.9(c). 5.9(b) and 5.9(d) show these after 50ns of simulation at 298K. Water molecules are omitted from the images for clarity.
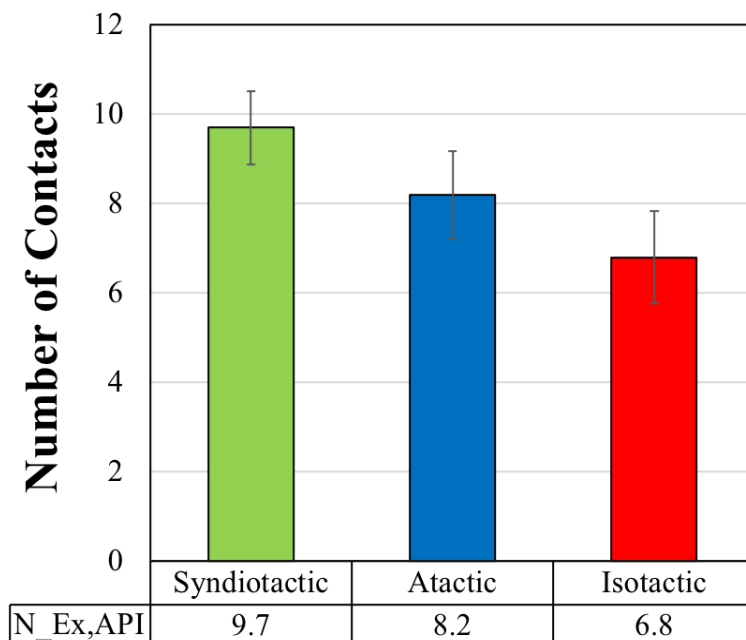
Figure 5.10. Average number of excipient-API contacts per excipient atom ($N_{Ex,API}$). The error bars are the standard deviations.

	Syndiotactic	Atactic	Isotactic
N_Ex,API	9.7	8.2	6.8

5.4.3 PNIPAAm and Copolymers

The next step is the simulation of multiple polymer chains, including homopolymer pNIPAAm and its copolymers in aqueous solutions to study their effect on API aggregation. For consistency with previous work [13], 3.3 wt% drug and 10wt% polymer is used in all cases, which results in 3-5 polymer chains (with 20 monomers) and 10-11 drug molecules, at body temperature $T = 310K$ and at $T = 295K$ which are respectively above and below the LCST of pNIPAAm. Both pNIPAAm-co-Am and pNIPAAm-co-DMA alternating block copolymers are simulated. We also study the block copolymers of pNIPAAm-co-DMA with different molar fractions of DMA content, a topic inspired by the results of Ting et al. [144]. Figure 5.2 depicts the structures of the different copolymers.

Table 5.2. Molar fraction of Am and DMA comonomers in copolymers used in simulations. a: number of monomers in NIPAAm block and b: number of monomers in DMA block.

Alternating Copolymers		Index numbering in figure 2
NIPAAm (isopropylacrylamide)	Am (Acrylamide)	
0.5	0.5	$a = 1, b = 1$
NIPAAm (isopropylacrylamide)	DMA (Dimethylacrylamide)	
0.5	0.5	$a = 1, b = 1$
Tetrablock Copolymers		
NIPAAm (isopropylacrylamide)	DMA (Dimethylacrylamide)	
0.9	0.1	$a = 9, b = 1$
0.8	0.2	$a = 8, b = 2$
0.7	0.3	$a = 7, b = 3$
0.5	0.5	$a = 5, b = 5$
0.3	0.7	$a = 3, b = 7$

As the number of polymer chains in the simulation box increases, the drug molecules are more likely to become trapped in the network formed by excipient macromolecules. Compared with single chain simulations, the multi-chain system reaches a steady, apparent equilibration, state much faster.

Different chain lengths (10, 15, 20mer) for each pure pNIPAAm and copolymer are tested to see the effect of chain length on excipient-API RDF, where the peak height is taken as a measure of the affinity of the excipient to interact with drug. The simulations are repeated with different random initial positions of API molecules and polymer chains. The first set of data is for pNIPAAm, pNIPAAm-co-Am and pNIPAAm-co-DMA alternating copolymer ($a = b = 1$ in Figure 5.2). Data are gathered after the system has reached apparent equilibrium, which we take to be the time, namely $25\ ns$, at which the number of excipient-API contacts reaches approximately a constant value (Figure 5.12). Figure 5.13(a)-(b) shows polymer-API RDFs for the alternating copolymers and for pure pNIPAAm chains at 295K and 310K for 20mers.
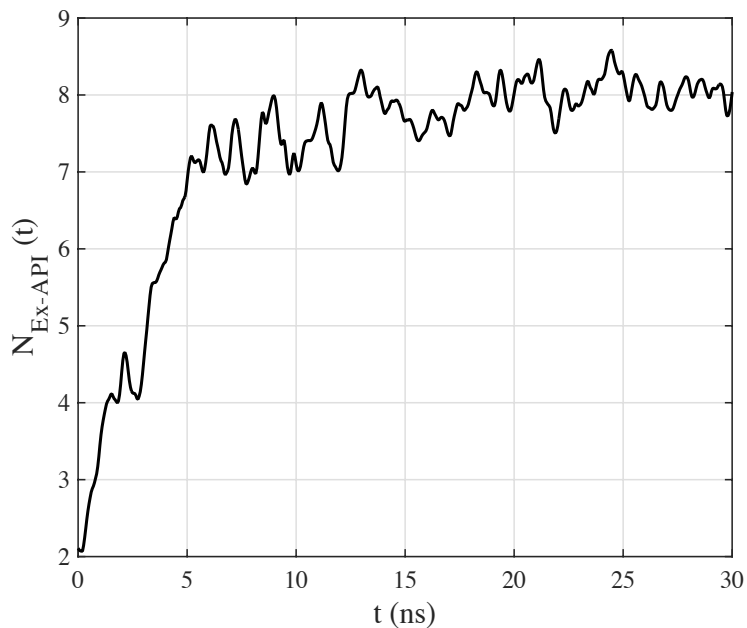
Figure 5.11. Number of contacts between pNIPAAm and phenytoin normalized by the number of pNIPAAm atoms, as defined in the methods section. The sample includes three 20mer atactic pNIPAAm chains and 10 drug moleucles.

For 20mer excipients, the homopolymer pNIPAAm chain has the highest excipient-API RDF peak at room temperature (~4.65); however, as the temperature reaches body temperature, which is above its LCST, the RDF peak drops by almost 22%. The normalized average number of contacts between excipient and API molecules per excipient atom drops from 9.1 to 7.6, and the number of hydrogen bonds between excipient and API molecules per donor or acceptor hydrogen bonding site on the excipient also drops from 0.09 to 0.07. Compared with the single chain simulations, the number of contacts increases with more chains in the simulation box, as expected. We generally expect a decrease in the number of hydrogen bonds as temperature increases [225] and the system passes through the coil-to-globule transition temperature of pNIPAAm. The chains' average R_g values as functions of temperature are depicted in Figure 5.13(e). At 310K the chains on average become more compact and reduce their contacts with surrounding water and API molecules, while at T = 295K, the radius of gyration fluctuates around higher average values. For copolymers, as shown in Figure 5.13(c), the number of hydrogen bonds decreases as temperature

increases, just as is the case for homopolymer pNIPAAm. As discussed before, Am is highly hydrophilic and has the same number of hydrogen donor and acceptor as NIPAAm and therefore the drop in N_H with increasing temperature is similar to that seen in NIPAAm.

Interestingly, pNIPAAm-co-DMA has more contacts with phenytoin molecules (N_{Ex-API}) at $310K$ than at $295K$; see Figure 5.13(d). It has been shown experimentally that pDMA polymers have a higher collapse transition temperature ($\sim48^\circ$C) than does pNIPAAm [223], since the functional groups of DMA are more hydrophilic than for NIPAAm. Therefore, adding DMA co-monomers reduces the number of hydrophobic sites that phenyl groups on phenytoin might interact with. DMA also lacks the highly polarized ($\delta^{-0.796}$) N-H ($\delta^{+0.374}$) bond present on NIPAAm that can interact with the charged ring of phenytoin. Thus, it seems initially puzzling that at body temperature DMA co-monomer would increase the peak in the API-excipient RDF by ~15% relative to pNIPAAm, as shown in Figure 5.13(b).

Experimental dissolution studies suggest that NIPAAm-co-DMA excipients improve interactions with API relative to NIPAAm excipients over a longer time scale (3 hours) while Am homopolymer can only maintain drug concentration for a limited amount of time (30 minutes) [144]. A possible explanation for both the increased RDF peak and the improved experimental API-polymer interactions seen in the copolymer relative to the homopolymer is suggested by comparing the R_g for the DMA copolymer in Figure 5.13(e) with that for the pNIPAAm homopolymer, in both cases obtained by averaging after $20\ ns$ of equilibration. At $T = 310K$, pNIPAAm chains have low (~0.9 nm) R_g while in the pNIPAAm-co-DMA copolymers chains are more extended at this temperature. This shows that the presence of DMA monomers raises the R_g values at body temperature, keeping the chain extended, thus presumably improving the steric

availability of binding sites for API molecules. pNIPAAm-co-Am copolymer shows the same trend in its R_g as well but as the experiments suggest, pNIPAAm-co-Am cannot hold its interaction with drug molecules for long compared to pNIPAAm-co-DMA. In other words, reducing the number of hydrophobic interactions within the polymer by addition of DMA co-monomers helps prevent the collapse of the chains at elevated temperature, but, presumably, at the cost of lower hydrophobic functionality, and consequently weaker interaction with phenytoin. To confirm this statement, in addition to the radius of gyration data in Figure 5.13(e), we perform single chain simulations to see how the existence of DMA comonomers affects the dimensions of the excipient chain as a function of temperature. The radius of gyration for a pNIPAAm homopolymer at the two temperatures $T = 280K$ and $T = 320K$ has been shown in Figure 5.5(a). We add the data for a single 20mer alternating copolymer chain of pNIPAAm-co-DMA, in Figure 5.14(a). As we can see, the radius of gyration of the copolymer shows no collapse at elevated temperature, unlike the behavior of the pNIPAAm homopolymer. We conclude that the presence of bulky DMA comonomers interferes with the interaction of hydrophobic groups of the remaining NIPAAm monomers with each other and consequently inhibits the coil-to-globule transition. Therefore, LCST property of pure pNIPAAm chains will be interrupted at this range of temperature and length scale, it acts like ordinary polymer chains.

Furthermore, to compare the ability of NIPAAm and DMA monomers to interact with API, we show in Figure 5.14(b)-(c), the excipient-API RDF, and the average number of contacts of syndiotactic 15mers of homo-pNIPAAm and of homo-pDMA with drug molecules at $295K$. Both plots show a weaker affinity of phenytoin drug molecules for pDMA than for pNIPAAm. Both chains are simulated at $T = 295K$, below the LCST of both pNIPAAm and of pDMA, so that both chains are in their extended conformations. NIPAAm itself has both hydrogen bonding and

hydrophobic binding sites with API molecules. DMA, on the other hand, has only one hydrogen bond acceptor, alongside weaker hydrophobic group compared to the isopropyl group in pNIPAAm.

Thus, adding DMA comonomers will reduce the affinity of API molecules for the excipient. On the other hand, DMA comonomers will prevent the collapse of pure pNIPAAm chains and consequently, provide more surface area for excipient-API interactions at $T = 310K$. Therefore, there should be a balance between maintaining both polymer chain extension and functionality of monomers, and DMA comonomer content can be tuned to achieve this balance.
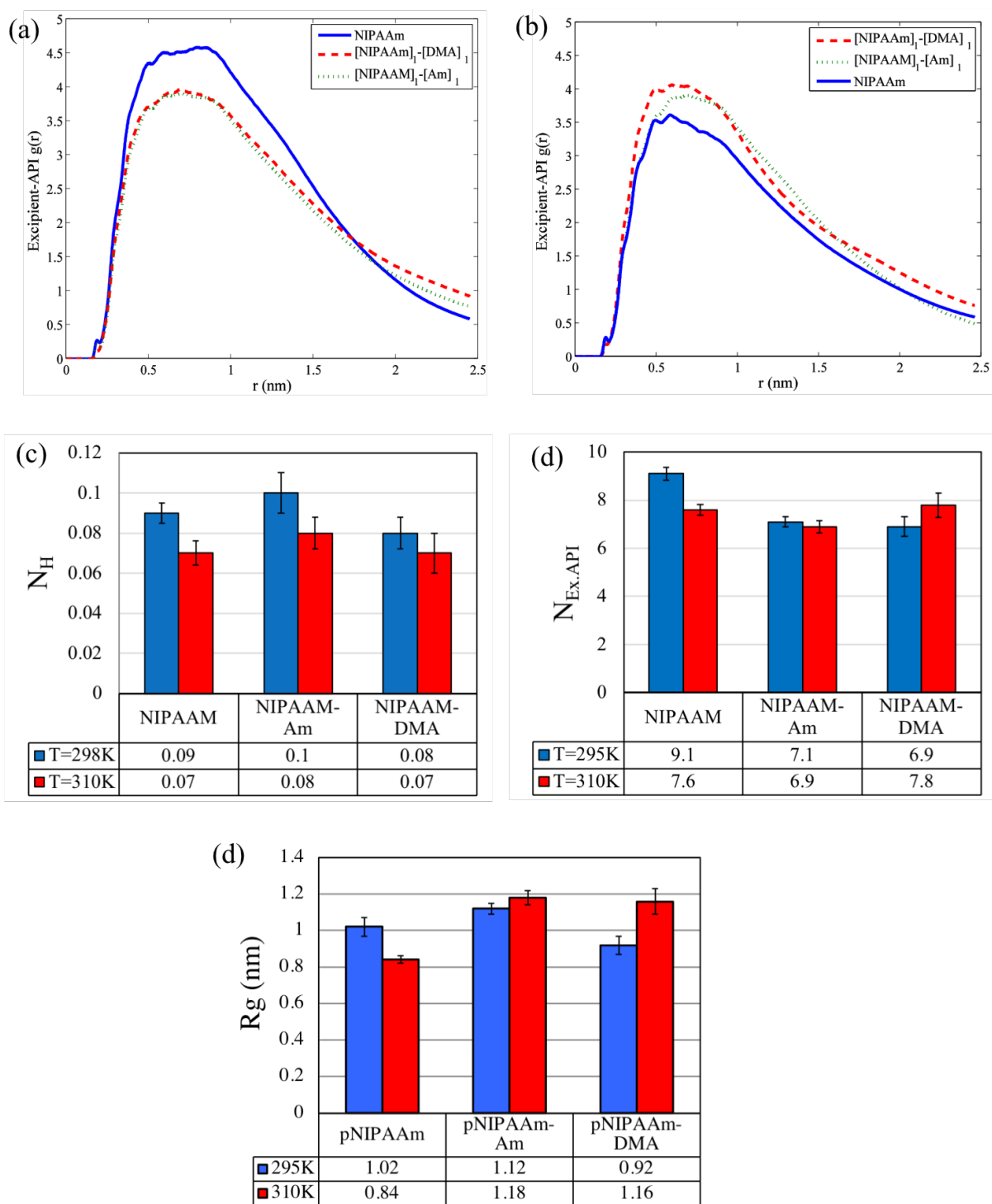
Figure 5.12. Simulation data for alternating copolymers of pNIPAAm 20mers with Am and DMA. (a) Excipient-API RDF at (a) $T = 295K$ and (b) $T = 310K$. (c) Number of hydrogen bonds per donor or acceptor hydrogen bonding site on the excipient and (d) number of contacts between polymer chains and API molecules per excipient atom. (e) Average radius of gyration of polymer chains. The error bars show standard errors.
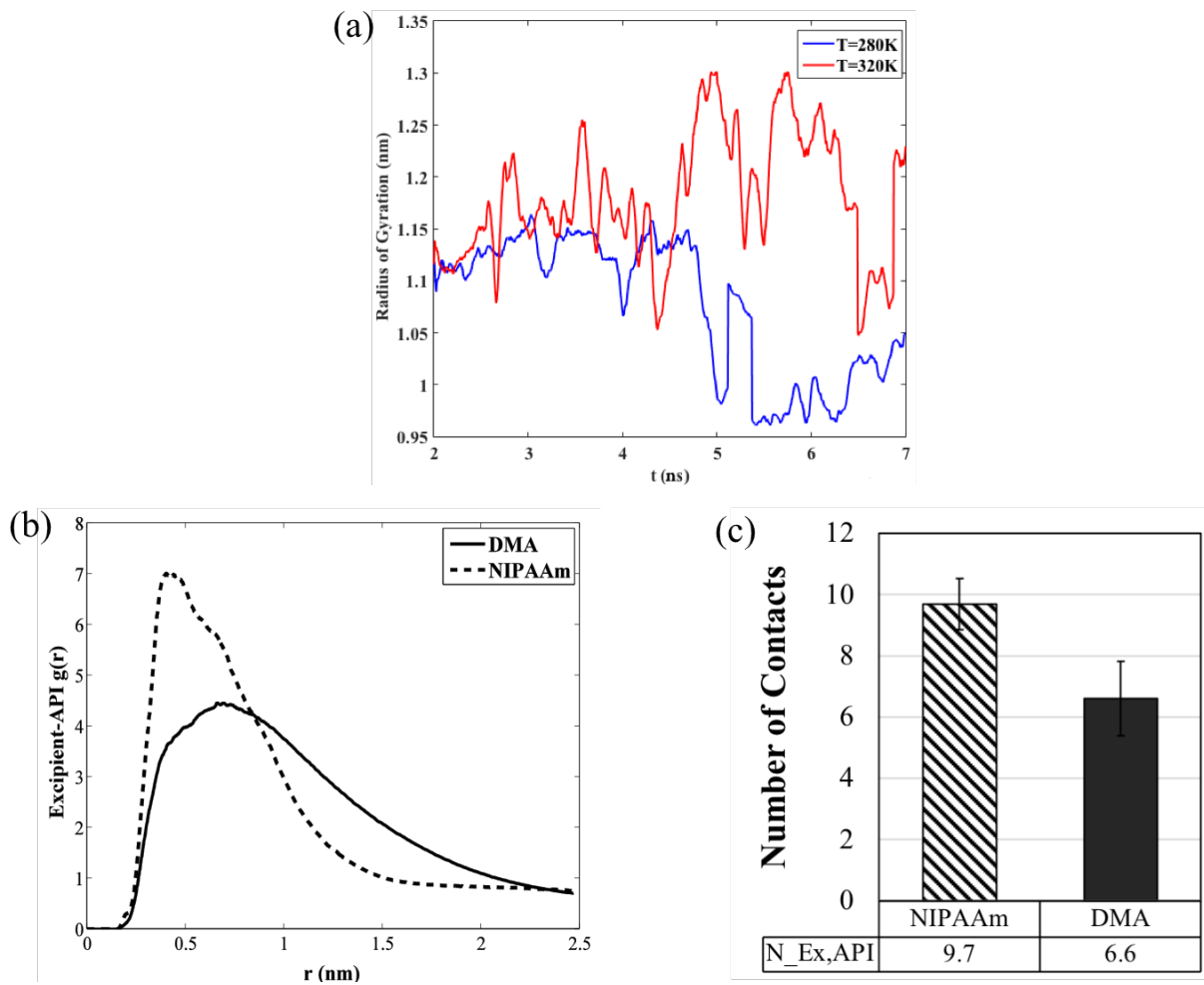
Figure 5.13. (a) Radius of gyration of pNIPAAm-co-DMA 20mer alternating copolymer (b) Excipient-API RDF and (c) averaged normalized number of contacts per excipient atom for one 15-mer syndiotactic pNIPAAm and one pDMA. There are 10 API molecules in the box at $T = 295K$. Error bars show standard deviations.

To study this balance in more detail, we perform simulations with different molar percentages of DMA, changing a and b in Figure 5.2 to achieve the molar fractions in Table 5.2 within a 20mer tetrablock copolymer at $310K$, and plot in Figure 5.15 the excipient-API and API-API RDF peak heights against copolymer composition. (The concentrations of polymer and drugs are kept at 10wt% Excipient-3.3wt% API by adjusting the number of molecules in the box.) Figure 5.15 clearly shows an optimum, or maximum in the excipient-API RDF peak height, in the range of $70 - 80$ molar fraction of NIPAAm. The maximum peak height (4.66) exceeds that for the alternating copolymer (4.09), in Figure 5.13(b), showing that that block copolymer with optimized

152

co-monomer content interacts more strongly with API molecules than does an alternating copolymer. Figure 5.16 shows the evolution of the system as a function of time for 20mer chain with phenytoin molecules, starting from random positions and into a cluster.
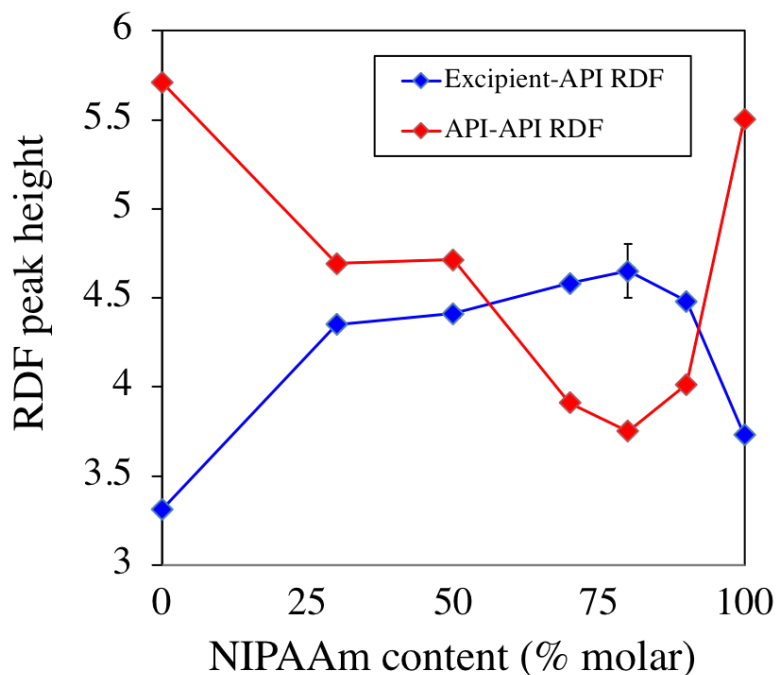
Figure 5.14. The peak heights of excipient-API (blue line) and API-API (red line) RDF for block copolymers of pNIPAAm (with different molar fractions) with DMA at $T = 310K$.

Finally, Figure 5.16 shows the effect of chain length on excipient-API interactions at two temperatures at fixed molar composition. For the shorter 10mer, the decrease in the peak height of the RDF is much less than for the 20mer, most likely because the 10mer is too short to collapse. This is related to the effect of chain length on globule transition of pNIPAAm studied by Tucker er al. [139] which showed that shorter chains (no. monomers < 11) only collapse at higher temperatures than are needed for regular longer-chain pNIPAAm LCST to collapse.
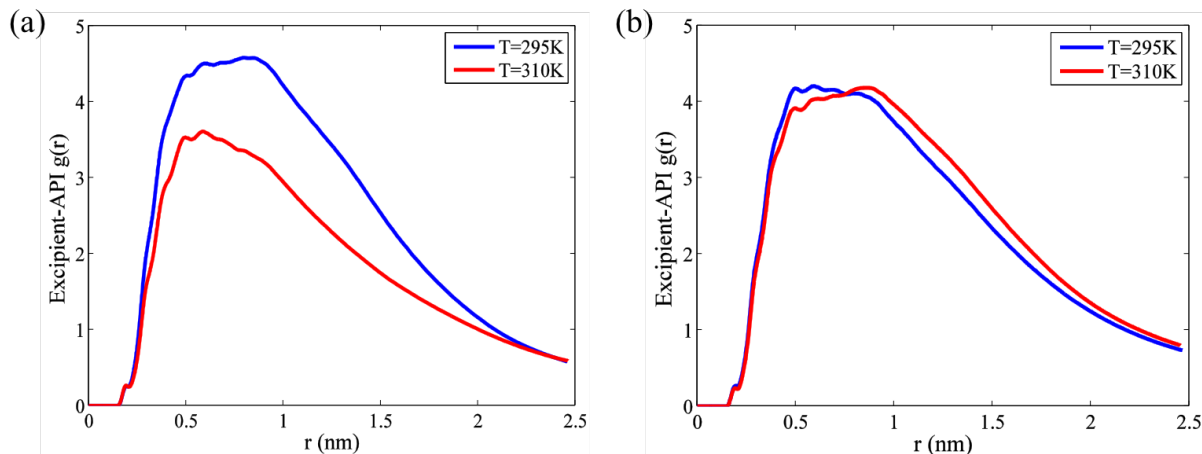
Figure 5.15. Excipient-API RDF for (a) 20mers and (b) 10mers of homo-pNIPAAm below and above the LCST.

The above results on copolymerization are in good agreement with experimental results [144]. They found in dissolution tests that 70%NIPAAm-30%DMA (% molar fraction) is the most efficient excipient in maintaining drug concentration in dissolution tests. Our model also predicts that low molecular weight (short) chains should be more efficient in binding with hydrophobic drug molecules, and eventually provide more prolonged solubility of API in solutions at body temperature compared to high molecular weight (long) chains, Figure 5.16.

Although this agreement is encouraging, possible differences due in part to the much longer chains ($l \gg l_p$) and much longer time scales used in the experiments relative to the simulations of course cannot be ruled out. The exploration of additional effects beyond those explored here would require simulations with $n > 50$ monomers and longer simulation times.
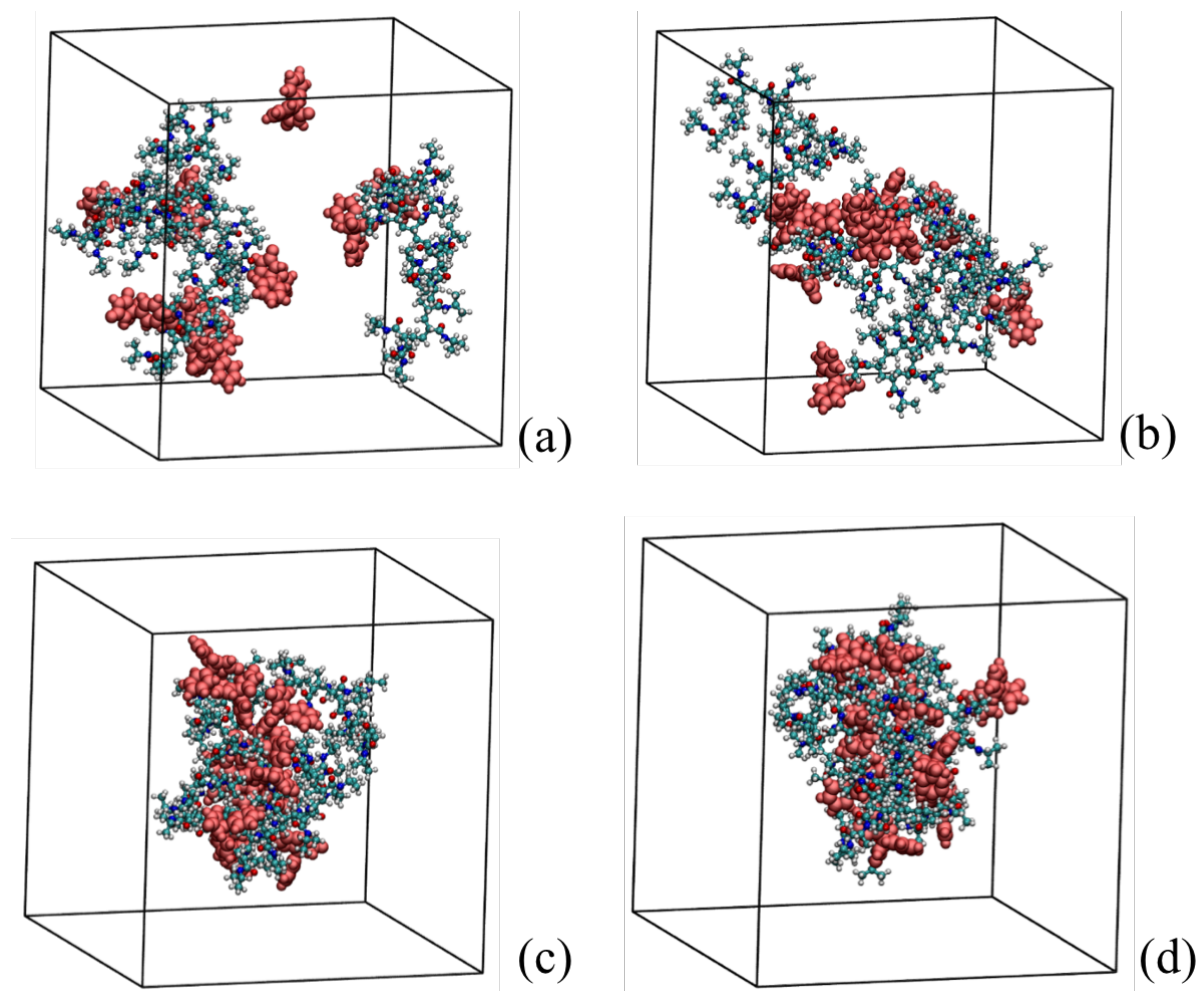
Figure 5.16. Evolution of polymer-API complex from initial state after energy minimization (a) to configuration after (b) $20 ns$ (c) $40\ ns$ (d) $60\ ns$. Comparing Figure 5.9(b) with 5.9(d), it is evident that the presence of polymer chains and their interactions with functional groups of phenytoin prevents API aggregation.

5.5   Conclusions and Future Directions

This study explores for the first time the molecular interactions between the thermo-sensitive biocompatible polymer of N-isopropyl acrylamide, (NIPAAm), and its copolymers with acrylamide (Am) and dimethylacrylamide (DMA) with phenytoin, a representative poorly soluble active pharmaceutical ingredient (API) in an aqueous solution.

The effects of chain length, tacticity, and comonomer content were investigated. Our simulations show that excipients complex with the API resulting in an inhibition of API

aggregation, as revealed by radial distribution functions between API and polymer. Short 20mer tetrablock copolymers of NIPAAm and DMA with around 20-30 molar percent of DMA increase this inhibition dramatically based on tuning the number of hydrophobic interactions to avoid coil collapse while maintaining enough hydrophobic groups to bind the API. These results, including an optimal DMA composition of around 20 mole percent, correlate nicely with the experimental results for the dissolution and release of solid dispersions of this API with NIPAAm-co-DMA polymers in experimental dissolution tests. Both simulations and experiments thus show that copolymers of NIPAAm with more hydrophilic monomers at optimized co-monomer composition perform better as excipients and help maintain highly supersaturated concentrations of APIs in water without aggregation, which could result in higher API absorption in the intestine.

At room temperature, due to hydrophobic attraction between isopropyl groups of excipient and phenyl rings of phenytoin, along with chain extension of pure pNIPAAm, it has stronger binding to APIs than do the copolymers. However, as the temperature increases and reaches body temperature, which is above the lower critical solution temperature, its interactions with API drops dramatically since it tends to make more compact conformations and reduce its contact with the environment. With the introduction of more hydrophilic comonomers into the chain, the number of potential hydrophobic interactions with API molecules decreases but avoidance of the collapse of the radius of gyration apparently helps maintain interactions between polymer and drug. A short pNIPAAm chain of 10 monomers shows a lower drop in excipient-API RDF between these two temperatures presumably because such short chains are too rigid to collapse easily and their LCST is much higher than body temperature. Thus, to achieve the best pNIPAAm-based excipient for inhibition of drug aggregation, for chains longer than the persistence length, a balance is needed between the LCST and the hydrophobicity of the comonomers.

Although the simulation results are promising, the length and time scales reachable by atomistic simulations are not sufficient to observe rare nucleation events and crystal growth nor the effect of polymer on these processes. Furthermore, even though our results clearly show the collapse of single chains in aqueous solutions as temperature increases above the LCST, to understand the dynamics of gels, which are composed of a complex network of these chains, we would need to simulate chains containing hundreds of monomers, which is far beyond the capability of atomistic simulations, and would require the development of coarse-grained models of both polymer and drug, perhaps also using implicit solvent to increase simulation time/length scale. With such a coarse-grained model, one might also study the diffusion of APIs in detail. Our atomistic simulation data are thus not only valuable in their own right, but could be used to build coarse-grained models that might reach the larger length and time scales at which additional information can be gather and better connections made with experimental studies.

Chapter 6 : Conclusions

In this thesis, I studied the unraveling dynamics of entangled polymer liquids, including polymer melts, entangled solutions and polymeric glass. For polymer melts and solutions, conventional tube theories assume that in strong extensional flows, as soon as the chain become locally fully stretched, at level of entanglement spacing, the entanglement network deforms affinely and the stress becomes fully saturated even if the chain is still in a folded state. This assumption results in a sudden rise in extensional stress, and viscosity, around Hencky strain of 3. We showed that even if the chain is fully stretched but still folded at some fold points, or kinks, the stress takes much smaller values than that predicted by the tube theory. Instead, beyond Hencky strain of 3, the unraveling dynamics at these fold points will dominate the entangled system. I developed a multiple-chain simulation technique to study the unraveling dynamics of an entangled system of linear chains at asymptotically high extension rates. By mutually entangling polymer chains, in a one-dimensional simulation box, at their fold points and requiring that the force and velocities of shared kinks are identical, we solve the tension equations of all chains, where Brownian motion is neglected, due to its much smaller values compared to drag and tension. However, to apply the kink dynamics to real polymer systems, such as Polystyrene samples shown in chapter 2, we need to know the chain statistics in an entangled system at high strains. Therefore, we develop a simple single chain slip-spring simulation method to study the evolution of a polymer chain in an entangled domain from equilibrium state to the kinked conformation. Single chain slip-spring model simply replaces the effect of entanglement network by a certain number of springs along the contour length of a bead-spring polymer chain. In developing the single chain method

158

for fast flows, we use some of the results of our kink dynamics analysis to mitigate the high

tensions generated due to affine motion of anchoring points of slip-springs. Finally, we compare

the predictions of kink dynamics with experimental data of Polystyrene samples at high extension

rates and show the much better agreement of the entangled kink dynamics technique compared to

the tube model's predictions. Therefore, by implementing a multi-scale scheme, we studied the

unraveling dynamics in an entangled system and the need for its implementation in theory to

achieve a quantitative agreement with experimental data. Inclusion of unraveling dynamics in tube

theory can result in a modified expression for the maximum tube stretch, λ_{max}, which in the current

version, is a constant and determined by the entanglement density of the network at equilibrium

state.

As another polymer liquid of importance, we analyzed the effect of kinks and locally highly

stretched strands on the stress and conformation evolution of polymer chains in polymeric glass.

Using a modified hybrid model and molecular dynamics simulations, we show that the underlying

physics behind strain hardening in loosely crosslinked polymer glasses is not the entanglement

network. The combination of HBD and MD simulations results offer a clear picture explaining the

large magnitude of glassy-polymer strain-hardening: hardening in the glassy state arises primarily

from chain stretching and orientation at scales well below that of the entanglement network. This

improved understanding, should help in the design of deformation and temperature protocols that

maximize properties of polymeric glasses for improved product performance. For pre-yield

regime, a modification of segmental dynamics is implemented into the previously established one-

mode model. Using stretched exponential concept and experimental values of β and τ_{prb}^r, we

developed a multi-mode relaxation dynamic for polymeric glass, which is important at low strains

in extension startup. The very good agreement between MD and our modified HBD show the

capability of our simple HBD technique to predict the whole regime, pre-yield and post-yield, of polymeric glass deformation.

For the last part of this thesis, we investigate the design of thermo-responsive polymer excipient at atomistic levels in aqueous solutions. Due to the biocompatibility and LCST response of Poly(N-isopropylacrylamide) at 32°C, it has become one of the most studied polymers for drug delivery applications. However, there has been no quantitative, systematic study on the pNIPAAm structure effect on its interaction with hydrophobic drug molecules. Therefore, using atomistic molecular dynamics simulations and close collaborations with experimentalists at university of Minnesota, we study the effects of tacticity and co-polymerization on the molecular level interactions of pNIPAAm with hydrophobic Phenytoin. We showed that block co-polymerization of pNIPAAm with a hydrophilic polymer such as poly(Dimethylacrylamide) improves its interaction with hydrophobic drug molecules in aqueous solution at body temperature, despite the fact that pDMA has weaker interaction with Phenytoin. In fact, the existence of hydrophilic functional groups between the amphiphilic functional groups of pNIPAAm, prevents the chains from collapsing at high temperatures, but at the same time decreases the interactions of copolymerized chain with neighboring drug molecules. Therefore, by studying different molar fractions of pNIPAAm and pDMA in the chain, we find a sweet spot for molar fraction of each component that gives us the highest affinity between polymer chain and drug molecule. Although the simulation results are promising, the length and time scales reachable by atomistic simulations are not sufficient to observe nucleation events, crystal growth and specifically the effect of polymer on these processes. However, as mentioned previously, output data of atomistic simulations can lead to efficient coarse-grained models. Therefore, our atomistic simulation data are thus not only valuable in their own right, but could be used to build coarse-grained models that might reach the

larger length and time scales at which additional information can be gathered and better connections be made with experimental studies

Bibliography

1. Luo, Z.; Zhang, L.; Jiang, J. Atomistic insight into micro-phase separation and gas diffusion in PEO–PBT multiblock copolymers. *Mol. Simul.* **2013**, *39*, 902–907.

2. Sengupta, S.; Pant, R.; Komarov, P.; Venkatnathan, A.; Lyulin, A. V Atomistic simulation study of the hydrated structure and transport dynamics of a novel multi acid side chain polyelectrolyte membrane. *Int. J. Hydrogen Energy* **2017**, *42*, 27254–27268.

3. Kyrychenko, A.; Korsun, O.M.; Gubin, I.I.; Kovalenko, S.M.; Kalugin, O.N. Atomistic Simulations of Coating of Silver Nanoparticles with Poly(vinylpyrrolidone) Oligomers: Effect of Oligomer Chain Length. *J. Phys. Chem. C* **2015**, *119*, 7888–7899.

4. Maiti, A.; Gee, R.H.; Bastea, S.; Fried, L.E. Phase separation in H2O:N2 mixture: Molecular dynamics simulations using atomistic force fields. *J. Chem. Phys.* **2007**, *126*, 44510.

5. Sethuraman, V.; Mogurampelly, S.; Ganesan, V. Multiscale Simulations of Lamellar PS–PEO Block Copolymers Doped with LiPF6 Ions. *Macromolecules* **2017**, *50*, 4542–4554.

6. Wu, R.; Qiu, X.; Zhang, T.; Fu, K.; Yang, X. Atomistic Molecular Insight into the Time Dependence of Polymer Glass Transition. *J. Phys. Chem. B* **2015**, *119*, 9959–9969.

7. Moghadam, S.; Larson, R.G. Assessing the efficacy of poly(N-isopropylacrylamide) for drug delivery applications using molecular dynamics simulations. *Mol. Pharm.* **2017**, *14*.

8. Luo, Z.; Jiang, J. Molecular dynamics and dissipative particle dynamics simulations for the miscibility of poly(ethylene oxide)/poly(vinyl chloride) blends. *Polymer (Guildf).* **2010**, *51*, 291–299.

9. Hung, J.-H.; Patra, T.K.; Meenakshisundaram, V.; Mangalara, J.H.; Simmons, D.S. Universal localization transition accompanying glass formation: insights from efficient molecular dynamics simulations of diverse supercooled liquids. *Soft Matter* **2019**, *15*, 1223–1242.

10. Ganesan, V.; Jayaraman, A. Theory and simulation studies of effective interactions, phase behavior and morphology in polymer nanocomposites. *Soft Matter* **2014**, *10*, 13–38.

11. Turci, F.; Royall, C.P.; Speck, T. Nonequilibrium Phase Transition in an Atomistic Glassformer: The Connection to Thermodynamics. *Phys. Rev. X* **2017**, *7*, 31028.

12. Gee, R.H.; Lacevic, N.; Fried, L.E. Atomistic simulations of spinodal phase separation preceding polymer crystallization. *Nat. Mater.* **2005**, *5*, 39.

13. Jha, P.K.; Larson, R.G. Assessing the Efficiency of Polymeric Excipients by Atomistic Molecular Dynamics Simulations. *Mol. Pharm.* **2014**, *11*, 1676–1686.

14.   Vogiatzis, G.G.; Theodorou, D.N. Local Segmental Dynamics and Stresses in Polystyrene–C60 Mixtures. *Macromolecules* **2014**, *47*, 387–404.

15.   Spyriouni, T.; Vergelati, C. A Molecular Modeling Study of Binary Blend Compatibility of Polyamide 6 and Poly(vinyl acetate) with Different Degrees of Hydrolysis: An Atomistic and Mesoscopic Approach. *Macromolecules* **2001**, *34*, 5306–5316.

16.   Brini, E.; Algaer, E.A.; Ganguly, P.; Li, C.; Rodríguez-Ropero, F.; van der Vegt, N.F.A. Systematic coarse-graining methods for soft matter simulations – a review. *Soft Matter* **2013**, *9*, 2108–2119.

17.   Larson, R.G. Principles for coarse-graining polymer molecules in simulations of polymer fluid mechanics. *Mol. Phys.* **2004**, *102*, 341–351.

18.   Kong, M.; Saha Dalal, I.; Li, G.; Larson, R.G. Systematic Coarse-Graining of the Dynamics of Self-Attractive Semiflexible Polymers. *Macromolecules* **2014**, *47*, 1494–1502.

19.   Marrink, S.J.; de Vries, A.H.; Mark, A.E. Coarse Grained Model for Semiquantitative Lipid Simulations. *J. Phys. Chem. B* **2004**, *108*, 750–760.

20.   Huang, W.; Mandal, T.; Larson, R.G. Computational Modeling of Hydroxypropyl-Methylcellulose Acetate Succinate (HPMCAS) and Phenytoin Interactions: A Systematic Coarse-Graining Approach. *Mol. Pharm.* **2017**, *14*, 733–745.

21.   Nielsen, S.O.; Lopez, C.F.; Srinivas, G.; Klein, M.L. Coarse grain models and the computer simulation of soft materials. *J. Phys. Condens. Matter* **2004**, *16*, R481–R512.

22.   Theodorou, D.N. Equilibration and Coarse-Graining Methods for Polymers BT - Computer Simulations in Condensed Matter Systems: From Materials to Chemical Biology Volume 2. In; Ferrario, M., Ciccotti, G., Binder, K., Eds.; Springer Berlin Heidelberg: Berlin, Heidelberg, 2006; pp. 419–448 ISBN 978-3-540-35284-6.

23.   Martin, M.G.; Siepmann, J.I. Transferable Potentials for Phase Equilibria. 1. United-Atom Description of n-Alkanes. *J. Phys. Chem. B* **1998**, *102*, 2569–2577.

24.   Chen, B.; Potoff, J.J.; Siepmann, J.I. Monte Carlo Calculations for Alcohols and Their Mixtures with Alkanes. Transferable Potentials for Phase Equilibria. 5. United-Atom Description of Primary, Secondary, and Tertiary Alcohols. *J. Phys. Chem. B* **2001**, *105*, 3093–3104.

25.   Wick, C.D.; Martin, M.G.; Siepmann, J.I. Transferable Potentials for Phase Equilibria. 4. United-Atom Description of Linear and Branched Alkenes and Alkylbenzenes. *J. Phys. Chem. B* **2000**, *104*, 8008–8016.

26.   Martin, M.G.; Siepmann, J.I. Novel Configurational-Bias Monte Carlo Method for Branched Molecules. Transferable Potentials for Phase Equilibria. 2. United-Atom Description of Branched Alkanes. *J. Phys. Chem. B* **1999**, *103*, 4508–4517.

27.   Huang, M.; Huang, W.; Wen, F.; Larson, R.G. Efficient estimation of binding free energies between peptides and an MHC class II molecule using coarse-grained molecular dynamics simulations with a weighted histogram analysis method. *J. Comput. Chem.* **2017**, *38*, 2007–2019.

28. Mandal, T.; Huang, W.; Mecca, J.M.; Getchell, A.; Porter, W.W.; Larson, R.G. A framework for multi-scale simulation of crystal growth in the presence of polymers. *Soft Matter* **2017**, *13*, 1904–1913.

29. Doi, M.; Edwards, S.F. Dynamics of concentrated polymer systems. Part 1.—Brownian motion in the equilibrium state. *J. Chem. Soc. Faraday Trans. 2 Mol. Chem. Phys.* **1978**, *74*, 1789–1801.

30. Doi, M.; Edwards, S.F. Dynamics of concentrated polymer systems. Part 2.—Molecular motion under flow. *J. Chem. Soc. Faraday Trans. 2 Mol. Chem. Phys.* **1978**, *74*, 1802–1817.

31. De Gennes, P.G. Reptation of a Polymer Chain in the Presence of Fixed Obstacles. *J. Chem. Phys.* **1971**, *55*, 572–579.

32. McLeish, T.C.B. Tube theory of entangled polymer dynamics. *Adv. Phys.* **2002**, *51*, 1379–1527.

33. Likhtman, A.E.; McLeish, T.C.B. Quantitative theory for linear dynamics of linear entangled polymers. *Macromolecules* **2002**, *35*, 6332–6343.

34. Marrucci, G.; Grizzuti, N. Fast Flows of concentrated polymers: Predictions of the tube model on chain stretching. *Gazz. Chim. Ital.* **1988**, *118*, 179–185.

35. Pearson, D.; Herbolzheimer, E.; Grizzuti, N.; Marrucci, G. Transient behavior of entangled polymers at high shear rates. *J. Polym. Sci. Part B Polym. Phys.* **1991**, *29*, 1589–1597.

36. Mead, D.W.; Yavich, D.; Leal, L.G. The reptation model with segmental stretch - I. Basic equations and general properties. *Rheol. Acta* **1995**, *34*, 360–383.

37. Mead, D.W.; Yavich, D.; Leal, L.G. The reptation model with segmental stretch - II. Steady flow properties. *Rheol. Acta* **1995**, *34*, 360–383.

38. Marrucci, G. Dynamics of entanglements: A nonlinear model consistent with the Cox-Merz rule. *J. Nonnewton. Fluid Mech.* **1996**, *62*, 279–289.

39. Mead, D.W.; Larson, R.G.; Doi, M. A molecular theory for fast flows of entangled polymers. *Macromolecules* **1998**, *31*, 7895–7914.

40. Ianniruberto, G.; Marrucci, G. A simple constitutive equation for entangled polymers with chain stretch. *J. Nonnewton. Fluid Mech.* **2002**, *102*, 383–395.

41. Graham, R.S.; Likhtman, A.E.; McLeish, T.C.B.; Milner, S.T. Microscopic theory of linear, entangled polymer chains under rapid deformation including chain stretch and convective constraint release. *J. Rheol. (N. Y. N. Y).* **2003**, *47*, 1171–1200.

42. Likhtman, A.E.; Graham, R.S. Simple constitutive equation for linear polymer melts derived from molecular theory: Rolie-Poly equation. *J. Nonnewton. Fluid Mech.* **2003**, *114*, 1–12.

43. McLeish, T.C.B.; Cates, M.E.; Higgins, J.E.; Olmsted, P.D.; Marrucci, G.; Ianniruberto, G. Flow-induced orientation and stretching of entangled polymers. *Philos. Trans. R. Soc. London. Ser. A Math. Phys. Eng. Sci.* **2003**, *361*, 677–688.

44. Bhattacharjee, P.K.; Nguyen, D.A.; McKinley, G.H.; Sridhar, T. Extensional stress growth

and stress relaxation in entangled polymer solutions. *J. Rheol. (N. Y. N. Y).* **2003**, *47*, 269–290.

45. Bhattacharjee, P.K.; Oberhauser, J.P.; Mckinley, G.H.; Leal, L.G.; Sridhar, T. Extensional Rheometry of Entangled Solutions. *Macromolecules* **2002**, *35*, 10131–10148.

46. Moghadam, S.; Saha Dalal, I.; Larson, R.G. Unraveling Dynamics of Entangled Polymers in Strong Extensional Flows. *Macromolecules* **2019**, *53*, 1296–1307.

47. Yaoita, T.; Isaki, T.; Masubuchi, Y.; Watanabe, H.; Ianniruberto, G.; Marrucci, G. Primitive Chain Network Simulation of Elongational Flows of Entangled Linear Chains : Stretch / Orientation-induced Reduction of Monomeric Friction. *Macromolecules* **2012**, *45*, 2773–2782.

48. Masubuchi, Y.; Yaoita, T.; Matsumiya, Y.; Watanabe, H.; Ianniruberto, G.; Marrucci, G. Stretch / orientation Induced Acceleration in Stress Relaxation in Coarse-grained Molecular Dynamics Simulations. *Nihon Reoroji Gakkaishi* **2013**, *41*, 35–37.

49. Matsumiya, Y.; Watanabe, H.; Masubuchi, Y.; Huang, Q.; Hassager, O. Nonlinear Elongational Rheology of Unentangled Polystyrene and Poly(p-tert-butylstyrene) Melts. *Macromolecules* **2018**, *51*, 9710–9729.

50. Ianniruberto, G. Extensional Flows of Solutions of Entangled Polymers Confirm Reduction of Friction Coefficient. *Macromolecules* **2015**, *48*, 6306–6312.

51. Yaoita, T.; Isaki, T.; Masubuchi, Y.; Watanabe, H.; Ianniruberto, G.; Marrucci, G. Primitive Chain Network Simulation of Elongational Flows of Entangled Linear Chains : Role of Finite Chain Extensibility. **2011**, 9675–9682.

52. O'Connor, T.C.; Alvarez, N.J.; Robbins, M.O. Relating Chain Conformations to Extensional Stress in Entangled Polymer Melts. *Phys. Rev. Lett.* **2018**, *121*, 47801.

53. Hsu, H.-P.; Kremer, K. Primitive Path Analysis and Stress Distribution in Highly Strained Macromolecules. *ACS Macro Lett.* **2018**, *7*, 107–111.

54. Murashima, T.; Hagita, K.; Kawakatsu, T. Elongational Viscosity of Weakly Entangled Polymer Melt via Coarse-Grained Molecular Dynamics Simulation. *Nihon Reoroji Gakkaishi* **2018**, *46*, 207–220.

55. Kremer, K.; Grest, G.S. Dynamics of entangled linear polymer melts : A molecular - dynamics simulation. *J. Chem. Phys.* **1990**, *92*, 5057–5086.

56. Daivis, P.J.; Matin, M.L.; Todd, B.D. Nonlinear shear and elongational rheology of model polymer melts by non-equilibrium molecular dynamics. *J. Nonnewton. Fluid Mech.* **2003**, *111*, 1–18.

57. Xu, W.-S.; Carrillo, J.-M.Y.; Lam, C.N.; Sumpter, B.G.; Wang, Y. Molecular Dynamics Investigation of the Relaxation Mechanism of Entangled Polymers after a Large Step Deformation. *ACS Macro Lett.* **2018**, *7*, 190–195.

58. Kröger, M.; Luap, C.; Muller, R. Polymer Melts under Uniaxial Elongational Flow: Stress−Optical Behavior from Experiments and Nonequilibrium Molecular Dynamics Computer Simulations. *Macromolecules* **1997**, *30*, 526–539.

59. McLeish, T.C.B.; Cates, M.E.; S., H.J.; D., O.P.; Doi, M.; Takimoto, J. Molecular

modelling of entanglement. *Philos. Trans. R. Soc. London. Ser. A Math. Phys. Eng. Sci.* **2003**, *361*, 641–652.

60. Masubuchi, Y.; Takimoto, J.; Koyama, K.; Ianniruberto, G.; Marrucci, G.; Masubuchi, Y.; Takimoto, J.; Koyama, K.; Greco, F. Brownian simulations of a network of reptating primitive chains Brownian simulations of a network of reptating primitive chains. *J. Chem. Phys.* **2001**, *115*, 4387–4394.

61. Uneyama, T. Single Chain Slip-Spring Model for Fast Rheology Simulations of Entangled Polymers on GPU. *J. Soc. Rheol. Japan* **2011**, *39*, 135–152.

62. Yaoita, T.; Isaki, T.; Masubuchi, Y.; Watanabe, H.; Ianniruberto, G.; Greco, F.; Marrucci, G. Statics , linear , and nonlinear dynamics of entangled polystyrene melts simulated through the primitive chain network model. *J. Chem. Phys.* **2008**, *128*, 154901–154911.

63. Uneyama, T.; Masubuchi, Y. Multi-chain slip-spring model for entangled polymer dynamics. *J. Chem. Phys.* **2012**, *137*, 154902.

64. Masubuchi, Y.; Ianniruberto, G.; Marrucci, G. Stress Undershoot of Entangled Polymers under Fast Startup Shear Flows in Primitive Chain Network Simulations. *J. Soc. Rheol. Japan* **2018**, *46*, 23–28.

65. Yaoita, T.; Isaki, T.; Masubuchi, Y.; Watanabe, H.; Ianniruberto, G.; Marrucci, G. Primitive Chain Network Simulation of Elongational Flows of Entangled Linear Chains: Role of Finite Chain Extensibility. *Macromolecules* **2011**, *44*, 9675–9682.

66. Schieber, J.D. Fluctuations in entanglements of polymer liquids. *J. Chem. Phys.* **2003**, *118*, 5162–5166.

67. Nair, D.M.; Schieber, J.D. Linear viscoelastic predictions of a consistently unconstrained brownian slip-link model. *Macromolecules* **2006**, *39*, 3386–3397.

68. Schieber, J.D.; Indei, T.; Steenbakkers, R.J.A. Fluctuating entanglements in single-chain mean-field models. *Polymers (Basel).* **2013**, *5*, 643–678.

69. Ramírez, J.; Sukumaran, S.K.; Likhtman, A.E. Hierarchical Modeling of Entangled Polymers. *Macromol. Symp.* **2007**, *252*, 119–129.

70. Likhtman, A.E. Single-Chain Slip-Link Model of Entangled Polymers: Simultaneous Description of Neutron Spin - Echo, Rheology, and Diffusion. *Macromolecules* **2005**, *38*, 6128–6139.

71. Zamponi, M.; Wischnewski, A.; Monkenbusch, M.; Willner, L.; Richter, D.; Likhtman, A.E.; Kali, G.; Farago, B. Molecular observation of constraint release in polymer melts. *Phys. Rev. Lett.* **2006**, *96*, 1–4.

72. Biondo, D. Del; Masnada, E.M.; Merabia, S.; Couty, M.; Barrat, J.-L. Numerical study of a slip-link model for polymer melts and nanocomposites. *J. Chem. Phys.* **2013**, *138*, 194902–194913.

73. Pilyugina, E.; Andreev, M.; Schieber, J.D. Dielectric relaxation as an independent examination of relaxation mechanisms in entangled polymers using the discrete slip-link model. *Macromolecules* **2012**, *45*, 5728–5743.

74. Andreev, M.; Khaliullin, R.N.; Steenbakkers, R.J.A.; Schieber, J.D. Approximations of

the discrete slip-link model and their effect on nonlinear rheology predictions. *J. Rheol. (N. Y. N. Y).* **2013**, *57*, 535–557.

75. Khaliullin, R.N.; Schieber, J.D. Self-Consistent Modeling of Constraint Release in a Single-Chain Mean-Field Slip-Link Model. *Macromolecules* **2009**, *42*, 7504–7517.

76. Schieber, J.D.; Nair, D.M.; Kitkrailard, T. Comprehensive comparisons with nonlinear flow data of a consistently unconstrained Brownian slip-link model. *J. Rheol. (N. Y. N. Y).* **2007**, *51*, 1111–1141.

77. Schieber, J.D.; Andreev, M. Entangled Polymer Dynamics in Equilibrium and Flow Modeled Through Slip Links. *Annu. Rev. Chem. Biomol. Eng.* **2014**, *5*, 367–381.

78. Cubuk, E.D.; Ivancic, R.J.S.; Schoenholz, S.S.; Strickland, D.J.; Basu, A.; Davidson, Z.S.; Fontaine, J.; Hor, J.L.; Huang, Y.-R.; Jiang, Y.; et al. Structure-property relationships from universal signatures of plasticity in disordered solids. *Science (80-.).* **2017**, *358*, 1033 LP-1037.

79. Zhang, K.; Meng, D.; Müller-Plathe, F.; Kumar, S.K. Coarse-grained molecular dynamics simulation of activated penetrant transport in glassy polymers. *Soft Matter* **2018**, *14*, 440–447.

80. Phillips, J.C. Microscopic aspects of Stretched Exponential Relaxation (SER) in homogeneous molecular and network glasses and polymers. *J. Non. Cryst. Solids* **2011**, *357*, 3853–3865.

81. Zhao, Y.; Liu, J.; Li, X.; Lu, Y.; Wang, S.-Q. How and Why Polymer Glasses Lose Their Ductility Due to Plasticizers. *Macromolecules* **2017**, *50*, 2024–2032.

82. Morgan, R.J.; O'neal, J.E. The Mechanical Properties of Polymer Glasses. *Polym. Plast. Technol. Eng.* **1975**, *5*, 173–197.

83. Zhang, W.; Douglas, J.F.; Starr, F.W. Dynamical heterogeneity in a vapor-deposited polymer glass. *J. Chem. Phys.* **2017**, *146*, 203310.

84. Hebert, K.; Ediger, M.D. Reversing Strain Deformation Probes Mechanisms for Enhanced Segmental Mobility of Polymer Glasses. *Macromolecules* **2017**, *50*, 1016–1026.

85. Chung, Y.G.(정용철); Lacks, D.J. Sheared polymer glass and the question of mechanical rejuvenation. *J. Chem. Phys.* **2012**, *136*, 124907.

86. Malekmotiei, L.; Voyiadjis, G.Z.; Samadi-Dooki, A.; Lu, F.; Zhou, J. Effect of annealing temperature on interrelation between the microstructural evolution and plastic deformation in polymers. *J. Polym. Sci. Part B Polym. Phys.* **2017**, *55*, 1286–1297.

87. Xu, W.-S.; Douglas, J.F.; Freed, K.F. Generalized entropy theory of glass-formation in fully flexible polymer melts. *J. Chem. Phys.* **2016**, *145*, 234509.

88. Arzhakov, M.S.; Lukovkin, G.M.; Arzhakov, S.A. Concept of Generalized Polymer Glass. *Dokl. Phys. Chem.* **2002**, *384*, 119–122.

89. Hoy, R.S.; Foteinopoulou, K.; Kröger, M. Topological analysis of polymeric melts: Chain-length effects and fast-converging estimators for entanglement length. *Phys. Rev. E* **2009**, *80*, 31803.

90. Paeng, K.; Lee, H.-N.; Swallen, S.F.; Ediger, M.D. Temperature-ramping measurement of dye reorientation to probe molecular motion in polymer glasses. *J. Chem. Phys.* **2011**, *134*, 24901.

91. Liu, J.; Lin, P.; Li, X.; Wang, S.-Q. Nonlinear stress relaxation behavior of ductile polymer glasses from large extension and compression. *Polymer (Guildf).* **2015**, *81*, 129–139.

92. Kumar, R.; Goswami, M.; Sumpter, B.G.; Novikov, V.N.; Sokolov, A.P. Effects of backbone rigidity on the local structure and dynamics in polymer melts and glasses. *Phys. Chem. Chem. Phys.* **2013**, *15*, 4604–4609.

93. Chen, K.; Saltzman, E.J.; Schweizer, K.S. Molecular Theories of Segmental Dynamics and Mechanical Response in Deeply Supercooled Polymer Melts and Glasses. *Annu. Rev. Condens. Matter Phys.* **2010**, *1*, 277–300.

94. Chen, K.; Schweizer, K.S. Theory of aging, rejuvenation, and the nonequilibrium steady state in deformed polymer glasses. *Phys. Rev. E* **2010**, *82*, 41804.

95. Zou, W.; Larson, R.G. A hybrid Brownian dynamics/constitutive model for yielding, aging, and rejuvenation in deforming polymeric glasses. *Soft Matter* **2016**, *12*, 6757–6770.

96. Chen, K.; Schweizer, K.S. Theory of Yielding , Strain Softening , and Steady Plastic Flow in Polymer Glasses under Constant Strain Rate Deformation. **2011**, 3988–4000.

97. Wang, S.-Q.; Cheng, S.; Lin, P.; Li, X. A phenomenological molecular model for yielding and brittle-ductile transition of polymer glasses. *J. Chem. Phys.* **2014**, *141*, 94905.

98. Chen, K.; Saltzman, E.J.; Schweizer, K.S. Molecular Theories of Segmental Dynamics and Mechanical Response in Deeply Supercooled Polymer Melts and Glasses. **2010**.

99. Chen, K.; Schweizer, K.S. Theory of Yielding, Strain Softening, and Steady Plastic Flow in Polymer Glasses under Constant Strain Rate Deformation. *Macromolecules* **2011**, *44*, 3988–4000.

100. Phys, J.C.; Chen, K.; Schweizer, K.S. Theory of relaxation and elasticity in polymer glasses. **2014**, *014904*.

101. van Breemen, L.C.A.; Klompen, E.T.J.; Govaert, L.E.; Meijer, H.E.H. Extending the EGP constitutive model for polymer glasses to multiple relaxation times. *J. Mech. Phys. Solids* **2011**, *59*, 2191–2207.

102. Nayak, K.; Read, D.J.; McLeish, T.C.B.; Hine, P.J.; Tassieri, M. A coarse-grained molecular model of strain-hardening for polymers in the marginally glassy state. *J. Polym. Sci. Part B Polym. Phys.* **2011**, *49*, 920–938.

103. Zou, W.; Larson, R.G. A hybrid Brownian dynamics/constitutive model for yielding, aging, and rejuvenation in deforming polymeric glasses. *Soft Matter* **2016**, *12*, 6757–6770.

104. Fielding, S.M.; Larson, R.G.; Cates, M.E. Simple Model for the Deformation-Induced Relaxation of Glassy Polymers. *Phys. Rev. Lett.* **2012**, *108*, 048301.

105. Fielding, S.M.; Moorcroft, R.L.; Larson, R.G.; Cates, M.E. Modeling the relaxation of polymer glasses under shear and elongational loads. *J. Chem. Phys.* **2013**, *138*.

106. Ge, T.; Tzoumanekas, C.; Anogiannakis, S.D.; Hoy, R.S.; Robbins, M.O. Entanglements

in glassy polymer crazing: Cross-links or tubes? *Macromolecules* **2017**, *50*, 459–471.

107. Smessaert, A.; Rottler, J. Recovery of Polymer Glasses from Mechanical Perturbation. *Macromolecules* **2012**, *45*, 2928–2935.

108. Ge, T.; Robbins, M.O. Anisotropic plasticity and chain orientation in polymer glasses. *J. Polym. Sci. Part B Polym. Phys.* **2010**, *48*, 1473–1482.

109. Liu, A.Y.-H.; Rottler, J. Aging under stress in polymer glasses. *Soft Matter* **2010**, *6*, 4858–4862.

110. Rottler, J. Relaxation times in deformed polymer glasses: A comparison between molecular simulations and two theories. *J. Chem. Phys.* **2016**, *145*, 64505.

111. Li, X.; Liu, J.; Liu, Z.; Tsige, M.; Wang, S. Illustrating the Molecular Origin of Mechanical Stress in Ductile Deformation of Polymer Glasses. *Phys. Rev. Lett.* **2018**, *120*, 77801.

112. Hasan, O.A.; Boyce, M.C. Energy storage during inelastic deformation of glassy polymers. *Polymer (Guildf).* **1993**, *34*, 5085–5092.

113. Hoy, R.S.; Robbins, M.O. Strain hardening in bidisperse polymer glasses : Separating the roles of chain orientation and interchain entanglement. *J. Chem. Phys.* **2009**, *131*, 244901–244905.

114. Hoy, R.S.; O'Hern, C.S. Viscoplasticity and large-scale chain relaxation in glassy-polymeric strain hardening. *Phys. Rev. E* **2010**, *82*, 41803.

115. Hoy, R.S. Why is understanding glassy polymer mechanics so difficult? *J. Polym. Sci. Part B Polym. Phys.* **2011**, *49*, 979–984.

116. Xu, J.; Li, D.; Chen, J.; Din, L.; Wang, X.; Tao, F.; Xue, G. Detection of Interchain Proximity and Segmental Motion of Polymer Glass. *Macromolecules* **2011**, *44*, 7445–7450.

117. Smessaert, A.; Rottler, J. Recovery of Polymer Glasses from Mechanical Perturbation. **2012**.

118. Hoy, R.S.; Robbins, M.O. Strain hardening of polymer glasses: Entanglements, energetics, and plasticity. *Phys. Rev. E* **2008**, *77*, 31801.

119. Nguyen, H.T.; Hoy, R.S. Effect of the Ratio lK/p on Glassy-Polymeric Shear Deformation Mechanisms. *Macromolecules* **2018**, *51*, 4370–4380.

120. Riggleman, R.A.; Lee, H.-N.; Ediger, M.D.; de Pablo, J.J. Free Volume and Finite-Size Effects in a Polymer Glass under Stress. *Phys. Rev. Lett.* **2007**, *99*, 215501.

121. Rottler, J.; Robbins, M.O. Growth, microstructure, and failure of crazes in glassy polymers. *Phys. Rev. E* **2003**, *68*, 11801.

122. Savjani, K.T.; Gajjar, A.K.; Savjani, J.K. Drug solubility: importance and enhancement techniques. *ISRN Pharm.* **2012**, *2012*, 195727.

123. Vemula, V.R.; Lagishetty, V.; Lingala, S. Solubility Enhancement Techniques. *Int. J. Pharm. Sci. Rev. Res.* **2010**, *5*, 41–51.

124. Serajuddin, A.T.M. Solid dispersion of poorly water‐soluble drugs: Early

promises, subsequent problems, and recent breakthroughs. *J. Pharm. Sci.* **1999**, *88*, 1058–1066.

125. Vo, C.L.-N.; Park, C.; Lee, B.-J. Current trends and future perspectives of solid dispersions containing poorly water-soluble drugs. *Eur. J. Pharm. Biopharm.* **2013**, *85*, 799–813.

126. Alarcón, C. de las H.; Pennadam, S.; Alexander, C. Stimuli responsive polymers for biomedical applications. *Chem. Soc. Rev.* **2005**, *34*, 276–285.

127. Lendlein, A.; Shastri, V.P. Stimuli-Sensitive Polymers. *Adv. Mater.* **2010**, *22*, 3344–3347.

128. Irie, M. Stimuli-responsive poly(N-isopropylacrylamide). Photo- and chemical-induced phase transitions BT - Responsive Gels: Volume Transitions II. In; Dušek, K., Ed.; Springer Berlin Heidelberg: Berlin, Heidelberg, 1993; pp. 49–65 ISBN 978-3-540-47836-2.

129. Wu, C.; Zhou, S. Thermodynamically Stable Globule State of a Single Poly(N-isopropylacrylamide) Chain in Water. *Macromolecules* **1995**, *28*, 5388–5390.

130. Wang, X.; Qiu, X.; Wu, C. Comparison of the Coil-to-Globule and the Globule-to-Coil Transitions of a Single Poly(N-isopropylacrylamide) Homopolymer Chain in Water. *Macromolecules* **1998**, *31*, 2972–2976.

131. Zhou, K.; Lu, Y.; Li, J.; Shen, L.; Zhang, G.; Xie, Z.; Wu, C. The Coil-to-Globule-to-Coil Transition of Linear Polymer Chains in Dilute Aqueous Solutions: Effect of Intrachain Hydrogen Bonding. *Macromolecules* **2008**, *41*, 8927–8931.

132. Tanaka, N.; Matsukawa, S.; Kurosu, H.; Ando, I. A study on dynamics of water in crosslinked poly (N-isopropylacrylamide) gel by n.m.r. spectroscopy. *Polymer (Guildf).* **1998**, *39*, 4703–4706.

133. Ray, B.; Okamoto, Y.; Kamigaito, M.; Sawamoto, M.; Seno, K.; Kanaoka, S.; Aoshima, S. Effect of Tacticity of Poly(N-isopropylacrylamide) on the Phase Separation Temperature of Its Aqueous Solutions. *Polym. J.* **2005**, *37*, 234.

134. Biswas, C.S.; Patel, V.K.; Vishwakarma, N.K.; Tiwari, V.K.; Maiti, B.; Maiti, P.; Kamigaito, M.; Okamoto, Y.; Ray, B. Effects of Tacticity and Molecular Weight of Poly(N-isopropylacrylamide) on Its Glass Transition Temperature. *Macromolecules* **2011**, *44*, 5822–5824.

135. Yang, J.; Yan, Q.; Liu, H.; Hu, Y. A molecular thermodynamic model for binary lattice polymer solutions. *Polymer (Guildf).* **2006**, *47*, 5187–5195.

136. Huang, Y.; Jin, X.; Liu, H.; Hu, Y. A molecular thermodynamic model for the swelling of thermo-sensitive hydrogels. *Fluid Phase Equilib.* **2008**, *263*, 96–101.

137. Zhi, D.; Huang, Y.; Han, X.; Liu, H.; Hu, Y. A molecular thermodynamic model for temperature- and solvent-sensitive hydrogels, application to the swelling behavior of PNIPAm hydrogels in ethanol/water mixtures. *Chem. Eng. Sci.* **2010**, *65*, 3223–3230.

138. Walter, J.; Sehrt, J.; Vrabec, J.; Hasse, H. Molecular Dynamics and Experimental Study of Conformation Change of Poly(N-isopropylacrylamide) Hydrogels in Mixtures of Water and Methanol. *J. Phys. Chem. B* **2012**, *116*, 5251–5259.

139. Tucker, A.K.; Stevens, M.J. Study of the Polymer Length Dependence of the Single Chain Transition Temperature in Syndiotactic Poly(N-isopropylacrylamide) Oligomers in Water. *Macromolecules* **2012**, *45*, 6697–6703.

140. Gangemi, F.; Longhi, G.; Abbate, S.; Lebon, F.; Cordone, R.; Ghilardi, G.P.; Fornili, S.L. Molecular Dynamics Simulation of Aqueous Solutions of 26-Unit Segments of p(NIPAAm) and of p(NIPAAm) "Doped" with Amino Acid Based Comonomers. *J. Phys. Chem. B* **2008**, *112*, 11896–11906.

141. Cho, E.C.; Lee, J.; Cho, K. Role of Bound Water and Hydrophobic Interaction in Phase Transition of Poly(N-isopropylacrylamide) Aqueous Solution. *Macromolecules* **2003**, *36*, 9929–9934.

142. Deshmukh, S.A.; Sankaranarayanan, S.K.R.S.; Suthar, K.; Mancini, D.C. Role of Solvation Dynamics and Local Ordering of Water in Inducing Conformational Transitions in Poly(N-isopropylacrylamide) Oligomers through the LCST. *J. Phys. Chem. B* **2012**, *116*, 2651–2663.

143. Likhtman, A.E.; Sukumaran, S.K.; Ramirez, J. Linear Viscoelasticity from Molecular Dynamics Simulation of Entangled Polymers. *Macromolecules* **2007**, *40*, 6748–6757.

144. Ting, J.M.; Tale, S.; Purchel, A.A.; Jones, S.D.; Widanapathirana, L.; Tolstyka, Z.P.; Guo, L.; Guillaudeu, S.J.; Bates, F.S.; Reineke, T.M. High-Throughput Excipient Discovery Enables Oral Delivery of Poorly Soluble Pharmaceuticals. *ACS Cent. Sci.* **2016**, *2*, 748–755.

145. Doi, M.; Edwards, S.F. Dynamics of Concentrated Polymer Systems. *J. Chem. Soc., Faraday Trans. 2* **1978**, *74*, 1802–1817.

146. Ianniruberto, G.; Marrucci, G. On compatibility of the Cox-Merz rule with the model of Doi and Edwards. *J. Nonnewton. Fluid Mech.* **1996**, *65*, 241–246.

147. Read, D.J.; Jagannathan, K.; Sukumaran, S.K.; Auhl, D. A full-chain constitutive model for bidisperse blends of linear polymers. *J. Rheol. (N. Y. N. Y)*. **2012**, *56*, 823–873.

148. Nguyen, D.A.; Bhattacharjee, P.K.; Sridhar, T. Response of an entangled polymer solution to uniaxial and planar deformation. *J. Rheol. (N. Y. N. Y)*. **2015**, *59*, 821–833.

149. Rubinstein, M.; Panyukov, S. Nonaffine deformation and elasticity of polymer networks. *Macromolecules* **1997**, *30*, 8036–8044.

150. Rubinstein, M.; Panyukov, S. Elasticity of polymer networks. *Macromolecules* **2002**, *35*, 6670–6686.

151. Marrucci, G.; Greco, F.; Ianniruberto, G. Simple strain measure for entangled polymers. *J. Rheol. (N. Y. N. Y)*. **2000**, *44*, 845–854.

152. Dealy, J.M.; Read, D.J.; Larson, R.G. Structure and Rheology of Molten Polymers. In *Structure and Rheology of Molten Polymers*; Carl Hanser Verlag GmbH & Co. KG, 2018 ISBN 978-1-56990-611-8.

153. Desai, P.S.; Larson, R.G. Constitutive model that shows extension thickening for entangled solutions and extension thinning for melts. *J. Rheol. (N. Y. N. Y)*. **2014**, *58*, 255–279.

154. Pearson, D.S.; Kiss, A.D.; Fetters, L.J.; Doi, M. Flow-Induced Birefringence of Concentrated Polyisoprene Solutions. *J. Rheol. (N. Y. N. Y).* **1989**, *33*, 517–535.

155. Larson, R.G. *Constitutive Equations for Polymer Melts and Solutions*; Howard Brenner, Ed.; Butterworth-Heinemann, 1988; ISBN 978-0-409-90110-1.

156. Cohen, A. A Padé approximant to the inverse Langevin function. *Rheol. Acta* **1991**, *30*, 270–273.

157. Huang, Q.; Hengeller, L.; Alvarez, N.J.; Hassager, O. Bridging the Gap between Polymer Melts and Solutions in Extensional Rheology. *Macromolecules* **2015**, *48*, 4158–4163.

158. Larson, R.G. The unraveling of a polymer chain in a strong extensional flow. *Rheol. Acta* **1990**, *29*, 371–384.

159. Hinch, E.J. Uncoiling a polymer molecule in a strong extensional flow. *J. Nonnewton. Fluid Mech.* **1994**, *54*, 209–230.

160. Rallison, J.M.; Hinch, E.J. Do we understand the physics in the constitutive equation? *J. Nonnewton. Fluid Mech.* **1988**, *29*, 37–55.

161. Hsiao, K.-W.; Sasmal, C.; Ravi Prakash, J.; Schroeder, C.M. Direct observation of DNA dynamics in semidilute solutions in extensional flow. *J. Rheol. (N. Y. N. Y).* **2016**, *61*, 151–167.

162. Larson, R.G. The rheology of dilute solutions of flexible polymers: Progress and problems. *J. Rheol. (N. Y. N. Y).* **2005**, *49*, 1–70.

163. Hsiao, K.; Sasmal, C.; Prakash, J.R.; Schroeder, C.M.; Hsiao, K. Direct observation of DNA dynamics in semidilute solutions in extensional flow. **2017**, *151*.

164. Cho, S.; Jeong, S.; Kim, J.M.; Baig, C. Molecular dynamics for linear polymer melts in bulk and confined systems under shear flow. *Sci. Rep.* **2017**, *7*, 9004.

165. Moghadam, S.; Saha Dalal, I.; Larson, G.R. Slip-Spring and Kink Dynamics Models for Fast Extensional Flow of Entangled Polymeric Fluids. *Polymers (Basel).* 2019, *11*.

166. Mai, D.J.; Saadat, A.; Khomami, B.; Schroeder, C.M. Stretching Dynamics of Single Comb Polymers in Extensional Flow. *Macromolecules* **2018**, *51*, 1507–1517.

167. Kirkwood, J.G.; Riseman, J. The intrinsic viscosities and diffusion constants of flexible macromolecules in solution. *J. Chem. Phys.* **1948**, *16*, 565–573.

168. Masubuchi, Y.; Ianniruberto, G.; Greco, F.; Marrucci, G. Entanglement molecular weight and frequency response of sliplink networks. *J. Chem. Phys.* **2003**, *119*, 6925–6930.

169. Sukumaran, S.K.; Likhtman, A.E. Modeling Entangled Dynamics: Comparison between Stochastic Single-Chain and Multichain Models. *Macromolecules* **2009**, *42*, 4300–4309.

170. Sukumaran, S.K.; Likhtman, A.E. Modeling Entangled Dynamics : Comparison between Stochastic Single-Chain and Multichain Models. **2009**, 4300–4309.

171. Glauber, R.J. Time-Dependent Statistics of the Ising Model. *J. Math. Phys.* **1963**, *4*, 294–307.

172. Kushwaha, A.; Shaqfeh, E.S.G. Slip-link simulations of entangled polymers in planar extensional flow : Disentanglement modified extensional thinning. *J. Rheol. (N. Y. N. Y).*

2011, *55*, 463–483.

173. Mead, D.W.; Banerjee, N.; Park, J. A constitutive model for entangled polymers incorporating binary entanglement pair dynamics and a configuration dependent friction coefficient. *J. Rheol. (N. Y. N. Y).* **2015**, *59*, 335–363.

174. Zartman, G.D.; Cheng, S.; Li, X.; Lin, F.; Becker, M.L.; Wang, S.-Q. How Melt-Stretching Affects Mechanical Behavior of Polymer Glasses. *Macromolecules* **2012**, *45*, 6719–6732.

175. De Focatiis, D.S.A.; Embery, J.; Buckley, C.P. Large deformations in oriented polymer glasses: Experimental study and a new glass-melt constitutive model. *J. Polym. Sci. Part B Polym. Phys.* **2010**, *48*, 1449–1463.

176. Chung, Y.G.; Lacks, D.J. Atomic Mobility in a Polymer Glass after Shear and Thermal Cycles. *J. Phys. Chem. B* **2012**, *116*, 14201–14205.

177. Kramer, E.J. Open questions in the physics of deformation of polymer glasses. *J. Polym. Sci. Part B Polym. Phys.* **2005**, *43*, 3369–3371.

178. Auhl, R.; Everaers, R.; Grest, G.S.; Kremer, K.; Plimpton, S.J. Equilibration of long chain polymer melts in computer simulations. *J. Chem. Phys.* **2003**, *119*, 12718–12728.

179. Deres, A.; Floudas, G.A.; Müllen, K.; Van der Auweraer, M.; De Schryver, F.; Enderlein, J.; Uji-i, H.; Hofkens, J. The Origin of Heterogeneity of Polymer Dynamics near the Glass Temperature As Probed by Defocused Imaging. *Macromolecules* **2011**, *44*, 9703–9709.

180. Plimpton, S. Fast Parallel Algorithms for Short-Range Molecular Dynamics. *J. Comput. Phys.* **1995**, *117*, 1–19.

181. Rouse, P.E.J. A Theory of the Linear Viscoelastic Properties of Dilute Solutions of Coiling Polymers. *J. Chem. Phys.* **1953**, *21*, 1272.

182. Casas, F.; Alba-Simionesco, C.; Montes, H.; Lequeux, F. Length-Scale of Glassy Polymer Plastic Flow: A Neutron Scattering Study. *Macromolecules* **2008**, *41*, 860–865.

183. Lee, H.-N.; Paeng, K.; Swallen, S.F.; Ediger, M.D.; Stamm, R.A.; Medvedev, G.A.; Caruthers, J.M. Molecular mobility of poly(methyl methacrylate) glass during uniaxial tensile creep deformation. *J. Polym. Sci. Part B Polym. Phys.* **2009**, *47*, 1713–1727.

184. Lee, H.-N.; Paeng, K.; Swallen, S.F.; Ediger, M.D. Direct Measurement of Molecular Mobility in Actively Deformed Polymer Glasses. *Science (80-.).* **2009**, *323*, 231 LP-234.

185. Bending, B.; Ediger, M.D. Comparison of mechanical and molecular measures of mobility during constant strain rate deformation of a PMMA glass. *J. Polym. Sci. Part B Polym. Phys.* **2016**, *54*, 1957–1967.

186. Lee, H.-N.; Riggleman, R.A.; de Pablo, J.J.; Ediger, M.D. Deformation-Induced Mobility in Polymer Glasses during Multistep Creep Experiments and Simulations. *Macromolecules* **2009**, *42*, 4328–4336.

187. Kalfus, J.; Detwiler, A.; Lesser, A.J. Probing Segmental Dynamics of Polymer Glasses during Tensile Deformation with Dielectric Spectroscopy. *Macromolecules* **2012**, *45*, 4839–4847.

188. Tzoumanekas, C.; Theodorou, D.N. Topological Analysis of Linear Polymer Melts: A

Statistical Approach. *Macromolecules* **2006**, *39*, 4592–4604.

189. Kramer, E.J. Microscopic and molecular fundamentals of crazing BT - Crazing in Polymers.; Kausch, H.H., Ed.; Springer Berlin Heidelberg: Berlin, Heidelberg, 1983; pp. 1–56.

190. Zou, W.; Larson, R.G. A mesoscopic simulation method for predicting the rheology of semi-dilute wormlike micellar solutions. *J. Rheol. (N. Y. N. Y).* **2014**, *58*, 681–721.

191. Chung, Y.G.; Lacks, D.J. How Deformation Enhances Mobility in a Polymer Glass. *Macromolecules* **2012**, *45*, 4416–4421.

192. Cavaille, J.Y.; Perez, J.; Johari, G.P. Molecular theory for the rheology of glasses and polymers. *Phys. Rev. B* **1989**, *39*, 2411–2422.

193. Pérez-Aparicio, R.; Cottinet, D.; Crauste-Thibierge, C.; Vanel, L.; Sotta, P.; Delannoy, J.-Y.; Long, D.R.; Ciliberto, S. Dielectric Spectroscopy of a Stretched Polymer Glass: Heterogeneous Dynamics and Plasticity. *Macromolecules* **2016**, *49*, 3889–3898.

194. Chow, T.S. Statistical entropy model for relaxation in stressed polymer glasses. *Polym. Eng. Sci.* **1984**, *24*, 915–920.

195. Sollich, P.; Lequeux, F.; Hébraud, P.; Cates, M.E. Rheology of Soft Glassy Materials. *Phys. Rev. Lett.* **1997**, *78*, 2020–2023.

196. Chen, K.; Schweizer, K.S. Theory of relaxation and elasticity in polymer glasses. *J. Chem. Phys.* **2007**, *126*, 14904.

197. Williams, H.D.; Trevaskis, N.L.; Charman, S.A.; Shanker, R.M.; Charman, W.N.; Pouton, C.W.; Porter, C.J.H. Strategies to Address Low Drug Solubility in Discovery and Development. *Pharmacol. Rev.* **2013**, *65*, 315 LP-499.

198. Jain, R.A. The manufacturing techniques of various drug loaded biodegradable poly(lactide-co-glycolide) (PLGA) devices. *Biomaterials* **2000**, *21*, 2475–2490.

199. Klose, D.; Siepmann, F.; Elkharraz, K.; Siepmann, J. PLGA-based drug delivery systems: Importance of the type of drug and device geometry. *Int. J. Pharm.* **2008**, *354*, 95–103.

200. Nan, J.; Chen, Y.; Li, R.; Wang, J.; Liu, M.; Wang, C.; Chu, F. Polymeric Hydrogel Nanocapsules: A Thermo and pH Dual-responsive Carrier for Sustained Drug Release. *Nano-Micro Lett.* **2014**, *6*, 200–208.

201. Prasannan, A.; Tsai, H.-C.; Chen, Y.-S.; Hsiue, G.-H. A thermally triggered in situ hydrogel from poly(acrylic acid-co-N-isopropylacrylamide) for controlled release of anti-glaucoma drugs. *J. Mater. Chem. B* **2014**, *2*, 1988–1997.

202. Chung, J.E.; Yokoyama, M.; Yamato, M.; Aoyagi, T.; Sakurai, Y.; Okano, T. Thermo-responsive drug delivery from polymeric micelles constructed using block copolymers of poly(N-isopropylacrylamide) and poly(butylmethacrylate). *J. Control. Release* **1999**, *62*, 115–127.

203. Cao, Z.; Liu, W.; Ye, G.; Zhao, X.; Lin, X.; Gao, P.; Yao, K. N-Isopropylacrylamide/2-Hydroxyethyl Methacrylate Star Diblock Copolymers: Synthesis and Thermoresponsive Behavior. *Macromol. Chem. Phys.* **2006**, *207*, 2329–2335.

204. Marsac, P.J.; Li, T.; Taylor, L.S. Estimation of Drug–Polymer Miscibility and Solubility

in Amorphous Solid Dispersions Using Experimentally Determined Interaction Parameters. *Pharm. Res.* **2008**, *26*, 139.

205. Zhao, Y.; Inbar, P.; Chokshi, H.P.; Malick, A.W.; Choi, D.S. Prediction of the Thermal Phase Diagram of Amorphous Solid Dispersions by Flory–Huggins Theory. *J. Pharm. Sci.* **2011**, *100*, 3196–3207.

206. Walter, J.; Ermatchkov, V.; Vrabec, J.; Hasse, H. Molecular dynamics and experimental study of conformation change of poly(N-isopropylacrylamide) hydrogels in water. *Fluid Phase Equilib.* **2010**, *296*, 164–172.

207. Katsumoto, Y.; Kubosaki, N.; Miyata, T. Molecular Approach To Understand the Tacticity Effects on the Hydrophilicity of Poly(N-isopropylacrylamide): Solubility of Dimer Model Compounds in Water. *J. Phys. Chem. B* **2010**, *114*, 13312–13318.

208. Du, H.; Wickramasinghe, R.; Qian, X. Effects of Salt on the Lower Critical Solution Temperature of Poly (N-Isopropylacrylamide). *J. Phys. Chem. B* **2010**, *114*, 16594–16604.

209. Kamath, G.; Deshmukh, S.A.; Baker, G.A.; Mancini, D.C.; Sankaranarayanan, S.K.R.S. Thermodynamic considerations for solubility and conformational transitions of poly-N-isopropyl-acrylamide. *Phys. Chem. Chem. Phys.* **2013**, *15*, 12667–12673.

210. Schwartz, P.A.; Rhodes, C.T.; Cooper Jr., J.W. Solubility and Ionization Characteristics of Phenytoin. *J. Pharm. Sci.* **1977**, *66*, 994–997.

211. Páll, S.; Abraham, M.J.; Kutzner, C.; Hess, B.; Lindahl, E. Tackling Exascale Software Challenges in Molecular Dynamics Simulations with GROMACS BT - Solving Software Challenges for Exascale.; Markidis, S., Laure, E., Eds.; Springer International Publishing: Cham, 2015; pp. 3–27.

212. Hess, B.; van der Spoel, D.; Lindahl, E.; Smith, J.C.; Shirts, M.R.; Bjelkmar, P.; Larsson, P.; Kasson, P.M.; Schulz, R.; Apostolov, R.; et al. GROMACS 4.5: a high-throughput and highly parallel open source molecular simulation toolkit. *Bioinformatics* **2013**, *29*, 845–854.

213. Hornak, V.; Abel, R.; Okur, A.; Strockbine, B.; Roitberg, A.; Simmerling, C. Comparison of multiple Amber force fields and development of improved protein backbone parameters. *Proteins Struct. Funct. Bioinforma.* **2006**, *65*, 712–725.

214. Case, D.A.; Cheatham III, T.E.; Darden, T.; Gohlke, H.; Luo, R.; Merz Jr., K.M.; Onufriev, A.; Simmerling, C.; Wang, B.; Woods, R.J. The Amber biomolecular simulation programs. *J. Comput. Chem.* **2005**, *26*, 1668–1688.

215. D.A. Case, J. T. B., R.M. Betz, D.S. Cerutti, T.E. Cheatham, III, T.A. Darden, R.E. Duke, T.J. Giese, H. Gohlke, A.W. Goetz, N. Homeyer, S. Izadi, P. Janowski, J. Kaus, A. Kovalenko, T.S. Lee, S. LeGrand, P. Li, T. Luchko, R. Luo, B. Madej, K.M. Merz, G., D.M.Y. and P.A.K. Amber 2014 2014.

216. Furuncuoğlu Özaltın, T.; Değirmenci, İ.; Aviyente, V.; Atılgan, C.; De Sterck, B.; Van Speybroeck, V.; Waroquier, M. Controlling the tacticity in the polymerization of N-isopropylacrylamide: A computational study. *Polymer (Guildf).* **2011**, *52*, 5503–5512.

217. Jakalian, A.; Bush, B.L.; Jack, D.B.; Bayly, C.I. Fast, efficient generation of high-quality

atomic charges. AM1-BCC model: I. Method. *J. Comput. Chem.* **2000**, *21*, 132–146.

218. Bayly, C.I.; Cieplak, P.; Cornell, W.; Kollman, P.A. A well-behaved electrostatic potential based method using charge restraints for deriving atomic charges: the RESP model. *J. Phys. Chem.* **1993**, *97*, 10269–10280.

219. Sousa da Silva, A.W.; Vranken, W.F. ACPYPE - AnteChamber PYthon Parser interfacE. *BMC Res. Notes* **2012**, *5*, 367.

220. Frisch, M. J.; Trucks, G. W.; Schlegel, H. B.; Scuseria, G. E.; Robb, M. A.; Cheeseman, J. R.; Scalmani, G.; Barone, V.; Mennucci, B.; Petersson, G. A.; Nakatsuji, H.; Caricato, M.; Li, X.; Hratchian, H. P.; Izmaylov, A. F.; Bloino, J.; Zheng, G.; Sonnenb, D.J. Gaussian 09 2009.

221. Ahmed, Z.; Gooding, E.A.; Pimenov, K. V; Wang, L.; Asher, S.A. UV Resonance Raman Determination of Molecular Mechanism of Poly(N-isopropylacrylamide) Volume Phase Transition. *J. Phys. Chem. B* **2009**, *113*, 4248–4256.

222. Humphrey, W.; Dalke, A.; Schulten, K. VMD: Visual molecular dynamics. *J. Mol. Graph.* **1996**, *14*, 33–38.

223. Piçarra, S.; Relógio, P.; Afonso, C.A.M.; Martinho, J.M.G.; Farinha, J.P.S. Coil−Globule Transition of Poly(Dimethylacrylamide): Fluorescence and Light Scattering Study. *Macromolecules* **2003**, *36*, 8119–8129.

224. Eisenhaber, F.; Lijnzaad, P.; Argos, P.; Sander, C.; Scharf, M. The double cubic lattice method: Efficient approaches to numerical integration of surface area and volume and to dot surface contouring of molecular assemblies. *J. Comput. Chem.* **1995**, *16*, 273–284.

225. Swiatla-Wojcik, D.; Pabis, A.; Szala, J. Density and temperature effect on hydrogen-bonded clusters in water - MD simulation study. *Cent. Eur. J. Chem.* **2008**, *6*, 555–561.